Local Methods

for the

Cosmic Microwave Background

Thesis submitted for the Degree of Doctor of Philosophy in Astrophysics

Department of Physics
Imperial College London

Jude William Bowyer

Abstract

The standard tools for analyzing the Cosmic Microwave Background (CMB), a key component for making cosmological inferences, are usually of global sampling type. Such a methodological bias may preclude the development of important techniques for cosmology. This thesis develops $local$, real-space tools for CMB analysis which may be complemented using harmonic space techniques or provide useful signal diagnostics on their own.

Particularly, *finite-difference* schemes for performing local derivatives are investigated. One can define derivatives which extract the primordial polarization modes from the measured CMB Stokes parameters by constructing real scalar and pseudo-scalar fields. The detection of a primordial curl-like ('B'-mode) CMB polarization signal would imply the existence of a background of primordial gravitational waves, the 'smoking gun' signal of an inflationary cosmology. On an obscured (masked) sky, the gradient-like ('E'-mode) signal leaks into the B-mode signal when the standard harmonic E/B signal decomposition is performed — using local techniques instead, this leakage can be reduced since the masked region is not sampled from. An algorithm and a software package are developed for just such a calculation. Furthermore, differencing errors in the presence of discontinuous signals are utilized to produce the 'Laplacian-difference' method, which enhances pathological and discontinuous signals. Such signals, in the absence of systematics, might reveal the presence of cosmic defects.

The scalar and pseudo-scalar fields produced will feature self-coupled mode-transfer due to masking; the mode-transfer matrices are related to the optimal apodization schemes for extracting power spectra. The transfer matrices for various spectral operations on scalar fields are presented, which for the polarization spectra provide important computational advantages over the direct utilization of the E- and B-modes.

Contents

List of Figures

List of Tables

Declaration and Copyright

Unless otherwise explicitly stated or referenced in the text, the work presented in this thesis is due to the author.

Jude Bowyer
February 2011

Acknowledgements

There are probably too many a number of personal influences in the development of this thesis, both direct and subtle, to name; no offence should be taken by an omittance, only a measure of my own limitations.

Most directly, I'd like to thank my supervisor Andrew Jaffe for his guidance, advice and for generally always making himself available when confusions arose. I've learnt some important lessons on the nature of research, and on this endeavour we call "science".

I'd also like to thank the other members of the astrophysics and theoretical physics groups for their continued warmth and enlightening discussion, of both scientific and cultural value. And for the table tennis. I'd like to think I've made friends rather than just colleagues.

Finally, I'd like to thank Norton, Milo, the Dot, and of course the Line.

Foreword

The contents of this thesis were produced at Imperial College London between October 2007 and November 2010. They can be summarised thus:

- Chapter 1 provides an overview of the general theoretical and observational status of early universe cosmology, providing a motivation for the development of the later chapters. Particular focus is borne upon the temperature and linear polarization observables of the CMB, and their connections to fundamental physics via inflation and topological defects.

- Chapter 2 then develops specific motivations for local methods in CMB analysis: after an account of Bayesian inference, a general finite-differencing algorithm for polarization analysis is developed and the harmonic tools used to detect non-Gaussianity in the CMB are discussed. Further, in anticipation of apodization issues the local scalar field formalism is utilized to develop the basis of a general theory of mode-transfer for observed cosmological fields in the presence of masks. Next, the Laplacian-difference technique for isolating discontinuities is developed. This is then complemented with a discussion of the needlet method for decomposing local power. Finally, signals of a finite-resolution CMB are speculated on.

- Chapter 3 presents the MasQU software, the main technological result of this thesis. The various technical phenomena manifested in implementing the software on the HEALPix grid are discussed, along with improvements that the method presents over harmonic methods in determining the B-mode spectrum. The determination of real-space weights required to apodize the polarization signal is discussed. Lastly, toy models of discontinuous signals and discrete real-space CMB phenomena are constructed and studied using the Laplacian-difference formalism.

- Chapter 4 reports an analysis of the MasQU techniques as applied to available WMAP 7-year data and details some crude limits obtainable from fu-

ture Planck Surveyor data. A galaxy boundary contaminant in the 7-year WMAP ILC data is isolated and analyzed in the context of the CMB anomalies.

- Finally, Chapter 5 concludes.

Chapters 2 and 4 contain material which can be found in Bowyer & Jaffe [1]. Material from Bowyer, Jaffe & Novikov [2] can be found in chapters 2 and 3. All other material will be made available in forthcoming publications.

Chapter 1

An Overview of Modern Cosmological Physics

It is a curiosity that, for the amount of time it has spent in the collective human consciousness, cosmology is one of the youngest scientific studies. The first breakthrough in the path leading to a scientific cosmology came with Einstein's publications of the special [3] and general [4] theories of relativity. The former theory altered the causal structure in Newton's mechanics and hence made it clear that — due to the finite velocity of light — every time one looks through a telescope, one is really using a sort of time machine. The latter allowed the explicit construction of mathematical cosmologies [5] that could in principle be tested. The cosmologies derived from the general theory, under the assumptions of large-scale spatial homogeneity, isotropy and perfect fluid behaviour, yielded Friedmann's celebrated equations [6] which govern the dynamics of the universe. The Friedmann equations demand a dynamic universe, either contracting or expanding — something Einstein was philosophically unhappy with [7], enough so as to introduce an ad hoc cosmological constant Λ, which acted to metastabilize the universe. Conversely, Lemaître suggested a theory of the 'primeval atom' [8], now referred to as the Big Bang theory), which required an expanding universe. It was then in 1929 that Einstein's cosmological constant was disproven, upon Hubble's observations that the distant galaxies were receding both from us [9] and from each other. Some astronomers were initially dissatisfied with the Big Bang theory, deeming it to bring creationism into science [10] and alternatives were devised, most famously the 'Steady State' theory of Hoyle, Bondi and others [11]. Ironically it was Hoyle who coined the term 'Big Bang' for Lemaître's theory [12].

However, beside successfully accounting for the abundance of helium in the

Universe (Big Bang Nucleosynthesis [13]), the Big Bang theory had one unique prediction that Gamow [14] and others determined: when one combines an expanding universe with thermodynamics and the known characteristics of particle interactions (Thomson scattering), the prediction of an approximately uniform background radiation relic from the formation of the *surface of last scattering* during recombination is made. Specifically it is the mere existence of this cosmic background radiation, and not its temperature, which is the sufficient unique prediction of the Big Bang theory. This radiation was then found quite accidentally in 1965 by Penzias and Wilson [15], who were working on satellite communications[1], ahead of the efforts of the CMB theorist Dicke. The Big Bang theory was verified, with the CMB temperature now known to be $T_0 = 2.725 \pm 0.002\mathrm{K}$ [17].
Of course, this was neither far from the end of the predictions made by the Big Bang theory, nor of the development of the theory itself. Peebles, Silk and others [18] developed a theory for the primary anisotropies of the radiation, later confirmed with spectacular success by the DMR instrument on the COBE[2] (Cosmic Background explorer [19]) satellite in 1992 which revealed that the CMB temperature was homogeneous to one part in 10^5 (and which resulted in the 2006 Nobel Prize for Physics). COBE was then followed by smaller-budget sub-orbital experiments attempting to measure the first peak in the power spectrum of the temperature anisotropies. Later, experiments like the balloon-borne Boomerang [20] satellite (1998), and more completely the WMAP mission [21] (COBE's space-based successor, launched in 2001) confirmed that the Universe is almost perfectly spatially flat (as a corollary of the power spectra seen in Fig. 1.1 and measurements of the Hubble parameter) and re-enforced the discovery of the 'dark energy' currently accelerating the cosmic expansion, using observations of the spectrum of anisotropies.
The CMB is then a primary window into what is now referred to as *precision cosmology*: the coupling of the CMB observations with those of the light element abundances, supernova data and galaxy surveys, and with the technological and software advances that now allow one to quickly create cosmological simulations on even low-end computers has led to a remarkable increase in the accuracy and reliability of cosmological inferences. The successes of precision cosmology are numerous, and cosmologists can now boast a standard Big Bang model that naturally incorporates the cosmological observations. The story that unfolds is one

[1] See the first chapter of Naselsky et al [16] for an account of the near-misses for detecting the background radiation.
[2] COBE website: `http://lambda.gsfc.nasa.gov/product/cobe/`

of primordial density variations (the anisotropies) in the microwave sky sourcing the (predominantly bottom-up) formation of structure via gravitation. The first stars alight in a period of reionization; these stars evolve the chemical abundances in the universe that allow carbon-dense planets to form and eventually populate with observers who can infer the present-day accelerated expansion of the universe, within a cosmic timeframe of $\sim \mathcal{O}(13)$ Gyr. This standard model is typified by a small set of parameters and a mostly well-understood set of mass/energy types, of which normal matter only makes a tiny fraction.

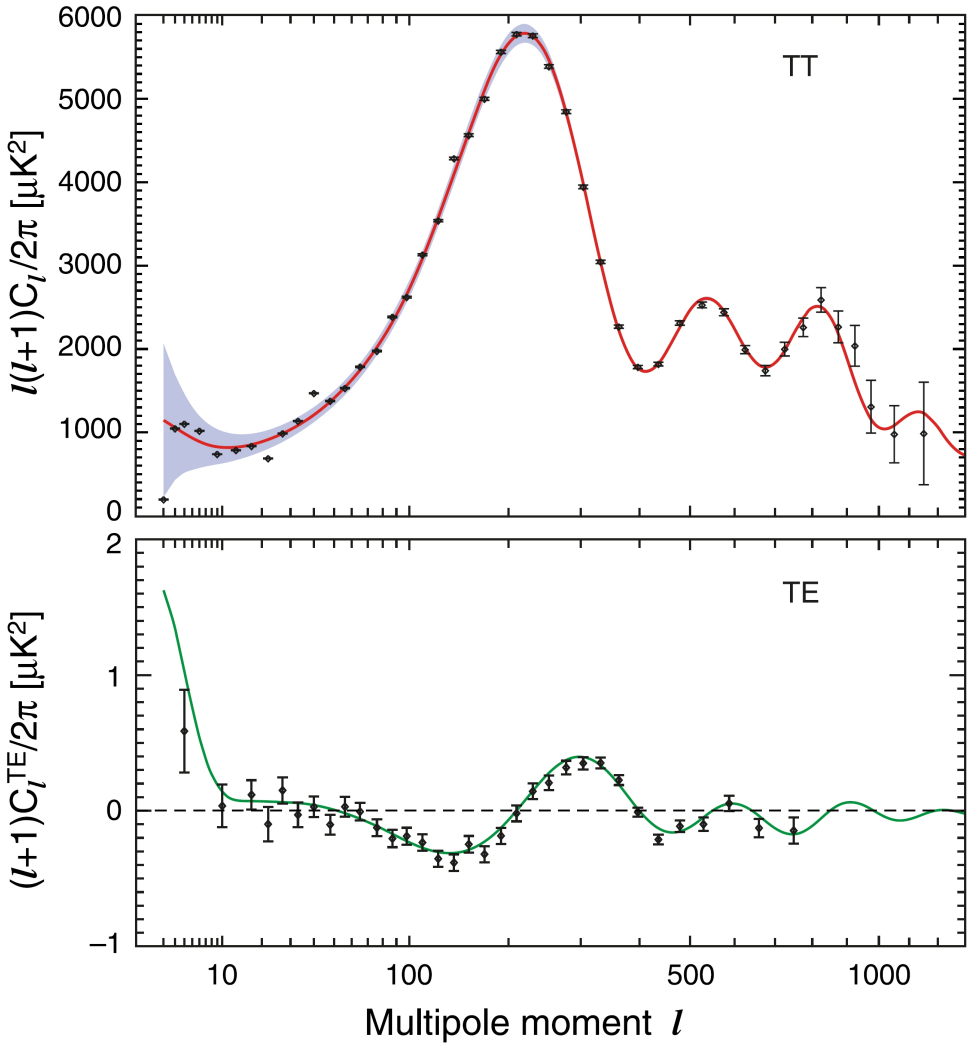

Figure 1.1: WMAP 7-year temperature-temperature (TT, top diagram) and temperature-E-mode polarization (TE, bottom diagram) correlation power spectra, from Jarosik et al [21]. The height of the first peak, and the acoustic oscillations in the TT spectrum betray the global geometry of the Universe and the physics of the CMB; the anti-phase correlation of the TE spectrum with the TT spectrum at around $l = 50$ is indicative of a predominantly adiabatic generation of fluctuations.

However, it has been determined that the standard model is in need of extension via an auxiliary hypothesis in order to explain various observational issues with the CMB — such as the 'flatness' and 'horizon' problems (more on these later). The simplest and most prominent hypothesis is *inflation*, first championed by Guth [22] as an economic solution to all the problems of the standard Big Bang model. In the simplest models, a slow-rolling scalar field inflates the universe, shrinking the comoving Hubble radius and inevitably leading to a dominantly Gaussian temperature perturbation field formed from adiabatic processes, with an almost scale-invariant spectrum as observed. Further to this, quantum effects from inflationary cosmology are sufficient to source the temperature anisotropies which in turn seed the formation of structure which is ubiquitous in the Universe. As will be shown, there is more useful information that can be gleaned from the CMB; particularly, its polarization can provide crucial insight into the nature of the inflationary mechanism. Whilst the consensus from observations is that inflation's initial competitor for structure formation, cosmic strings, is no longer viable as the main source of structural seeds there remain competitors that are yet to be falsified (variable-speed-of-light and ekpyrotic scenarios are examples). The prediction of large-scale curl-type ('B'-mode) polarization is a unique and generic consequence of inflation that would cement the status of inflation in cosmology, much as the detection of the CMB did for the original Big Bang model. This will be probed further by a number of future and current experiments, most notably by the *Planck* mission [23], which was launched in May 2009.

This chapter describes a rough account of the status of modern cosmology, with a focus towards the connection with fundamental physics; the relativistic framework underlying cosmology is described first and then the physics of the CMB along with the standard tools used to characterize it. The inflationary cosmological paradigm is then introduced, which most explicitly provides links between cosmology and fundamental physics, and describes how inflation provides the perturbations found in the CMB. Inflation is then linked with CMB polarization via gravitational waves and experimental issues and future observational prospects are briefly discussed. This discussion sets up an exploration of a number of outstanding problems and questions in early universe cosmology in the following chapter.

Unless stated otherwise, the details presented in this chapter can be found in standard textbooks on general relativity [24, 25], cosmology [16, 26, 27, 28, 29], and inflation in particular [30, 31, 32]. The notes on gravitational waves from the ICTP summer school in cosmology in 2008 [33] were also useful.

1.1 The Standard Big Bang

1.1.1 The General Relativistic Cosmology

The framework used to describe the cosmos is that of the general theory of relativity (GR). Since it is a theory of classical variables, it is expected to be valid only up until the Planck time where the consensus is that one expects a quantum theory of gravitation to take over; otherwise one is free to impose quantum fields over a relativistic background, so long as they are renormalizable. GR was conceptually revolutionary due to the way that spacetime works in the theory. The special theory of relativity showed that the field equations of Maxwell's electromagnetism were physically compatible with the Lorentz transformations, deformations of the Galilean relativity parameterized by c, the speed of light. It thus superceded Newton's mechanics with a theory wherein rotations can be made in time as well as space — this is popularly referred to as a unification of space and time, described by the rotation group $SO(3,1)$ — with all the requisite surprising results, such as the complete overthrow of the concept of absolute simultaneity for observers.

The general theory extended the special theory from inertial frames of reference to accelerated frames of reference, and in doing so swallowed up Newton's theory of gravitation. It turns out that observers in an accelerated frame of reference are equivalent to observers in a gravitational field. The mass of a body determines the geometry of spacetime, which in turn determines the gravitational field — in this sense the dynamics of the field are entirely dependent on the metric. Following the standard variational approach, one can start with the Einstein-Hilbert action

$$S_{EH} = \int \sqrt{-g} \left[\frac{c^4}{16\pi G} \mathcal{R} + \mathcal{L}_M \right] d^4x, \tag{1.1}$$

where G is the gravitational constant, $\mathcal{R}$ the Ricci scalar, $\mathcal{L}_M$ the matter Lagrangian and g the determinant of the metric $g_{\mu\nu}$, and perform an infinitesimal variation with respect to the metric to yield the stress-energy tensor (which describes the density and flux of energy and momentum)

$$T_{\mu\nu} = -\frac{2\delta \mathcal{L}_M}{\delta g^{\mu\nu}} + g_{\mu\nu}\mathcal{L}_M. \tag{1.2}$$

From here on in the theory convention is made use of, where units are defined such that the speed of light $c = 1$. One can then construct Einstein's field equa-

tions of gravitation

$$R_{\mu\nu} - \frac{g_{\mu\nu}}{2}\mathcal{R} = 8\pi G T_{\mu\nu} \tag{1.3}$$

which, in the presence of a cosmological constant Λ, have a factor $+\Lambda g_{\mu\nu}$ appended . The construction of cosmologies begins with these field equations and make use of the Friedmann-Lemaître-Robertson-Walker (FLRW) metric, a consequence of assuming a homogeneous and isotropic universe and so utilizing spherical symmetry. The FLRW metric is defined with a scale factor a and radius r which describes the evolution of the scale of the universe:

$$g_{\mu\nu} = \begin{pmatrix} 1 & 0 & 0 & 0 \\ 0 & -a^2(t) & 0 & 0 \\ 0 & 0 & -a^2(t)F^2(r) & 0 \\ 0 & 0 & 0 & -a^2(t)F^2(r)\sin^2\theta \end{pmatrix}. \tag{1.4}$$

Computing the scalar curvature $\mathcal{R}$ yields three general solutions in terms of the spatial curvature parameter k

$$F(r) = \begin{cases} \sin r & k = +1 \\ r & k = 0 \\ \sinh r & k = -1 \end{cases} \tag{1.5}$$

allowing the construction of $T_{\mu\nu}$; these solutions correspond to 'closed', 'flat' and 'open' cosmological models respectively. From the components of the (strictly diagonal) stress-energy tensor for a perfect fluid one yields Friedmann's celebrated equations:

$$\begin{aligned} \left(\frac{\dot{a}(t)}{a(t)}\right)^2 &= \frac{8\pi G\rho(t)}{3} - \frac{k}{a(t)^2} \\ \frac{\ddot{a}(t)}{a(t)} &= -\frac{4\pi G}{3}(\rho(t) + 3p) \end{aligned} \tag{1.6}$$

where the first Friedmann equation is normally encoded in the Hubble parameter $H = \dot{a}/a$ which determines the expansion rate of the universe and the overdot signifies a derivative with respect to t. The Friedmann equations can be solved exactly for a number of simple model universes; since gravitational collapse competes with the expansion rate, a critical density $\rho_{\rm cr} = 3H^2/(8\pi G)$ can be defined wherein gravitational and expansion dynamics are balanced. Defining the den-

sity ratio $\Omega = \rho/\rho_{\rm cr}$, one can obtain the evolution of the Hubble parameter

$$H^2 = H_0^2(\Omega_{m,0}a^{-3} + \Omega_{r,0}a^{-4} + \Omega_{k,0}a^{-2} + \Omega_{\Lambda,0}) \tag{1.7}$$

in terms of the functional densities for matter, radiation, the intrinsic curvature and a cosmological constant, where the implicit time-dependence notation has been dropped for simplicity and the subscript 0 indicates the value of the parameter today. For example, one can solve equation (1.7) for a matter-dominated universe with $\Omega_\Lambda = 0$, $\Omega_k = 0$ and $\Omega_r = 0$ yielding $a^3 \sim 2H_0t^2$. More generally, if the universe is dominated by a fluid with equation-of-state parameter $w = p/\rho$, then

$$\rho \propto a^{-3(1+w)}. \tag{1.8}$$

These simplistic details for homogeneous and isotropic universes were developed in the early 1920s; since physical considerations of the large-scale structure of the universe, which have since been borne out by observations [34], suggest that the universe is spatially isotropic and homogeneous on large scales it makes sense to utilize this analysis as a first-order approach, to be appended by perturbation analysis informed by the content of the universe. The time derivative of the scale factor a was confirmed to be positive by Hubble's famous observations (where Hubble's law is $v = Hr$ for the velocity v of receding galaxies at a distance r from the observer).

Following the observations of the likes of COBE and WMAP there exists now a *standard cosmological model* composed of a small number of mass-energy types; the large scale properties of the early universe are well-modelled by a homogeneous, isotropic perfect fluid featuring nonrelativistic 'baryons' and dark matter, photons, Dirac neutrinos and a cosmological constant Λ. This favoured cosmology is confirmed by Bayesian statistical analysis; its main remaining descriptive elements are a flat expanding universe with Hubble parameter $H_0 \approx 70$ kms^{-1}Mpc^{-1}, whose density is dominated by a cosmological constant ($\Omega_\Lambda \approx 0.73$), with cold dark matter (CDM) accounting for $\Omega_{\rm cdm} \approx 0.23$ whilst baryonic matter contributes just $\Omega_b \approx 0.04$. The main observations required for the construction of this model are the CMB, redshift-distance relations of type-Ia supernovae and large-scale structure surveys such as the Sloan Digital Sky Survey (SDSS) [35]. The combination of these observations alleviates the geometric degeneracies inherent in deriving cosmological parameters from the CMB alone and helps cosmologists to fully understand systematic and foreground issues. The focus of this thesis is the contribution made by the CMB.

1.1.2 The Cosmic Microwave Background

Once one appends the simplistic FLRW structure in the previous section with slightly more detail, i.e., a matter and radiation-filled universe with the general properties of the dominant particle specie, the inevitable prediction of an afterglow of the Big Bang is made. It can be argued that this afterglow, the CMB, has been the most useful observable for cosmology since it provides the earliest observational snapshot of the universe, occurring at a redshift of $z \sim 1100$ ($\sim 300,000$ years after the 'initial singularity'). Studies of the CMB by WMAP, Boomerang and others have resulted in a description of the large-scale Universe characterized by only one small table of parameters[3] (Table 1.1); with just this small table of inputs and the known laws of physics, a powerful enough computer could in principle simulate the entire universe.

Table 1.1: Summary of parameters generated from combined WMAP 7-year CMB, SDSS baryon acoustic oscillation and Hubble Space Telescope H_0 data, in the best-fit ΛCDM model.

Parameter	Value	Parameter	Value
Ω_b	0.0458 ± 0.0016	$\Omega_{\rm cdm}$	0.229 ± 0.015
Ω_Λ	0.725 ± 0.016	n_s	0.968 ± 0.012
τ	0.088 ± 0.014	$\mathcal{P}_\mathcal{R}(k_0)$	$(2.430 \pm 0.091) \times 10^{-9}$
σ_8	0.816 ± 0.024	$z_{\rm reion}$	10.6 ± 1.2
H_0	70.2 ± 1.4 km s^{-1} Mpc^{-1}	t_0	13.76 ± 0.11 Gyr

In an expanding universe filled with a non-exotic fluid, the mean temperature decreases with time; this has the corollary that the earlier, smaller universe was hotter. If the universe contains more than one type of entity, then since these energy densities correspond to different expansion rates it must have been through a range of phase transitions (some of which are enumerated in Table 1.2), marking changes of domination of energy density type, from radiation through matter to the present day dark energy.

It is instructive to analyze the effect of the phase transitions, occurring at mass/energy-type density equality points in the cosmic timeframe; of particular relevance here is the time of matter-radiation equality. Until an age $t_{\rm uni} \sim 70,000$

[3] Ω_b, Ω_Λ and $\Omega_{\rm cdm}$ are the density parameters for baryons, dark energy and cold dark matter respectively, τ is the optical depth, $\mathcal{P}_\mathcal{R}$ the power spectrum of the curvature perturbations, $z_{\rm reion}$ the redshift at which reionization occurred, t_0 the age of the Universe, H_0 the Hubble parameter today, σ_8 is the size of fluctuations on scales of 8 Mpc h^{-1} and n_s is the scalar spectral index. WMAP website parameters page: `http://lambda.gsfc.nasa.gov/product/map/current/parameters.cfm`.

Table 1.2: Stages in the evolution of the universe, adapted from Mukhanov [28]

Time after the 'initial singularity'	Mean temperature	Description
$< 10^{-43}$ s	$> 10^{19}$ GeV	Planck-era physics; the need for a theory of quantum gravity becomes unavoidable.
$10^{-36} \rightarrow 10^{-32}$ s	$\sim 10^{16}$ TeV$\rightarrow\sim 10^{14}$ GeV	Inflationary period.
$10^{-14} \rightarrow 10^{-10}$ s	~ 10 TeV$\rightarrow\sim 100$ GeV	Origin of electroweak symmetry-breaking and baryogenesis — the universe becomes filled with matter.
10^{-5} s	~ 200 MeV	Quark-gluon phase transition.
0.2 s	~ 1 MeV	Neutrino decoupling.
$200 - 300$ s	0.05 MeV	Nucleosynthesis.
10^{11} s	1 eV	Matter-radiation equality.
$10^{12} \rightarrow 10^{13}$ s	0.25 eV	CMB last scattering.
10^{13} yr	1 meV	Today.

years, long after the inflationary period is supposed to have run its course, the Universe was radiation-dominated. Since the mean radiation density would have been too high for the formation of stable atoms, the Universe would have been mainly filled with an opaque 'photon-baryon'[4] plasma, in thermal equilibrium. As the particle density must decrease with time then there is a period in the early universe when the expansion rate starts to exceed the mean collision rate between quanta; for photons and baryons this is the *decoupling time*, a period after which the universe is no longer an opaque plasma, but when photons can stream freely with low probabilities of collision. Such a decoupling time corresponds to a *surface of last scattering* (LSS), the origin of the CMB. One can calculate the expected CMB temperature at decoupling starting at the mean energy of a photon $\langle E_\gamma \rangle = 3k_B T_\gamma$ (with k_B the Boltzmann constant), leading to the number density of photons capable of ionizing hydrogen at temperature T

$$\frac{n_{\rm ion}}{n_\gamma} = \exp\left[-\frac{E_{\rm ion}}{k_b T}\right] \tag{1.9}$$

where the energy required to ionize Hydrogen is $E_{\rm ion} \approx 13.6$ eV. An electrically neutral universe ($n_e = n_b = 10^{-9} n_\gamma$) then implies a mean decoupling temperature of ~ 3000 K.

[4]This is somewhat of a misnomer among astrophysical terms, since the plasma contains leptons too.

The main features of the CMB remain intact during cosmic evolution, meaning that observations of the CMB now allow one to determine its state at decoupling. Standard thermodynamics suggests that such a plasma would be in thermal equilibrium, best described by a Planck blackbody spectrum; it can be shown that a blackbody CMB at redshift z_{LSS} will be a blackbody at a later z_{obs}. Indeed this is what COBE's FIRAS instrument found in 1992, and it is said that the CMB spectrum is the most perfect blackbody curve observed yet in nature [36].

The details of decoupling produce the observables that modern cosmologists are interested in. At $z \sim 1100$, the mean temperature of the blackbody spectrum reached 0.3 eV and the average photon was no longer energetic enough to prevent formation of H atoms[5]; immediately before this decoupling period, the universe was opaque. The elastic scattering of photons off electrons is described by Thomson scattering. Thomson scattering generically results in a dipole due to the coupling of the electron's motion with the oscillation of the photon field. The electric and magnetic fields of a photon oscillate transverse to the direction of propagation. One might assume then that the CMB radiation is unpolarized since Thomson scattering is a necessary but not sufficient means to produce polarized radiation: if the radiation field is isotropic, the intensities of polarized photons incoming from opposite directions cancel. The scattering cross-section σ_T over the scattering surface Ω is governed by

$$\frac{d\sigma_T}{d\Omega} = \frac{3\sigma_T}{8\pi}|\hat{\epsilon} \cdot \hat{\epsilon}'|^2 \tag{1.10}$$

where the ϵ terms describe the propagation directions of the incoming and outgoing photon. For isotropic radiation incident on the electron from all directions, the radiation quanta from incoming and outgoing directions have equal intensities so the outgoing wave intensities along the x- and y-axes are equal, resulting in an unpolarized emission. It will later be seen that the CMB is in fact weakly polarized, and that this has important ramifications.

The Thomson scattering effectively ceases due to an increase in the photon mean free path, forming the surface of last scattering and allowing photons to stream freely. This process is an extended one due to the tail in the Planck blackbody function. As previously mentioned, the temperature distribution has fluctuations of one part in 10^5. Temperature fluctuations in the CMB are induced by a range of physical processes, including:

[5]This is lower than the binding energy due to the large photon-to-baryon ratio introduced in equation (1.9).

- A change in radiation density at a given point due to dark-matter-enhanced photon acoustic oscillations.
- A Doppler shift due to the motion of the CMB with respect to the observer; together with the density oscillations these dominate perturbations on scales characterized by multipoles $50 \lesssim l \lesssim 600$.
- The Sachs-Wolfe effect, the gravitational redshift of a photon leaving a potential well; this effect dominates perturbations on super-Hubble-radius scales at decoupling. There is also the integrated SW effect, which is simply the same effect but for time-evolving gravitational potentials.
- Diffusion (Silk) damping, the statistical random walk of photons through an opaque plasma; this exponentially suppresses fluctuations on small scales, combining with rescattering from reionization to wash out fine-grained anisotropies.

The most important of these mechanisms for the purposes of this text is the radiation density variation which is seeded by acoustic oscillations in the photon-baryon fluid. During the radiation era, competition between gravitational collapse and radiation pressure sets up acoustic waves in the plasma. The density modes will be either expanding or collapsing during the recombination period, and hence when Thomson scattering ceases, the modes will be frozen in on the horizon scale (i.e., depending on their collapse/expansion radius at the time of last scattering). So the acoustic modes will exist at different scales — this manifests itself in temperature overdensities. Furthermore, the modes are affected further by the presence of a pressureless dark matter component (enhancing the gravitational well of a dense region).
This radiation density variation informs cosmologists about the large-scale properties of the universe; one example is geometry. Due to the sizable distance between the LSS and Earth, any large intrinsic curvature in the universe will have observable curved geodesics. For example, in a positively curved universe, non-identical geodesics bearing from the same point bend toward each other. This is essentially the reason that the search for a justification of Euclid's parallel postulate was to put to bed: it turns out to be the special case for a flat space. The angular diameter distance $D_A = d/\theta$, the ratio of the intrinsic size of a region over the angular size as viewed by an observer, should then change with geometry: for a flat geometry with a dominant dark energy component, the horizon at the LSS subtends approximately 2 degrees on the sky. The prominent peak in

the CMB power spectrum at $l \sim 200$, combined with Hubble data, then implies a flat universe. By comparing the apparent observed scale with a known physical scale at the LSS, one can determine the large-scale geometry of the universe — two such scales are the sound horizon after scattering (which is set by the wavelengths of the acoustic oscillations) and the Silk (diffusion) damping scale. This measurement must be coupled with a determination of the matter content Ω_m and cosmological constant term Ω_Λ in order to avoid a geometrical degeneracy.
The CMB provides a context against which which two other important cosmological processes take place: nucleosynthesis and galaxy formation. Nucleosynthesis is the mechanism for generating the observed quantities of the light elements such as D, ^{3}He and ^{7}Li; at around approximately the first three minutes, the neutron-proton ratio froze as the universe cooled to ~ 1 MeV since the expansion rate dilutes neutron-to-proton inter-conversion. β-decay further reduced the ratio to $\sim 1/7$, whilst light element production started at ~ 0.1 MeV. Since the vast majority of neutrons are combined into ^{4}He and the formation rates of the other elements are dependent on both the Hubble expansion rate and the baryon density, one can use the observations to check the consistency of standard particle physics with reality. The timespan for Big Bang nucleosynthesis is further constrained by the requirement of a dearth of elements heavier than Beryllium in the early universe.
The decoupling of photons has its analogous process with neutrinos, forming a neutrino background (which remains only indirectly detected [37]). These neutrinos free-stream and also contribute to the cosmological radiation energy density; the main effect of this is as radiative pressure, the anisotropic stress damping the photon acoustic oscillations. Indeed, cosmological observations also provide a method with which to determine the mass of neutrinos — the accepted solution to the solar neutrino problem[6] is to allow mass eigenstate mixing in the Pontecorvo-Maki-Nakagawa-Sakata (PMNS) matrix, inducing neutrino flavour oscillations and a non-zero neutrino mass. Observations imply that this mass, if the solution is correct, must be tiny — less than ~ 1eV [38].
In order to take further information from the CMB, one looks to the anisotropies that exist on a small scale by the utility of power spectra. These anisotropies are responsible for the formation of structure. The details of structure formation are left for the next section, when the matter power spectrum is discussed.

[6] A discrepancy between the theoretical and observed solar flux of electron neutrinos, approximately a third of what is expected from the standard model of particle physics combined with known solar physics. Neutrino flavour oscillation, indicative of a non-zero neutrino mass, can resolve this issue.

1.1.3 Power Spectra

One can only observe one universe, from one vantage point; in order to make rigorous statements about cosmology, it is necessary to consider what statistics can be used to make valid inferences since, for a random field, individual samplings on the observed sky imply very little about the underlying processes. The angular n-point function

$$\left\langle f(\hat{\Omega}_1) f(\hat{\Omega}_2) \cdots f(\hat{\Omega}_n) \right\rangle \tag{1.11}$$

is just such a statistic, which describes the ensemble average clustering of a random field; since the CMB at last scattering is a collection of random and independent processes, the central limit theorem ensures that the n-point function can be applied to CMB studies. Unfortunately, it is not always the case that data points of the correlation function at different scales are independent of each other. Instead one should use a basis which is necessarily orthogonal, such as a harmonic basis. This is where the power spectrum comes in.

The power spectrum is a measure of the amplitude of a signal at different scales (the statistically isotropic harmonic transform of the two-point correlation function), and for a purely Gaussian signal is the most compact and complete description of a signal. In cosmology it comes in two forms: the theoretical power spectrum and the observable angular power spectrum. The power spectra are of central importance to CMB studies since they are the major descriptors of CMB physics, complementary to that of the correlation function, although later the importance for cosmology of spectra associated with non-Gaussianity shall be seen.

To understand where the power spectra come from, consider a random field g in a comoving box of length L, with harmonic components g_k in momentum space k. The probability of finding the real part R of g_k with variance σ^2 is given by

$$P(R) = \frac{1}{\sqrt{2\pi}\sigma} \exp\left[-\frac{R^2}{2\sigma^2}\right], \qquad \sigma^2 = \frac{1}{2}\left\langle |g_k|^2 \right\rangle. \tag{1.12}$$

As the box becomes large, the variance becomes independent of the direction of the modes k, so the power spectrum $\mathcal{P}_g$ can be defined thus:

$$\mathcal{P}_g(k) \equiv \left(\frac{L}{2\pi}\right)^3 4\pi k^3 \left\langle |g_k|^2 \right\rangle, \qquad \left\langle g^2(x) \right\rangle = \int_0^\infty \mathcal{P}_g(k) \frac{dk}{k}. \tag{1.13}$$

By taking the harmonic transform of the two-point average, the power spectrum takes the form

$$\langle g_k^* g_{k'} \rangle = \delta^3(k - k') \frac{2\pi^2}{k^3} \mathcal{P}_g(k), \tag{1.14}$$

which is statistically invariant under rotations and translations. The CMB power spectra depend on almost all the cosmological parameters, making for a powerful probe of cosmology. For the case of the observational CMB one works on the sphere, so it is necessary to determine the angular power spectra. Given the harmonic decomposition of a field F on the sphere into harmonic coefficients

$$a_{lm}^F = \int F(\Omega) Y_{lm}^*(\Omega) d\Omega, \tag{1.15}$$

and assuming statistical isotropy, the angular spectrum has variance and mean governed by

$$C_l^{FF'} \delta_{ll'} \delta_{mm'} = \left\langle a_{lm}^{F*} a_{l'm'}^{F'} \right\rangle, \qquad \left\langle a_{lm}^F \right\rangle = 0 \tag{1.16}$$

respectively, where isotropy is confirmed by checking for invariance under rotation by the operation of the Wigner D-matrices. A corollary of all this is that if the signal is fully Gaussian, all that is needed to describe it is its mean and variance, naturally encoded in the power spectrum. Specifically, one averages over azimuthal multipoles m to construct the observable power spectrum, meaning that the correlation function is only dependent on the separation angle θ between two points on the sphere. For a statistically isotropic universe this has the effect of averaging over noise.

The statement that the CMB is primarily constructed from an ensemble of independent processes neglects gravity. In this sense then, one can decompose the fluctuations of the CMB signal into (Gaussian-distributed) non-gravitationally-enhanced physics and the remaining non-Gaussian distribution, which is known to be small. Unlike the Gaussian case, a non-Gaussian signal can manifest itself in any number of the higher-order correlation functions corresponding to the bispectrum (harmonic transform of the 3-point function), trispectrum (4-point), and so on. If the CMB is fully Gaussian, the angular spectra at different multipoles l are uncorrelated.

In modern cosmology, the main types of spectra cosmologists are concerned with are the matter power spectrum, the CMB temperature anisotropy spectrum that seeds it, and the CMB polarization spectra; in order to make the connection between the anisotropies of the CMB measured now and their state at decoupling one needs a construction of the theoretical power spectra based on physical the-

ory and a transfer function between epochs.
Since the initial temperature fluctuations are randomly-distributed and their evolution via gravitation is non-random, each mode has the same direction-independent phase. These initial fluctuations that form the seeds of structure formation are enhanced by the presence of dark matter haloes which are probed via the matter power spectrum. The Newtonian potential today is given by

$$\Phi_{\mathbf{k}}(a) = \frac{9}{10}\Phi_{\mathbf{k},0}T(k)D(a), \tag{1.17}$$

where $T(k)$ is the transfer function for mode transfer across the horizon (dependent only on k), $D(a)$ is the growth function and $\Phi_{\mathbf{k},0}$ is the initial potential, determined by the inflationary mechanism. The Poisson equation for dark matter density perturbations leads to a calculation of the density contrast $\delta = \delta\rho/\rho$

$$\delta_{\mathbf{k}}(a) = \frac{3k^2}{5\Omega_m H_0^2}\Phi_{\mathbf{k},0}T(k)D(a). \tag{1.18}$$

This information is used to define a power spectrum for the density perturbations and the potential

$$\langle \delta_{\mathbf{k}}, \delta^*_{\mathbf{k}'} \rangle = (2\pi)^3\delta(k-k')\mathcal{P}_\delta(k,a), \qquad \langle \Phi_{\mathbf{k}}, \Phi^*_{\mathbf{k}'} \rangle = (2\pi)^3\delta(k-k')\mathcal{P}_\Phi(k,a) \tag{1.19}$$

with $\mathcal{P}_\Phi$ the primordial value of the curvature power spectrum

$$\mathcal{P}_\Phi(k) \propto k^{n_s-4}, \qquad \mathcal{P}_\delta(k) \equiv A_S k^{n_s} T^2(k) D^2(a) \tag{1.20}$$

where $n_s = 1$ is the Harrison-Zel'dovich (HZ) scale-invariant case for the scalar spectral index n_s, as predicted by standard inflation models and A_S the scalar spectral amplitude at horizon-crossing. Since primordial perturbations are expected to behave the same way on all scales except at the sound horizon, it makes sense that the initial power spectrum should be approximately given by the featureless power law HZ case.
Taking the ensemble average of the temperature field, the theoretical temperature anisotropy spectrum is obtained:

$$C_l^{TT} = \frac{2}{\pi}\int k^2 \mathcal{P}_\Phi(k) \left|\frac{T_l(k)}{\Phi(k)}\right|^2 dk \tag{1.21}$$

where T_l is the photon transfer function with source function S

$$T_l(\eta_0, k) = i^l \int_0^{\eta_0} S(\eta, k) j_l(k(\eta_0 - \eta)) d\eta \tag{1.22}$$

in terms of Bessel functions j_l. In order to determine the relation between observations today and the primordial power spectrum, one must solve the Boltzmann equations for radiative transfer[7],

$$\left.\begin{aligned} \Pi &= T_2 + T_{P2} + T_{P0} \\ \dot{T} + ik\mu T &= -\dot{\Phi} - ik\mu\Psi - \dot{\tau}\left[T_0 - T + \mu v_b - \tfrac{P_2(\mu)}{2}\Pi\right] \\ \dot{T}_P + ik\mu T_P &= -\dot{\tau}\left[-T_P + \tfrac{1}{2}(1 - P_2(\mu))\Pi\right] \end{aligned}\right\} \text{photons}$$

$$\left.\begin{aligned} \dot{\delta} + ikv &= -3\dot{\Phi} \\ \dot{v} + \tfrac{\dot{a}}{a} v &= -ik\Psi \end{aligned}\right\} \begin{matrix}\text{dark} \\ \text{matter}\end{matrix} \tag{1.23}$$

$$\left.\begin{aligned} \dot{\delta}_b + ikv_b &= -3\dot{\Phi} \\ \dot{v}_b + \tfrac{\dot{a}}{a} v_b &= -ik\Psi + \tfrac{\dot{\tau}}{R}[v_b + 3iT_1] \end{aligned}\right\} \text{baryons}$$

$$\dot{N} + ik\mu N = -\dot{\Phi} - ik\mu\Psi \qquad \begin{matrix}\text{massless} \\ \text{neutrinos}\end{matrix}$$

and the Einstein equations for the perturbations,

$$\begin{aligned} k^2\Phi + 3\frac{\dot{a}}{a}\left(\dot{\Phi} - \Psi\frac{\dot{a}}{a}\right) &= 4\pi G a^2[\rho_m \delta_m + 4\rho_\gamma T_0] \\ k^2(\Phi + \Psi) &= -32\pi G a^2 \rho_\gamma T_2 \end{aligned} \tag{1.24}$$

at first-order. The Boltzmann equations describe the evolution of the particle distributions. The full range of equations is shown to portray the intricacy of the required calculations. These coupled equations had been quite time-expensive to solve until the introduction of CMBFAST[8] [39], which uncoupled the geometric and dynamic aspects of the Boltzmann equations on super- and sub-horizon scales[9]; the temperature anisotropy is written as a time integral over the product of a geometrical term and a source term. Furthermore, whilst previous methods

[7] τ is the optical depth, μ is the direction of photon propagation, v is the electron velocity (or baryon velocity if subscripted with a b), N is the neutrino distribution function, P_2 is the Legendre polynomial for $l = 2$, whilst T_0 and T_2 represent the monopole and quadrupole parts of the temperature perturbations, with T_P and T_{P2} their polarization field counterparts. The Φ and Ψ terms are Bardeen's gauge-invariant potentials. These equations are written with respect to conformal time $d\tau = dt/a$ rather than time.

[8] CMBFAST website: `http://cfa-www.harvard.edu/~mzaldarr/CMBFAST/cmbfast.html`

[9] See chapter 8 of Dodelson [27] for an excellent account of the evolution of anisotropies.

had computed the evolution of each primordial photon perturbation moment to the present day, the CMBFAST method uses a line-of-sight approach (in effect, the ray-tracing approach) to speed up the calculation.

The Matter Power Spectrum

The matter power spectrum allows one to probe the density of matter and the evolution of structure. Measurements of the galaxy power spectrum (in order to characterize the galaxy distribution), which is related to the matter power spectrum via a bias $\mathcal{P}_{\rm gal} = b^2\mathcal{P}_m$, provides an observational handle on the matter distribution. The bias is related to the existence of dark matter haloes enveloping the galaxies, meaning that one can also trace the underlying dark matter distribution; since galaxies are the peak densities of the matter distribution, $\mathcal{P}_{\rm gal}$ represents the regions of matter density above some threshold. The requirement for dark matter has its roots in Zwicky's [40] observations that the virial mass within clusters was considerably larger than that accounted for by mass-luminosity relations; further evidence came from the famous galactic rotation curve plots [41] which are approximately flat scaling against distance from the galactic origin, whereas Keplerian dynamics would demand an inverse square relation. Recently, alternatives to dark matter such as Modified Newtonian Dynamics (MOND) have been dealt a significant blow by observations of the Bullet cluster [42] 1E 0657-56, showing a clear discrepancy between the x-ray emittance map for the gas component and the weak lensing map that describes purely the mass distribution in the cluster. The dark component is popularly expected to be of the 'cold' WIMP[10]-type [43, 44], since neutrino-based 'hot' dark matter is excluded due to their inhibiting of small-scale structure.

In order to make predictions of the observed structure from underlying cosmological constraints, it is possible to perform hydrodynamical n-body simulations, the Millenium simulation being the most famous example (Fig. 1.2). Since these simulations need to evolve gravitationally, they can be understood analytically in terms of collapse models, and (along with much of the remaining computational physics involved) are highly simplified in order that computation at large n is even feasible. The simplest model is the spherical collapse model, wherein each cluster is approximated by a 'baby universe' bubble in which a collapse proceeds. For any collapse to occur at all, the minimum constraint is that the bubble contains a mean density $\rho = \rho_{\rm cr}$. This scenario corresponds to the linear regime. One

[10]Weakly-Interacting Massive Particle.

then wishes to produce a small perturbation δ in an infinitesimally thin spherical shell, in order to induce the collapse and enter the non-linear regime ($k = 1$) from $\Omega_{\text{bubble}} = 1 + \delta_c$. Newton's iron sphere theorem implies that the universe outside the bubble is entirely unaffected by that inside the bubble. The space outside the bubble ('background') has $\Omega_m < 1$, so evolves similarly to a $k = -1$ universe. For a universe composed of multiple bubbles (i.e., more than one cluster), it is important that shell lines must not cross if the simplicity of the analysis is to be maintained. This model requires that the virialization process be built-in *by hand*, since in reality clusters do not collapse to a point.

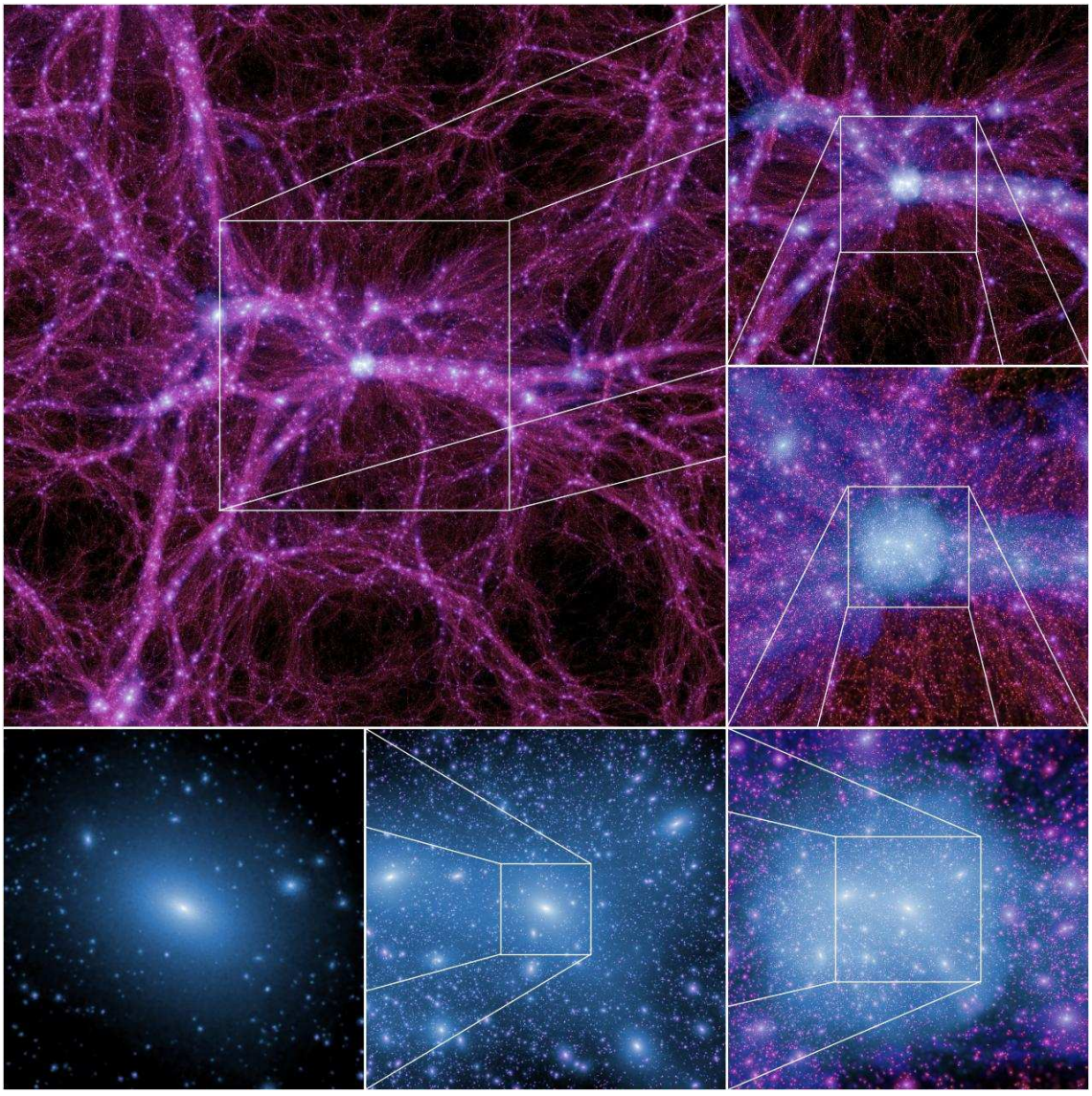

Figure 1.2: Sequential zoom through the Millenium-II simulation due to the Virgo consortium, from Boylan-Kolchin et al [45].

Starting with a local scale factor A of the bubble in the Friedmann equations

(equation (1.6)), one can derive

$$H_0^2 \Omega_{m,0} \mathrm{A}_0^3 = \frac{\Omega_{m,0}}{H_0 |\Omega_{m,0} - 1|^{3/2}} \tag{1.25}$$

which is constant by definition. Further analysis then reparameterizes the evolution of the model in terms of the horizon coordinate η

$$\mathrm{A}(\eta) = \frac{\Omega_{m,0}}{2H_0 |\Omega_{m,0} - 1|^{3/2}} (1 - \cos\eta), \qquad t(\eta) = \frac{\Omega_{m,0}}{2H_0 |\Omega_{m,0} - 1|^{3/2}} (\eta - \sin\eta). \tag{1.26}$$

In a collapsing universe the scale factor reaches a maximum $\mathrm{A}_{\max}$ at $\eta = \pi$,

$$\mathrm{A}_{\max} = \frac{\Omega_{m,0}}{H_0 |\Omega_{m,0} - 1|^{3/2}}, \qquad t_{\max} = \frac{\pi \Omega_{m,0}}{2H_0 |\Omega_{m,0} - 1|^{3/2}}. \tag{1.27}$$

It is then possible to study perturbations by utilizing low-order expansion terms

$$\frac{\mathrm{A}_{\mathrm{lin}}}{\mathrm{A}_{\max}} \simeq \frac{1}{4} \left(6\pi \frac{t}{t_{\max}} \right)^{2/3} \left[1 - \frac{1}{20} \left(6\pi \frac{t}{t_{\max}} \right)^{2/3} \right], \tag{1.28}$$

yielding the linear expression for the growth of a perturbation in a spherical bubble where the first term represents the expansion of the background universe, whilst the second term is the lowest-order expansion of the perturbation. For the full non-linear description, one would want to use the expansion to all orders. At turnaround, the point at which the bubble has reached maximum expansion and starts to collapse, the linear term yields a density contrast $\delta_c = 1.06$; at collapse, $\delta_c = 1.686$. In the real universe (i.e., in presence of pressure) this collapse never reaches $a = 0$. Also, one cannot expect that the density perturbation will be symmetric about the shell; in fact one can see the result of asymmetries in the collapse mechanism by the fact that 'pancake'-like structures are observed in the Universe. However, the analysis serves as a reasonable approximation. One also needs to determine the density contrast for the non-linear regime, both at turnaround and at the final collapse stage. It turns out that solutions give values of $\Omega_m + \delta_c = 5.55$ for the density at turn-around and $\Omega_m + \delta_c = 177.6$ (the cluster overdensity) for the density at virialization in the non-linear regime.

The utility of the overdensities that have been determined is in a suitable theory that defines a mass function with which to calculate the number of collapsed objects of a given mass M. Such a theory was developed by Press and Schechter [46] in 1974, and shows a remarkable correspondence with numerical simulations, despite some theoretical shortcomings [27, 47]. The theory is based on taking a ran-

dom Gaussian density field and smoothing it beyond some density threshold; in other words one assumes that only the largest overdensities (confined to smaller regions) collapse to form clusters. The smoothing is invariant across mass scales. For such a density field, the number distribution above a given mass decays exponentially. One problem with neglecting densities beyond a threshold, is that it limits the number of objects that can form bound structures to less than that in the real universe; an area with a small non-zero overdensity will still collapse to form a bound structure, albeit it will take longer to do so (this is known as the 'cloud-in-cloud' problem).

The root-mean-square (rms) mass fluctuation parameter in PS theory features a spherical top-hat window function in momentum-space that defines the scale of the fluctuations. If one assumes the cluster mass follows the spherical model and that the probability for finding a given overdensity at a given point in space is given by a Gaussian distribution, then by following through arguments for the probability densities of clusters with mass M forming within a radius A one can obtain the PS mass function:

$$M^2 \frac{dn}{dM} = 2\delta_c \rho_0 \left| \frac{d \ln \sigma}{d \ln M} \right| P(\delta_c) \tag{1.29}$$

where the factor of 2 comes from the cloud-in-cloud problem, σ is the density variance and $P(\delta_c)$ is the probability of the overdensity. The PS mass function provides an indispensable weapon with which to determine the evolution of density perturbations, in such a way that cosmological models can be differentiated. As one might expect, there are some small deviations of PS theory from full numerical simulations. A more exact form of the number density per object of mass M has been determined, such as that given by the Virgo consortium [48].

Such constructions allow one to place constraints on cosmological parameters such as Ω_m, the cluster-scale matter power spectrum, and even dark energy, which can affect the comoving cluster volume term $dV/d\Omega dz$, the growth factor in the mass function dn/dM, where its effect is most prominent, and the limiting mass $M_{\rm lim}$ over which one can evaluate expected cluster populations.

Complementary to large-scale simulations are the ambitious surveys which have sought to map the quantities which inform the matter power spectrum. The 2dF galaxy redshift survey [49] for example, took photometry of over 200,000 galaxies in the local universe allowing for a measurement of $\Omega_m h$ and confirming the acoustic oscillations of baryonic matter. Later, the SDSS survey mapped spectra for over 1 million objects, mostly galaxies and quasars, detailing the void and

filamentary details of the large-scale structure of the Universe [50], further confirming the baryonic acoustic oscillations [51] — notably the acoustic peak that conforms to the standard cosmological parameters — and detailing such properties as the cluster mass function [52]. Curiously, the cross-correlation of the galaxy density with the CMB temperature field can be used to infer the late-time integrated Sachs-Wolfe effect (the linear Rees-Sciama effect [53]), providing further evidence for dark energy [54]. Further to these are observations of weak gravitational lensing (which traces the mass distribution via distortion of the photon geodesic from background luminous bodies — 'cosmic shear'), and the Lyman-α forest, the absorption lines in the spectra of distant quasars produced by the neutral hydrogen in regions of overdense intergalactic gas along the line of sight at a redshift $z \sim 2-4$, which allows one to probe the population of neutral hydrogen clouds.

The Observed Temperature Power Spectrum

Complementing the matter power spectrum which relates to gravity-driven spherical collapse, the CMB temperature angular power spectrum codifies the observed scalar perturbations which source the collapse mechanism. One can decompose the temperature field into the mean part $\bar{T}$ and the anisotropic fluctuations δT

$$T_{\rm CMB}(\Omega) = \bar{T} + \delta T(\Omega) \tag{1.30}$$

Since there is no further need of the mean temperature in this thesis, the anisotropy field is referred to simply by T; it can be expanded in spherical harmonic space (using the spherical harmonics Y_{lm}) as

$$T(\Omega) = \sum_{l=1}^{\infty} \sum_{m=-l}^{l} a_{lm}^{T} Y_{lm}(\Omega), \qquad a_{lm}^{T} = \int T(\hat{n}) Y_{lm}^{*}(\Omega) d\Omega. \tag{1.31}$$

From here on in, the notational identity $\sum_{lm} \equiv \sum_{l=1}^{\infty} \sum_{m=-l}^{l}$ shall be used to denote the summation of harmonic components. For observational purposes it is necessary to construct an unbiased (i.e., with $\left\langle \hat{C}_l \right\rangle = C_l$) estimator $\hat{C}_l$ of the power spectrum:

$$\hat{C}_l^{TT} = \frac{1}{2l+1} \sum_{m=-l}^{l} a_{lm}^{T*} a_{lm}^{T} \tag{1.32}$$

with the $2l+1$ factor due to normalization. The multipoles scale as $l \sim 180^o/\theta$, so multipoles at larger l correspond to a smaller angular resolution. Since for a

Gaussian field the power spectrum already specifies all the information, then the correlation function is simply

$$C^{TT}(\theta) \equiv \langle T(\hat{\mathbf{n}}_1)T(\hat{\mathbf{n}}_2)\rangle_{\cos\theta=\hat{\mathbf{n}}_1\cdot\hat{\mathbf{n}}_2} = \sum_l \frac{2l+1}{4\pi} C_l^{TT} P_l(\cos\theta) \tag{1.33}$$

where the P_l are the Legendre functions and statistical isotropy is assumed. Measuring the temperature power spectrum is not quite as simple as this, of course. One can only ever measure one sky (which is a rather small statistic), so the ensemble average variance of the sampled harmonic coefficients limits what can be said about low-l cosmology; this is known as cosmic variance, expressed by

$$\delta C_l = \frac{C_l}{\sqrt{l+\frac{1}{2}}}. \tag{1.34}$$

This fundamental limit to the accuracy of statements at a given l has not stopped cosmologists attempting to overcome it [55, 56, 57, 58].
Of course, one wants to connect the angular power spectrum with the theoretical power spectrum; as mentioned, this mapping is achieved by determining the photon transfer function in equation (1.22) and solving the Boltzmann transfer equation given in equation (1.23). Solutions to the Boltzmann equations yield the form of the peaks in the power spectrum, such as the first peak of the TT spectrum, which is dependent on the angular diameter distance D_A, describing the horizon scale at recombination. Observationally, there are complications involved with noise and the fact that one cannot observe the whole sky (due to i.e., galaxy obscuration). A variety of methods then exist to produce estimators of the temperature power spectrum [59]; maximum likelihood methods compute the determinants of non-sparse $n \times n$ covariance arrays, with computations scaling as $\sim \mathcal{O}(n^3)$; quicker, less accurate calculations can be performed using quadratic methods, which scale as $\sim \mathcal{O}(n^{3/2})$.

Polarization Spectra

The first to realize that the CMB should be polarized was Rees [60]. In order for a photon field to be polarized, it needs to feature anisotropies. Fortunately, it is already known that anisotropies are produced in the CMB and that Thomson scattering will produce a dipole. However, a dipole pattern is not enough since this leads only to intensity cancellations. The incoming radiation is required to have a nonzero quadrupole in order to produce linear polarized radiation (Fig.

1.3) — such a quadrupole is generated, for example, by velocity distributions in the CMB plasma that are not in phase with the density modes. Rapid Thomson scattering (i.e., a small optical depth for the LSS) would destroy any quadrupole anisotropy, so it is only thanks to an extended optical depth that the quadrupole can be measured.

For a nearly monochromatic plane wave propagating in the z-direction, the electric field vector $\mathbf{E}$ can be decomposed into a combination of $n = 2$ basis terms ϵ_n

$$\mathbf{E} = (E_+\epsilon_+ + E_-\epsilon_-)e^{i(\mathbf{k}\cdot\mathbf{x}-\omega t)}, \tag{1.35}$$

where the E_n are the wave amplitudes (in this case, a circular basis has been chosen). For a polarized wave, there will be a correlation between the two elements E_1 and E_2 of the vector in a linear basis given by basis terms ϵ_1 and ϵ_2 — if they have the same phase then the wave is linearly polarized, else the wave is elliptically polarized. The properties ($\epsilon_1 \cdot \mathbf{E}$, $\epsilon_2 \cdot \mathbf{E}$) and ($\epsilon_+^* \cdot \mathbf{E}$, $\epsilon_-^* \cdot \mathbf{E}$) are then amplitudes of radiation: respectively these correspond to linear polarization in the (x, y) directions, and (positive, negative) helicities.

Polarized photons are conveniently described in terms of the Stokes parameters,

$$\begin{aligned} I &= \langle a_+^2 \rangle + \langle a_-^2 \rangle & V &= \langle a_+^2 \rangle - \langle a_-^2 \rangle \\ Q &= \langle 2a_+a_- \cos(\theta_- - \theta_+) \rangle & U &= \langle 2a_+a_- \sin(\theta_- - \theta_+) \rangle \end{aligned} \tag{1.36}$$

where I is the radiation intensity (the temperature), the remaining terms define the polarization state of the wave (Q and U are mutually orthogonal linear states, whilst V is circular polarization), and $a_n = E_n e^{i\theta_n}$ defines the phase information per basis. Whilst I and V are coordinate-system-invariant, the terms Q and U are not. The Q and U parameters rotate via

$$\begin{pmatrix} Q' \\ U' \end{pmatrix} = \begin{pmatrix} \cos(2\phi) & \sin(2\phi) \\ -\sin(2\phi) & \cos(2\phi) \end{pmatrix} \begin{pmatrix} Q \\ U \end{pmatrix} \tag{1.37}$$

where the angle of rotation in the $x - y$ plane is given by ϕ and the polarization angle $\alpha \equiv (1/2)\tan^{-1}(U/Q)$ becomes $\alpha - \phi$. It then follows that the quantity $Q^2 + U^2$ is an invariant with respect to rotation.

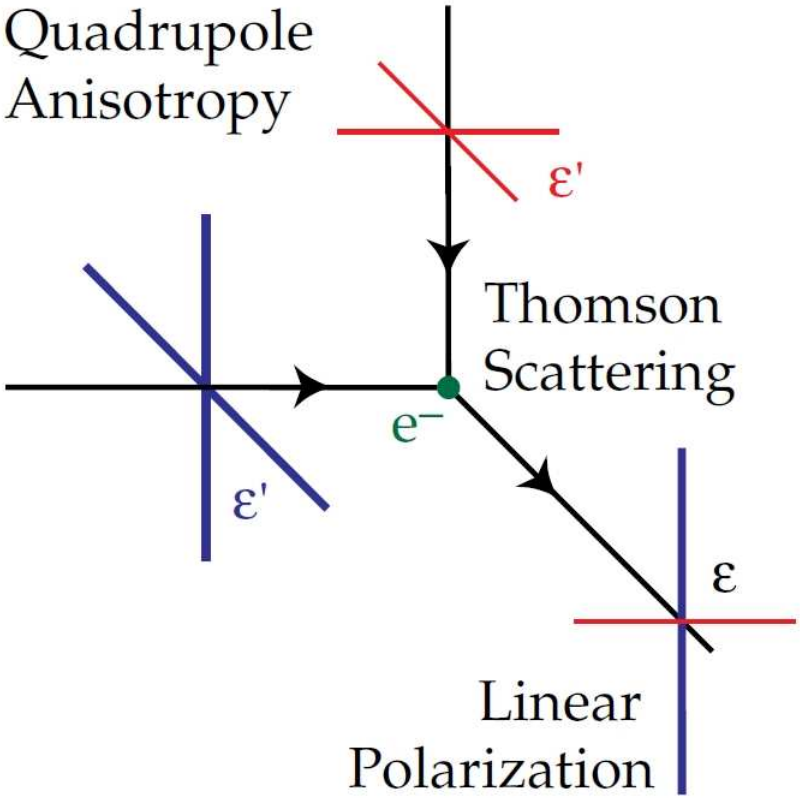

Figure 1.3: Thomson scattering of quadrupole radiation induces linear polarization in the outgoing radiation. From Hu & White [62].

If one wants to make a proper analysis of CMB polarization then it is necessary to work in a basis-independent framework; gradient-like (E) and curl-like (B) modes, in analogy to to the electric and magnetic terms in Maxwell theory, can be produced from the Q and U states which satisfy just this requirement. Polarization is a spin-two quantity; hence rotation through an angle π leaves the Stokes parameters invariant. One can form an equivalent polarization tensor from $\rho \propto \langle \mathbf{E}\mathbf{E}^{\dagger} \rangle$

$$\rho = \frac{1}{2}\begin{pmatrix} I+Q & U-iV \\ U+iV & I-Q \end{pmatrix} = \frac{I}{2}g_{ab} - \frac{i}{2}V\epsilon_{ab} + P_{ab}^{\mathrm{STF}} \tag{1.38}$$

where the displayed components are in an orthonormal basis, ϵ_{ab} is the (covariant) Levi-Civita tensor and P_{ab}^{STF} denotes the symmetric, trace-free (STF) polar-

ization tensor. In spherical polar coordinates,

$$P_{ab}^{\rm STF} = \frac{1}{2}\begin{pmatrix} Q & -U\sin\theta \\ -U\sin\theta & -Q\sin^2\theta \end{pmatrix}. \tag{1.39}$$

Since Thomson scattering can generate no circular polarization, in non-exotic scenarios $V = 0$. The STF polarization tensor can be transformed into two basis-independent variables by making use of the E and B decompositions of the tensor spherical harmonic basis:

$$a_{lm}^{E} = \int P_{ab} Y_{lm}^{E(ab)*} d\Omega, \qquad a_{lm}^{B} = \int P_{ab} Y_{lm}^{B(ab)*} d\Omega. \tag{1.40}$$

Looking at the pattern that a single plane wave (aligned with the **z** direction) will produce, in terms of spherical harmonics Y_{lm} the quadrupole anisotropy corresponds to $m = 0, \pm 1, \pm 2$ for a CMB populated by scalar, vector and tensor modes respectively. Fig. 1.4 shows the patterns for the E and B modes generated from the Q and U modes for each type of perturbation. Clearly scalars, vectors and tensors correspond to distinct patterns in the polarization of the CMB. The polarization pattern is altered across the LSS by the plane wave spatial dependence of the perturbation, producing B-modes from local E-modes. For scalars, the polarization field is a pure Q-field and so no B-modes are generated; for vectors the U-field is dominant, producing mostly B-modes for short wavelength fluctuations; tensors have Q and U components of approximately the same strength, so comparable E- and B-modes are produced at short wavelengths. Unfortunately, they do not separate cleanly into m polarization patterns for a spectrum of fluctuations each with a different k; but parity and the temperature correlations do survive superposition of perturbations. Since one does not want to confuse the E-modes with the plane wave amplitudes, the plane wave amplitudes shall no longer be referred to.

It will later be shown that inflationary cosmological models make a generic potential-dependent prediction of a stochastic background of gravitational waves. This comes from the tensor perturbations of the metric in the same fashion as the scalar temperature perturbations generate overdensities which lead to structure. Since tensor modes have chirality, one can measure these through detecting the B-modes in the polarization of the CMB. This is possible since all tensor fields can be decomposed into divergence-like and curl-like parts [61, 62]. Existing vector (vorticity) modes are exponentially diluted during inflation, implying a unique probe of the inflationary mechanism.

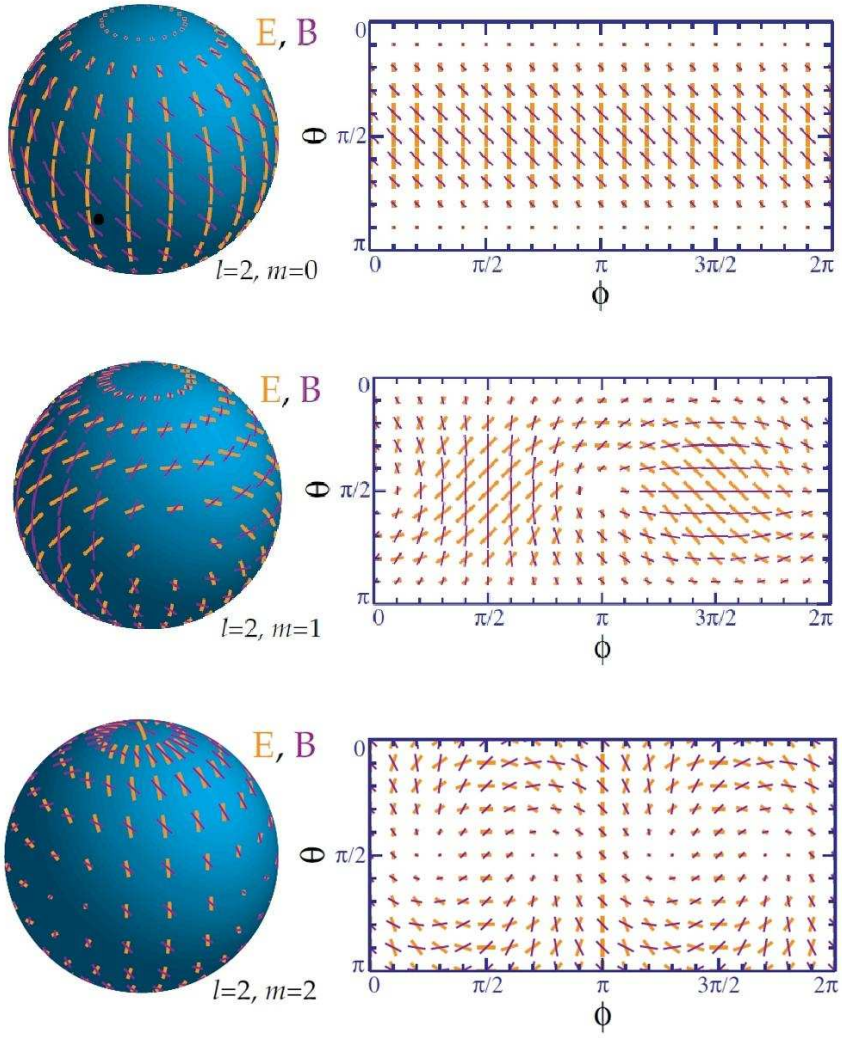

Figure 1.4: Top diagram: The polarization pattern on the sky from a scalar mode; note that only the intensity of the headless vectors change across the sphere. Middle diagram: The vector pattern, with a curl-like component. Bottom diagram: The tensor pattern — this, like the vector pattern, switches parity upon reflection at $\phi = \pi$. Taken from Hu & White [62].

For completeness, the Q, U correlation functions relate to the E, B spectra by

$$
\begin{aligned}
C^{QQ}(\theta) &= -\sum_l \frac{2l+1}{2\pi} N_l^2 (C_l^{EE} G_{l2}^+(\cos\theta) + C_l^{BB} G_{l2}^-(\cos\theta)) \\
C^{UU}(\theta) &= -\sum_l \frac{2l+1}{2\pi} N_l^2 (C_l^{BB} G_{l2}^+(\cos\theta) + C_l^{EE} G_{l2}^-(\cos\theta)) \\
C^{TQ}(\theta) &= \sum_l \frac{2l+1}{4\pi} N_l C_l^{TE} P_l^2(\cos\theta),
\end{aligned}
\tag{1.41}
$$

with the reverse relations being

$$\begin{aligned} C_l^{EE} &= -\pi N_l^2 \int_0^\pi \sin\theta (C^{QQ}(\theta) G_{l2}^+(\cos\theta) + C^{UU}(\theta) G_{l2}^-(\cos\theta)) d\theta \\ C_l^{BB} &= -\pi N_l^2 \int_0^\pi \sin\theta (C^{UU}(\theta) G_{l2}^+(\cos\theta) + C^{QQ}(\theta) G_{l2}^-(\cos\theta)) d\theta \end{aligned} \tag{1.42}$$

where

$$\begin{aligned} G_{lm}^+ &= -\left((l-m^2)\csc^2\theta + \frac{l(l-1)}{2} \right) P_{lm}(\cos\theta) + (l+m)\cos\theta \csc\theta^2 P_{l-1,m}(\cos\theta) \\ G_{lm}^- &= m\csc^2\theta \left((l-1)\cos\theta P_{lm}(\cos\theta) - (l+m) P_{l-1,m}(\cos\theta) \right) \end{aligned} \tag{1.43}$$

and the P_{lm} are the associated Legendre functions, related to the normal Legendre functions P_l. The existence of E-type polarization power as predicted by the existence of a Q field from scalar anisotropies has been confirmed by DASI [63] and others; the cross-correlation spectra C_l^{TE} also show a characteristic antiphase with the C_l^{TT} signal around $l = 50$ that confirms adiabatic modes as the dominant structure-forming processes (typical of inflationary cosmology) as opposed to the characteristic in-phase signal of isocurvature-dominated structure formation (as in defect models). So far then, uses for the TT, EE and TE spectra have been discussed. The BB spectra can be sourced by gravitational waves; in the next section it shall transpire that the inflationary cosmology predicts precisely such a BB spectra, which has thus far eluded detection.

1.2 Inflation

The inflationary cosmology paradigm, a widely-accepted extension to the standard Big Bang picture of the previous section, is now fully introduced. As mentioned in the introduction, the standard Big Bang theory does have some discrepancies with observations of the CMB. The most significant of these is probably the causal, or horizon, problem. Regions of the CMB separated by $\sim 2^\circ$ should be out of causal contact with each other, but it has already been seen that the CMB is uniform to 1 part in 10^5. Unless it is postulated that the Universe started off with such small-scale temperature variations, how is this phenomenon to be explained in terms of thermodynamic equilibrium? The regions simply would not have time to communicate and settle on such similar temperatures. A second major problem is the 'flatness' problem. Measurement of the first acoustic peak in

the TT spectrum suggests that the Universe is approximately flat — and would need to be flat to 1 part in 10^{15} at recombination since the curvature scales with radius like a^{-2}. Again, there is no natural way in the standard theory to accommodate this very fine tuning.

Inflationary cosmology extends the standard theory to account for these and other problems in a very simple manner, but with some surprising results. By postulating a scalar field (the 'inflaton') that accelerates the early expansion of the Universe exponentially, one can apparently causally separate regions that were initially causally connected and flatten out a universe with high initial curvature. There is then no need to postulate special initial conditions to account for these. Not only can this solve the problems of the standard theory, but when perturbation analysis is performed on the inflaton field that powers inflation, it is found that the inflaton naturally generates the fluctuations required to create the structure seen in the modern universe. Finally, and crucially, inflation makes predictions about the spectral tilt which are borne out in observation.

Linde's account [64] of the history of the development of inflation suggests that the first semi-realistic inflation model was developed by Alexei Starobinsky [65, 66] in 1979, but with aims very different to solving the standard CMB problems, making a first prediction of a cosmic gravitational wave background (CGB). Predictions of adiabatic perturbations followed through the analysis of Starobinsky's model by Mukhanov and Chibisov in 1981 [67]. The western world's exposure to the inflationary paradigm occurred predominantly through Guth [22] (also in 1981), whose grand unified theory (GUT)-inspired inflationary model was seen to be simpler than Starobinsky's, with the first explicit description of how inflation solves the major cosmological problems. Unfortunately, issues with bubble nucleation meant that the model could not work (a manifestation of the 'graceful exit' problem), and it was superceded by Linde's 'new inflation' [68], of the standard slow-roll type. A later introduction, the 'chaotic inflation' [69] model, allowed for the embedding of the inflationary mechanism into a multiverse-type paradigm.

One can stimulate an accelerated expansion by introducing a cosmological constant into the Einstein equations of an empty universe; this is identical to filling the universe with a classical scalar field. The first Friedmann equation is then solved to yield

$$a(t) = e^{\sqrt{\frac{\Lambda}{3}}t}, \qquad \ddot{a} = \frac{\Lambda}{3} e^{\sqrt{\frac{\Lambda}{3}}t} > 0 \tag{1.44}$$

where Λ is a positive cosmological constant term. This is just the exponential expansion that is termed 'inflation', equivalent to a Lorentzian manifold with constant positive curvature (a de Sitter space). During inflation, since the Hubble rate is approximately constant

$$\Omega - 1 = \frac{k}{a^2 H^2} \propto e^{-2\sqrt{\frac{\Lambda}{3}}t} \qquad \Rightarrow \qquad \frac{|\Omega - 1|_t}{|\Omega - 1|_{t_0}} \ll 1, \tag{1.45}$$

it can immediately be seen that the curvature decreases exponentially; it turns out that in this simple picture approximately at least 50-70 e-folds $\mathcal{N} = \ln\left[a(t_{\rm end})/a(t)\right]$ are needed in order to satisfy the observational constraints. Meanwhile, the comoving causal horizon can be expressed via

$$\eta_h = \int_0^{t_0} \frac{dt}{a(t)}; \tag{1.46}$$

so distributions that existed on scales that were in causal contact before inflation appear to be out of contact in the aftermath of inflation. If a particle is located at $\eta > \eta_h$, it is out of causal contact. During matter- and radiation-dominance, the density scales like a^{-3} and a^{-4} respectively, yielding horizons for either type of particle of order $\sqrt{t_0}$ and t_0. Since the integral equation (1.46) does not converge for an inflation-dominated universe, it can be seen from the exponential expansion that causal regions can be separated during inflation quite easily.
Beside the causal and flatness problems, inflation can solve a number of other mysteries in a similar fashion. A good example is the defect problem: all reasonable attempts to produce unified theories of fundamental physics predict the existence of topological defects, most notably monopoles. The predicted abundances of these particles, often with large masses, should be enough that the universe collapsed in a 'big crunch' long before the current age of the universe had transpired; it is just as well then that no such particles have been found experimentally. Inflation can solve this by exponentially diluting the abundance of such defects, so that no such 'overclosing' takes place[11].

1.2.1 The Standard Inflaton Formalism

The inflationary theory is now given a more solid treatment, using the simplest, canonical example. One starts with a generic scalar field — the inflaton ϕ —

[11]Of course they could simply not exist, but there are strong theoretical reasons to suspect that they do.

minimally coupled to gravity, in a standard FLRW universe. Beginning with the standard Lagrangian formalism

$$S = \int \sqrt{-g}\mathcal{L}d^4x, \qquad \mathcal{L} = \frac{1}{2}\partial^\mu\phi\partial_\mu\phi - V(\phi), \qquad \sqrt{-g} = a^3 \tag{1.47}$$

with $V(\phi)$ the field potential, variation with respect to ϕ yields the harmonic oscillator equation (HOE) for the field

$$\ddot{\phi} + 3H\dot{\phi} - \frac{\nabla^2\phi}{a^2} + V'(\phi) = 0, \qquad V' \equiv \frac{dV(\phi)}{d\phi} \tag{1.48}$$

where one is reminded that the overdot signifies differentiation with respect to time t. The stress-energy tensor for the field follows:

$$T_{00} = \rho_\phi = \frac{\dot{\phi}^2}{2} + V(\phi) + \frac{(\nabla\phi)^2}{2a^2}, \qquad T_{ii} = p_\phi = \frac{\dot{\phi}^2}{2} - V(\phi) - \frac{(\nabla\phi)^2}{6a^2}. \tag{1.49}$$

The standard inflationary phenomena can be recovered in the limit of the slow-roll condition ($\dot{\phi}^2 \to 0$). By substituting the pressure and density terms into the Friedmann equations (reformulated in terms of the Planck mass $M_{\rm Pl} = (8\pi G)^{-1/2}$), one finds for a flat universe:

$$H^2 = \frac{1}{3M_{\rm Pl}^2}\left(V(\phi) + \frac{1}{2}\dot{\phi}^2\right), \qquad \ddot{\phi} + 3H\dot{\phi} = -V', \tag{1.50}$$

so the potential determines how the universe evolves (where spatial variation in ϕ has been neglected). For a slow-rolling scalar with $p_\phi \simeq -\rho_\phi$, the FLRW metric can be written as

$$H^2 \sim \frac{8\pi G}{3}V(\phi), \qquad 3H\dot{\phi} = -V'(\phi), \tag{1.51}$$

allowing one to define the slow-roll parameters

$$\epsilon = -\frac{\dot{H}}{H^2} \approx \frac{M_{\rm Pl}^2}{2}\left(\frac{V'}{V}\right)^2, \qquad \eta \approx M_{\rm Pl}^2\frac{V''}{V} = \frac{V''}{3H^2}, \tag{1.52}$$

which must both be much smaller than unity for inflation to work; ϵ encodes the rate of change of H during inflation. A typical potential that achieves this aim is shown in Fig. 1.5.

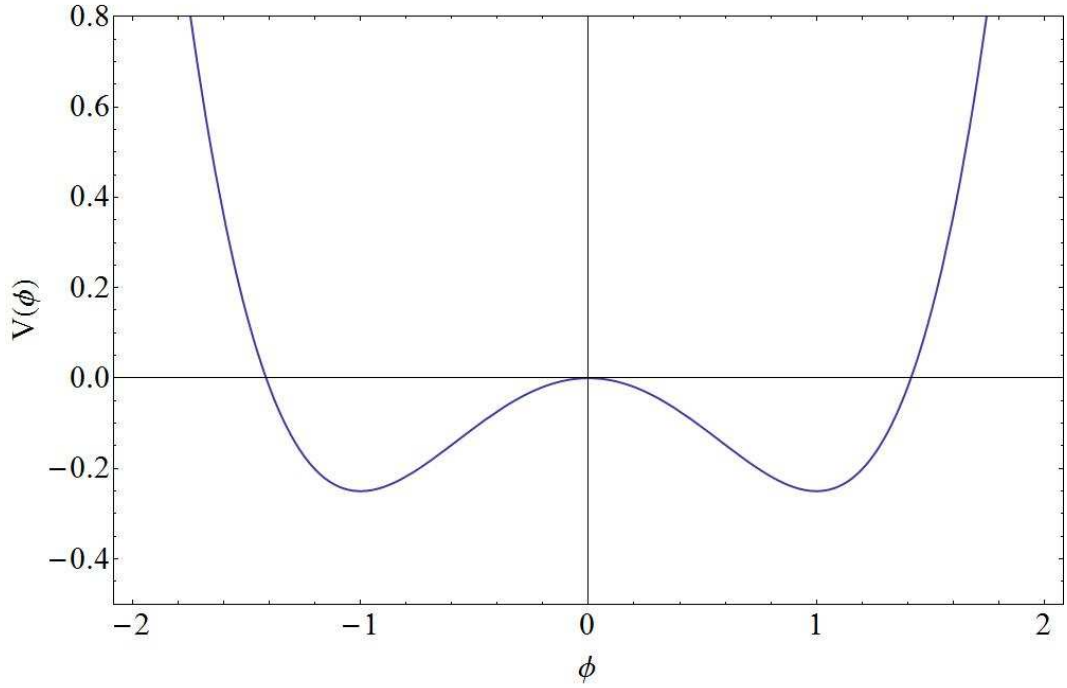

Figure 1.5: A quartic inflaton potential. The expectation value for the field is in a metastable state (false vacuum) until it is perturbed slightly and rolls down to the true vacuum, the energy release powering the accelerated expansion of the Universe.

Since reality obeys quantum mechanics, the inflaton should be split into the sum of a classical field and quantum perturbations $\phi(t) = \phi_0(t) + \delta\phi(x,t)$. To analyze the quantum perturbations, one starts by quantizing the harmonic oscillator, so generally canonical coordinates are promoted to operators, such as $x \to \hat{x}$. This leads to a description of the field perturbations in terms of raising and lowering operators ($\hat{a}$, $\hat{a}^\dagger$):

$$\phi_k = u_k(t)\hat{a}_k + u_k^*(t)\hat{a}_{-k}^\dagger, \qquad u_k(t) = (2E_k)^{-1/2}e^{-iE_k t} \tag{1.53}$$

where the expectation value $\langle|\phi_k^2|\rangle$ defines the spectrum for fluctuations, making it clear that the quantum fluctuations are dependent on the inflationary potential via the expansion rate. A quantum vacuum which is both de Sitter-invariant and time-invariant is known as a Bunch-Davies vacuum [70].

The simplest scalar analysis is of the quantum fluctuations of a massless scalar field. By expanding the fluctuations in harmonic space, the harmonic equation

for the fluctuations can be written

$$\delta\ddot{\phi}_{\mathbf{k}} + 3H\delta\dot{\phi}_{\mathbf{k}} + \frac{k^2}{a^2}\delta\phi_{\mathbf{k}} = 0, \qquad \delta\phi(\mathbf{x},t) = \frac{1}{(2\pi)^{3/2}}\int \delta\phi_{\mathbf{k}}(t)e^{i\mathbf{k}\cdot\mathbf{x}}d^3\mathbf{k}. \tag{1.54}$$

The qualitative behaviour of the solutions can be split into two regimes:

- Within the horizon, where $k \gg aH$, the fluctuations are oscillatory since one can neglect friction.
- Outside the horizon ($k \ll aH$) the k^2/a^2 term can be neglected, so the fluctuations are constant: $|\delta\phi_{\mathbf{k}}| \sim H/\sqrt{2k^3}$.

This can be calculated alternatively from the action

$$\delta S_{\mathbf{k}} = \int \left[\frac{\delta\sigma_{\mathbf{k}}'^2}{2} - \frac{1}{2}\left(k^2 - \frac{a''}{a}\right)\delta\sigma_{\mathbf{k}}^2\right]d\tau, \qquad \delta\sigma_{\mathbf{k}} \equiv a\delta\phi_{\mathbf{k}} \tag{1.55}$$

where the prime implies differentiation with respect to conformal time τ. The dynamics of the inflaton are however slightly more complicated than a generic massless scalar. Since the inflaton field dominates the energy-momentum of the Universe during inflation and has a coupling to gravity, then $\delta\phi \Rightarrow \delta T_{\mu\nu} \Rightarrow \delta g_{\mu\nu}$; the scalar field fluctuations will induce curvature fluctuations in the metric. The perturbation of the metric on the other hand influences the evolution of the inflaton perturbation via the perturbed Klein-Gordon equation

$$\delta\ddot{\phi} + 3H\delta\dot{\phi} - \frac{\nabla^2\delta\phi}{a^2} + V''\delta\phi = 0, \tag{1.56}$$

so $\delta g_{\mu\nu} \rightarrow \delta\phi$, meaning that the perturbations are coupled to each other. The FLRW metric can be perturbed most generally via

$$\begin{aligned} g_{\mu\nu} &= a^2\begin{pmatrix} -1-2A & \partial_i B \\ \partial_i B & (1-2\psi)\delta_{ij} + D_{ij}E \end{pmatrix} \\ D_{ij} &= \partial_i\partial_j - \frac{1}{3}\delta_{ij}\nabla^2, \end{aligned} \tag{1.57}$$

with B the shift function, A the lapse function and ψ the potential. The Einstein components of the perturbed field then determine the components of the per-

turbed stress-energy tensor

$$T_{00} = \frac{\dot{\phi}^2}{2} + V(\phi)a^2 \qquad T_{ij} = \left(\frac{\dot{\phi}^2}{2} - V(\phi)a^2\right)\delta_{ij}$$
$$\delta T_{00} = \dot{\phi}\delta\dot{\phi} + 2AV(\phi)a^2 + a^2\frac{\partial V}{\partial\phi}\delta\phi \qquad \delta T_{0i} = \partial_i\delta\phi\dot{\phi} + \frac{1}{2}\partial_i B\dot{\phi}^2 - \partial_i BVa^2$$
$$\delta T_{ij} = \left(\dot{\phi}\delta\dot{\phi} - A\dot{\phi}^2 - a^2\frac{\partial V}{\partial\phi}\delta^{(1)}\phi - \psi\dot{\phi}^2 + 2\psi V(\phi)a^2\right)\delta_{ij} + \frac{1}{2}D_{ij}E\dot{\phi}^2 - D_{ij}EV(\phi)a^2. \tag{1.58}$$

The coupled scalar and metric perturbations can be split into

- Adiabatic/curvature perturbations

$$H\delta t = H\frac{\delta\phi}{\dot{\phi}}$$

- Isocurvature perturbations (for a fluid with energy density ρ):

$$\left.\frac{\delta\phi}{\dot{\phi}}\right|_{\delta\rho=0} = \frac{\delta\phi}{\dot{\phi}} - \frac{\delta\rho}{\dot{\rho}}$$

  which give the value of a perturbation on uniform-density contours.

This provides information on which physical processes are most responsible for the formation of structure seeds; the adiabatic modes are density fluctuations, whilst the isocurvature modes can be generated by anisotropic stress — and they yield different forms for the theoretical power spectra.
Following the adiabatic modes, the curvature perturbation is defined on slices of uniform energy density ζ and Bardeen's gauge-invariant metric perturbation potentials Φ, Ψ by:

$$\zeta = \psi + H\frac{\delta\rho}{\dot{\rho}} \qquad \Phi = -A + \frac{1}{a}\left[\left(-B + \frac{E'}{2}\right)a\right]' \qquad \Psi = -\psi - \frac{\nabla^2 E}{6} + \frac{a'}{a}\left(B - \frac{E'}{2}\right). \tag{1.59}$$

A gauge choice refers to a choice of the configuration of the field (analogous to choosing a coordinate system). In a dynamical spacetime environment i.e., with curvature, particular choices of gauge lead to unphysical gauge modes. This makes a gauge-invariant approach particularly useful. By rewriting the Einstein equations in terms of the gauge-invariant perturbations one can then find

$$\Phi_k = -\frac{4\pi G z}{k^2}Hu_k, \qquad u \equiv a\delta\phi_{\rm GI} + \Psi z, \qquad z \equiv \frac{a\dot{\phi}}{H}. \tag{1.60}$$

The full harmonic equation can then be written

$$u'' - \nabla^2 u - \frac{z''}{z} u = 0, \tag{1.61}$$

giving as sub- and super-horizon solutions for the potential Φ:

$$\Phi_{k \gg aH} \sim i \frac{4\pi G \dot{\phi}}{\sqrt{2k^3}} e^{-\frac{ik}{a}}, \qquad \Phi_{k \ll aH} \sim \eta \mathcal{R}_k, \qquad \mathcal{R} \equiv -\Psi - \frac{H \delta\phi_{\mathrm{GI}}}{\phi'}, \tag{1.62}$$

hence the power spectrum $\mathcal{P}_\mathcal{R}$ of the comoving curvature perturbations and their spectral index n_s are given by

$$\mathcal{P}_\mathcal{R}(k) = \frac{k^3 H^2}{2\pi^2 \dot{\phi}^2} |\delta\phi_k|^2 \approx \frac{1}{2M_{\mathrm{Pl}}^2 \eta} \left(\frac{H}{2\pi}\right)^2 \left(\frac{k}{aH}\right)^{n_s - 1}, \qquad n_s = \frac{d \ln \mathcal{P}_\mathcal{R}}{d \ln k} = 2\eta - 6\epsilon \tag{1.63}$$

which is an almost scale-invariant quantity, i.e., approximately an HZ power law. Different inflation models make testable predictions for n_s and its running $dn_s/d\ln k$; this means that the expansion history of the early universe can be reconstructed by determining the potential V from the primordial power spectrum.

Models of Inflation

It has been seen just how rich a phenomenon inflation is; however, there is as yet no consensus on the precise details of inflation such as the functional form of the potential. There is a vast literature on inflation models, and no reasonable way one can accommodate them all in such a text; examples include DBI ('brane') inflation [71], supersymmetric F-term inflation [72] and many more (an overview of a selection of models can be found in Lyth [73]). Instead, just some of the different types of models are outlined:

- Small-field inflation: Typically these arise from spontaneous symmetry-breaking, such as in the slow-roll inflationary mechanism and in 'natural' inflation where the inflaton is a pseudo-Nambu-Goldstone boson. The field starts in a metastable state and rolls down to the true vacuum.

- Large-field inflation: Often found in the chaotic inflationary theory (wherein the universe is thought of as having a fractal structure on the largest scales) — the scalar field is perturbed from its minimum by a value $\sim \mathcal{O}(M_{\mathrm{Pl}})$, the potential usually a polynomial or exponential . Since then $V(\phi) \sim M_{\mathrm{Pl}}^4$, there is a large friction term in the Friedmann equation leading to the required slow-roll phenomena.

- Hybrid inflation: These are multi-field theories, where another field ψ rather than the inflaton ϕ provides the majority of the energy density. It is only when the ϕ field reaches a critical value that slow-roll occurs — when the ψ field is tachyonic, slow-roll must come to an end. Often a phase transition occurs at the end of inflation in these models, producing topological defects. One extra concern regarding hybrid models is that of the *type* of perturbation: isocurvature perturbations are expected only of multi-field inflation models, so this provides an extra discriminatory factor.

Inflation appears to be the simplest paradigm that solves the most problems. Competitors do exist, such as variable-speed-of-light [74] theories (often breaking global Lorentz-invariance [75]) and ekpyrotic/cyclic [76] theories (often proposed as resulting from brane collision, not without its own fine-tuning issues [77]), however it is often difficult to reproduce the successes of inflation in competitor theories [78] without invoking a scalar field, in particular the flat HZ spectrum. Crucially, these alternatives make a fundamentally contrary prediction to that of the inflationary paradigm: that there are no primordial gravitational waves.
One interesting result of the chaotic inflation regime is that it leads to 'eternal inflation': large quantum fluctuations are produced which increase ϕ in some parts of the universe — these regions then expand at a greater rate than their parent domains, and quantum fluctuations inside them lead to the production of new inflationary domains, ad infinitum. This results in a universe which is eternally self-reproducing. Since any regions separated by a distance greater than the Hubble radius are causally disconnected, this is essentially a multiverse theory[12]. This could then find a natural setting in the landscape program of string theory, where scalar fields are ubiquitous and the potential energies of these scalar fields can have different minima — and hence different vacuum states, with different types of symmetry-breaking between fundamental interactions and different laws of low-energy physics. The number of minima has been estimated at perhaps some 10^{500} which is for all practical reasons almost infinite. It has been argued that an anthropic selection process is then the correct way to determine which, if any, vacuum is correct — however, such an idea has attracted criticism from across the high energy physics and astrophysics communities [80, 81, 82].
It has now been seen how inflation can generically solve the problems of the Big Bang theory, and also generate the observed spectrum of density fluctuations (temperature anisotropies). Fluctuations in the energy density of the inflaton will

[12]See Tegmark [79] for a discussion of classes of multiverse theories.

also impose fluctuations on the metric (independent of quantum gravity) beyond the standard curvature perturbations; these are gravitational waves — a generic prediction of inflation that results in a non-zero BB spectrum, explored after a brief discussion of symmetry-breaking mechanisms and topological defects.

1.2.2 Symmetry-breaking, Topological Defects and Non-Gaussianity

One of the most elegant potential causations for inflation lies in symmetry-breaking. Symmetry-breaking is a generic phenomenon in quantum field theory, and much of the basis of unification programs[13]. Examples include the symmetry-breaking of the electroweak Lagrangian in the early universe to yield the weak nuclear and electromagnetic forces and the symmetry-restoration that accurately describes superconductivity. Given a particular Lagrangian, one can inspect it to see what symmetries it respects. For example,

$$V(\phi) = V_0 - \frac{m^2\phi^2}{2} + \frac{\lambda\phi^4}{4} \tag{1.64}$$

is invariant under $\phi \to -\phi$, with minima $\phi_{\min} = \pm m/\sqrt{\lambda}$. By taking the positive minima, one can define a new field $\bar{\phi} = \phi - m/\sqrt{\lambda}$. By defining V_0 such that the potential vanishes at the minimum, near the minimum the vacuum energy value (VEV) is

$$V = \frac{2m^2\bar{\phi}^2}{2} + A\bar{\phi}^2 + B\bar{\phi}^4 + \cdots . \tag{1.65}$$

Since the original symmetry is not explicit in this theory, it is said to be 'broken'. In physical systems there is usually a critical temperature associated with symmetry-breaking and restoration; when the field energy is larger than the critical temperature, it resides in a 'false' vacuum (not the lowest minima), with a zero VEV. Upon reaching the critical temperature, spontaneous symmetry-breaking occurs, forming a new 'true' vacuum which the scalar field rolls into. This is precisely the kind of behaviour that one would want to start the inflationary expansion. When symmetries are spontaneously broken, stable field configurations called topological defects [85] may form. Kibble [86] was the first to realise this in 1976 when studying the Higgs scalar field which induces mass in fermions; phase transitions in an expanding universe produce domains that coalesce, pro-

[13]More information on symmetry-breaking mechanisms in a quantum field theory context can be found in Peskin & Schroeder [83] and in Weinberg [84].

ducing the relic defects. Since there is no correlation between separate domains, the Higgs field in those domains take on arbitrary orientations — not unlike the magnetic domains of a ferromagnet. The interfaces between the domains are then the defects (Fig. 1.6). As high-energy phenomena, Higgs-type defects are difficult to produce in the lab (although see Burgess [87] for some novel discussions of such analysis via the AdS/CFT correspondence) but can in principle be observed astronomically. In cosmological terms, one would expect that spontaneous symmetry-breaking would occur in different parts of the universe and spread relativistically, leading to the formation of networks of defects.

Since different theories break different symmetries, one can have a range of defects. For example, the breaking of a discrete mirror symmetry creates domain walls, infinitesimally thin planar surfaces with intense mass-energy densities. Other such defects are the famous cosmic strings, which are 1-dimensional structures with no loose ends in order that the phases of regions with different field configurations do not get mixed up — this means they come in only 2 flavours, loops or infinitely long strings. Again, the masses of these objects are usually large, and they radiate their energy away via the production of gravitational waves. Finally, textures were once thought to be a valid seed of structure formation; these are global field configurations, with no core. Since they are unstable to collapse, texture knots collapse to a microscopic size, unwind and radiate via gravitational waves — the generated gravitational field was supposed to be able to produce structure. Whilst defects are no longer expected to exist in numbers relevant to the large-scale structure of the universe almost all reasonable GUTs predict their existence. Of course, topological defects have as yet remained undetected bar for tantalising claims [88].

Upon settling in the new true vacuum, inflation stops. Thus symmetry-breaking provides the required graceful exit from the inflationary phase as the inflaton settles on the true vacuum. However, the field does not necessarily stop in an immediate manner — it may oscillate about the minimum for a time, thus releasing enough energy with which to produce the abundance of particles in the universe. This effect is known as *reheating*.

For inflation, the type of phase transition induced by spontaneous symmetry-breaking is also important. First-order transitions (with a discontinuity in first derivative of the Gibbs' free energy i.e., the transition of liquid water to steam) result in bubble nucleations, whilst second-order transitions like the ferromagnetic transition often result in divergent correlation lengths. Guth's early work found that bubble collisions in a first-order-type transition would lead to a highly

granular universe in contrast with observations.

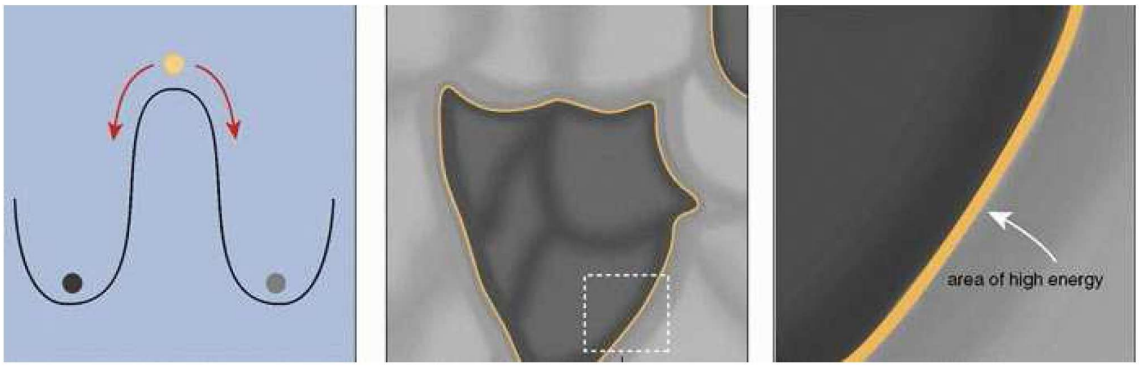

Figure 1.6: Formation of topological defects (from Gangui [85]). Two regions occupy different true vacuum states following spontaneous symmetry-breaking (left diagram). The physical boundary between the configurations is a high-energy defect (centre and right diagram).

Whilst inflation dilutes the density of defects following a spontaneous symmetry-breaking it would be useful if the Higgs field that breaks electroweak symmetry could itself be the inflaton. Brandenberger [89] showed why this is not in fact the case — a Higgs inflaton does not generate enough inflation to remove the Higgs-generated defects. In fact, preheating physics can lead to an onset of new defect generation via energy transfer to other fields. This has been explored by numerical simulations [90, 91].

It is, of course, not impossible that we live in a horizon which features one of these defects. This being the case it can be asked what the general observational effects of, say, cosmic strings are. Spacetime around a cosmic string is conical; this results in a tiny deficit angle which would show up by the deflection of photons, giving a double image of the photon source. Secondly, anisotropies in the CMB from primordial strings would induce a Doppler shift due to the conical geometry they create; a difference between the photon redshifts either side of the string results in a discontinuity, known as the Kaiser-Stebbins [92] effect. String oscillations tend to lead to cusp singularities (a singular point on a curve), which decay by emitting gravitational radiation. Since defects actively seed perturbations, they can produce both vector and tensor modes, leading to a characteristic polarization signature. Much of the numerical work involving cosmic strings has been focused on evolving the string networks formed from symmetry-breaking, which should permeate the entire universe if such entities exist; active structure formation via defects are predominantly of isocurvature type, which has been so far been ruled out by WMAP as the major source of structure formation.

The observational effects of strings are mostly dependent on the dimensionless string tension $G\mu$. Currently, this sets the best limit on string detection with $G\mu \lesssim 10^{-6}$ [93]. Curiously, B-mode detections may further limit the influence of defects such as strings. It has been shown [94] that even if defects contribute 1% or less in the CMB temperature anisotropy spectrum, their signature in the local B-mode polarization correlation function at angular scales of tens of arc minutes is much larger than that due to gravitational waves from inflation, even if the latter contribute with a ratio as large as $r \sim 0.1$ to the temperature anisotropies.
Of course, defects are also likely to induce non-Gaussianity in the CMB temperature field. This is turned to next.

Non-Gaussianity

One further way of discriminating inflation models or searching for defect signals, particularly as a degeneracy-breaker when combined with polarization measurements, is non-Gaussianity in the CMB [95, 96]. Inflation generically predicts nearly-Gaussian CMB fluctuations; however, non-linearity in inflation can produce weakly non-Gaussian fluctuations in the CMB. The simplest models of inflation predict a level of local non-Gaussianity ($\sim 10^{-6}$ [97]) far below the detection threshold of foreseeable CMB experiments. A large non-Gaussian signal would then significantly rule against simple single-field-type inflation models. Non-Gaussianity can also be provided by astrophysical sources that have avoided removal during CMB map synthesis, by nonlinearity in the Einstein-Boltzmann equations, or by topological defects.
For a Gaussian signal, all odd n-point correlation functions vanish and all even n-point correlation functions can be completely expressed as the combination of two-point correlation functions. This means that a non-Gaussian signal can be characterized by the degree to which it violates these correlation function characteristics, often expressed by forming a ratio between the particular non-Gaussian correlation function and an appropriate combination of two-point correlation functions. The theoretical non-Gaussianity, given that one requires more information than the 2-point correlation function, is also studied in terms of correlation shapes — triangles on the sky. This comes from the fact that the Fourier modes of the 3-point correlation form a closed triangle. These shapes include the 'local', 'equilateral' and 'folded' types (Fig. 1.7), appended most recently by studies of the 'orthogonal' type; the local shape is typical of multi-field models, while the equilateral one is typical of single field models; the orthogonal type peaks for both equilateral and flat-triangle configurations.

Starting with the perturbation expansion of the temperature anisotropy field

$$T \approx g_T(\phi + f_\phi \phi^2 + \cdots) \tag{1.66}$$

and restricting the analysis to the linear theory gives a linear relation between the curvature pertubations ϕ and T

$$T \approx g_T \phi, \tag{1.67}$$

where g is the radiative transfer function; T is Gaussian if ϕ is Gaussian. Conversely, at higher order T can be non-Gaussian for a Gaussian ϕ. Higher-order corrections to the inflaton also yield non-Gaussian fluctuations $\delta\phi$

$$\phi \approx M_{\rm Pl}^{-1} g_\phi (\delta\phi + M_{\rm Pl}^{-1} f_{\delta\phi} \delta\phi^2). \tag{1.68}$$

Interaction terms in the inflationary harmonic oscillator equation or a non-linear coupling between long-wavelength classical fluctuations and short-wavelength quantum fluctuations in the context of chaotic inflation can produce a non-Gaussian $\delta\phi$. This imprints on the scalar perturbations by [99]

$$T \approx g_T \left[\phi_L + (f_\phi + g_\phi^{-1} f_{\delta\phi} + g_\phi^{-1} g_{\delta\phi}^{-1} f_n)\phi_L^2\right] \equiv g_T \left[\phi_L + f_{NL}\phi_L^2\right] \tag{1.69}$$

where ϕ_L is an auxiliary Gaussian curvature perturbation. This gives

$$\phi(x) = \phi_L(x) + f_{NL}\left[\phi_L^2(x) - \left\langle \phi_L^2(x)\right\rangle\right] + g_{NL}\phi_L^3(x) + \cdots \tag{1.70}$$

where the f_{NL} and g_{NL} terms characterize the lowest-order departures from Gaussianity. The Fourier transform of the 3-point correlation function relates to f_{NL} by

$$\begin{aligned}
\langle \phi_{k_1}\phi_{k_2}\phi_{k_3}\rangle &= (2\pi)^3\delta^3(k_1+k_2+k_3)F \\
F^{\rm local} &= 2 f_{NL}^{\rm local}\Delta_\Phi^2\left(\frac{1}{k_1^{4-n_s}k_2^{4-n_s}} + \frac{1}{k_1^{4-n_s}k_3^{4-n_s}} + \frac{1}{k_2^{4-n_s}k_3^{4-n_s}}\right) \\
F^{\rm equil} &= 6 f_{NL}^{\rm equil}\Delta_\Phi^2\left(-\frac{1}{k_1^{4-n_s}k_2^{4-n_s}} + (2\text{ perm.}) - \frac{2}{(k_1k_2k_3)^{2-\frac{2}{3}(n_s-1)}}\right. \\
&\qquad\left. + \frac{1}{k_1^{1-\frac{1}{3}(n_s-1)}k_2^{1-\frac{2}{3}(n_s-1)}k_3^{4-n_s}}\right)
\end{aligned} \tag{1.71}$$

where Δ_Φ is the amplitude of the primordial power spectrum.

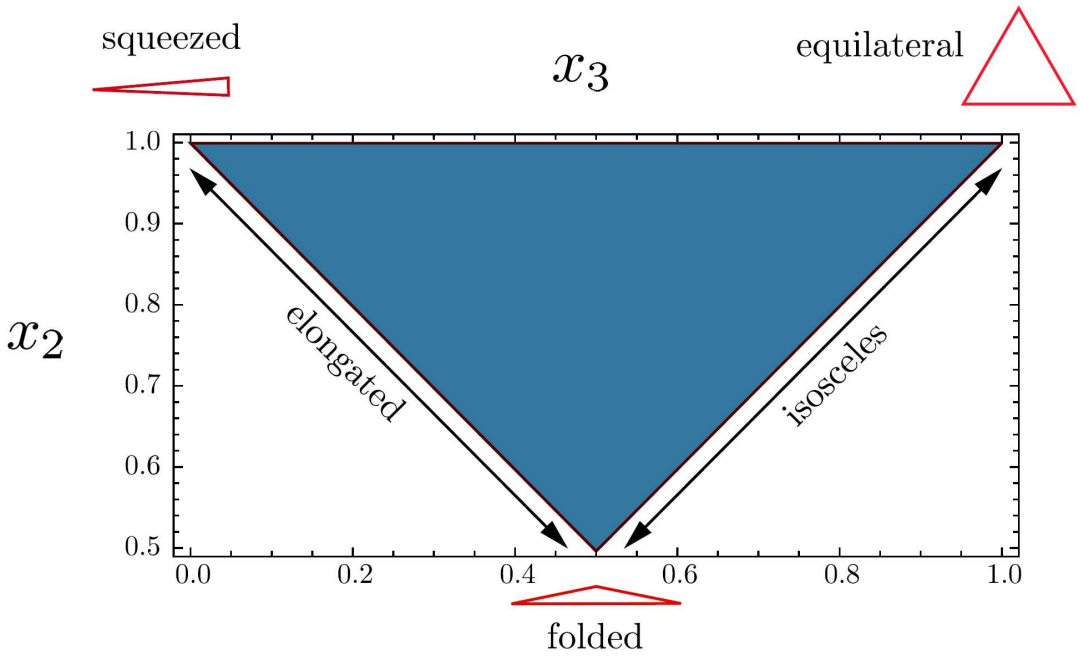

Figure 1.7: Triangular shapes used in CMB non-Gaussianity studies (from Baumann [98]), where $x_2 \propto k_2/k_1$ and $x_3 \propto k_3/k_1$. A contour plot of the bispectrum shows that the local shape is configured towards squeezed states, while the equilateral is obviously named for its equilateral shape.

It has been shown that one can relate [100] the inflationary potential to the primordial non-Gaussian terms via

$$\begin{aligned} f_{NL}^{\rm local} &= -\frac{5}{6}\frac{[\ln V(\phi)]''}{8\pi G} \\ g_{NL}^{\rm local} &= \frac{25}{54}\frac{2\,[\ln V(\phi)]'^2 - [\ln V(\phi)]'''\,[\ln V(\phi)]'}{(8\pi G)^2}, \end{aligned} \tag{1.72}$$

using the δN formalism in single-field inflation models.

To measure the non-Gaussianity of the CMB anisotropies, it is necessary to use higher-order statistics. For example, using the skewness of the one-point probability density distribution function, one can measure down to $|f_{NL}^{\rm local}| \sim 60$, whilst using the bispectrum this limit reduces to $|f_{NL}^{\rm local}| \sim 3$. Further options such as Minkowski functionals and wavelets have also been proposed. In this thesis, the 3-point spectra $B_{l_1 l_2 l_3}$ bear some relevance; an estimator for the non-Gaussian measure, in the full-sky coverage and homogeneous noise regime, can be given by

$$\hat{f}_{NL}^{\rm local} = \frac{1}{N}\sum_{l_i,m_i}\begin{pmatrix} l_1 & l_2 & l_3 \\ m_1 & m_2 & m_3 \end{pmatrix}\frac{B_{l_1 l_2 l_3}}{C_{l_1}C_{l_2}C_{l_3}} a_{l_1 m_1} a_{l_2 m_2} a_{l_3 m_3}, \tag{1.73}$$

where N is a normalization term which can be calculated to ensure that the estimator is unbiased. The 7-year WMAP constraints currently set the values of f_{NL} to $f_{NL}^{\rm local} = 32 \pm 21$, $f_{NL}^{\rm equil} = 26 \pm 140$ and $f_{NL}^{\rm orthog} = -202 \pm 104$ all at 1σ. Conversely, detections of non-Gaussianity have been claimed by a number of authors [101, 102], which may or may not be biased by systematics; a possible systematic in the WMAP data will be exposed in Chapter 4.

The determination of the bispectrum is further complicated by not only foreground statistics and the sheer storage size and computation time (not to mention numerical overflow issues) of the computation at large l_i due to evaluations of the Wigner $3jm$-symbol, but also from the fact that higher-order recombination calculations can produce a small non-Gaussian signal [103] along with the non-linear evolution of higher-order terms in the gravitational interaction [104].

To append all the success of inflation one should wish to get a better handle on the form of the inflationary potential and CMB non-Gaussianity in order to constrain which inflation models are viable, which should lead to the correct links with fundamental physics. This would be doubly enhanced by measuring the non-Gaussianity of the e and b fields. With this in mind the next subsection discusses the physics which can generate B-modes.

1.2.3 Gravitational Waves

The final aspect of underlying physical theory that has relevance to this thesis is a revisit of the final statement in the section about CMB polarization: polarization B-modes can be created from tensor perturbations. Since the only accepted tensor field theory is GR, then these correspond to gravitational waves.

In linearized tensor perturbation theory, one usually starts with a flat Minkowski metric $\eta_{\mu\nu}$, and perturbs it slightly

$$g_{\mu\nu} = \eta_{\mu\nu} + h_{\mu\nu}, \tag{1.74}$$

where $\eta_{\mu\nu}$ is the unperturbed metric and $h_{\mu\nu}$ is an infinitesimal perturbation. Using this approach one can find the process for generating gravitational radiation. To solve the wave equations of gravity, one starts by specifying the gauge; in a coordinate shift $x'^{\alpha} = x^{\alpha} + \zeta^{\alpha}$ where the prime no longer specifies differentiation with respect to ϕ, the linear perturbation transforms as

$$h'_{\mu\nu} = h_{\mu\nu} - \partial_{\mu}\zeta_{\nu} - \partial_{\nu}\zeta_{\mu}. \tag{1.75}$$

One can also construct the Einstein tensor:

$$G_{\alpha\beta} = \frac{1}{2}\left[\partial_\alpha\partial^\mu h_{\mu\beta} + \partial_\beta\partial^\mu h_{\mu\alpha} - \partial_{\alpha\beta}h - \Box h_{\alpha\beta} + \eta_{\alpha\beta}\Box h - \eta_{\alpha\beta}\partial^\mu\partial^\nu h_{\mu\nu}\right] \tag{1.76}$$

where $h \equiv \eta^{\mu\nu}h_{\mu\nu}$. By using the Lorenz gauge $\partial^\mu\bar{h}_{\mu\nu}$ which is manifestly Lorentz-invariant, then applying the Green's function for the box operator it can be found that

$$\bar{h}_{\alpha\beta} = h_{\alpha\beta} - \frac{\eta_{\alpha\beta}}{2}h = 4\pi G\int\frac{T_{\alpha\beta}(\mathbf{x}', t - |\mathbf{x} - \mathbf{x}'|)}{|\mathbf{x} - \mathbf{x}'|}d^3x'. \tag{1.77}$$

Only the spatial, transverse and traceless components of h, which shall now take on the use of the term h exclusively, encode radiation in a gauge-invariant manner. The solution for spatial components for a distant infinitesimal source is:

$$\bar{h}_{ij} = \frac{4\pi G}{r}\int T_{ij}(t - r, \mathbf{x}')d^3x'. \tag{1.78}$$

Using this, one can project out the quadrupole component

$$I_{ij} = \int\rho x_i' x_j' d^3x', \qquad \bar{h}_{ij} = \frac{2G}{r}\frac{d^2I_{ij}}{dt^2} \tag{1.79}$$

and the other components via the projector

$$P_{ij} = \delta_{ij} - n_i n_j \qquad \Rightarrow \qquad h_{ij} = \bar{h}_{kl}(P_{ki}P_{lj} - \frac{1}{2}P_{kl}P_{ij}), \tag{1.80}$$

with n_i a unit vector pointing from the source to the observer, and higher moments suppressed by further factor of the internal velocity $\sim v^l$. So by analogy to the electric and magnetic multipoles in Maxwell's theory, there are mass and current moments in gravity:

$$h_l^M \sim \frac{G}{r}\frac{d^lM_l}{dt^l}, \qquad h_l^S \sim \frac{G}{r}\frac{d^lS_l}{dt^l}. \tag{1.81}$$

For a linearly perturbed metric, one can consider each multipole individually. First the mass monopole, mass dipole and current dipole: h_0^M is merely the Newtonian potential, and not a source for radiation. h_1^M is proportional to the total linear momentum of the system, so is a purely gauge term and hence not a radiation source. For h_1^S conservation of angular momentum requires that this is no source for radiation. The mass quadrupole is then the first term which is not conserved — hence the mass quadrupole is the first term that generates gravitational radiation. Gravitational waves are oscillatory fields, where h describes the tidal

strain; the energy flux for gravitational waves is then $dE/dt \sim |dh/dt|^2$. For the CMB, the source would be an ultra-low frequency one, i.e., $10^{-5}H_0^{-1} < \lambda < H_0^{-1}$ — corresponding to the limits between the angular resolution that can be probed and the size of the Universe. Currently, only indirect detections of gravitational waves have been achieved, most famously with the Hulse-Taylor observations of the orbital decay of the binary system containing the pulsar PSR B1913+16 — the decay rate being in precise agreement with that of the energy loss to the system due to gravitational radiation. Direct attempts at detection, such as LIGO, have only given upper bounds — it is expected that the ambitious LISA space interferometer should be able to detect the characteristic 'chirp' from coalescing black holes, potentially ushering in an era of gravitational wave astronomy.
Looking at gravity waves in an inflationary setting makes use of the most general first-order perturbation of the metric (equation (1.57)). It is also necessary to define the perturbed stress tensor where Σ_{ij} is the anisotropic stress, and a dimensionless counterpart to this, Π, via

$$T_{ij} = p\delta_{ij} + \Sigma_{ij}, \qquad \Pi_{ij} = \frac{\Sigma_{ij}}{p}. \tag{1.82}$$

By working out the perturbation in the left-hand side of the Einstein equation and equating with $8\pi G\delta T^{\mu\nu}$, the resulting equations can be broken into scalar, vector and tensor parts

$$\begin{aligned} v_i &= v_i^S + v_i^V \qquad & \Pi_{ij} &= \Pi_{ij}^S + \Pi_{ij}^V + \Pi_{ij}^T \\ B_i &= B_i^S + B_i^V \qquad & E_{ij} &= E_{ij}^S + E_{ij}^V + E_{ij}^T. \end{aligned} \tag{1.83}$$

Utilizing the metric for space-space tensor perturbations gives

$$\ddot{E}_{ij}^T + 2aH\dot{E}_{ij}^T + k^2 E_{ij}^T = 8\pi G a^2 p \Pi_{ij}^T. \tag{1.84}$$

The anisotropic stress after matter-domination can be neglected, and after E_{ij} enters the horizon it is represented by gravitational waves $h_{ij} = aE_{ij}^T$, so the evolution of the Fourier component of h is

$$\ddot{h}_{ij} + 3H\dot{h}_{ij} + \left(\frac{k}{a}\right)^2 h_{ij} = 0, \tag{1.85}$$

which is the same equation as for a massless scalar field. The Fourier components have the form

$$h_{ij} = h_+ e_{ij}^+ + h_\times e_{ij}^\times \tag{1.86}$$

where the e_{ij} are polarization tensors. The action for the tensor modes

$$S = \frac{M_{\rm Pl}^2}{2}\int d^4x\sqrt{-g}\frac{1}{2}\partial_\sigma h_{ij}\partial^\sigma h_{ij} \tag{1.87}$$

yields a harmonic equation for the gauge-invariant tensor amplitude: $v_{\mathbf{k}} = h_k a M_{\rm Pl}/\sqrt{2}$

$$v_{\mathbf{k}}'' + \left(k^2 + \frac{a''}{a}\right)v_{\mathbf{k}} = 0 \qquad \Rightarrow \qquad |v_{\mathbf{k}}| \approx \left(\frac{H}{2\pi}\right)\left(\frac{k}{aH}\right)^{\epsilon}, \tag{1.88}$$

where the prime momentarily represents differentiation with respect to conformal time $\eta = \int dt/a(t)$. So, for

- $k^2 > \frac{a''}{a}$, $v_{\mathbf{k}}$ is oscillatory hence $h_{\mathbf{k}}$ falls off as a increases;
- $k^2 < \frac{a''}{a}$, $v_{\mathbf{k}}$ grows with the scale factor;

hence gravitational modes $h_{\mathbf{k}}$ inside the horizon die, and outside the horizon they remain approximately constant. This means that during inflation the scale of the perturbations is significantly amplified. Like the scalar case, the tensor perturbation is almost scale-invariant:

$$\mathcal{P}_T(k) = \frac{8}{M_{\rm Pl}^2}\left(\frac{H}{2\pi}\right)^2\left(\frac{k}{aH}\right)^{n_T}, \qquad n_T = \frac{d\ln\mathcal{P}_T}{d\ln k} = 3 - 2v_T = -2\epsilon. \tag{1.89}$$

Since the amplitude depends on H during inflation, which depends on the inflaton potential, detection of gravitational waves from inflation will measure the energy scale of inflation.

If the energy density of the gravitational waves is non-zero, they will influence the temperature anisotropies. This being the case, one desires a particular observational quantity which is only non-zero for a non-zero gravitational wave background — given by the ratio of gravitational waves to adiabatic density perturbations, the tensor-to-scalar ratio r. The literature for measuring r has focused on three definitions [105]:

$$r_{\mathcal{R}} = \frac{\mathcal{P}_T^2(k_0)}{\mathcal{P}_{\mathcal{R}}^2(k_0)} \qquad r_\Phi = \frac{\mathcal{P}_T^2(k_0)}{\mathcal{P}_\Phi^2(k_0)} \qquad r_Q = \frac{C_2^T}{C_2^S} \tag{1.90}$$

which preclude any running of r [106]. For single-field inflation models, there is a consistency relation for the tensor spectral tilt:

$$n_T = -\frac{r}{8}. \tag{1.91}$$

Meanwhile, it can be shown generically that the tensor-to-scalar ratio is related to the primordial non-Gaussian signal by the inequality $\tau_{NL} \lesssim r/50$ [107].
For 2-dimensional STF tensors, the decomposition theorem

$$P_{ab} = \nabla_{\langle a}\nabla_{b\rangle}P_E - \epsilon^c_{(a}\nabla_{b)}\nabla_c P_B \tag{1.92}$$

exists, where the first term is the trace-free gradient and the second is the curl. Similarly for vectors the Helmholtz decomposition theorem is

$$V_i = \nabla_i\Phi + \epsilon^j_i\nabla_j\chi \tag{1.93}$$

with Φ and χ the scalar gradient and curl potentials. In order to verify that a detection of a low-l BB signal uniquely implies tensor modes, one needs to show that vector modes from inflation are negligible. From the Einstein equations, in the absence of a constant physical source for vector modes, one sets $\Pi^V = 0$. Conservation of angular momentum then implies a non-growing vorticity if $c_s^2 \leq \frac{1}{3}$, where c_s is the speed of sound. Vector perturbations created in the early universe on super-horizon scales will then decay exponentially[14]; the main point is that any vector modes need a constant source in order to be detectable in the modern sky. Furthermore, there is no model-independent way to geometrically separate vector and tensor-curl modes on the sphere so if the modes are of similar power in a given band they will be difficult to distinguish.
The coupling of the inflaton with other fields beside gravity may also impact inflationary observables; a good example is the axion, a particle suggested in studies of the charge-parity (CP) problem of the strong interactions. The axion is motivated from the Goldstone theorem: when any global symmetry is broken, a massless field is always produced. In the standard model Lagrangian, a term θ violates CP in the strong force sector. This is a small fine-tuning term that must be put in by hand. Alternatively, one can postulate a particle for its causation, by promoting the CP-violating term to a field, such that its VEV is at a CP-conserving point. So $\theta(x)$ is the Nambu-Goldstone field of a U(1) 'Peccei-Quinn' symmetry, named after its inventors. Since every light field becomes inhomogeneous due to amplification of vacuum fluctuations via inflation, the fluctuations of the axion

[14]More strictly, it has been shown that with some contrived models [108], one can produce vector modes in the CMB which could be confused for an $r \sim 10^{-6}$ signal; meanwhile it has also been shown [109] that the higher-order vorticity equations create vorticity sourced by density gradients. These degeneracies with the tensor signal, if large enough, may require either (or both) an understanding of the model-dependent running of r or a method to decompose the tensor/vector components on the spherical surface.

field before inflation must have $\langle(\delta\theta)^2\rangle \propto H^2$ which stays time-independent until the QCD epoch. The axion oscillations then produce isocurvature perturbations, which must be (via WMAP) at least 10 times smaller than the adiabatic perturbations. If $f_{PQ} \sim 10^{12}$ GeV then the inflation scale is low, at $M_{\rm infl} \lesssim 10^{13}$ GeV ($r \sim \mathcal{O}(10^{-10})$), from which gravity waves cannot be measured in the foreseeable future [110].

Recall the argument for the existence of primoridal tensor modes: a scalar field with quantum fluctuations induced in it is coupled to a classical metric which is 'dragged along' with the expansion of the density perturbation of the scalar field. However, if one considers the so-called Planck scale and that the number of e-folds for inflation is typically of order 60 it might not be impossible that quantum gravitational effects could manifest in the B-mode sky.

The full inflaton is not without its own theoretical issues — for hybrid models, the 'η problem' describes the difficulties of trans-Planckian calculations: UV corrections to the effective inflaton potential tend to give a slow-roll parameter of $\eta \sim 1$ which rules out the inflationary phenomenology. Meanwhile, difficulties exist related to more fundamental issues such as moduli stabilization in the string theories that many such inflationary scenarios are based on. Also, inflaton models generically require that the inflaton potential be artificially flat, when compared to the vacuum energy. The range of values for the tensor-to-scalar ratio from inflationary models include chaotic inflation with $r \gtrsim 2 \times 10^{-2}$, and natural inflation with an expected $r \gtrsim 10^{-3}$ [111]; single-field models scale anywhere up to $r \sim 0.3$. On the other hand, it has been shown that of the inflationary models that can be derived from more fundamental (i.e., string theoretical/supergravity) physics, very few yield an appreciable r — with brane-type models being essentially tensor-mode-free, this phenomena being related to the issue of moduli stabilization. Finally, there is perhaps the deepest outstanding remaining issue of the inflationary formalism, the question of how the quantum fluctuations in the inflaton become classical perturbations in the density field. This is related to the measurement problem in quantum mechanics. Since in the inflationary scenario the collapse of the wavefunction cannot be brought about by measurement before observers exist then decoherence is a necessary condition for the continued acceptance of the Copenhagen interpretation. For Mukhanov [28], it appears that decoherence is necessary but not sufficient. The choice of a Bunch-Davies state in which quantization is performed is itself not immune to criticism [112]. Other authors have argued that cosmological implications must alter the standard set-up in quantum mechanics [113, 114], whilst others still have taken the obverse

stance by championing the potential that primordial perturbations may have for discriminating interpretations of quantum mechanics [115].

Tensor Perturbations & Exotic Physics

Beyond the inflationary paradigm there are further, more exotic, links between tensor perturbations and fundamental physics that a positive B-mode detection may shed light on. It can be shown [116] that the statistical properties of a stochastic gravitational wave background are independent of the basis if $|h_+|^2 = |h_\times|^2$. For parity considerations, it is more convenient to use circular polarization states h_L, h_R. Parity-symmetry is then violated unless $|h_L|^2 = |h_R|^2$; if parity is conserved in the electromagnetic Lagrangian and in gravity (and foregrounds have not yet been considered) then $C_l^{TB} = C_l^{EB} = 0$.
Generally, parity-odd terms in the effective Lagrangian lead to a rotation of the polarization axis of the radiation. So long as one can postulate some reason for $a_{lm}^V \neq 0$, 'cosmological birefringence' [117] (double refraction) can be produced. This could typically be spotted as some sort of polarization basis rotation between the surface of last scattering, and Earth; one can show that the rotation of the (Q, U) basis by an angle α implies a mixing between E- and B-modes:

$$\begin{pmatrix} a_{lm}'^E \\ a_{lm}'^B \end{pmatrix} = \begin{pmatrix} \cos(2\alpha) & \sin(2\alpha) \\ -\sin(2\alpha) & \cos(2\alpha) \end{pmatrix} \begin{pmatrix} a_{lm}^E \\ a_{lm}^B \end{pmatrix}. \tag{1.94}$$

In such a case, the correlation relations become

$$\begin{aligned} C_l'^{TE} &= C_l^{TE}\cos(2\alpha) \\ C_l'^{TB} &= C_l^{TE}\sin(2\alpha) \\ C_l'^{EB} &= \frac{1}{2}(C_l^{EE} - C_l^{BB})\sin(4\alpha) \\ C_l'^{EE} &= C_l^{EE}\cos^2(2\alpha) + C_l^{BB}\sin^2(2\alpha) \\ C_l'^{BB} &= C_l^{BB}\cos^2(2\alpha) + C_l^{EE}\sin^2(2\alpha). \end{aligned} \tag{1.95}$$

One can break parity-invariance by for example introducing a parity-odd Chern-Simons[15] term into the electromagnetic field equations [118], yielding a massive photon. This then leads to a modified photon dispersion relation. If the photons travel for a time interval $\delta\eta$, they obtain a differential rotation (birefringence) whose rotation rate $\delta\theta$ is determined by the Chern-Simons term and the variation

[15]Chern-Simons theory is a topological quantum field theory. In condensed matter studies, it describes topological order in fractional quantum Hall states.

in H over the time slice $\delta\eta$. The latter term also gives rise to a change in the photon energy. Therefore, the differential rotation is correlated to the change in the photon energy. This effect is purely due to the time dependence of H. Thus, the resulting optical birefringence can become a function of the frequency change.
Another possibility is that gravity could be chiral on some small scale. Contaldi et al [119] provide a general formalism by replacing the linearized action with $S \sim s^R + s^L$ leading to power spectra for left- and right-handed gravitons. This sort of behaviour has been realised as a generic consequence of tensor perturbations in a loop quantum universe [120]. If parity is violated in either of these ways, a non-zero C_l^{TB} is produced. In the same way that TE correlations are easier to measure than EE ones, this is the property that one would measure (rather than C_l^{EB}) to constrain the effect since one is correlating a large quantity with a small quantity as opposed to two small quantities. Similarly, string-type inflationary models (such as shown in Staoh et al [121]) or a fundamental pseudoscalar field [122] may also provide parity-breaking phenomenology.
Another potentially fundamental reason Faraday rotation may be detectable is if there exists some kind of primordial magnetic field [123] B_0. This has been speculated as an explanation for cluster magnetic fields of order 1 μG. A perfect knowledge of foregrounds would allow some future experiments to constrain such a field to $\sigma_{B_0} \sim 10^{-11}$ Gauss [124], complicated in reality by the further problem that from beam systematics the fractional bias in the TB cross-correlations will be larger than the the corresponding fractional bias in the BB power spectrum [125].

1.3 Foregrounds and Secondary Anisotropies

Ignoring systematic errors, one of the major problems in CMB polarization observations are the secondary anisotropies — between the LSS and Earth, there are a range of processes which serve to introduce noise into the signal that is desired — and foreground material [126, 127]. Beside the scattering of CMB photons off cluster gas electrons along the line-of-sight and cluster magnetic fields which may also affect the polarization signal, the other main culprits are weak lensing and reionization:

- Weak lensing: The presence of any mass bends the path of light passing near it. The Universe as a whole experiences statistical weak lensing, or cosmic shear, wherein a single background source cannot be determined. Nonethe-

less, there is usually stronger shear in the direction of clusters and other extended massive bodies; the important thing about gravitational lensing is that it makes no statements about the astrophysical conditions occurring — only the intervening mass matters.

Lensing distorts the direction of incident light, so a pure E-mode signal at the LSS will be observed to include B-modes after lensing. The lensing signal modifies the CMB damping tail via transfer of power from large to small scales. Since the effect is non-Gaussian, higher-order statistics can be used for the detection of CMB lensing. One way to deal with this might be to reconstruct the lensing by the mass distribution. Unfortunately there are secondary effects which are prominent at the same frequency as lensing, such as the kinetic Sunyaev-Zel'dovich effect or residual foreground contaminations, so this is far from trivial for an accurate reconstruction. Density fluctuations distort E-modes [128, 129]; on the lower l scales, these modifications will be swallowed up by the cosmic variance errors, but on smaller angular scales these corrections become important for maps with other foreground and systematic noise removed.

The weak lensing of the CMB could also cause problems regarding inflation model elimination via cross-analysis of the tensor-to-scalar ratio with signals of non-Gaussianity. Again, this is because the lensed CMB is not Gaussian.

- Reionization: After recombination at the LSS, the Universe entered its 'dark ages', when it was mostly populated by neutral hydrogen. At some point, reionization would have began as the first ionizing sources formed, likely to be the first stars. It is the second of two major phase changes of hydrogen gas in the universe.

  Reionization [130] affects the E-mode polarization by producing a characteristic polarization bump on large scales. Evidence from the IGM, such as quasar absorption lines, suggests that reionization needs to have occurred before $z \sim 6$; the convention is now accepted at a redshift between 7 and 20. The most popular candidates for reionization sources are Population III stars and miniquasars, since the ionizing sources cannot be normal galaxies or known quasars due to luminosity function constraints.

  On small scales, the additional polarization signal from reionization is caused by coupling between primary quadrupole and electron density fluctuations at the region where scattering of CMB photons off the reionized gas occurs. As yet models are still indecisive as to whether the universe

reionized homogeneously, with fluctuations from the electron position or inhomogeneously, with fluctuations of the ionizing fraction.

The probability that a photon has avoided re-scattering is $P(t) = e^{-\tau(t)}$, where τ is the optical depth. For instantaneous reionization at $z_{\rm rec} \gg z_{\rm reion} \gg 1$ for a flat universe (where $z_{\rm rec}$ is the redshift at recombination and $z_{\rm reion}$ the redshift at reionization), the optical depth at reionization is

$$\tau(z_{\rm reion}) \sim 0.03 \frac{\Omega_b h_{75}^2}{\sqrt{\Omega_m h_{75}^2}} z_{\rm reion}^{3/2} \tag{1.96}$$

i.e., for $z_{\rm reion} \sim 5 \rightarrow \tau = 0.02$ the effect on fluctuations is no greater than 2 per cent. Hence the power spectra are modified by

$$C_{l,{\rm obs}}^{TT} = \begin{cases} C_l^{TT} & l \ll l_{\rm reion} \\ \exp[-2\tau] C_l^{TT} & l \gg l_{\rm ion} \end{cases} \qquad l_{\rm reion} \sim z_{\rm reion}^{1/2} \Omega_m^{0.09}. \tag{1.97}$$

Beside using information from CMB polarization, reionization can be probed by another promising frontier in observational cosmology: the 21cm hydrogen line background at between 9 and 200 MHz [131, 132, 133], which should yield not only an accurate account of the matter power spectrum in the period after recombination but also a precise picture of how the Universe was reionized, since neutral hydrogen which has been ionized by radiation from stars or quasars will appear as holes in the 21cm background.

These known physical foreground effects are further muddled by galactic foregrounds, such as dust effects. Examples include spinning dust models (rapid rotation of grain dipole moments) and models that use grains with a strong magnetic response (via thermal vibrations of magnetic dipoles [134]), which would make for small-scale noise although this is generally more of a problem at frequencies greater than ~ 100 GHz. Galactic synchrotron [135] is expected to dominate at low frequencies, motivating projects such as S-PASS [136] to complete an accurate galactic polarization profile.

Further to these, larger bodies such as cluster magnetic fields may act to produce Faraday rotation, producing mixing between the primordial E and B-modes [137] as previously mentioned. Studies of a potential primordial magnetic field at the recombination epoch, or after the Universe was reionized, also realize Faraday rotation. This modifies the evolution equations for the polarization Fourier modes. The rotated B-mode polarization from these potential phenomena includes dependences on all of the plasma frequencies and Larmor frequencies

(precession of the magnetic moment of particles in a magnetic field). Fortunately, this means that if the frequency channels of a given experiment are larger than the magnetic field pseudo-scalar rotation rate one can attribute B-mode autocorrelations to Faraday rotation from these phenomena [138]. For B-mode-less models, it is possible to perform a de-rotation in the linear polarization (detector) frame [139]. How one might de-rotate the polarization in the more general scenario of both E- and B-modes present has yet to be established.

1.4 Experimental Status

Here the typical observational strategies, instrumentation types and potential experimental errors are briefly summarized, with a discussion of current and ongoing experiments and their implications for polarization cosmology.

1.4.1 Systematics

Many factors go into designing a CMB observing mission; the main characters are observing frequency, survey type and beam size. The most obvious initial factor is of ground- versus balloon- versus space-based missions. These define the integration time necessary to make a statistically significant detection of polarization; balloon-type experiments and high-altitude observing stations offer low column density observations and a heightened ability to understand the instrument systematics due to the ready accessibility of the instrumentation. This is contrasted with the atmosphere-free but largely expensive method of space-based observations.
The path from experimental read-out data to cosmological observations is fraught with inferential danger. The process (as shown on Tegmark's website[16]) of

$$\begin{aligned}\text{sky} \rightarrow \text{measurement} \rightarrow \text{raw data} \rightarrow \text{cleaning} \rightarrow \text{time} - \text{ordered data} \\ \rightarrow \text{mapmaking} \rightarrow \text{multi} - \text{frequency maps} \rightarrow \text{foreground removal} \rightarrow \text{sky map}\end{aligned}$$

is not usually straight-forward. Calibration and cleaning provide the lengthiest of tasks, requiring the removal of foregrounds, a good understanding of the beam, leakage between observables from systematic effects in the underlying technical satellite equipment and more besides.
For example [140], errors on E/B mode power spectrum estimation can depend

[16] http://space.mit.edu/home/tegmark/

on the type of polarization instrument used. Miscalibration of the polarization reference is another systematic [141], which would effect both the self- and cross-polarization spectra; the potential for a false positive detection of gravitational waves being greater on the large scales corresponding to a primordial signal than for the smaller foreground scales. Data reduction also has to deal with semi-arbitrary physics such as cosmic ray hits and instrument scanning issues; usually the entire reduction technique is completely experiment-specific. Photon noise from quantum fluctuations in the environment, amplifier noise and thermal fluctuations in the detectors also play their part in contaminating data.

Yadav et al [142, 143] show how one can describe the line-of-sight distortion of the polarization signal in terms of a finite number of fields, leaving a distinctive signal in the other zero $\langle EB \rangle$ and $\langle TB \rangle$ correlations: these include distortions in a single perfectly known direction $\hat{n}$, mixing of the polarization fields in a local region of length scale σ around $\hat{n}$, modulation in the amplitude of the fields, rotation of the plane of polarization, coupling between two spin states (spin-flip), leakage from the temperature to polarization and change in the photon direction amongst others. One can then attempt to construct an estimator for the distortion field $\mathcal{D}$, whose effect can also be used to reveal signals of non-standard cosmological physics such as cosmological rotation and patchy reionization.

The required beam size is usually determined by the experimental goals; optical systems at CMB wavelengths produce large diffraction-limited beams. Polarization detectors usually consist of either half-wave plates which modulate the incoming polarization pattern, wire grids or polarization sensitive detectors which analyze the polarization of two separate beams, wherein differences in the sidelobe and off-axis detector responses need to be accounted for; bolometers are an alternative which measure both senses of linear polarization in a single beam.

For the rotation of a cryogenic half-wave plate [144] in front of the primary optics of each telescope, the linear polarization is found by combining the signals measured by several detectors, whose planes of polarization are rotated with respect to each other in multiples of $\pi/4$. Many polarization analyzers (such as half-wave plates) display chromatic aberration; this is a result of the devices having different refractive indices for different wavelengths. The atmospheric emission and absorption typical of ground-based observations varies strongly with wavelength; longer wavelengths reduce background detector loading from sky temperature but increase sensitivity to galactic synchrotron emission, which can be highly polarized. The combination of these effects with the unknown characteristics of foreground polarized emission make multi-frequency observations important

for analysis. This has its own set of caveats since multi-frequency, multi-pixel focal planes require off-axis pixels, which can introduce polarization offsets. Beam asymmetry [145] can produce signals which would masquerade as a non-zero polarization rotation angle.
Furthermore, there are typical issues arising from other aspects of the survey and the underlying physics: $1/f$ noise is induced in the polarization measurements by gain and noise temperature fluctuations in the amplifiers, whilst incomplete sky coverage increase sample variance by $\sim$(area covered)$^{-1/2}$, and smears out power spectrum features.

1.4.2 Current Constraints & Future Surveys

A number of experiments contribute to the state-of-art CMB measurements; foremost are probably WMAP's 7-year observations. WMAP, launched in 2001, was the space telescope which succeeded the COBE satellite. It has provided many fundamental observations, most spectacularly the excellent agreement of the accurate temperature anisotropy power spectrum with the ΛCDM expectations; the WMAP satellite has only recently concluded its operations, and the scientific community await its final 9-year data analysis. Whilst the WMAP satellite does not contain a direct polarimeter, polarization data (albeit highly noisy) is obtained by differential temperature analysis via the differential radiometers [146]; the differencing of signals from the horns approximately cancels the systematic $1/f$ signal drift in order to reveal the cosmological signal. In comparison with the temperature-polarization correlation data, the WMAP polarization autocorrelation data are much more prone to systematic error [147]; the Q and U maps are noise-dominated.
Figure 1.8 shows the tensor-to-scalar ratio computed by Komatsu et al [148], with uniform Bayesian priors for n_s and $dn_s/d\ln k$. The upper limit on r is obtained via a Monte Carlo Markov Chain likelihood analysis, yielding $r < 0.43$ (95 percent confidence limit (CL)). Since there is a degeneracy with n_s, it is important to perform a multi-survey analysis. Data from baryonic acoustic oscillations (BAO) and supernovae (SN) constrains the distance scale and hence matter density better, thus a determination of $r < 0.20$ (95 percent CL, no running spectral index) or $-0.256 < 1 - n_s < 0.025$ and $r < 0.54$ (running spectral index) are obtained.
The anti-correlation of C_l^{TE} with C_l^{TT} at $l \sim 50$ found by WMAP is consistent with superhorizon adiabatic fluctuations rather than active perturbations such as topological defects, which predict a correlation instead. Since all the values

for r are only upper limits, more accurate future observations are required. Intriguingly, the 7-year analysis also shows the tangential and radial polarization patterns around hot and cold spots of temperature fluctuations, consistent with the concordance cosmological physics.

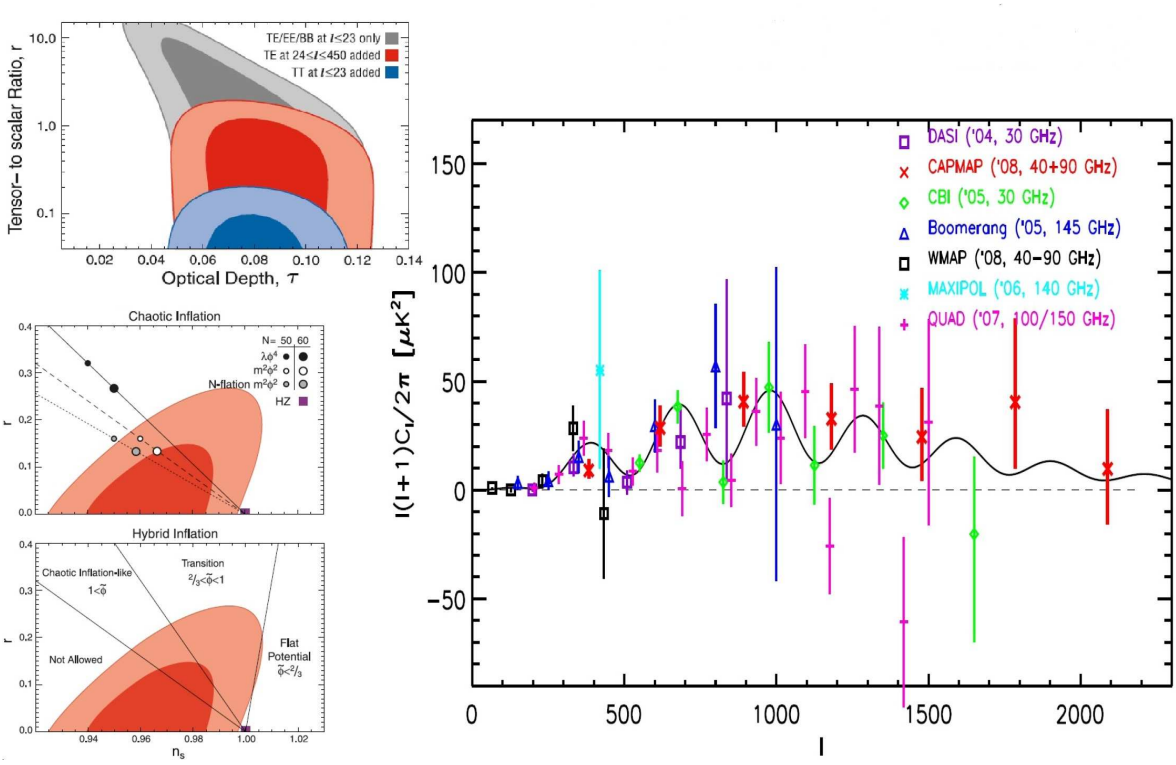

Figure 1.8: Top-left diagram: WMAP 5-year r - τ plane, from Komatsu et al [148]. Bottom-left and mid-left diagrams: WMAP 5-year constraints [148] on inflation models; it can be seen for example, that flat-potential hybrid inflation models are unlikely to account for the data. The 7-year results are essentially unchanged [149]. Right diagram: Combined EE measurements across a range of surveys (from Samtleben [150]).

A number of experiments have been led purely for the polarization data. The first to unambiguously detect the E-mode spectrum was DASI (Degree Angular Scale Interferometer [151, 63]), a ground-based interferometric array at the South Pole; with 13 feed horns fitted with broadband achromatic polarizers DASI operated in 10 1-GHz bins across the 26 - 36 GHz bandrange, and sampling points equivalent to the multipole range $l \sim 140$ to $l \sim 900$. Unlike the WMAP case, the Stokes parameters were derived from 'Stokes states', related to the response of the interferometer on a given baseline. The observation of two 3.4° FWHM fields separated by one hour RA resulted in a detection of E-mode polarization at 4.9σ, and a B-mode amplitude upper-limit of 0.59 times that of the temperature ampli-

tude.

Following the first positive detection by DASI, further significant detection was made by Boomerang in 2003 [152, 153], again situated at the South Pole but instead a balloon-borne experiment. Boomerang combined the utility of polarization bolometers at 145 GHz with polarizing grids at 245 and 345 GHz to measure the EE spectrum, yielding a 4.8σ detection in the $100 < l < 1000$ range and 2σ upper limits of $8.6\mu\mathrm{K}^2$ and $7.0\mu\mathrm{K}^2$ on the BB and EB signals respectively. This was further complemented by CBI's measurements [154], which revealed the detail in the EE spectrum.

An important later experiment was QUaD, a ground-based polarimeter making use of the DASI infrastructure, whose third and final data release was in June 2009 [155, 156]. QUaD's array of 62 polarization bolometers, sensitive at 100 and 150 GHz resulted in values of $r < 0.33$ at 95% CL (when combined with WMAP) and most importantly constrained the B-mode amplitude to less than $0.57\mu\mathrm{K}^2$, all extracted from observations of a ~ 100 square degree sky area.

There are a range of planned further probes of CMB polarization, with only really the space-based missions able to map the full CMB sky. However, Earth-based missions are not without their own charms: recall that ground- and balloon-based experiments are considerably cheaper than space-based ones — balloon experiments have the added advantage of being above most of the atmosphere (and hence absorption is negligible). The most prominent of the space-based missions is ESA's Planck satellite.

Planck (launched in 2009 [157]) is an ambitious all-sky survey to measure the remaining information in the CMB temperature anisotropies, with 3 times the angular resolution of WMAP, an order of magnitude lower noise at the optimal frequency bands around 100 GHz and frequency coverage from 30 - 857 GHz, which will allow improved separation of the primordial signal from foregrounds. It is also expected to improve by 16 times the number of modes measured with signal-to-noise ratio of around unity. Some details of the expected yield from the Planck instruments are given in Fig. 1.9; the two main instruments, the LFI and HFI, are HEMT (high-electron-mobility transistors) and bolometer arrays respectively. The HEMT are differential receivers that provide a significant improvement on WMAP's, with improved sensitivity due to their being cooled on the LFI. Meanwhile, the 52 bolometers in the HFI are split into channels aimed at optimizing detections of signals of cosmological relevance. For the E-modes, it is expected that Planck will accurately map the spectrum out to $l \sim 1000$; meanwhile, if r is greater than ~ 0.01 Planck should be able to directly detect B-modes which

would be the first detection of its kind. The scale at which B-modes are detected (if at all) deeply affects the kind of models of inflation that are viable, and indeed the type of techniques that are useful to understanding inflation. Similarly, there is continued competition to make a first BB detection before Planck. Balloon- and ground-based experiments such as the ongoing Q/U Imaging ExperimenT (QUIET [150]) — designed specifically with the CMB polarization in mind, and observing since late 2008 — is one such example. QUIET is a ground-based telescope in Chile detecting at 40 and 90 GHz via coherent correlation polarimeters, with proposed extensions expected to detect a B-mode signal correpsonding to an r down to 10^{-2}. As it is in the process an order-of-magnitude upgrade of its detector facilities, then beside Planck it can be seen as a major competitor for the first detection of B-modes.

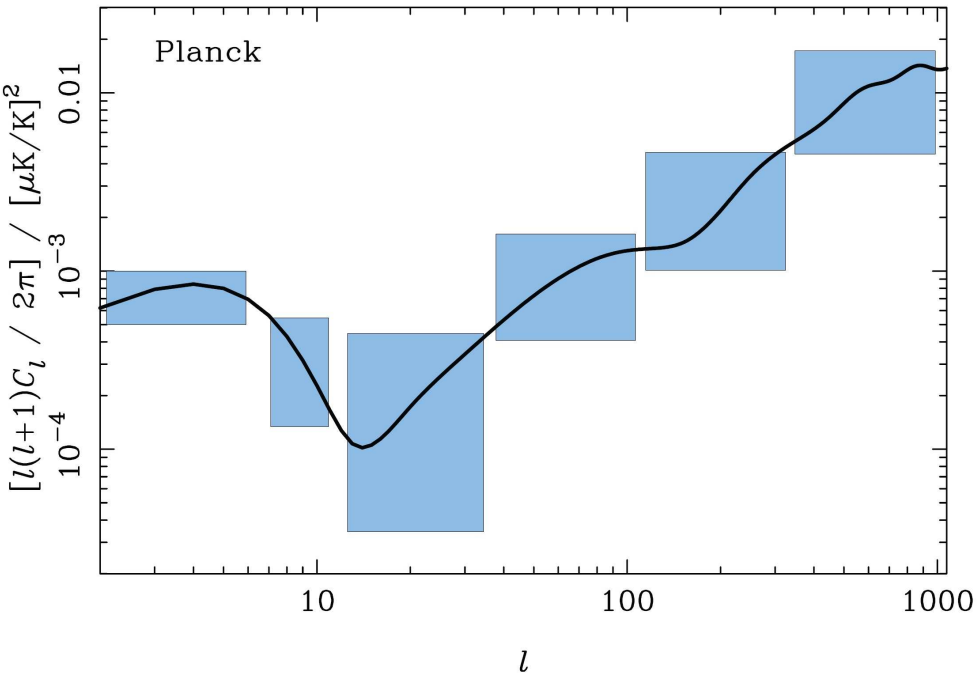

Summary of Planck Instrument Characteristics

	LFI			HFI					
Instrument Characteristic									
Detector Technology	HEMT arrays			Bolometer arrays					
Center Frequency [GHz]	30	44	70	100	143	217	353	545	857
Bandwidth ($\Delta\nu/\nu$)	0.2	0.2	0.2	0.33	0.33	0.33	0.33	0.33	0.33
Angular Resolution (arcmin)	33	24	14	10	7.1	5.0	5.0	5.0	5.0
$\Delta T/T$ per pixel (Stokes I)[a]	2.0	2.7	4.7	2.5	2.2	4.8	14.7	147	6700
$\Delta T/T$ per pixel (Stokes Q &U)[a]	2.8	3.9	6.7	4.0	4.2	9.8	29.8	...	...

[a] Goal (in μK/K) for 14 months integration, 1σ, for square pixels whose sides are given in the row "Angular Resolution".

Figure 1.9: Top diagram: Planck B-mode spectrum forecasts with 1σ errors, from the Planck Blue Book [23]; the primordial signal above $l \sim 150$ is dominated by the weak lensing component. Bottom diagram: Planck instrumental limits for the LFI (Low Frequency Instrument) and HFI (High Frequency Instrument).

Further along, plans are afoot for more advanced studies. On the terrestrial front, EBEX[17] is a balloon-based polarimeter (main flight due in 2011) designed to measure the polarization sky with a resolution of less than 8 arcminutes at frequency bands centered at 150, 250, 350, and 450 GHz. The sky patch covered by the ~ 1300-detector instrument is ~ 350 square degrees, allowing EBEX to probe on scales of $20 < l < 1000$ for a B-mode signal induced by a scalar-to-tensor ratio $r \sim 0.035$. Other future balloon experiments include Spider ([158], also due in 2011) with a larger sky coverage than EBEX and frequency bands located at 90, 145 and 280 GHz; the ground-based QUBIC (due 2012 [159]) and Polarbear [160]; and the CMBPol [161] program working on the next generation (post-Planck) CMB space satellite, for example EPIC-IM, designed to go after precisely the tensor modes from inflation and plausibly bring the detection limit down to an r of 10^{-3} or less.

The prospects for a full characterization of the EE spectrum and a first detection of B-modes this decade — either from lensing or gravity waves — are strong. The range of experiments should provide a nigh-full understanding of contaminants when survey data are combined.

1.5 Summary

The use of CMB data, particularly the temperature power spectrum, has allowed for the construction of a standard cosmological model featuring an expanding universe that is $\sim 73\%$ dark energy, $\sim 23\%$ cold dark matter and $\sim 4\%$ baryonic matter. This standard model suffers from problems that can be resolved by appending the inflationary universe hypothesis to the standard Big Bang. The field powering inflation features quantum fluctuations that seed the formation of structure as described by the matter power spectrum, whilst also generating a stochastic background of gravitational waves which could be detected by analyzing the polarization characteristics of the CMB, notably the large-scale B-modes. The detection of B-modes could not only determine the energy scale of inflation but could also determine more exotic physics such as chiral gravity by utilizing the EB cross-spectrum and cosmic defects from the large-l BB spectrum, which also leave a signal in the non-Gaussianity of the CMB. Ambitious experimental efforts such as EBEX and Planck are underway to make a first detection of these B-modes, expected to be a mere fraction of the magnitude of the E-mode polar-

[17] EBEX website: `http://groups.physics.umn.edu/cosmology/ebex/`

ization. These efforts need to deal with difficult systematic and foreground issues in order to make a clear detection, but the cosmology community is up to the task.

Chapter 2

Local Methods for the CMB

In the previous chapter, a context was set up within which to discuss some techological problems in CMB cosmology and methods by which these can be solved. These methods are focused on *locally*-calculated properties (i.e., sampling in a small region about the focal pixel, in real space) as opposed to the more usual global methods (such as harmonic-type analyses, which sample from every point on the map).

Real-space methods in the cosmological literature have mostly been limited to statistical analyses of the sky maps generated by the likes of WMAP, rather than the development of analytical methods which take advantage of the localized properties of real-space maps themselves or utilize localized mathematical constructs. For example, much of the current real-space CMB technology is limited to the correlation function between two fields X and Y

$$C^{XY}(\theta) = \langle X(\hat{\mathbf{n}})Y(\hat{\mathbf{n}}')\rangle_{\hat{\mathbf{n}}\cdot\hat{\mathbf{n}}=\cos\theta}\,, \tag{2.1}$$

which determines the probability for two points on the sky to have the same value. This can then expose signals of the causal horizon and shock waves from point sources.

Particularly, the prime motivation of this thesis was originally a solution for the *ambiguous modes problem* of separating out the E and B polarization modes. The favoured method in this thesis requires the use of *finite-difference* schemes. Later, it transpired that it should be possible to modify the use of the finite-difference method in order to detect discontinuities in the microwave sky. This is geared towards another unsolved problem in cosmology — the detection of topological defects arising from (inflationary or otherwise) symmetry-breaking. The enhanced-discontinuity maps that shall be developed can be studied in a num-

ber of ways, including by-eye-detection of anomalies, *needlet* decomposition and non-Gaussianity tests. Whilst the first two can be used without further alteration of the underlying sky map, the third method motivates the need to define an apodization scheme for the map since one is calculating spectra, discussed in chapter 3.

Further, the methods presented may eventually provide some use for more exotic phenomena. As an example, the phenomenology for a fundamental resolution of the CMB is developed. This is of course, likely an unphysical realization — but with Planck-scale-limited volumes and applications of the holographic principle implying that there may be signals from quantized spacetimes in the CMB sky maps, this is a first step in developing real-space signals for the more exotic physics typical of such spacetimes. Beside which, an actual detection of such a fundamental resolution would provide a highly unexpected challenge for theorists.

This chapter then describes techniques used for solving problems in cosmology, which are then implemented in the remaining chapters. Proceedings begin with an account of the general inferential calculus, Bayesian inference (section 2.1), with which one may make statements about the implications of data. This method is actually standard fare in cosmology; the new developments begin with a description of the ambiguous modes problem in CMB polarization and its solution (section 2.2) using the local method of finite differences (constructed in section 2.3). Following this, modifications of standard harmonic technology are discussed in order to make statements about non-Gaussianity in the temperature and polarization fields (section 2.4). Section 2.5 then considers the problem of detecting anomalies by combining local and global (harmonic) methods. Finally, potential uses for the discontinuity-detecting technology in the scenario of a finite-resolution sky map are speculated on in section 2.6.

2.1 Likelihoods and the Like

In order that later expositions on detection make sense, the dominant epistemic paradigm in modern cosmology, Bayesian statistics, is described. It is with this tool that cosmologists can go from a raw dataset to rigorous testing of the available theories, despite only having one universe to observe. The key characteristic of Bayesian methods which allows for single-sample inference is the *likelihood function*, allowing one to stipulate the degree of belief in a theory given the data. Bayesian statistics incurs the laws of probability as the calculus of inference; if

one wishes to have a *general* inferential formalism, as opposed to the disjointed toolkit more familiar to the frequentist approach, it is in some sense inevitable that one might follow the Bayesian approach. Indeed, it has been shown [162] that a small set of reasonable assumptions about degrees of belief necessarily implies the laws of probability. Given that one cannot reproduce the Universe in a laboratory it is then unsurprising that Bayesianism has quickly become dominant in the community of cosmologists. This next section describes the calculus; none of this section contains any new developments, but much of its content is both relevant and harnessed in later analyses.

2.1.1 Model Comparison: Bayes' Method

Bayesian statistics [163, 164, 165], a measure-theoretic probability theory, is a now-standard tool for CMB analysis. The formalism is set up from the very simple mathematical foundations of a partially-ordered lattice whose measure obeys addition, multiplication, commutativity and associativity [166]. Fundamental to the Bayesian approach is the focus on information theory, which was given its modern form by Shannon [167, 168]. One can define information in terms of the measures of the lattice and thus develop the rules of probability theory:

$$\begin{aligned} P(A) &\geq 0 && \text{Positivity} \\ \int P(A)dA &= 1 && \text{Sum rule} \\ P(A \cap B) &= P(A|B)P(B) && \text{Product rule.} \end{aligned} \tag{2.2}$$

From the product rule for the probability of event A and B, one can find Bayes' theorem:

$$P(H|D,I) = \frac{P(D|H,I)P(H|I)}{P(D|I)} \tag{2.3}$$

where H is the hypothesis, D the data and I the information.
The elements of this equation are given particular names in the literature: $P(H|I)$ is called the *prior* (current state of knowledge, or the assumptions therein such as known physics), $P(D|H,I)$ the *likelihood* $\mathcal{L}$, whilst $P(D|I)$ is the *evidence*. Bayesian statistics then states explicitly one's assumptions in contrast to the frequentist approach; this defines a *degree of belief* in a given theory. The underlying Bayesian philosophy is that probability is subjective, unlike the almost Platonic realism of probabilities for frequentists. This can be summed up by Jaynes' robot argument [169]: given a robot which can track precisely the fall of a tossed unbiased coin, from the point of view of the robot the initial heads/tails probability is 50:50,

whilst the probability is vanishingly small for one or the other just before the coin rests. It is this prior information which shows that probabilities are psychological phenomena which betray how much ignorance of a situation one has, rather than a property of an infinite ensemble. For a physical world with an uncertainty principle, this has interesting implications for claims of inherently probabilistic ontologies.

Furthermore, the Bayesian approach penalises extra parameters in a theory — and so automatically incorporates a form of Occam's razor. The *posterior* $P(H|D,I)$ is the thing one is after, yielding statistics for the parameter under analysis, in response to data available. By finding the peak likelihood and its shape around the peak it is possible to find the shape of the posterior. Since the information is defined as the difference between the prior and the posterior then in the presence of background knowledge one can modify the prior by minimizing the information. According to Shannon [168], this is equivalent to maximizing the entropy of a system, and is thus known as the maximum entropy or 'MaxEnt' approach. In the absence of any constraints, one would use a normalized uniform prior

$$P(H_i|I) = \frac{1}{K} \qquad \sum_{i=1}^{K} P(H_i|I) = 1, \tag{2.4}$$

equivalent to 'maximum ignorance' since this has nothing to say about any of the theories in the calculation. Bayesian inference is no technique for saying whether a given theory is correct; all one can do is make comparisons of the suitability of a set of two or more competing theories. For example, one could use the *Bayes factor*

$$B_{ij} \equiv \frac{P(H_i|I)}{P(H_j|I)} \tag{2.5}$$

as the discriminant. The remaining problem is to calculate the evidence; by redefining the evidence via a probability density p

$$P(D|H_i)_\lambda = \int P^\lambda(D|\theta_i, H_i) dp_i \qquad dp_i = P(\theta_i|H_i)d\theta_i, \tag{2.6}$$

one can integrate over the likelihood $\mathcal{L}(\theta_i) = P(D|\theta_i, H_i)$[1].

It can also be asked how Bayesian statistical inference incorporates Occam's Ra-

[1]One of the more interesting aspects of Bayesian inference is that one can use this form to relate thermodynamic and Bayesian inference:

$$\frac{d\log P(D|H_i)_\lambda}{d\lambda} = \frac{\int dp_i L^\lambda \log L}{\int dp_i L^\lambda} \equiv \langle \log L \rangle_\lambda \Leftrightarrow \frac{\int dp_i E e^{-E/T}}{\int dp_i e^{-E/T}} = \langle E \rangle_T .$$

zor. If the parameters θ (or the hypothesis) are marginalized over the data

$$P(\theta|D,I) = \int P(\theta,\phi|D,I)d\phi \tag{2.7}$$

then the Occam factor can be defined via:

$$\begin{aligned} P(D|H_i) &= \int p(\theta_i|H)\mathcal{L}(\theta_i)d\theta_i \approx \mathcal{L}(\hat{\theta}_i)\frac{\delta\theta_i}{\Delta\theta_i} \\ &= \text{Maximum likelihood } \times \text{ Occam factor.} \end{aligned} \tag{2.8}$$

where $\Delta\theta$ is the prior range and $\delta\theta$ is the likelihood width. Since a model with more parameters can always fit the data, the Occam factor penalizes models for wasted volume of parameter space; predictive probabilities favour simpler models.

If the CMB is assumed to be fully Gaussian, then its likelihood can be well approximated by a multi-variate Gaussian

$$\mathcal{L} = \frac{1}{(2\pi)^{n/2}|\text{Det}[C]|^{1/2}} \exp\left[-\frac{1}{2}\sum_{i,j}(D-\bar{D})_i C_{ij}^{-1}(D-\bar{D})_j\right], \tag{2.9}$$

where C_{ij} is the correlation matrix of the data D. For large numbers of parameters, finding the likelihood (or posterior) surface becomes computationally difficult. One can use Markov Chain Monte Carlo (MCMC) simulations to circumvent this problem, which scales linearly with parameter numbers, now a standard approach for CMB analyses; the MCMC generates a random sample from the posterior distribution, from which one can estimate the required parameters.

When making statements about degrees of belief in the values of parameters, confidence intervals are useful. Confidence intervals are regions R in the space of models (theories) with a volume such that the integrated posterior $\int_R P(\theta|D)d\theta$ is, say, 0.68 — this then corresponds to a 68 percent confidence; the confidence interval gives the probability that the interval contains the true value for the parameter. This encloses the prior information. To report results independently of the prior the likelihood ratio is used; the likelihood at a particular point in model space $\mathcal{L}(\theta)$ is compared with the maximum likelihood $\mathcal{L}_{\max}$. A model is said to be

where one can see an interesting analogy between the log likelihood of an inferential set-up and the energy E of a physical system. See Jaynes [169] or MacKay [170] for further detail on this connection.

acceptable if

$$-2\ln\left(\frac{\mathcal{L}(\theta)}{\mathcal{L}_{\max}}\right) \leq \text{ threshold} \tag{2.10}$$

with the threshold calibrated by calculating the distribution of the likelihood ratio in the case where a particular model is the true model.
Ideally, one wants to answer the question of how accurately one can measure model parameters from a given data set (without simulating the data set). For a data set given by m real numbers $x_1 \cdots x_m$ arranged in a vector and x a random variable with probability distribution which depends in some way on the vector of model parameters θ, the *Fisher information matrix* can be defined by

$$F_{ij} = \left\langle \frac{\partial^2 L}{\partial\theta_i \partial\theta_j} \right\rangle, \qquad L = -\ln\mathcal{L}, \tag{2.11}$$

which is taken from the Taylor expansion of the likelihood function around its maximum. This gives the minimum possible variance with which a parameter can be measured, and is of utility for forecasting the expected performance of future CMB experiments. The parameter covariance matrix C_{ij} is then just the inverse of the Fisher matrix, where one can identify the maximum likelihood value of the parameter with the parameter mean. One can then compute the Fisher matrix for some fiducial model. For example if the likelihood is a Gaussian $L = (\theta - \theta_0)^2/2\sigma_\alpha^2$, then by expansion

$$\Delta L = \frac{d^2 L}{2d\theta^2}(\theta - \theta_0)^2. \tag{2.12}$$

Setting $2\Delta L = 1$, the 68 per cent (1 sigma) case is equivalent to $1/\sqrt{d^2L/d\theta^2}$. For many parameters, one usually inverts the Fisher matrix, takes the minors and inverts again in order to plot joint 2D contours. For high-l CMB analyses, the Fisher matrix is approximately

$$F_{ij} = \sum_l \frac{2l+1}{2}\frac{\partial C_l}{\partial\theta_i}\frac{\partial C_l}{\partial\theta_j}(C_l + \mathcal{N}e^{\sigma^2 l^2})^{-2} \tag{2.13}$$

where $\mathcal{N}$ is the noise model and σ the beam size. For low-l CMB analyses, errors are dominated by cosmic variance and equation (2.13) over-estimates the errors by a factor of 2 or so. More generally, the Fisher matrix for all TT, EE, TE and

BB spectra is [105, 171]

$$F_{ij} = \sum_{l,X,Y} \frac{\partial C_l^X}{\partial \theta_i} \left[C^{XY}(\theta)\right]^{-1} \frac{\partial C_l^Y}{\partial \theta_j}, \tag{2.14}$$

where X, $Y = \{TT, EE, TE, BB\}$. Of course, the Fisher method is not the only way to get at the parameters; one can instead attempt to find unbiased estimators for the required parameters; the least-variance estimator out of any set of estimators usually being the optimal choice.

One may wonder whether classical field-theoretical techniques can be applied to inference, and indeed they can [166, 172]. By analyzing the infinitesimal variation in measures across a field of information, it is possible to import all the machinery of differential geometry into the inferential calculus; the only problem with this being that the priors developed from such geometric considerations tend to be strictly of the 'deep ignorance' variety, which is far too restrictive for inference on physical systems.

The frequentist equivalent for measuring one's confidence in data is to determine how close to the Cramer-Rao bound the error bars of a statistic are. For an unbiased estimator $\hat{\theta}$ of the parameter θ, the Cramer-Rao inequality is [173]

$$\text{Var}(\hat{\theta}) \geq \frac{1}{F(\theta)} \tag{2.15}$$

where $F(\theta)$ is the Fisher information. If more accuracy than the Fisher matrix estimate is required, it is necessary to turn to numerical methods for computing likelihoods. The dominant numerical method in cosmology is the Markov chain Monte Carlo method.

2.1.2 Monte Carlo Methods

In order to calculate the likelihood distribution in a large-dimensional space corresponding to many cosmological parameters, one can take advantage of Monte Carlo integration utilized with Markov chains [174]. Monte Carlo integration is the process of picking random, uniformly distributed points in the parameter space volume and then estimating the integral by

$$\int f dV \approx V \langle f \rangle \tag{2.16}$$

where $\langle f \rangle$ is the arithmetic mean over the sampled points of the function. The Markov property requires that the method of estimation is memoryless, i.e., independent of past and future states. This means that the points in a Markov chain are locally correlated but visit every point in the distribution in proportion to some density function; each step in the chain is only influenced by the step immediately preceding it.

In such large parameter spaces as in cosmological studies or if the posterior is mostly unknown, one wants a method that converges quicker than the uniform random sampling of Monte Carlo integration. Instead one may use Monte Carlo Markov chains (MCMC), which similarly samples randomly but this time from a non-uniform distribution; the process visits a point x with probability proportional to some given distribution function $p(x)$. The posterior probability of a model is proportional to the distribution function, allowing one to calculate the likelihood surface by sampling from the distribution function. This method of biasing the probability space sampling can lead to huge savings in computation time. In this thesis, use is made of the CosmoMC package [175] for performing such MCMC computations, as suggested by Christensen et al [176].

The MCMC process is to produce a chain of samples that will allow convergence to the correct posterior distribution. One iterates from an initial proposal matrix and halts the program after some convergance criterion A has been met. For an unknown posterior distribution, a Gaussian proposal density is a reasonable choice. The choice of convergence criteria is fundamental in ensuring convergence to the correct posterior; specifically, CosmoMC makes use of the *Metropolis-Hastings* (MH) [177, 178] algorithm for this purpose by default. For a Markov chain moving from parameter space positions θ_1 to θ_2, the transition probability kernel $T(\theta_1, \theta_2)$ can be set to ensure that the Markov chain has a stable asymptotic distribution equivalent to the posterior distribution by use of an arbitrary proposal density distribution q and the MH acceptance probability α:

$$\begin{aligned} T(\theta_n, \theta_{n+1}) &= \alpha(\theta_n, \theta_{n+1}) q(\theta_n, \theta_{n+1}) \\ \alpha(\theta_n, \theta_{n+1}) &= \min\left\{1, \frac{P(\theta_{n+1}) q(\theta_{n+1}, \theta_n)}{P(\theta_n) q(\theta_n, \theta_{n+1})}\right\}. \end{aligned} \tag{2.17}$$

In CosmoMC, the chain starts at a random position in parameter space and equilibrates ('burns in'), after which posterior sampling begins. This burn-in period is set to allow the chain to settle into a sequence that has no dependence on the randomly-seeded starting point. Thinning the chain can help protect against producing correlated chains. If such information is available, it is often best that the

proposal density is a similar shape to that of the posterior, allowing faster convergence. This is the case for known cosmological parameters. The proposal is the probability density function; one can tune it in such a way that it fills the parameter space but usually it is preferable to centre it on the current known parameters set. By setting the proposal's geometry close to the expected posterior, the speed at which the likely parts of the parameter space are explored is enhanced; in advance of this, a burn-in chain is produced to yield a crude estimate of the shape, commonly using a Gaussian as the start shape since it is a common posterior. The proposal choice then amounts to being a trade-off between a small proposal width with a high acceptance rate and a large width with a quicker convergence/exploration rate.

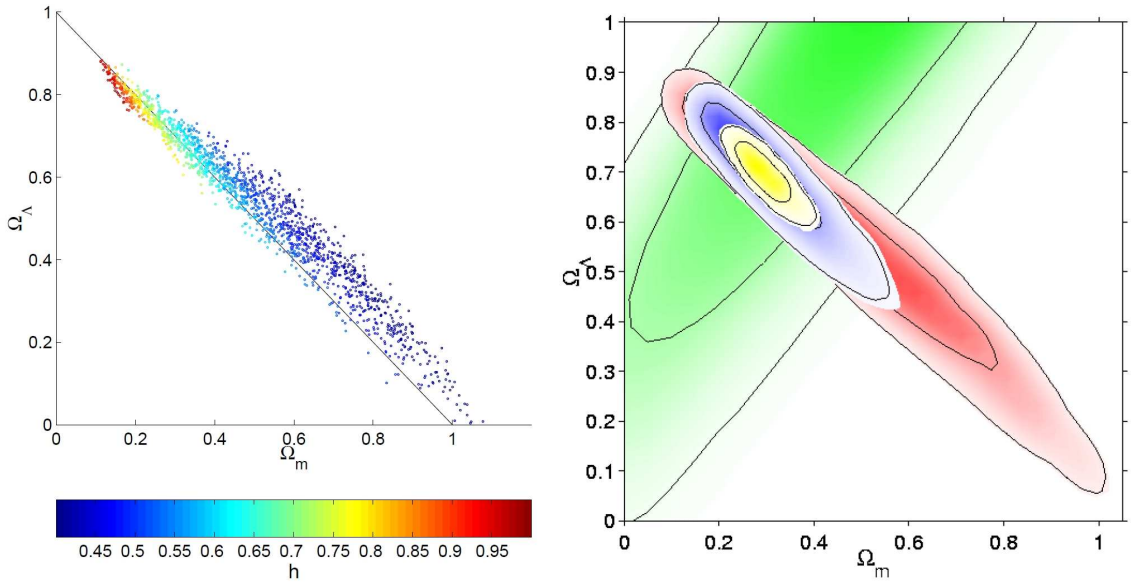

Figure 2.1: Example posterior distribution sampling (left diagram) and resulting confidence intervals (right diagram), from Lewis & Bridle [175], calculated from a combination of WMAP, HST and supernova data. From the peak contour on the right diagram, it can be seen that Bayesian methods currently favour a ΛCDM cosmological model.

The criteria for convergence is defined by the nearness of the approximate posterior to the actual posterior; the computation time is proportional to the number of parameters in the distribution. Various methods exist which check for bias in the converged distribution due to factors such as stepsize [179, 180]. In particular, CosmoMC provides a convergence ratio, with which one may compare statistics for multiple sequences of chains. In order to compare CMB data with CMB theory, CosmoMC takes power spectra from CAMB (a variant of CMBFAST) cal-

culations, resulting in plots like Fig. 2.1 when combined with other survey data.

2.1.3 Bayesianism & Non-Gaussianity

In the previous chapter it was seen that non-Gaussianity is an important aspect of CMB studies with regard to inflation and cosmic defects. For example, a significant primordial non-Gaussian signal may be able to rule out the simplest slow-rolling inflationary scenarios. Often the approach for calculating non-Gaussianity involves the use of cubic combinations of filtered CMB sky maps [181] by looking for specific bispectrum signatures. The bispectral estimator in chapter 1 (equation (1.73)) is optimal [173], but only for small non-Gaussianity [182]. Fuller Bayesian methods instead of the frequentist estimator-type analysis have proven more challenging, but have been pursued in Elsner et al [183] by deriving a joint posterior for f_{NL} and the curvature perturbation, and an implementation in Elsner er al [184] using Hamiltonian MC sampling (a hybrid of Gibbs and Metropolis sampling methods).

In order to make more general statements about non-Gaussianity, one can use the Edgeworth expansion [185, 186, 187, 188], essentially an expansion of a probability density function in terms of Hermite polynomials. The Edgeworth series is an asymptotic expansion which approximates a $given$ probability distribution in terms of its cumulants. In this sense it is then possible to use the Edgeworth expansion to define a non-Gaussian likelihood function. The expansion contains a number of undesirable properties such as the series truncation not in general being a density (truncation necessarily precludes asymptoticity), although such problems can be bypassed. Alternatively, one can adopt a harmonic oscillator approach [188] to set up an exact likelihood function, dependent on the power spectrum and on a set of parameters, which vanishes if the signal is fully Gaussian. This then does not suffer from the truncation issues of the standard Edgeworth approach. Another suggested alternative is to make use of the Gamma distribution [189].

The Bayesian formalism is the gold standard for cosmological inference. However, for reasons of computation time some use of frequentist estimators will be made instead. An estimator, whilst lacking the foundational rigour of the Bayesian formalism, can give a first approximation to the correct form of the power spectra, which can then be used as a prior with which to speed up the convergence of the MCMC calculations.

2.2 Separating E- & B-modes: The Ambiguous Modes Problem

In chapter 1, the use of studying the polarization of the CMB for detecting the cosmic gravitional wave background produced by cosmological inflation was touched upon. The standard methods for performing this analysis come in two flavours: the tensor-harmonic formalism and the spin-weighted-harmonic formalism, both of which are equivalent. In the tensor harmonic approach the polarization tensor can be expanded in terms of tensor spherical harmonics [61]

$$P_{ab}(\Omega) = \sum_{lm} \left(a^E_{lm} Y^E_{(lm)\ ab}(\Omega) + a^B_{lm} Y^B_{(lm)\ ab}(\Omega) \right), \tag{2.18}$$

where the polarization tensor has been decomposed into E and B components[2] and the explicit coordinate-dependence Ω is dropped for convenience, with

$$a^X_{lm} = \int P_{ab} Y^{Xab*}_{(lm)} d\Omega, \qquad a^{X*}_{lm} = (-1)^m a^X_{l,-m} \tag{2.19}$$

where $X = (E, B)$ and the $Y^{Xab}_{(lm)}$ are the E- and B-type decomposed tensor spherical harmonics (see Appendix). Equivalently, one can make use of the spin-weighted operators of Newman & Penrose [190]:

$$\eth_s = -(\partial_\theta + i \csc\theta \partial_\phi - s\cot\theta), \qquad \bar{\eth}_s = -(\partial_\theta - i \csc\theta \partial_\phi + s\cot\theta), \tag{2.20}$$

where for clarity in spin-counting of entities operated on, the standard operator definitions are appended with the spin-weight of the operator. These operators are 'square roots' of the Laplacian operator on a spherical surface ($\nabla^2{}_s f = \bar{\eth}\eth_s f$) and act to raise and lower the integer spin-weight s of a function ${}_s f$ well-defined in s-space, by creating and annihilating spinors o and their conjugates $\hat{o}$:

$$\eth_{\frac{1}{2}} o^A = 0 \qquad \bar{\eth}_{\frac{1}{2}} o^A = -\hat{o}^A \qquad \eth_{-\frac{1}{2}} \hat{o}^A = o^A \qquad \bar{\eth}_{-\frac{1}{2}} \hat{o}^A = 0, \tag{2.21}$$

with the integer spin-weight s defined by the transformation $o \to o' = e^{is\psi} o$ about the pole of a tangent space defined at every point on the sphere. It can be demonstrated that the operation of $\eth$ with the wrong spin-s value leads to

[2] Any symmetric trace-free tensor can be decomposed into the sum of $A_{;ab} - \frac{g_{ab} A^c_{;c}}{2}$ and $B_{;ac}\epsilon^c{}_b + B_{;bc}\epsilon^c{}_a$.

entitities with an ambiguous spin-weight: first one chooses a spinor basis

$$o^A = \begin{pmatrix} e^{-\frac{i\phi}{2}} \cos\frac{\theta}{2} \\ e^{\frac{i\phi}{2}} \sin\frac{\theta}{2} \end{pmatrix} \qquad \hat{o}^A = \begin{pmatrix} -e^{-\frac{i\phi}{2}} \sin\frac{\theta}{2} \\ e^{\frac{i\phi}{2}} \cos\frac{\theta}{2} \end{pmatrix} \tag{2.22}$$

and then calculates

$$\begin{aligned} \eth_{\frac{s}{2}} o^A &= \frac{s-1}{4} \cos\theta \Lambda^A & \bar{\eth}_{\frac{s}{2}} \hat{o}^A &= \frac{s+1}{4} \cos\theta \hat{\Lambda}^A \\ \bar{\eth}_{\frac{s}{2}} o^A &= \frac{\Lambda^A_\pm}{2} - \frac{s+1}{4} \cos\theta \Lambda^A & \eth_{\frac{s}{2}} \hat{o}^A &= \frac{\hat{\Lambda}^A_\pm}{2} - \frac{s+1}{4} \cos\theta \hat{\Lambda}^A \\ \Lambda^A &= \begin{pmatrix} e^{-i\phi/2} \csc\frac{\theta}{2} \\ e^{i\phi/2} \sec\frac{\theta}{2} \end{pmatrix} & \hat{\Lambda}^A &= \begin{pmatrix} -e^{i\phi/2} \sec\frac{\theta}{2} \\ e^{i\phi/2} \csc\frac{\theta}{2} \end{pmatrix} \\ \Lambda^A_\pm &= \begin{pmatrix} e^{-i\phi/2} \csc\frac{\theta}{2} \\ -e^{i\phi/2} \sec\frac{\theta}{2} \end{pmatrix} & \hat{\Lambda}^A_\pm &= \begin{pmatrix} e^{-i\phi/2} \sec\frac{\theta}{2} \\ e^{i\phi/2} \csc\frac{\theta}{2} \end{pmatrix}. \end{aligned} \tag{2.23}$$

The resulting vectors from operation of incorrect spin-weight derivatives cannot be written in terms of spinors, so do not transform as such. The spin-weighted spherical harmonics of order (s, l, m) can be constructed by combining $(l+m)$ spinors and $(l-m)$ conjugate spinors, of which one uses the first element from $(l+s)$ spinors and the second element from $(l-s)$ spinors:

$$N_{slm}\, {}_sY_{lm} = \overbrace{\underbrace{o^{A_1} o^{A_2} \cdots o^{A_2}}_{s+m} \underbrace{\hat{o}^{B_1} \cdots \hat{o}^{B_2}}_{l-s}}^{l+m \qquad\qquad l-m} \tag{2.24}$$

where the summation convention is not used and N_{slm} is a normalization factor. Alternatively, it can be shown that

$$\eth_s {}_sY_{lm} = \sqrt{(l-s)(l+s+1)}\, {}_{s+1}Y_{lm}, \qquad \bar{\eth}_s {}_sY_{lm} = -\sqrt{(l+s)(l-s+1)}\, {}_{s-1}Y_{lm}. \tag{2.25}$$

Since

$$Q' \pm iU' = e^{\mp 2i\theta}(Q \pm iU) \qquad \Rightarrow \qquad Q \pm iU = \sum_{lm} {}_{\pm 2}a_{lm\pm 2} Y_{lm}, \tag{2.26}$$

then the orthogonal Stokes parameters can be described in terms of $s = \pm 2$ spin-weighted spherical harmonics:

$$\begin{aligned} Q &= \mathrm{Re}\left[-\frac{1}{2}\sum_{lm} a^E_{lm}({}_2Y_{lm} + {}_{-2}Y_{lm}) + i a^B_{lm}({}_2Y_{lm} - {}_{-2}Y_{lm})\right] \\ U &= \mathrm{Re}\left[-\frac{1}{2}\sum_{lm} a^B_{lm}({}_2Y_{lm} + {}_{-2}Y_{lm}) - i a^E_{lm}({}_2Y_{lm} - {}_{-2}Y_{lm})\right] \end{aligned} \tag{2.27}$$

where the E and B harmonic coefficients are defined via

$$a^E_{lm} = -\frac{{}_2a_{lm} + {}_{-2}a_{lm}}{2} \qquad a^B_{lm} = \frac{i({}_2a_{lm} - {}_{-2}a_{lm})}{2} \qquad {}_{\pm 2}a_{lm} = -(a^E_{lm} \pm i a^B_{lm}). \tag{2.28}$$

One of the remaining problems in the analysis of the polarization of the CMB, besides foregrounds, is the 'ambiguous modes' problem. Since one usually works in harmonic space, any obscured parts of the sky will contain missing information (for example, the galactic plane of the Milky Way). For an unbounded manifold, the polarization field can be decomposed uniquely into an E and a B field. An obscured sky has a necessarily bounded information sampling region, so that the decomposition is not unique — in other words, on a cut sky there are modes that simultaneously satisfy the conditions for both E-mode and B-modes. This is why the problem is called the ambiguous mode problem — it is ambiguous as to whether such modes correspond to either E or B signals or some mixture. For a low magnitude B-mode signal this will become more cumbersome when one wishes to determine the inflationary potential since leakage from the larger E-modes would dominate the B-mode signal (Fig. 2.2). An easy way to visualize this is the analogous vector field decomposition in real space [191] given by equation (1.93). From this, one can calculate $\nabla^2\Phi = \nabla^i V_i$ and $\nabla^2\chi = -\nabla^i \epsilon^j_i V_j$. On the full sky, the Laplacian inversion may be achieved uniquely. This is not true with masking; one can always think of adding charged sources for the potentials outside of the patch on which V is measured, which alter the potentials without changing V. Additionally [192], for the mode-mixing due to pixellization a Fourier space decomposition implies that due to the Heisenberg Uncertainty Principle and the limiting resolution on the sky, the directions of the estimated and actual modes on the sky in a region about some wavevector will differ, leading to E/B mixing.

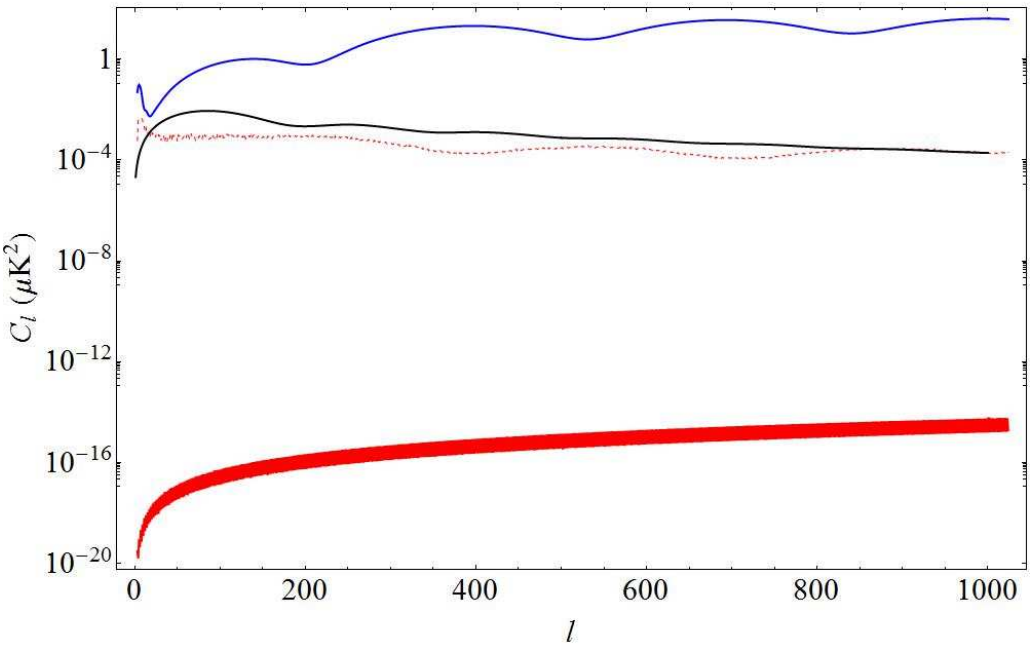

Figure 2.2: Leakage from a tensor-modes-less model; E-mode (blue line), B-mode leakage due to map pixellization (solid red line) and B-mode leakage due to a WMAP polarization mask (dashed red line). The black line is a typical $r = 0.1$ tensor-mode spectrum. The area per pixel is $4\pi/N_{\rm pix}$, with $N_{\rm pix} = 12 \times 512^2$.

2.2.1 Derivative Method of Excluding Leakage

In general, since the E-mode signal is expected to be at least an order of magnitude larger than the B-mode signal, full-sky analysis of a masked sphere will produce signal leakage from the E-modes that may swamp a primordial B-signal. Alternatively then, instead of using harmonic space techniques, one might consider real-space techniques. Starting with real-space scalar analogues of the $E-$ and B-modes

$$e(\Omega) = \sum_{lm} \sqrt{\frac{(l-2)!}{(l+2)!}} a^E_{lm} Y_{lm}(\Omega), \qquad b(\Omega) = \sum_{lm} \sqrt{\frac{(l-2)!}{(l+2)!}} a^B_{lm} Y_{lm}(\Omega), \tag{2.29}$$

one can then relate the spherical surface bi-Laplacians $\nabla^4 \equiv \nabla^2(\nabla^2+2)$ of these e and b fields to the Stokes parameters (where $\eth^n = \overbrace{\eth\cdots\eth}^{\times n}$ and $\bar{\eth}^n = \overbrace{\bar{\eth}\cdots\bar{\eth}}^{\times n}$):

$$\begin{aligned}\nabla^4 e &= -\frac{1}{2}[\bar{\eth}^2(Q+iU)+\eth^2(Q-iU)] = -D^+_{\mp 2}Q - D^-_{\mp 2}U \\ \nabla^4 b &= \frac{i}{2}[\bar{\eth}^2(Q+iU)-\eth^2(Q-iU)] = D^-_{\mp 2}Q - D^+_{\mp 2}U.\end{aligned} \tag{2.30}$$

The 'inverse' relations for forming Stokes fields from the underlying e and b fields are

$$Q = -D^+_0 e + D^-_0 b, \qquad U = -D^+_0 b - D^-_0 e, \tag{2.31}$$

where the bi-Laplacian can be written $\nabla^4 = D^-_{\mp 2}D^-_0 + D^+_{\mp 2}D^+_0$ and on the sphere

$$\begin{aligned}D^+_0 &= \frac{\eth_1\eth_0 + \bar{\eth}_{-1}\bar{\eth}_0}{2} = \partial_{\theta\theta} - \csc^2\theta\partial_{\phi\phi} - \cot\theta\partial_\theta \\ D^-_0 &= \frac{\eth_1\eth_0 - \bar{\eth}_{-1}\bar{\eth}_0}{2i} = 2\csc\theta(\partial_{\theta\phi} - \cot\theta\partial_\phi),\end{aligned} \tag{2.32}$$

hence

$$D^+_0 Y_{lm} = \frac{1}{2}\sqrt{\frac{(l+2)!}{(l-2)!}}({}_2Y_{lm} + {}_{-2}Y_{lm}), \qquad D^-_0 Y_{lm} = \frac{1}{2i}\sqrt{\frac{(l+2)!}{(l-2)!}}({}_2Y_{lm} - {}_{-2}Y_{lm}). \tag{2.33}$$

The operators acting on Q and U to obtain the bi-Laplacians of the scalar and pseudo-scalar fields are

$$\begin{aligned}D^+_{\mp 2} &= \frac{\eth_{-1}\eth_{-2} + \bar{\eth}_1\bar{\eth}_2}{2} = -2 - \csc^2\theta\partial_{\phi\phi} + 3\cot\theta\partial_\theta + \partial_{\theta\theta} \\ D^-_{\mp 2} &= \frac{\eth_{-1}\eth_{-2} - \bar{\eth}_1\bar{\eth}_2}{2i} = 2\csc\theta(\cot\theta\partial_\phi + \partial_{\theta\phi}).\end{aligned} \tag{2.34}$$

By keeping account of the spin-weights of the E and B terms produced by the combinations of each of the four operators, one can show that the ambiguous-spin terms cancel, hence

$$D^+_{\mp 2}({}_2Y_{lm} + {}_{-2}Y_{lm}) = 2\sqrt{\frac{(l+2)!}{(l-2)!}}Y_{lm}, \qquad D^-_{\mp 2}({}_2Y_{lm} - {}_{-2}Y_{lm}) = 2i\sqrt{\frac{(l+2)!}{(l-2)!}}Y_{lm}. \tag{2.35}$$

One can then work in harmonic space to integrate a boundary-condition-less function via

$$\nabla^4 f_{lm} = \nabla^2(\nabla^2 + 2) f_{lm} = \frac{(l+2)!}{(l-2)!} f_{lm}, \tag{2.36}$$

thus relating the power spectra of the scalar and pseudo-scalar fields to that of the E- and B-modes is trivially

$$C_l^{\nabla^4 e} = \frac{(l+2)!}{(l-2)!} C_l^E, \qquad C_l^{\nabla^4 b} = \frac{(l+2)!}{(l-2)!} C_l^B. \tag{2.37}$$

In the small-angle (flat sky) limit,

$$\begin{aligned} \eth \to -(\partial_x + i\partial_y) \qquad & \bar{\eth} \to -(\partial_x - i\partial_y) \\ D^{\pm}_{\mp 2} \to D^{\pm}_0 \qquad D^+_0 \to \partial_{xx} - \partial_{yy} \qquad & D^-_0 \to 2\partial_{xy}, \end{aligned} \tag{2.38}$$

where the spin-weight-dependence of the operators vanishes. One should notice that merely taking the $\theta \to \pi/2$ limit of (2.34) does not yield the flat-sky limit; one needs to specify $s = 0$ before constructing the operators. This is a general artefact of second-order covariant differentiation, related to the fact that Christoffel terms do not transform as tensors. An example can illustrate this; on the metric of the spherical surface $g_{ab} = \mathrm{Diag}(1, \sin^2\theta)$, one can construct [61]

$$\begin{aligned} M^{ab}_{;ab} = M^{\theta\theta}_{,\theta\theta} + 2M^{\theta\phi}_{,\theta\phi} + M^{\phi\phi}_{,\phi\phi} - \sin\theta\cos\theta M^{\phi\phi}_{,\theta} + 2\cot\theta M^{\theta\theta}_{,\theta} + 4\cot\theta M^{\theta\phi}_{,\phi} \\ + (1 - 3\cos^2\theta) M^{\phi\phi} - M^{\theta\theta} \end{aligned} \tag{2.39}$$

where the standard comma notation for covariant derivatives is used. In the $\theta \to \pi/2$ limit, where $\theta \to x$, $\phi \to y$ this yields

$$M^{ab}_{;ab} = M^{xx}_{,xx} + 2M^{xy}_{,xy} + M^{yy}_{,yy} + M^{xx} - M^{yy} \tag{2.40}$$

which is inequivalent to computing $M^{ab}_{;ab}$ from a flat metric $g_{ab} = \mathrm{Diag}(1, 1)$:

$$M^{ab}_{;ab} = M^{xx}_{,xx} + 2M^{xy}_{,xy} + M^{yy}_{,yy}. \tag{2.41}$$

The important thing about the use of real-space derivatives is that by not sampling in masked regions of the sky, *there are no leakage contributions from the ambiguous modes*. Of course, the implementation may yield leakage of its own due to pixellization; aliasing of harmonic modes in a pixellated scheme is the result of harmonic decomposition of components of the map at a frequency greater than the Shannon-Nyquist limit for the map. This results in power being transfered to

lower modes (since the power has to fit into the harmonic space binning available); the new sets of modes being mapped to have no requirement to be consistent with the aliased modes, which in a polarization context means mixing of E and B-modes. The only realistic way around this issue is to sample one's map at a resolution where the effect of aliasing on the required mode range l is minimal.

2.2.2 Alternative Methods

Of course, alternative methods have been proposed to ameliorate the effect of mode-mixing. MCMC methods would be able to tackle this problem, but with the large datasets coming from projects such as Planck such a method would be hugely computationally expensive; the full Fisher matrix utilizes the covariance matrix [105]

$$C(\theta) = \begin{pmatrix} \zeta_l^{TT,TT} & \zeta_l^{TT,EE} & \zeta_l^{TT,TE} & 0 \\ \zeta_l^{TT,EE} & \zeta_l^{EE,EE} & \zeta_l^{EE,TE} & 0 \\ \zeta_l^{TT,TE} & \zeta_l^{EE,TE} & \zeta_l^{TE,TE} & 0 \\ 0 & 0 & 0 & \zeta_l^{BB,BB} \end{pmatrix} \tag{2.42}$$

$$\zeta^{xyx'y'} = \frac{1}{(2l+1)f_{\rm sky}\Delta l} \times \left[(C_l^{xy'} + N_l^{xy'})(C_l^{yx'} + N_l^{yx'}) + (C_l^{xx'} + N_l^{xx'})(C_l^{yy'} + N_l^{yy'})\right].$$

for an observed sky fraction $f_{\rm sky}$, with bandwidth Δl and noise spectrum N_l.
The quadratic maximum likelihood (QML) approach [193] is an approximate method which specifies the full covariance matrix by

$$C(\theta) = \begin{pmatrix} C^{TT} & C^{TQ} & C^{TU} \\ C^{QT} & C^{QQ} & C^{QU} \\ C^{UT} & C^{UQ} & C^{UU} \end{pmatrix} \tag{2.43}$$

to yield the optimal QML power spectrum

$$C_l^{r,\rm QML} = x_i x_j E_{ij}^{rl}, \qquad E^{rl} = \frac{1}{2} C^{-1} \frac{\partial C}{\partial C_l^r} C^{-1} \tag{2.44}$$

where $x = (\Delta T, Q, U)$ and $r = (T, X, E, B)$. For a survey that is not noise-free, one needs to subtract the noise bias and then renormalize. In order to avoid contamination of power spectrum estimates by the systematic errors in the T mea-

surements, one reshapes the matrix via

$$E^{rl} \rightarrow \hat{E}^{rl} = \frac{1}{2}\hat{C}^{-1}\frac{\partial C}{\partial C_l^r}\hat{C}^{-1} \tag{2.45}$$

to

$$\hat{C} = \begin{pmatrix} C^{TT} & 0 & 0 \\ 0 & C^{QQ} & C^{QU} \\ 0 & C^{UQ} & C^{UU} \end{pmatrix}. \tag{2.46}$$

The estimator from this reshaped covariance matrix is no longer minimum variance; one then defines a Fisher matrix

$$\hat{F}_{ll'}^{r,\mathrm{sig}} = \frac{1}{2}\mathrm{Tr}\left[\frac{\partial C}{\partial C_{l'}^{\mathrm{sig}}}\hat{C}^{-1}\frac{\partial C}{\partial C_l^r}\hat{C}^{-1}\right], \qquad \left\langle C_l^{r,\mathrm{QML}}\right\rangle = \hat{F}_{ll'}^{r,\mathrm{sig}}C_{l'}^{\mathrm{sig}} \tag{2.47}$$

and follows the likelihood analysis method as described in section 2.1.
A number of cheaper alternatives exist, which have been adapted to the e and b formalism where appropriate. The Pseudo-C_l attempt [194], with which the derivative method in subsection 2.2.1 has some overlap, works by taking linear combinations of the measured C_l's to eliminate the E-mode contribution in order to reveal the cosmological B-modes. In other words, a weight function is used; for a trivial weight function identical to the galaxy mask, the noise-free QML and pseudo-C_l estimators are statistically equivalent. The idea is to make the B-mode power spectrum estimator independent of E on average, a limit of the derivative method where the full b map is created. However, estimator variance for a given polarization mode will still have a dominant contribution from leaked signals from the other mode. The measured harmonic coefficients are computed using a cut-sky-dependent weighting scheme W to produce pseudo-bandpowers in the band β

$$\begin{aligned} \bar{C}_\beta &\equiv \sum_{l\in\beta}\frac{l(l+1)}{2\pi}\sum_{m=-l}^{l}\tilde{b}_{lm}^*\tilde{b}_{lm} \\ \tilde{b}_{lm} &\equiv \frac{1}{\sqrt{(l-1)l(l+1)(l+2)}}\int b(x)W(x)Y_{lm}^*(x)d^2x. \end{aligned} \tag{2.48}$$

The expectation values of the pseudo-bandpowers are related to the true spectrum by the transfer tensor

$$\begin{pmatrix} \left\langle \tilde{C}_l^{EE} \right\rangle \\ \left\langle \tilde{C}_l^{BB} \right\rangle \end{pmatrix} = \sum_{l'} \begin{pmatrix} K_{ll'}^{+} & K_{ll'}^{-} \\ K_{ll'}^{-} & K_{ll'}^{+} \end{pmatrix} \begin{pmatrix} C_{l'}^{EE} \\ C_{l'}^{BB} \end{pmatrix} + \begin{pmatrix} \tilde{N}_{l'}^{EE} \\ \tilde{N}_{l'}^{BB} \end{pmatrix}, \tag{2.49}$$

which can be solved by inversion:

$$\begin{pmatrix} \hat{C}_l^{EE} \\ \hat{C}_l^{BB} \end{pmatrix} = \sum_{l'} \begin{pmatrix} K_{ll'}^{+} & K_{ll'}^{-} \\ K_{ll'}^{-} & K_{ll'}^{+} \end{pmatrix}^{-1} \begin{pmatrix} \tilde{C}_{l'}^{EE} - \tilde{N}_{l'}^{EE} \\ \tilde{C}_{l'}^{BB} - \tilde{N}_{l'}^{BB} \end{pmatrix}. \tag{2.50}$$

Equation (2.48) is by construction pure; instead of performing the derivatives necessary to construct b, counterweights which perform a 'purification' of E- and B-modes are determined by solving

$$b_{lm} = \frac{i}{2} \int d\Omega (Q + iU) \left(W\, {}_2Y_{lm}^{*} + \frac{2 {}_1W^{*}\, {}_1Y_{lm}^{*}}{\sqrt{(l-1)(l+2)}} + \frac{{}_2W^{*} Y_{lm}^{*}}{\sqrt{(l-1)l(l+1)(l+2)}} + \text{c.c.} \right) \tag{2.51}$$

where spin-weighted apodization weights are defined by operating on the scalar mask $W(\Omega)$

$${}_sW = \eth_{s-1} \cdots \eth_0 W. \tag{2.52}$$

The apodization weights are then determined in a minimum-variance fashion as described later in chapter 3, in a manner that relates to the E/B transfer tensor. The expansion shows that taking the analytic derivatives is equivalent to the pseudo-C_l counterterms method. Currently this method has only been used in a flat-sky, small-angle approximation. However for wide surveys (such as Planck), curvature may begin to introduce notable errors; this is particularly important given the possibility of a small B-mode signal at low-l.

Zhao & Baskaran [195] solve the mode-mixing problem in a similar fashion to the derivative method by explicitly calculating the correction terms which come from the ambiguous modes. Defining

$$\begin{aligned} P_{\pm}(\Omega) &= Q(\Omega) \pm iU(\Omega) \\ \nabla^4 \tilde{e} &= -\frac{1}{2} \left(\bar{\eth}^2 (P_{+} W) + \eth^2 (P_{-} W) \right) \\ \nabla^4 \tilde{b} &= -\frac{1}{2i} \left(\bar{\eth}^2 (P_{+} W) - \eth^2 (P_{-} W) \right), \end{aligned} \tag{2.53}$$

one has

$$\bar{\eth}^2 P_+ = -\nabla^4(e+ib), \qquad \bar{\eth}^2(P_+W) = -\nabla^4(\tilde{e}+i\tilde{b}). \tag{2.54}$$

This shows that the pseudo- and full e and b fields can be related by studying how $\bar{\eth}^2(P_+W)$ and $\bar{\eth}^2 P_+$ relate, arriving at

$$\nabla^4(e+ib)W^2 = \nabla^4(\tilde{e}+i\tilde{b})W + \alpha, \tag{2.55}$$

where the correction term is

$$\begin{aligned}\alpha = &(\bar{\eth}W)(\bar{\eth}(P_+W) - P_+\bar{\eth}W - 2\cot\theta P_+W)\\ &+(\bar{\eth}W)(\bar{\eth}(P_+W) - P_+\bar{\eth}W - \cot\theta P_+W)\\ &+P_+W(\bar{\eth}^2W) + \cot\theta\bar{\eth}(P_+W) + 2W^2P_+ + 2W\cot\theta\bar{\eth}(P_+W),\end{aligned} \tag{2.56}$$

so the pure-field recontruction is achieved via

$$\nabla^4(e+ib) = \nabla^4(\tilde{e}+i\tilde{b})W^{-1} + \alpha W^{-2}. \tag{2.57}$$

The W^{-1} and W^{-2} utilized were found to be ill-behaved at the edge of observed region due to their discontinuous form, forcing edge (and thus information) removal of the constructed polarization maps.

Kim & Naselsky [196] looked at the pixel-space properties of the leakage problem, producing E/B decomposed maps by convolving polarization maps with certain filter functions. First, they identified

$$\begin{aligned}e &= -\frac{1}{2}\left(\int F_+(Q-iU)d\Omega + \int F_-(Q+iU)d\Omega\right)\\ b &= \frac{i}{2}\left(\int F_+(Q-iU)d\Omega - \int F_-(Q+iU)d\Omega\right),\end{aligned} \tag{2.58}$$

where

$$F_\pm = \sum_{lm}\sqrt{\frac{(l+2)!}{(l-2)!}}{}_{\pm2}Y_{lm}Y^*_{lm} \tag{2.59}$$

is a pixel-space filter for the decomposition. This is used to define the expected leakage power $\left\langle \tilde{B}^2_E(\hat{n})\right\rangle$ in terms of the operation of such filters on the Stokes parameters. By retaining only the pixels which satisfy the constraint

$$\frac{\left\langle \tilde{B}^2_E(\hat{n})\right\rangle}{\left\langle \tilde{B}^2_B(\hat{n})\right\rangle} < \frac{r_{\rm theory}}{r_{MC}}, \tag{2.60}$$

implying that the sky fraction kept scales with $r_{\rm theory}$ (where r_{MC} is the assumed Monte Carlo simulation value for r), an optimal $r_{\rm theory}$ which minimizes estimation error is then derived.
It was found that E/B mixing due to incomplete sky is localized in pixel-space, and negligible in the regions far away from the masked area. The diagnosis of the expected local leakage power and expected pure mode power defines the ambiguous pixels to be excluded, by solving $\partial\Delta C_l/\partial r_{\rm theory} = 0$ and obtaining the optimal $r_{\rm theory}$, which minimizes the estimation error given a foreground mask and noise level. Simulations showed that leakage power is subdominant in comparison with unlensed B-mode power spectrum of $r \sim 10^{-3}$ at a wide range of multipoles $(50 \lesssim l \lesssim 2000)$, while a sky fraction of 0.48 is retained. It is claimed that the leakage in their method does not bias the B-mode power spectrum estimation but increases the variance when the estimation is made by a pseudo-C_l method and leakage is taken care of. However, the removal of pixels necessarily removes potentially useful information. Recently, Kim [197] has attempted to combat leakage by observing that ringing artifacts can be reduced using smoothing filters. By utilizing a widened Gaussian smoothing kernel ringing artifacts are minimized, informed by a spectral reconstruction of the processing mask.
Bunn [198], meanwhile, runs the following algorithm on P_+:

- Calculate E and B from P_+ while disregarding purity issues, by finding a pair of potentials p_E and p_B such that

$$P_+ = D_E p_E + D_B p_B, \tag{2.61}$$

  which are related to the derivatives in subsection 2.2.1 by

$$D_E = (D_0^+, D_0^-), \qquad D_B = (-D_0^-, D_0^+) \tag{2.62}$$

  in the flat-sky regime.

- Find the biharmonic functions α_E and α_B, i.e., under the condition that

$$\nabla^4 \alpha_E = 0, \qquad \nabla^4 \alpha_B = 0 \tag{2.63}$$

  with boundary conditions

$$\begin{aligned} \alpha_E|_{\partial\Omega} &= p_E|_{\partial\Omega}, \qquad & \hat{n}\cdot\nabla\alpha_E|_{\partial\Omega} &= \hat{n}\cdot\nabla p_E|_{\partial\Omega} \\ \alpha_B|_{\partial\Omega} &= p_B|_{\partial\Omega}, \qquad & \hat{n}\cdot\nabla\alpha_B|_{\partial\Omega} &= \hat{n}\cdot\nabla p_B|_{\partial\Omega}. \end{aligned} \tag{2.64}$$

- 'Purify' the potentials by defining

$$p_{\mathrm{pure},E} = p_E - \alpha_E, \qquad p_{\mathrm{pure},B} = p_B - \alpha_B \tag{2.65}$$

- Apply the differential operators to obtain the pure E, pure B, and ambiguous polarization fields:

$$P_{\mathrm{pure},E} = D_E p_{\mathrm{pure},E} \qquad P_{\mathrm{pure},B} = D_B p_{\mathrm{pure},B} \qquad P_a = D_E\alpha_E + D_B\alpha_B \tag{2.66}$$

where the differential operators are applied in harmonic space. The advantage of this method is that it computes directly the polarization map components, and finds the ambiguous modes. The ambiguous modes are removed via a hard cut-off near the boundary; since the distance an ambiguous mode persists into the interior of a map depends on the frequency of the source function on the boundary [196], the Bunn method determines how far from the border the ambiguous modes persist. One possible limitation of this method is that the polarization field is extended into the unobserved patch, with Gaussianity assumed and the observed and unobserved patches forced to match over some boundary region of thickness t; it is reasonable to assume for the purpose of just detecting pure B-modes that the field in the unobserved patch is Gaussian, but this will necessarily bias any calculations of non-Gaussianity in the polarization modes across the sphere. By contrast, the local derivative method requires no such assumptions about the unobserved region since it is not removing leakage by estimating the ambiguous mode contributions. Further, the Laplacian-difference method for detecting discontinuities proposed in section 2.5 as applied to this proposal would be a useful check for smoothness across such a boundary region.

Wavelet-type methods such as the wavelet-Galerkin method of Cao & Fang [199] and the spin needlet approach of Geller et al [200] complete this overview of the types of analyses proposed. These usually involve dropping modes located about the boundary, since the majority of ambiguous leakage contributes from such regions. Much like the derivative method, the locality of the wavelet approaches allows the recovery of the spatial structures of the E- and B-mode fields. But note again, like the Kim & Naselsky method and unlike the local derivative method, that the signal is purified by removing information (an operation which is by necessity biased toward a zero B-mode signal). It remains to be seen which of the methods proposed, or combination thereof, may be optimal for unambiguously detecting B-modes or setting their upper limit.

2.3 Discrete Derivatives

Since in any real-space computation of derivatives one can only calculate on a discrete grid, it is necessary to calculate discrete derivatives. This can be achieved using the finite-difference method, wherein the value of the derivative of a function at a given point is taken to be some weighted function of the values of the function at surrounding pixels,

$$\partial F \to \tilde{\partial} F + \text{Err} \tag{2.67}$$

where the $\sim$ indicates a discrete derivative. In the limit of an infinite resolution, the error term should vanish; the uncertainty due to the pixellization will need to be estimated.
Standard finite-difference schemes for regularly-spaced grids are well-known; in anticipation of chapter 3 it will be necessary to generalize this to irregular grids.

2.3.1 Basic Idea

A derivative (of order m) of a function at a given pixel i can be computed as the sum of weighted values of the function at a surrounding sample of pixels j (the pixel 'stencil'):

$$\partial_{x^m} f_i \approx \sum_{j}^{\text{pixels}} w_{ij}^{(m)} f_j \tag{2.68}$$

where w is the weight matrix. For example, the canonical finite-difference schemes with uniform spacing can be derived starting with a 1-dimensional Taylor expansion on an infinite regular grid with separation Δ

$$f_{i\pm1} = \sum_{r=0}^{\infty} \frac{(\pm\Delta)^r \partial_{x^r} f_i}{r!}, \tag{2.69}$$

to yield for the first- and second-order derivatives

$$\partial_x f_i \approx \frac{f_{i+1} - f_{i-1}}{2\Delta} + \mathcal{O}(\Delta^2) \qquad \partial_{xx} f_i \approx \frac{f_{i+1} + f_{i-1} - 2f_i}{\Delta^2} + \mathcal{O}(\Delta^2) \tag{2.70}$$

corresponding to weight matrices

$$w_{ij}^{(1)} = \begin{pmatrix} -\frac{1}{2\Delta} & 0 & \frac{1}{2\Delta} \\ -\frac{1}{2\Delta} & 0 & \frac{1}{2\Delta} \\ \vdots & \vdots & \vdots \end{pmatrix}, \qquad w_{ij}^{(2)} = \begin{pmatrix} \frac{1}{\Delta^2} & -\frac{2}{\Delta^2} & \frac{1}{\Delta^2} \\ \frac{1}{\Delta^2} & -\frac{2}{\Delta^2} & \frac{1}{\Delta^2} \\ \vdots & \vdots & \vdots \end{pmatrix}. \tag{2.71}$$

Since the focal pixel in this case is the central pixel f_i between $f_{i\pm1}$, this is usually referred to as the 'second-order central difference scheme'. If the grid is finite, the first and last rows in the weight matrix must correspond to 'forward' and 'backward' difference schemes respectively, where the focal pixel is $f_{i\mp1}$ in the second-order case. Such schemes can be constructed using the same Taylor analysis as in the central difference case.

The second derivative shall now be used as an example in which to construct a method of solution to a differential equation. The most general form for the 1d differential function is

$$f_i'' = \alpha_i f_i' + \beta_i f_i + \gamma_i. \tag{2.72}$$

The discrete derivatives can then be used to yield

$$\left(-\frac{\Delta}{2}\alpha_i - 1\right) f_{i-1} + \left(\frac{\Delta}{2}\alpha_i - 1\right) f_{i+1} + (2 + \Delta^2\beta_i) f_i = -\Delta^2\gamma_i. \tag{2.73}$$

This equation can be solved in the form of a *tri-diagonal matrix*, soluble through the use of boundary conditions: equation (2.73) is of the form

$$a_i u_{i-1} + b_i u_i + c_i u_{i+1} = d_i; \tag{2.74}$$

which can be solved by constructing a matrix equation of the form

$$\begin{pmatrix} b_1 & c_1 & & & \mathbf{0} \\ a_1 & b_2 & c_2 & & \\ & \ddots & \ddots & \ddots & \\ & & & & c_{n-1} \\ \mathbf{0} & & & a_n & b_n \end{pmatrix} \begin{pmatrix} u_1 \\ u_2 \\ \vdots \\ u_{n-1} \\ u_n \end{pmatrix} = \begin{pmatrix} d_1 - a_1 u_1 \\ d_2 \\ \vdots \\ d_{n-1} \\ d_n - c_n u_n \end{pmatrix}. \tag{2.75}$$

In the case of equation (2.72) this manifests as

$$\begin{pmatrix} 2+\Delta^2\beta_1 & \frac{\Delta}{2}\alpha_1-1 & & & \mathbf{0} \\ -\frac{\Delta}{2}\alpha_2-1 & 2+\Delta^2\beta_2 & \frac{\Delta}{2}\alpha_2-1 & & \\ & \ddots & \ddots & \ddots & \\ & & & \frac{\Delta}{2}\alpha_{n-1}-1 & \\ \mathbf{0} & & & -\frac{\Delta}{2}\alpha_n-1 & 2+\Delta^2\beta_n \end{pmatrix} \times \begin{pmatrix} f_1 \\ f_2 \\ \vdots \\ f_{n-1} \\ f_n \end{pmatrix} = \begin{pmatrix} -\Delta^2\gamma_1+e_1 \\ -\Delta^2\gamma_2 \\ \vdots \\ -\Delta^2\gamma_{n-1} \\ -\Delta^2\gamma_n+e_n \end{pmatrix} \tag{2.76}$$

where the e_1 and e_n terms determine the boundary conditions. This equation is then solved by either direct or iterative methods, i.e., the Gauss-Seidel technique. Since finite-difference methods are used for solving partial differential equations, then in this sense there are a range of potential uses for finite differences in cosmology and related areas, ranging from quantum gravitational field equations [201, 202, 203] to numerical relativity [204, 205, 206, 207] to studies of cosmological magnetohydrodynamics [208, 209] and beyond; anywhere that a partial differential equation is featured, when there are boundary conditions available and the solution can be made stable. In the e and b case, it is necessary instead to perform the inverse operation, that of applying derivative operators to fields. It is with this in mind that a more general finite-difference scheme is developed.

2.3.2 A General Finite-Difference Scheme

The following more general formalism shall be constructed to approximate the derivatives at a single pixel (many of the results synthesized here come from previous expositions on finite differences [210, 211, 212, 213, 214]); in that sense the weight vector w_j (at fixed but unlabelled pixel i) shall be utilized instead of w_{ij}. For the set of all pixels on a pixellated grid, the weight vector w_j corresponds to rows of w_{ij}.

A general finite-difference method, for any number of regular or irregular pixel schemes can be derived using interpolating polynomials. In the Lagrange basis,

a 1d polynomial interpolating a set of n datapoints can be written as

$$f(x) \approx \sum_{i=1}^{n} f_i L_i(x) \tag{2.77}$$

where the f_i are the datavalues at each point x_i and the Lagrange basis polynomial is

$$L_i(x) = \prod_{1 \leq j \leq n; j \neq i} \frac{x - x_j}{x_i - x_j}, \tag{2.78}$$

such that on a sample of n pixels

$$\begin{pmatrix} L_1(x_1) & \cdots & L_n(x_1) \\ \vdots & & \vdots \\ L_n(x_1) & \cdots & L_n(x_n) \end{pmatrix} \begin{pmatrix} f_1 \\ \vdots \\ f_n \end{pmatrix} = \begin{pmatrix} f_1 \\ \vdots \\ f_n \end{pmatrix} \tag{2.79}$$

where clearly $L_i(x_j) = \delta_{ij}$. It can be shown that for a given nondegenerate distribution of points, the Lagrange basis polynomial both exists and is unique. Interpolation problems over n pixels arranged on a 1d grid can often be expressed using a geometric progression matrix, also called the 'Vandermonde' matrix:

$$v = \begin{pmatrix} x_1^0 & \cdots & x_1^{n-1} \\ \vdots & & \vdots \\ x_n^0 & \cdots & x_n^{n-1} \end{pmatrix} \tag{2.80}$$

which is constructed by rewriting the interpolating polynomial in the monomial basis, by a simple rearrangement of terms in equation (2.78):

$$L_i = c_1 + c_2 x_i + \cdots = \sum_{r=1}^{n} c_r x_i^{r-1} \tag{2.81}$$

and then filling the rows of the matrix v as appropriate, such that

$$\begin{pmatrix} x_1^0 & \cdots & x_1^{n-1} \\ \vdots & & \vdots \\ x_n^0 & \cdots & x_n^{n-1} \end{pmatrix} \begin{pmatrix} c_1 \\ \vdots \\ c_n \end{pmatrix} = \begin{pmatrix} L_1 \\ \vdots \\ L_n \end{pmatrix}. \tag{2.82}$$

Using this, a scheme for approximating the derivatives of the interpolating polynomial can be constructed; if equation (2.82) is written in the compact form $vc = L$, noting that the positive definiteness of v implies that $(v^{-1})^T = (v^T)^{-1}$,

one can define a unique unspecified array α which solves the transpose equation

$$v^T \alpha = L, \tag{2.83}$$

corresponding to the summation

$$L_i = \sum_{r=1} \alpha_r x_r^i. \tag{2.84}$$

The linear equation for these interpolation weights is then

$$\begin{pmatrix} x_1^0 & \cdots & x_n^0 \\ \vdots & & \vdots \\ x_1^{n-1} & \cdots & x_n^{n-1} \end{pmatrix} \begin{pmatrix} \alpha_1 \\ \vdots \\ \alpha_n \end{pmatrix} = \begin{pmatrix} L_1 \\ \vdots \\ L_n \end{pmatrix}. \tag{2.85}$$

By isolating a single pixel of interest, with position x, and replacing the positions of the surrounding pixels x_i with the position difference

$$\Delta_i = x_i - x \tag{2.86}$$

one is led to an equation (with an unspecified array W)

$$v' = WL' \tag{2.87}$$

defined in powers of Δ_i

$$\begin{pmatrix} \Delta_1^0 & \cdots & \Delta_n^0 \\ \vdots & & \vdots \\ \Delta_1^{n-1} & \cdots & \Delta_n^{n-1} \end{pmatrix} \begin{pmatrix} W_1 \\ \vdots \\ W_n \end{pmatrix} = \begin{pmatrix} 0!L_1 \\ \vdots \\ (n-1)!L_1^{(n-1)} \end{pmatrix} \tag{2.88}$$

which can be modified for calculating the differencing weights (where $L_i^{(n)}$ is a shorthand for the n^{th} derivative of L_i). The array v' is referred here as the 'differenced Vandermonde' array. Now consider a Taylor series more general than equation (2.69) for the polynomial function L in order to modify equation (2.88) for calculating differencing weights:

$$L_{i\pm n} = \sum_{r=0}^{\infty} \frac{(\pm\Delta_n)^r L_i^{(r)}}{r!}. \tag{2.89}$$

In a matrix format, since the summation is realistically limited to the $(n-1)^{\text{th}}$ derivative this is none other than

$$\begin{pmatrix} \frac{(\pm\Delta_1)^0}{0!} & \cdots & \frac{(\pm\Delta_1)^{n-1}}{(n-1)!} \\ \vdots & & \vdots \\ \frac{(\pm\Delta_n)^0}{0!} & \cdots & \frac{(\pm\Delta_n)^{n-1}}{(n-1)!} \end{pmatrix} \begin{pmatrix} L_i^{(0)} \\ \vdots \\ L_i^{(n-1)} \end{pmatrix} = \begin{pmatrix} L_{i\pm1} \\ \vdots \\ L_{i\pm n} \end{pmatrix}. \tag{2.90}$$

By inverting this matrix equation, one can calculate each of the derivatives of the polynomial L. It is then clear that in order to isolate a particular derivative m, one must append the left-hand-side of the inverted equation with a Kronecker delta thus:

$$\begin{pmatrix} 0!L_i^{(0)}\delta_{0,m} \\ \vdots \\ (n-1)!L_i^{(n-1)}\delta_{n-1,m} \end{pmatrix} = \begin{pmatrix} (\pm\Delta_1)^0 & \cdots & (\pm\Delta_1)^{n-1} \\ \vdots & & \vdots \\ (\pm\Delta_n)^0 & \cdots & (\pm\Delta_n)^{n-1} \end{pmatrix}^{-1} \begin{pmatrix} L_{i\pm1} \\ \vdots \\ L_{i\pm n} \end{pmatrix} \tag{2.91}$$

where the array $(\pm v'^T)^{-1}$ has been made use of. Correspondingly, equation (2.88) is modified for the same purpose:

$$\begin{pmatrix} \Delta_1^0 & \cdots & \Delta_n^0 \\ \vdots & & \vdots \\ \Delta_1^{n-1} & \cdots & \Delta_n^{n-1} \end{pmatrix} \begin{pmatrix} w_1^{(m)} \\ \vdots \\ w_n^{(m)} \end{pmatrix} = \begin{pmatrix} L_1\delta_{m,0} \\ \vdots \\ (n-1)!L_1^{(n-1)}\delta_{m,n-1} \end{pmatrix} \tag{2.92}$$

in order to separate out the derivative of interest. By extension, replacing the Kronecker term via $\delta_{m,r} \to \delta_{m||m',r}$ which evaluates to 1 if $either$ m or m' is equal to r, will calculate the weights required to compute the summed derivative $L^{(m)} + L^{(m')}$. Thus the array W is related to the vector weights $w^{(m)}$ by

$$W_i = \sum_{j=0}^{n-1} w_i^{(j)}. \tag{2.93}$$

One can then solve for the weight vector by isolating the derivative polynomial of choice. For example, the central difference system for a regular grid where $\Delta = 1$ can be obtained from

$$\begin{pmatrix} 1 & 1 & 1 \\ -1 & 0 & 1 \\ 1 & 0 & 1 \end{pmatrix} \begin{pmatrix} w_0^{(1)} \\ w_1^{(1)} \\ w_2^{(1)} \end{pmatrix} = \begin{pmatrix} 0 \\ 1 \\ 0 \end{pmatrix} \tag{2.94}$$

or a backward difference equation for the second derivative via

$$\begin{pmatrix} 1 & 1 & 1 \\ 0 & 1 & 2 \\ 0 & 1 & 4 \end{pmatrix} \begin{pmatrix} w_0^{(2)} \\ w_1^{(2)} \\ w_2^{(2)} \end{pmatrix} = \begin{pmatrix} 0 \\ 0 \\ 2 \end{pmatrix} \tag{2.95}$$

with results in agreement with the known results. A range of standard regular finite-difference weights is displayed in Table 2.1.

Table 2.1: 2-, 3-, and 4-point equidistant first-order difference equations.

Points	2-step backward	1-step backward	Central	1-step forward	2-step forward
2	—	$\frac{F_i - F_{i-1}}{\Delta}$	—	$\frac{F_{i+1} - F_i}{\Delta}$	—
3	$\frac{-3F_{i-2} + 4F_{i-1} - F_i}{2\Delta}$	—	$\frac{F_{i+1} - F_{i-1}}{2\Delta}$	—	$\frac{F_i - 4F_{i+1} + 3f_{i+2}}{2\Delta}$
4	$\frac{-2F_{i-2} - 3F_{i-1} + 6F_i - F_{i+1}}{6\Delta}$	—	—	—	$\frac{F_{i-1} - 6F_i + 3F_{i+1} + 2F_{i+2}}{6\Delta}$

The extension of this to an irregular grid merely requires the reparameterization

$$\Delta_{ij} = x_j - x_i. \tag{2.96}$$

So for the derivatives at a pixel *i* one solves

$$\begin{pmatrix} \Delta_{i,1}^0 & \cdots & \Delta_{i,n}^0 \\ \vdots & & \vdots \\ \Delta_{i,1}^{n-1} & \cdots & \Delta_{i,n}^{n-1} \end{pmatrix} \begin{pmatrix} w_{i,1}^{(m)} \\ \vdots \\ w_{i,n}^{(m)} \end{pmatrix} = \begin{pmatrix} 0!\delta_{m,0} \\ \vdots \\ (n-1)!\delta_{m,n-1} \end{pmatrix}. \tag{2.97}$$

A general solution to this set-up for a derivative of order m can be determined by constructing the LU decomposition (see section 3.2) of the inverse of the trace of the Vandermonde matrix into lower- and upper-triangular arrays Λ and Υ respectively:

$$(v^T)^{-1} = \Lambda\Upsilon \tag{2.98}$$

where

$$\Lambda = \begin{pmatrix} 1 & -x_1 & x_1x_2 & -x_1x_2x_3 & \dots \\ 0 & 1 & -(x_1+x_2) & x_1x_2+x_2x_3+x_3x_1 & \dots \\ 0 & 0 & 1 & -(x_1+x_2+x_3) & \dots \\ \vdots & \vdots & \vdots & \vdots & \ddots \end{pmatrix}$$
$$\Upsilon = \begin{pmatrix} 1 & 0 & 0 & \dots \\ \frac{1}{x_1-x_2} & \frac{1}{x_2-x_1} & 0 & \dots \\ \frac{1}{(x_1-x_2)(x_1-x_3)} & \frac{1}{(x_2-x_1)(x_2-x_3)} & \frac{1}{(x_3-x_1)(x_3-x_2)} & \dots \\ \vdots & \vdots & \vdots & \ddots \end{pmatrix}. \tag{2.99}$$

The analogous decomposition for the differenced Vandermonde matrix leads to the general solution for an n-point finite-difference scheme in 1 dimension

$$w_{ij}^{(m)} = \frac{(\partial_\Delta)^m \left[\prod_{l=1,p_l\neq i}^{n} \Delta_{p_1 j} \cdots \Delta_{p_l j}\right]}{\prod_{k=1,k\neq i}^{n}(\Delta_{ij}-\Delta_{kj})} \tag{2.100}$$

where i is the focal pixel and j denotes weights applied to the stencil pixels and the following operator has been defined:

$$\partial_\Delta = \sum_{j=1}^{n} \partial_{\Delta_{ij}} \tag{2.101}$$

yielding for example

$$\begin{aligned} \partial_{xx,4-pt} f^i = & \frac{2(\Delta_{i2}+\Delta_{i3}+\Delta_{i4})}{(\Delta_{i1}-\Delta_{i2})(\Delta_{i1}-\Delta_{i3})(\Delta_{i1}-\Delta_{i4})} f^1 \\ & + \frac{2(\Delta_{i1}+\Delta_{i2}+\Delta_{i4})}{(\Delta_{i2}-\Delta_{i1})(\Delta_{i2}-\Delta_{i3})(\Delta_{i2}-\Delta_{i4})} f^2 \\ & + \frac{2(\Delta_{i1}+\Delta_{i3}+\Delta_{i4})}{(\Delta_{i3}-\Delta_{i1})(\Delta_{i3}-\Delta_{i2})(\Delta_{i3}-\Delta_{i4})} f^3 \\ & + \frac{2(\Delta_{i1}+\Delta_{i2}+\Delta_{i3})}{(\Delta_{i4}-\Delta_{i1})(\Delta_{i4}-\Delta_{i2})(\Delta_{i4}-\Delta_{i3})} f^4. \end{aligned} \tag{2.102}$$

If the determinant of an n-point Vandermonde array is labelled $\text{Det}[v]_n$, then by utilizing standard linear algebra techniques it can be shown that

$$\text{Det}[v]_n = \prod_{j=2}^{n}(x_j - x_1)\text{Det}[v]_{n-1}. \tag{2.103}$$

By iteration, the determinant of the Vandermonde array is then

$$\text{Det}[v]_n = \prod_{1 \leq i < j \leq n}^{n} (x_j - x_i) \tag{2.104}$$

which, for a given unknown x_j, with positions x_i known, is precisely the factorised interpolating polynomial. It can then be seen that the Lagrange polynomials can be identified with the determinants for Vandermonde arrays determined by the pixel sample surrounding pixel j (where the n has been dropped):

$$L_i(x_j) = \left. \frac{\text{Det}[v_i]}{\text{Det}[v]} \right|_j , \tag{2.105}$$

where the subscripts on v indicate that the Vandermonde matrix defined at pixel j has the column i replaced by a column of undetermined values for x, i.e., for the 1-dimensional case

$$v_2 = \begin{pmatrix} x_1^0 & x^0 & x_3^0 & \cdots & x_n^0 \\ \vdots & \vdots & \vdots & \ddots & \vdots \\ \vdots & \vdots & \vdots & \ddots & \vdots \\ x_1^{n-1} & x^{n-1} & x_3^{n-1} & \cdots & x_n^{n-1} \end{pmatrix}, \tag{2.106}$$

since the Lagrange polynomial is merely the weighted sum of the unique polynomials at each point on the grid. Thus in the d-dimensional case, one would also have

$$f_j \approx \sum_{i}^{n} f_i \left. \frac{\text{Det}[v_i^{(d)}]}{\text{Det}[v^{(d)}]} \right|_j \tag{2.107}$$

where the correct form of the d-dimensional geometric array has yet to be specified. One corollary of the interpolating polynomial being in the form of a geometric array is that one can immediately test for the existence of a unique polynomial (in the powers that have been specified in the geometric array) with roots at each pixel. Such a polynomial does not exist if the geometric array is singular. The construction of higher-dimensional geometric arrays can start with the construction of the regular d-dimensional array using the tensor product

$$v_{\text{reg}}^{(d)} = \overbrace{v_{\text{reg}} \otimes \cdots \otimes v_{\text{reg}}}^{d} \tag{2.108}$$

and then following the generalizations to irregular grids equivalent to those con-

structed for the 1-dimensional case. Since one can define the solutions to the geometric array equations in terms of the determinants and minors of the geometric arrays, the general solutions for the construction of the derivative weights in d dimensions as functions of the determinant of v' can be written as

$$w_{ij}^{(m^a)} = \frac{(\partial_{\Delta^a})^{m_a} P_{ij}^{(d)}}{\mathrm{Det}[v'^{(d)}]}, \tag{2.109}$$

where the derivative operator is

$$(\partial_{\Delta^a})^{m_a} = \overbrace{\partial_{\Delta_{e_1}}}^{\times m_1} \cdots \overbrace{\partial_{\Delta_{e_d}}}^{\times m_d} \tag{2.110}$$

with $\Delta^a = (\Delta_{e_1}, \Delta_{e_2}, \cdots, \Delta_{e_d})$ the vector of position differences in each of the dimensions e_i, m^a the vector enumerating the derivative orders in each dimension and $P^{(d)}$ is a multinomial of Δ which can be constructed from the $(n-1)^{\mathrm{th}}$ minors of the $n \times n$ geometric array. The determinant is highly dependent on the geometry specified by the geometric array; meanwhile, the polynomial $P^{(d)}$ is determined from the minors as previously stated. The general solution is nontrivial, and so has been left open in this text.

It is also necessary to determine the error on the terms. From the standard 1d Taylor expansion, one has at truncation order n

$$L_{i\pm n} = \sum_{r=0}^{n} \frac{(\pm\Delta_n)^r L_i^{(r)}}{r!} + R_{n+1} \qquad |R_{n+1}| \approx \frac{\Delta_n^{n+1} L_i^{(n+1)}}{(n+1)!} \tag{2.111}$$

which can be generalized to d dimensions by utilizing the Hessian form of the Taylor expansion

$$L_{i\pm 1} = L_i \pm \Delta^a \partial_a L_i + \frac{\Delta^a \Delta^b \partial_{ab} L_i}{N_{ab}} + \cdots \tag{2.112}$$

where the summation convention is assumed, $\partial_{ab\cdots}$ are the partial derivative tensors of Hessian type i.e., in 2 dimensions

$$\partial_a = \begin{pmatrix} \partial_x \\ \partial_y \end{pmatrix} \qquad \partial_{ab} = \begin{pmatrix} \partial_{xx} & \partial_{xy} \\ \partial_{yx} & \partial_{yy} \end{pmatrix}, \tag{2.113}$$

and $N_{ab\cdots}$ is a numerical factor corresponding to the factorial terms in the expan-

sion. It can then be shown that the leading order error is

$$R_n \sim \frac{\Delta_{n+1}^{a_1 \cdots a_d} \partial_{n+1}^{a_1 \cdots a_d} f(\zeta)}{N_{n+1}^{a_1 \cdots a_d}} \tag{2.114}$$

where Δ is the difference tensor (in powers of its elements which mimic the Hessian). From the 1d monomial expansion $f_i = c_j v^{ji}$, the differenced monomial equation is

$$f_1^{(i)} = \sum_{n=0}^{\infty} \frac{C_n \Delta_{i1}^n}{n!} \tag{2.115}$$

with which can be yielded [212]

$$R_n \sim \frac{\det V_{ik}}{(n+1)!} \sum_{j}^{n} \frac{f^{(n+1)}(\zeta) \Delta_{ij}^{n+1}}{\det V_{jk}} \tag{2.116}$$

with its d-dimensional generalization

$$R_n \sim \frac{\det V_{ik}}{N_{n+1}^{a_1 \cdots a_d}} \sum_{j}^{n} \frac{\partial_{n+1}^{a_1 \cdots a_d} f(\zeta) \Delta_{n+1}^{a_1 \cdots a_d}}{\det V_{jk}}. \tag{2.117}$$

From geometric and matrix-conditioning considerations the optimal error amongst stencil arrangements is that for a regular grid, which on the general d-dimensional finite-difference scheme for a square array is of order

$$\delta f_{\text{diff},i} \sim \mathcal{O}\left((\prod_{i \neq j} \Delta_{ij})^{1/d} \right), \tag{2.118}$$

where $\mathcal{O}(\Delta^2)$ is recovered for 1-point radius regular central schemes in d-dimensions, or $\mathcal{O}(\Delta^{2n})$ for n-point radius regular central schemes. For non-pathological functions such as polynomials, the accuracy of the differencing scheme generally improves with the number of points used (Fig. 2.3).
Finally, there may yet be some value in using geometric arrays featuring inverse powers. Whilst the Taylor series does not permit negative powers in the expansion, the Laurent expansion [215] of a complex function

$$f(x) = \sum_{n=-\infty}^{\infty} a_n (x-b)^n \tag{2.119}$$

(where the a_n terms are constants and b is a point on the complex plane) does, suggesting that one can deal with a pixel at a coordinate singularity by applying

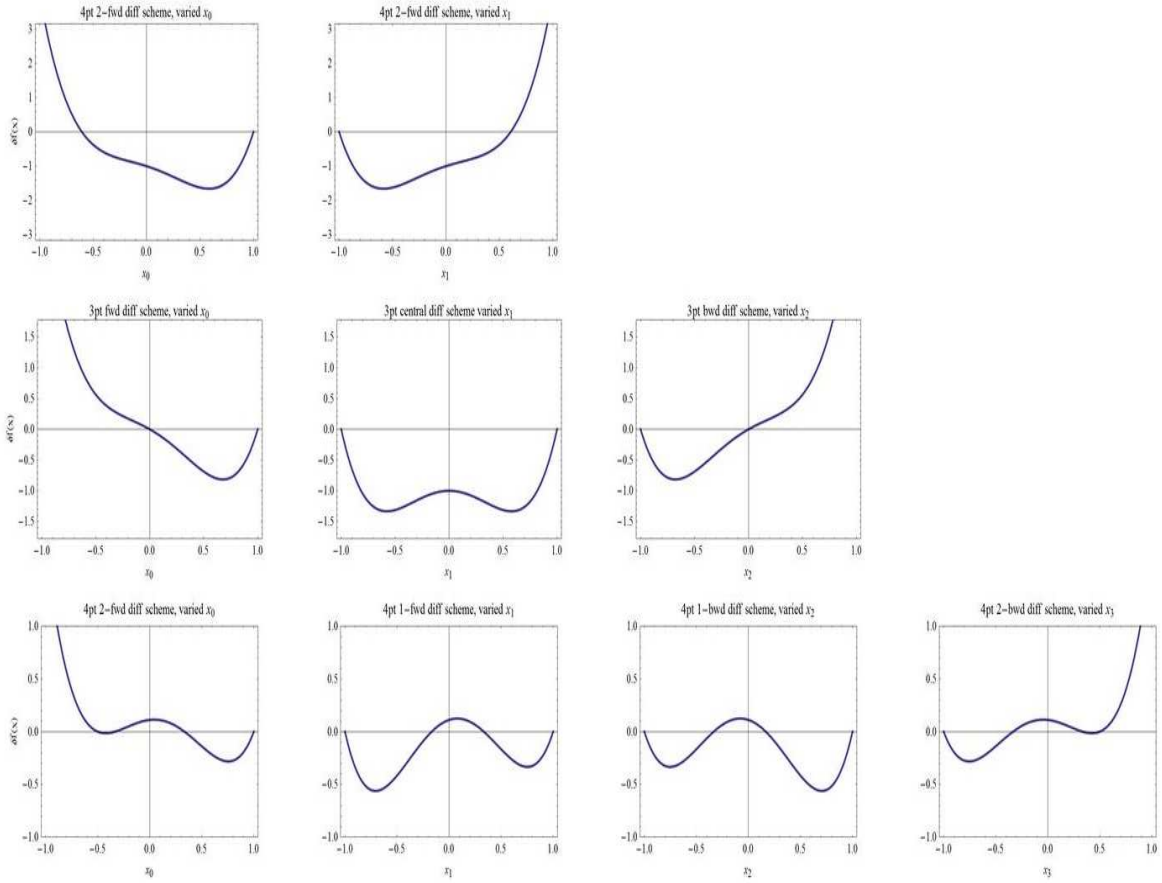

Figure 2.3: Accuracy $\delta f(x) = f_{\text{exact}}(x) - f_{\text{calc}}(x)$ of 2-, 3-, and 4-point finite-difference schemes on regular and irregular 1d grids (positions on the grid are denoted $x_0 \leq x_1 \leq x_2 \leq x_3$, assuming existence), for a first-order derivative. The test function $f(x) = x^5$ is used, since there are less datapoints available in these schemes than can specify the function exactly. The differences blow up only as the coordinate variation produces degeneracy in the datapoints.

the hyperbolic part of the interpolation at that pixel. This would, for example, correspond to the following algorithm for the differencing weights to approximate the first-order derivative on a 1d grid:

$$\begin{pmatrix} \Delta_1^{-1} & \Delta_2^{-1} & \Delta_3^{-1} \\ 1 & 1 & 1 \\ \Delta_1 & \Delta_2 & \Delta_3 \end{pmatrix} \begin{pmatrix} w_0^{(1)} \\ w_1^{(1)} \\ w_2^{(1)} \end{pmatrix} = \begin{pmatrix} 0 \\ 0 \\ 1 \end{pmatrix}. \tag{2.120}$$

One might consider whether a more general method can be found, or whether one can improve on the accuracy by utilizing a different method. More general methods are constrained by the uniqueness theorem; this means that it is indeed necessary to go beyond Lagrange interpolating polynomials if greater generality

is required. Looking at the issue of accuracy, then of course at a given point one can define a set of numerical weights which compute the derivative *at that point only*, exactly. On a regular unbounded grid, the set of weights at each point on the grid have to be identical to the set of weights at every other grid point if the weights are dependent on the geometry alone. Again since the interpolating polynomial is unique, then there can be no other general function-independent weighting scheme in the Lagrange regime.

2.4 Departures from Gaussianity and Statistical Isotropy in the e, b Approach

Inflation generically predicts large-scale B-modes, and scalar non-Gaussianity at low levels. Non-Gaussianity in the CMB can be described by any number of higher n-point statistics where $n > 2$, as discussed in the previous chapter. Since density perturbations also invoke perturbations in the metric which manifest as a primordial B-mode signal, one might expect to find non-Gaussianity in the B-mode signal too. This would manifest itself in the real pseudo-scalar b-field. Further, if an anomalous sky signal is detected one also may wish to continue the analysis having removed the anomaly, by applying a further mask to what may already be limited sky coverage. These considerations suggest it is necessary to produce a method of studying non-Gaussianity on the masked sky, without the internal (self-coupled) mode-mixing that masking entails.

The non-linear sources in inflation are often expressed in terms of the quantity f_{NL}. Since a primordial non-Gaussian signal is expected to be small compared with the Gaussian signal, it will be necessary to deal with mode-mixing in the higher n-point spectra.

Later it will be necessary to consider how to optimize the detection of any primordial B-mode signal. This also requires understanding the transfer of power between multipoles due to the presence of the mask when taking the harmonic transform. It can be shown that, in the regime where noise, instrumental and data processing issues are negligible, the masked observed temperature spectrum and underlying theoretical spectrum are related in the ensemble average by the transfer matrix K [216]

$$\left\langle \tilde{C}_l \right\rangle = \sum_{l'} K_{ll'} C_{l'} \tag{2.121}$$

where C_l is the theoretical power spectum. The inverse of K can then be used to invert the mode-coupling induced by a mask, which gives a quick method of estimating the power spectrum; such an estimation provides a useful prior to speed up the full MCMC calculations. In the next chapter, further comment will be made on how to define an apodization scheme (a smoothing of the mask) which yields a power spectrum which is as close as possible to the optimal spectrum. First, Smith & Zaldarriaga [217] is followed to construct the transfer matrix for the scalar fields, using the temperature anisotropy field as an analogue.

2.4.1 Scalar Mode-Transfer

In the pseudo-C_l formalism, the pseudo-multipoles are defined as

$$\tilde{T}_{lm} = \sum_x T(x) W(x) Y^*_{lm}(x) \tag{2.122}$$

for a mask W, with consequent pseudo-power spectrum

$$\tilde{C}_l^{TT} = \frac{1}{2l+1} \sum_m \tilde{T}^*_{lm} \tilde{T}_{lm}. \tag{2.123}$$

By adding noise, the expectation values of the pseudo spectra are given by

$$\left\langle \tilde{C}_l^{TT} \right\rangle = \sum_{l'} K_{ll'} C_{l'}^{TT} + \tilde{N}_l^{TT} \tag{2.124}$$

where the transfer matrix K will be calculated shortly. Adding noise is particularly important in the polarization case, since the derivative operation biases the noise by a factor $\sim l^4$ in harmonic space, leading to a blue noise spectrum which dominates power at large l, unlike a white noise spectrum. The noise bias can be computed exactly in cases where the noise is uncorrelated between pixels, or by Monte Carlo in the general case. Unbiased power spectrum estimators can be obtained from the pseudo-power spectra by simply subtracting the noise bias and applying the inverse of the transfer matrix:

$$\hat{C}_l^{TT} \equiv K^{-1}_{ll'} (\tilde{C}_{l'}^{TT} - \tilde{N}_{l'}^{TT}). \tag{2.125}$$

The preceding construction has assumed that the power spectrum is estimated at every multipole l. For reasons of sky coverage and signal-to-noise ratios, it is often necessary to bin multipoles into bandpowers with $\Delta l > 1$. In this case, for

each band β, one defines pseudo-bandpowers

$$\tilde{C}_\beta^{TT} = \sum_l P_{\beta l} \tilde{C}_l^{TT} \tag{2.126}$$

where the matrix P defines the l weighting within each bandpower estimator. One can also introduce a matrix $\bar{P}_{l\beta}$, which defines an interpolation scheme by which the signal power spectra depend on the bandpowers:

$$C_l^{TT} = \sum_\beta \tilde{P}_{l\beta} C_\beta^{TT}. \tag{2.127}$$

The binned analogues are then

$$\left\langle \tilde{C}_\beta^{TT} \right\rangle = K_{\beta\beta'} C_{\beta'}^{TT} + \tilde{N}_{\beta'}^{TT} \qquad \hat{C}_\beta^{TT} = K_{\beta\beta'}^{-1} (\tilde{C}_{\beta'}^{TT} - \tilde{N}_{\beta'}^{TT}). \tag{2.128}$$

where $K_{\beta\beta'}$ is the transfer matric for the binned spectra. Now to construct the standard transfer matrix. Starting from the unbinned estimator and utilizing the following results for the correlation function and the Legendre polynomial

$$\langle T(x)T(x')\rangle = \sum_{l'} \frac{2l'+1}{4\pi} P_{l'}(z) C_{l'}, \qquad P_l(z) = \frac{4\pi}{2l+1} \sum_m Y_{lm}^*(x) Y_{lm}(x') \tag{2.129}$$

gives

$$\frac{1}{4\pi} \left\langle \tilde{C}_l^{TT} \right\rangle = \sum_{x,x',l'} \left(\frac{2l'+1}{4\pi} \right) P_{l'}(z) P_l(z) W(x) W(x') C_{l'}. \tag{2.130}$$

This is of the form

$$S = \sum_{x,x'} W(x) F(z = x \cdot x') W(x') \tag{2.131}$$

which can be evaluated using $F(z) = \sum_l F_l P_l(z)$:

$$S = \sum_{l,x,x'} W(x) W(x') F_l P_l(z) = 8\pi^2 \int_{-1}^{1} \zeta^{WW}(z) F(z) \tag{2.132}$$

where

$$\zeta^{WW}(z) = \frac{1}{4\pi} \sum_{l,m} |W_{lm}|^2 P_l(z). \tag{2.133}$$

Thus the transfer matrix is

$$K_{ll'} = 2\pi \int_{-1}^{1} dz \zeta^{WW}(z) P_l(z) \left(\frac{2l'+1}{4\pi} \right) P_{l'}(z), \tag{2.134}$$

which can also be written as

$$K_{ll'} = \frac{2l'+1}{4\pi} \sum_{l''m''} |W_{l''m''}|^2 \begin{pmatrix} l & l' & l'' \\ 0 & 0 & 0 \end{pmatrix}^2. \tag{2.135}$$

2.4.2 E/B-Unmixing Counterterms

In the e/b formalism, the scalar fields obey the same transfer matrix for mode-mixing as the temperature anisotropy. These fields are by construction pure. For future discussion, and as an illustration of the mode-mixing issues, it will also be instructive to calculate the transfer matrices for the E/B case. This is done in the tensor formalism, which can be shown to be equivalent to the spin-weight formalism — Smith [194] is followed in the construction of these terms. For E and B mode estimators, the mode-transfer equation becomes

$$\begin{pmatrix} \left\langle \tilde{C}_l^{EE} \right\rangle \\ \left\langle \tilde{C}_l^{BB} \right\rangle \end{pmatrix} = \sum_{l'} \begin{pmatrix} K_{ll'}^{+} & K_{ll'}^{-} \\ K_{ll'}^{-} & K_{ll'}^{+} \end{pmatrix} \begin{pmatrix} C_{l'}^{EE} \\ C_{l'}^{BB} \end{pmatrix} + \begin{pmatrix} \tilde{N}_{l'}^{EE} \\ \tilde{N}_{l'}^{BB} \end{pmatrix}. \tag{2.136}$$

In order to yield pure B-modes (without worrying about the purity in E), one inverts thus:

$$\begin{pmatrix} \hat{C}_l^{EE} \\ \hat{C}_l^{BB,\mathrm{pure}} \end{pmatrix} = \sum_{l'} \begin{pmatrix} K_{ll'}^{+} & K_{ll'}^{-} \\ K_{ll'}^{-,\mathrm{pure}} & K_{ll'}^{+,\mathrm{pure}} \end{pmatrix}^{-1} \begin{pmatrix} \tilde{C}_{l'}^{EE} - \tilde{N}_{l'}^{EE} \\ \tilde{C}_{l'}^{BB} - \tilde{N}_{l'}^{BB,\mathrm{pure}} \end{pmatrix}. \tag{2.137}$$

To compute $K_{ll'}^{\pm,\mathrm{pure}}$ one extends the scalar formalism; this includes the following vector and tensor weight components computed as the sum of combinations of

terms denoted with $(\alpha, \beta) \in \{W, X, Y, Q, U\}$:

$$\begin{aligned} S &= 8\pi^2 \int_{-1}^{1} dz \sum_{\alpha,\beta}^{\text{combins}} \zeta^{\alpha\beta} f^{\alpha\beta} \\ &= \sum_{xx'} \begin{pmatrix} W(x) & W^a(x) & W^{bc}(x) \end{pmatrix} F(x,x') \begin{pmatrix} W(x) \\ W^{a'}(x') \\ W^{b'c'}(x') \end{pmatrix} \\ &= \sum_{lm} \begin{pmatrix} W_{lm} & W^G_{lm} & W^E_{lm} \end{pmatrix} \begin{pmatrix} F_l^{WW} & F_l^{WG} & F_l^{WE} \\ F_l^{WG} & F_l^{GG} & F_l^{GE} \\ F_l^{WE} & F_l^{GE} & F_l^{EE} \end{pmatrix} \begin{pmatrix} W^*_{lm} \\ W^{G*}_{lm} \\ W^{E*}_{lm} \end{pmatrix} \\ &\qquad + \begin{pmatrix} W^C_{lm} & W^B_{lm} \end{pmatrix} \begin{pmatrix} F_l^{CC} & F_l^{CB} \\ F_l^{CB} & F_l^{BB} \end{pmatrix} \begin{pmatrix} W^{C*}_{lm} \\ W^{B*}_{lm} \end{pmatrix} \end{aligned} \tag{2.138}$$

where parity-invariance is assumed and

$$W_a = \nabla_a W, \qquad W_{ab} = \left(\nabla_a \nabla_b - \frac{g_{ab}}{2}\nabla^2\right) W. \tag{2.139}$$

In the tensor formalism, the pure pseudo-B modes are

$$\begin{aligned} \sqrt{\frac{(l+2)!}{(l-2)!}}\tilde{b}_{lm} = &\sum_x 2P^{ab}(x) W(x) Y^{B*}_{(lm)ab}(x) \\ &+ N'_l \sum_x 2T^{abcd} P_{ab}(x) W_c(x) Y^{C*}_{(lm)d}(x) \\ &+ N_l \sum_x 2T^{abcd} P_{ab}(x) W_{cd}(x) Y^*_{lm}(x) \end{aligned} \tag{2.140}$$

with $T_{abcd} = (\epsilon_{ac}g_{bd} + \epsilon_{ad}g_{bc} + \epsilon_{bc}g_{ad} + \epsilon_{bd}g_{ac})/4$, normalization terms $N_l = 1/\sqrt{(l-1)l(l+1)(l+2)}$ and $N'_l = 2/\sqrt{(l-1)(l+2)}$, and similarly the pure E-modes are defined by replacing the harmonic terms in the above equation using $B \to E$ and $C \to G$. The grad and curl decompositions of the tensor spherical harmonics are

$$\begin{aligned} Y^E_{(lm)ab} &= \frac{(-\nabla_a\nabla_b + \frac{g_{ab}}{2}\nabla^2)Y_{lm}}{\sqrt{(l-1)l(l+1)(l+2)}} & Y^B_{(lm)ab} &= \frac{(\frac{\epsilon_{ac}}{2}\nabla^c\nabla_b + \frac{\epsilon_{bc}}{2}\nabla^c\nabla_a)Y_{lm}}{\sqrt{(l-1)l(l+1)(l+2)}} \\ Y^G_{(lm)a} &= \frac{\nabla_a Y_{lm}}{\sqrt{l(l+1)}} & Y^C_{(lm)a} &= -\frac{\epsilon_{ab}\nabla^b Y_{lm}}{\sqrt{l(l+1)}}. \end{aligned} \tag{2.141}$$

Computing the F-matrix

$$F(x,x') = \frac{2l'+1}{\pi(2l+1)}\left(R^{22}_{l'}(z)Q^{de}Q'^{d'e'} + Q^{22}_{l'}(z)U^{de}U'^{d'e'}\right) \times \sum_m \begin{pmatrix} Y^{B*}_{(lm)de} \\ N'_l T^f_{dea} Y^{G*}_{(lm)f} \\ N_l T_{debc} Y^*_{lm} \end{pmatrix} \begin{pmatrix} Y'^B_{(lm)d'e'} & N'_l T^{f'}_{d'e'a'} Y^G_{(lm)f'} & N_l T_{d'e'b'c'} Y_{lm} \end{pmatrix} \tag{2.142}$$

yields for the transfer arrays

$$\begin{aligned} K^{+,\text{pure}}_{ll'} &= 2\pi \int_{-1}^{1} dz \left(\frac{2l'+1}{4\pi}\right)(A_l Q^{22}_{l'}(z) + B_l R^{22}_{l'}(z)) \\ K^{-,\text{pure}}_{ll'} &= 2\pi \int_{-1}^{1} dz \left(\frac{2l'+1}{4\pi}\right)(A_l R^{22}_{l'}(z) + B_l Q^{22}_{l'}(z)), \end{aligned} \tag{2.143}$$

where the $K^{-,\text{pure}}_{ll'}$ term is non-zero since we are not purifying both E and B, and

$$\begin{aligned} A_l &= \zeta^{WW} Q^{22}_l 2N_l \zeta^{WQ} P^{02}_l + N'^2_l(\zeta^{XX} Q^{11}_l + \zeta^{YY} R^{11}_l) \\ &\quad -2N'_l \zeta^{WX} Q^{12}_l + -2N_l N'_l \zeta^{XQ} P^{01}_l + N^2_l \zeta^{QQ} P^{00}_l \\ B_l &= \zeta^{WW} R^{22}_l + N'^2_l(\zeta^{XX} R^{11}_l + \zeta^{YY} Q^{11}_l) \\ &\quad -2N'_l \zeta^{WX} R^{12}_l - 2N_l N'_l \zeta^{YU} P^{01}_l + N^2_l \zeta^{UU} P^{00}_l. \end{aligned} \tag{2.144}$$

The exact form of the ζ, Q_l, R_l, Q^{ab} and U^{ab} terms given are not of great importance in this chapter (they can be found in section 3.5), but do highlight that the calculation of the mode-transfer matrices directly from the tensor fields is much more involved than the scalar case. Finally, the noise is given by

$$\begin{aligned} \tilde{N}^{EE}_l &= \sum_x \frac{\sigma^2(x)}{4\pi} W(x)^2 \\ \tilde{N}^{BB,\text{pure}}_l &= \sum_x \frac{\sigma^2(x)}{4\pi}\left(W(x)^2 + N'^2_l W_a(x) W^a(x) + 2N^2_l W_{bc}(x) W^{bc}(x)\right). \end{aligned} \tag{2.145}$$

To take a more general approach, the transfer matrices can be written thus:

$$\begin{pmatrix} \tilde{C}^{TT}_l \\ \tilde{C}^{EE}_l \\ \tilde{C}^{BB}_l \end{pmatrix} = \sum_{l'} \begin{pmatrix} K^{TT}_{ll'} & 0 & 0 \\ 0 & K^{++}_{ll'} & K^{--}_{ll'} \\ 0 & K^{--}_{ll'} & K^{++}_{ll'} \end{pmatrix} \begin{pmatrix} C^{TT}_{l'} \\ C^{EE}_{l'} \\ C^{BB}_{l'} \end{pmatrix} \tag{2.146}$$

where the notation has been altered slightly, using $K^{+}_{ll'} \to K^{++}_{ll'}$ and $K^{-}_{ll'} \to K^{--}_{ll'}$; this set of arrays is actually part of a 3-dimensional linear equation where another non-zero slice is given by

$$\begin{pmatrix} \tilde{C}^{EB}_{l} \\ \tilde{C}^{TE}_{l} \\ \tilde{C}^{TB}_{l} \end{pmatrix} = \sum_{l'} \begin{pmatrix} K^{+-}_{ll'} & 0 & 0 \\ 0 & K^{T+}_{ll'} & K^{T-}_{ll'} \\ 0 & K^{T-}_{ll'} & K^{T+}_{ll'} \end{pmatrix} \begin{pmatrix} C^{EB}_{l'} \\ C^{TE}_{l'} \\ C^{TB}_{l'} \end{pmatrix}. \tag{2.147}$$

with couplings between the EE, BB and EB terms also non-zero. The pure scalar-field formalism then moves to a diagonalized basis

$$\begin{aligned} \begin{pmatrix} \tilde{C}^{TT}_{l} \\ \tilde{C}^{ee}_{l} \\ \tilde{C}^{bb}_{l} \end{pmatrix} &= \sum_{l'} \begin{pmatrix} K^{TT}_{ll'} & 0 & 0 \\ 0 & K^{TT}_{ll'} & 0 \\ 0 & 0 & K^{TT}_{ll'} \end{pmatrix} \begin{pmatrix} C^{TT}_{l'} \\ C^{ee}_{l'} \\ C^{bb}_{l'} \end{pmatrix} \\ \begin{pmatrix} \tilde{C}^{eb}_{l} \\ \tilde{C}^{Te}_{l} \\ \tilde{C}^{Tb}_{l} \end{pmatrix} &= \sum_{l'} \begin{pmatrix} K^{TT}_{ll'} & 0 & 0 \\ 0 & K^{TT}_{ll'} & 0 \\ 0 & 0 & K^{TT}_{ll'} \end{pmatrix} \begin{pmatrix} C^{eb}_{l'} \\ C^{Te}_{l'} \\ C^{Tb}_{l'} \end{pmatrix}, \end{aligned} \tag{2.148}$$

meaning that there is no need to perform the tedious calculation of the spin-mixing terms for the cross-spectra, trivializing mode-mixing issues in the case of the TB modes that would betray chirality in the gravitational sector.

2.4.3 Higher-Order Spectra

Having constructed a set of real scalar and pseudo-scalar fields analogous to the pure E- and B-modes, one is in the unique position of being able to consider constructing optimal estimators for the higher n-point polarization spectra, since phase information is no longer automatically discarded unlike the Smith & Zaldarriaga method. Starting with the bispectrum, an unbiased estimator is given by [218]

$$\hat{B}_{ll'l''} = \sum_{\text{all } m} \begin{pmatrix} l & l' & l'' \\ m & m' & m'' \end{pmatrix} a_{lm} a_{l'm'} a_{l''m''}. \tag{2.149}$$

Analogously to the angular power spectrum, one can postulate a rank-6 tensor that maps in the average between pseudo- and full-sky bispectra. It is then necessary to perform the same mode-transfer analysis on the bispectrum, if one wishes to avoid ambiguity in the sensitive results for 3-point non-Gaussianity. In partic-

ular, one wishes to calculate the transfer tensor K used in

$$\left\langle \tilde{B}_{ll'l''} \right\rangle = \sum_{LL'L''} K^{TT}_{ll'l''LL'L''} B_{LL'L''} \tag{2.150}$$

and then optimize. In fact, the formalism is readily generalizable to any n-point correlation function in harmonic space. By extension, for the pseudo-n-spectrum $\tilde{N}_{l_1\cdots l_n}$, the harmonic transform of the n-point correlation function, mode-mixing between polarization modes of one type can be given by

$$\begin{pmatrix} \tilde{N}^{E\cdots E}_{l_1\cdots l_n} \\ \tilde{N}^{B\cdots B}_{l_1\cdots l_n} \end{pmatrix} = \sum_{l'} \begin{pmatrix} K^{++}_{l_1\cdots l_n l'_1\cdots l'_n} & K^{--}_{l_1\cdots l_n l'_1\cdots l'_n} \\ K^{--}_{l_1\cdots l_n l'_1\cdots l'_n} & K^{++}_{l_1\cdots l_n l'_1\cdots l'_n} \end{pmatrix} \begin{pmatrix} N^{E\cdots E}_{l'_1\cdots l'_n} \\ N^{B\cdots B}_{l'_1\cdots l'_n} \end{pmatrix}, \tag{2.151}$$

where the number of elements in l_i depends on the points n in the n-point spectrum. By including polarization, a general estimator for the temperature and polarization bispectrum signal can then be written as [219]

$$\hat{S} = \sum_{ijk} \sum_{\{lm\}} W^{ijk}_{\{lm\}} a^i_{l_1 m_1} a^j_{l_2 m_2} a^k_{l_3 m_3} \tag{2.152}$$

where the i, j, k indices refer to the T, E, B parameters and W is some well-chosen weight function, defined in terms of the covariance matrix of the possible bispectra. This quantity S is the radial integral of a cubic combination of the scalar potentials. Further analysis provided by [220] yields an unbiased estimator for the local f_{NL}, linearly related to $\hat{S}$. Meanwhile, Shiraishi et al [221] provide the theoretical bispectra for the CMB temperature and polarization sourced from non-Gaussianity in the vector and tensor modes.

As an alternative estimator for 3-point functions, one may consider [100, 222] the skew-spectrum estimator

$$C_l^{XY,Z} = \sum_{l_1 l_2} B^{XYZ}_{l_1 l_2 l} \sqrt{\frac{(2l_1+1)(2l_2+1)}{4\pi(2l+1)}} \begin{pmatrix} l_1 & l_2 & l \\ x+y & 0 & -(x+y) \end{pmatrix}, \tag{2.153}$$

where x, y and z enumerate the spins of the fields X, Y and Z. This is then a two-point statistic for correlations between 2-point and 1-point anisotropies, containing compressed information from the bispectrum with the advantage of ease of calculation. Again, the advantage of the scalar field formalism will be the simplicity in which the mode-mixing arrays can be constructed. The basis for this compact spectrum is to consider that the bispectrum will be related to the power spectrum of the products of two fields with a third, i.e., by utilizing the integrated

product for spin-weighted harmonics, or spin-weighted Gaunt integral

$$
\begin{aligned}
{}_{s_1s_2s_3}\mathcal{G}^{m_1m_2m_3}_{l_1l_2l_3} &= \int {}_{s_1}Y_{l_1m_1}(\Omega)\,{}_{s_2}Y_{l_2m_2}(\Omega)\,{}_{s_3}Y_{l_3m_3}(\Omega)d\Omega \\
&= \sqrt{\frac{(2l_1+1)(2l_2+1)(2l_3+1)}{4\pi}} \begin{pmatrix} l_1 & l_2 & l_3 \\ -s_1 & -s_2 & -s_3 \end{pmatrix} \begin{pmatrix} l_1 & l_2 & l_3 \\ m_1 & m_2 & m_3 \end{pmatrix}
\end{aligned} \tag{2.154}
$$

and the addition properties of spin-weight

$$
{}_aA = {}_bB_cC \qquad \Rightarrow \qquad a = b + c \tag{2.155}
$$

one can express the harmonic coefficients of the products of the fields A, B and C (with spin-weights a, b and c) in terms of the 2-to-1, or skew, spectrum

$$
C_l^{AB,C} = \frac{1}{2l+1}\sum_m (AB)_{lm}C^*_{lm} \tag{2.156}
$$

which clearly involves averages over three-point correlations. In the presence of a mask, these results generalize to

$$
\begin{aligned}
(ABw)_{lm} &= \sum_{l_im_i} (-1)^{l'} A_{l_1m_1}B_{l_2m_2}w_{l_3m_3}\sqrt{\frac{(2l_1+1)(2l_2+1)(2l+1)}{4\pi}} \\
&\quad \times \begin{pmatrix} l_1 & l_2 & l' \\ a & b & -(a+b) \end{pmatrix} \begin{pmatrix} l_1 & l_2 & l' \\ m_1 & m_2 & -m \end{pmatrix} {}_{-(a+b),0,a+b}\mathcal{G}^{m'm_3m}_{l'l_3l} \\
(Cw)_{lm} &= \sum_{l_im_i} C_{l_1m_1}w_{l_2m_2}\,{}_{-c0c}\mathcal{G}^{m_1m_2m}_{l_1l_2l}
\end{aligned} \tag{2.157}
$$

such that the pseudo-skew-spectrum is

$$
\hat{C}_l^{AB,C} = \frac{1}{2l+1}\sum_m (ABw)_{lm}(Cw)^*_{lm} = \sum_{l'} K^{ab,c}_{ll'}C^{AB,C}_{l'} \tag{2.158}
$$

which relates to the full-sky spectrum by the mode-coupling term K. The mode-coupling matrix with spin-mixing discounted is then given by

$$
K^{ab,c}_{ll'} = \frac{1}{4\pi}\sum_{l''}(2l'+1)(2l+1) \begin{pmatrix} l & l'' & l' \\ a+b & 0 & -(a+b) \end{pmatrix} \begin{pmatrix} l & l'' & l' \\ c & 0 & -c \end{pmatrix} w_{l''}. \tag{2.159}
$$

Similarly, analogous calculations for the bispectrum can be performed. The expectation value of the angle-averaged pseudo-bispectrum can be defined as

$$\left\langle \tilde{B}_{l_1 l_2 l_3} \right\rangle = \sum_{\text{all } m} \begin{pmatrix} l_1 & l_2 & l_3 \\ m_1 & m_2 & m_3 \end{pmatrix} \left\langle \tilde{T}_{l_1 m_1} \tilde{T}_{l_2 m_2} \tilde{T}_{l_3 m_3} \right\rangle, \tag{2.160}$$

which describes triangular associations in the sky. For $l \lesssim 50$ with 32-bit accuracy this can be calculated exactly; beyond that numerical errors creep in requiring that one instead calculates

$$\tilde{B}_{l_1 l_2 l_3} = \begin{pmatrix} l_1 & l_2 & l_3 \\ 0 & 0 & 0 \end{pmatrix}^{-1} \int \tilde{e}_{l_1} \tilde{e}_{l_2} \tilde{e}_{l_3} d\Omega, \tag{2.161}$$

where

$$e_l(\hat{n}) = \sqrt{\frac{4\pi}{2l+1}} \sum_m a_{lm} Y_{lm}(\hat{n}) \tag{2.162}$$

is the azimuthally-averaged harmonic transform. It is also possible to utilize the reduced bispectrum $b_{l_1 l_2 l_3}$, which is related to the full and angle-averaged bispectra by:

$$\begin{aligned} B^{m_1 m_2 m_3}_{l_1 l_2 l_3} &= \mathcal{G}^{m_1 m_2 m_3}_{l_1 l_2 l_3} b_{l_1 l_2 l_3} \\ B_{l_1 l_2 l_3} &= \sqrt{\frac{(2l_1+1)(2l_2+1)(2l_3+1)}{4\pi}} \begin{pmatrix} l_1 & l_2 & l_3 \\ 0 & 0 & 0 \end{pmatrix} b_{l_1 l_2 l_3}. \end{aligned} \tag{2.163}$$

In some sense, the reduced bispectrum is more useful than the angle-averaged bispectrum since it is approximately equal to the theoretical bispectrum in the flat-sky limit. However, this is not a concern here since moving between formalisms is trivial. Since the expectation value of the angle-averaged pseudo-term is related to the true values by equation (2.150), it is necessary to calculate the harmonic correlation term; expanding harmonic coefficients gives

$$\begin{aligned} \tilde{T}_{l_1 m_1} \tilde{T}_{l_2 m_2} \tilde{T}_{l_3 m_3} = \int\int\int & T(\Omega) T(\Omega') T(\Omega'') W(\Omega) W(\Omega') W(\Omega'') \\ & \times Y^*_{l_1 m_1}(\Omega) Y^*_{l_2 m_2}(\Omega') Y^*_{l_3 m_3}(\Omega'') d\Omega d\Omega' d\Omega'', \end{aligned} \tag{2.164}$$

and expanding the T and W terms into harmonic coefficients again gives

$$\left\langle \tilde{T}_{l_1 m_1} \tilde{T}_{l_2 m_2} \tilde{T}_{l_3 m_3} \right\rangle = \sum_{\text{all } LMlm} \begin{pmatrix} l & l' & l'' \\ m & m' & m'' \end{pmatrix} W^{MM'M''}_{LL'L''} B_{ll'l''} \mathcal{G}^{Mmm_1}_{Ll_1} \mathcal{G}^{M'm'm_2}_{L'l'l_2} \mathcal{G}^{M''m''m_3}_{L''l''l_3} \tag{2.165}$$

where $W_{LL'L''}^{MM'M''}$ is the bispectrum of the mask. The transfer tensor is then

$$K_{l_1 l_2 l_3 l l' l''} = \sum_{\text{all } LMm} \begin{pmatrix} l & l' & l'' \\ m & m' & m'' \end{pmatrix} W_{LL'L''}^{MM'M''} \mathcal{G}_{Lll_1}^{Mmm_1} \mathcal{G}_{L'l'l_2}^{M'm'm_2} \mathcal{G}_{L''l''l_3}^{M''m''m_3}. \quad (2.166)$$

As with the bispectrum, the trispectrum can be decomposed into 'two-to-two' and 'three-to-one' power spectra, where mode-coupling must be determined for each. Calculation of $2n$-point spectra should be carefully analysed, since Gaussianity imprints a signal on them that it does not on the $2n + 1$-point spectra. General estimators for the full trispectrum have been proposed in Regan et al [223]; the identification of shapes with which to measure higher-order non-linear perturbations such as g_{NL}, τ_{NL} follows the same flavour of problems as finding an optimal shape for measuring f_{NL}; Kamionkowski et al [224] provide an argument that the trispectrum can contribute additional information on f_{NL}, which by extension may imply the usefulness of arbitrarily higher order estimators.
In this sense, it should be possible to exclude masking leakage between polarization n-point spectra which would further rigorize detection methods for non-Gaussian signals (and allow for a more accurate statement on the nature of that non-Gaussianity). The full wealth of inflation-model-discriminating data could be harnessed by a clean combination of harmonic n-point spectra across all temperature and polarization variables.
A general account of scalar mode-coupling matrices for $(\alpha + \beta)$-to-1 spectra (where points on the sky have been compacted to correlation spectra between α coupled points and β coupled points)

$$\langle A_1 \cdots A_\alpha, B_1 \cdots B_\beta \rangle \,, \quad (2.167)$$

and extended to multipolar spectra, is now provided. It should be clear that all bi- and trispectra (and higher combinations) are a subset of the $(\alpha + \beta + \cdots)$-to-$n$ spectra since one can reduce a given n-point spectrum to a variety of combinations of lower-order point-correlation spectra. To perform the calculation one also needs the n-point integral

$$\mathcal{G}_{l_1 \cdots l_n}^{m_1 \cdots m_n} = \int Y_{l_1 m_1} \cdots Y_{l_n m_n} d\Omega \quad (2.168)$$

which is evaluated by reduction of the integral to products of a smaller number of harmonics using the Clebsch-Gordon expansion

$$Y_{l_1m_1}\cdots Y_{l_nm_n} = \sum_{L_n} B_{L_n} Y_{L_nM_n}$$
$$B_{L_n} = \sqrt{\frac{4\pi}{2L_n+1}} \sum_{L_1\cdots L_{n-1},M_1\cdots M_{n-1}} \prod_{i=1}^{n} \left(\sqrt{\frac{2l_i+1}{4\pi}} C^{L_i0}_{L_{i-1}0l_i0} C^{L_iM_i}_{L_{i-1}M_{i-1}l_im_i} \right), \tag{2.169}$$

where the Clebsch-Gordon coefficients are related to the Wigner $3lm$ symbols by

$$C^{l_3m_3}_{l_1m_1l_2m_2} = (-1)^{l_1-l_2+m_3}\sqrt{2l_3+1} \begin{pmatrix} l_1 & l_2 & l_3 \\ m_1 & m_2 & -m_3 \end{pmatrix}, \tag{2.170}$$

and a slight variation on the integral by making a substitution

$$Y_{l_nm_n} \to Y^*_{l_nm_n} \qquad \mathcal{G}^{m_1\cdots m_n}_{l_1\cdots l_n} \to \mathcal{G}^{m_1\cdots m^*_n}_{l_1\cdots l^*_n} \qquad Y^*_{l_nm_n} = (-1)^m Y_{l_1,-m_1} \tag{2.171}$$

where the star indicates in $\mathcal{G}$ which harmonic term has been conjugated. The harmonic expansion of n coupled scalar fields is then

$$(A_1\cdots A_n)_{lm} = \sum_{l_i} A^{(1)}_{l_1m_1}\cdots A^{(n)}_{l_nm_n} \mathcal{G}^{m_1\cdots m_nm^*}_{l_1\cdots l_nl^*} \tag{2.172}$$

which, when in the presence of a mask W is

$$(A_1\cdots A_nW)_{lm} = \sum_{l_i} A^{(1)}_{l_1m_1}\cdots A^{(n)}_{l_nm_n} W_{l_nm_n} \mathcal{G}^{m_1\cdots m_{n+1}m^*}_{l_1\cdots l_{n+1}l^*}. \tag{2.173}$$

The $(\alpha+\beta)$-point pseudo-power spectrum is then

$$\begin{aligned} \left\langle \tilde{C}_l^{A_1\cdots A_\alpha, B_1\cdots B_\beta} \right\rangle &= \frac{1}{2l+1} \sum_m (A_1\cdots A_\alpha W)_{lm} (B_1\cdots B_\beta W)^*_{lm} \\ &= \sum_{l'} K_{ll'}^{A_1\cdots A_\alpha, B_1\cdots B_\beta} C_l^{A_1\cdots A_\alpha, B_1\cdots B_\beta} \end{aligned} \tag{2.174}$$

where the $(\alpha+\beta)$-point theoretical power spectrum is

$$C_l^{A_1\cdots A_\alpha, B_1\cdots B_\beta} = \frac{1}{2l+1} \sum_m (A_1\cdots A_\alpha)_{lm} (B_1\cdots B_\beta)^*_{lm} \tag{2.175}$$

and, from the spin-weight addition theorem, the transfer matrix is

$$K_{ll'}^{A_1\cdots A_\alpha,B_1\cdots B_\beta} = \frac{1}{4\pi}\sum_{l''}(2l'+1)(2l''+1)\begin{pmatrix} l & l'' & l' \\ 0 & 0 & 0 \end{pmatrix}^2 \sum_{m''}|W_{l''m''}|^2 \qquad (2.176)$$

which is the same as for the standard power spectrum. The same spin-addition properties will mean that all the scalar decompositions of n-point spectra into bispectral (and trispectral and so on) compactifications will also have the same form as their standard temperature n-point counterpart.

It now makes sense to generalize the mode-coupling matrices for the standard bispectra, trispectra and other n-point spectra. For the scalar n-spectra $N_{l_1\cdots l_n}$, by following the derivation as for the scalar bispectrum it can be shown that

$$\left\langle \tilde{T}_{l_1m_1}\cdots\tilde{T}_{l_nm_n}\right\rangle = \sum_{LM\Lambda\mu} N_{\Lambda_1\cdots\Lambda_n} R^{\mu_1\cdots\mu_n}_{\Lambda_1\cdots\Lambda_n} W^{M_1\cdots M_n}_{L_1\cdots L_n} \mathcal{G}^{M_1\mu_1m_1}_{L_1\Lambda_1l_1}\cdots\mathcal{G}^{M_n\mu_nm_n}_{L_n\Lambda_nl_n}, \qquad (2.177)$$

where the rotation-coupling term $R^{\mu_1\cdots\mu_n}_{\Lambda_1\cdots\Lambda_n}$ can be calculated from the product of n Wigner D-functions using the generalized Clebsch-Gordan expansion (p.85, [225]), such that the mode-coupling tensor is

$$K_{l_1\cdots l_n\Lambda_1\cdots\Lambda_n} = \sum_{LM\Lambda\mu m} R^{\mu_1\cdots\mu_n}_{\Lambda_1\cdots\Lambda_n} W^{M_1\cdots M_n}_{L_1\cdots L_n} \mathcal{G}^{M_1\mu_1m_1}_{L_1\Lambda_1l_1}\cdots\mathcal{G}^{M_n\mu_nm_n}_{L_n\Lambda_nl_n}. \qquad (2.178)$$

These are then the tools for calculating the mode-coupling for almost any given type of scalar spectrum, with any given type of compactification. What remains are the multipolar harmonics for the tensor product of p 2-spheres $\mathbb{S}^2$, starting with the bipolar ($p=2$) harmonics. The bipolar harmonics

$$\Upsilon^{l_1l_2}_{LM}(\Omega_1,\Omega_2) \equiv \{Y_{l_1}(\Omega_1)\otimes Y_{l_2}(\Omega_2)\}_{LM} = \sum_{m_i} C^{LM}_{l_1m_1l_2m_2} Y_{l_1m_1}(\Omega_1)Y_{l_2m_2}(\Omega_2) \quad (2.179)$$

can be used to constrain deviations from statistical isotropy [226, 227] since they provide a fuller description of the correlation matrix between fields A and B

$$C^{AB}(\Omega_1,\Omega_2) = \sum_{l_1l_2LM} (AB)^{LM}_{l_1l_2}\Upsilon^{l_1l_2}_{LM}(\Omega_1,\Omega_2) \qquad (2.180)$$

where the harmonic coefficients are given by

$$(AB)^{LM}_{l_1l_2} = \int\int C^{AB}(\Omega_1,\Omega_2)\Upsilon^{l_1l_2*}_{LM}(\Omega_1,\Omega_2)d\Omega_1 d\Omega_2 \qquad (2.181)$$

which then define the bipolar power spectrum:

$$\kappa_L^{ABCD} = \sum_{l_1 l_2 M} (AB)_{l_1 l_2}^{LM} (CD)_{l_1 l_2}^{LM*}. \tag{2.182}$$

These harmonics obey the following orthogonality relation:

$$\int\int \Upsilon_{LM}^{l_1 l_2}(\Omega_1, \Omega_2) \Upsilon_{L'M'}^{l_1' l_2'*}(\Omega_1, \Omega_2) d\Omega_1 d\Omega_2 = \delta_{l_1 l_1'} \delta_{l_2 l_2'} \delta_{LL'} \delta_{MM'}. \tag{2.183}$$

The pseudo-bipolar spectrum is then

$$\tilde{\kappa}_L^{ABCD} = \sum_{l_1 l_2 M} (\tilde{AB})_{l_1 l_2}^{LM} (\tilde{CD})_{l_1 l_2}^{LM*} \tag{2.184}$$

where the mask is introduced via

$$(\tilde{AB})_{l_1 l_2}^{LM} = \int\int C^{AB}(\Omega_1, \Omega_2) W^{AB}(\Omega_1, \Omega_2) \Upsilon_{LM}^{l_1 l_2 *}(\Omega_1, \Omega_2) d\Omega_1 d\Omega_2 \tag{2.185}$$

since the full correlation mask is the pixelwise product of the masks used on both spheres. This yields

$$\begin{aligned} \tilde{\kappa}_L^{ABCD} = \sum_{l_1 l_2 M} \int\int\int\int & C^{AB}(\Omega_1, \Omega_2) W^{AB}(\Omega_1, \Omega_2) \Upsilon_{LM}^{l_1 l_2 *}(\Omega_1, \Omega_2) \\ & \times C^{CD}(\Omega_3, \Omega_4) W^{CD}(\Omega_3, \Omega_4) \Upsilon_{LM}^{l_1 l_2}(\Omega_3, \Omega_4) d\Omega_1 d\Omega_2 d\Omega_3 d\Omega_4. \end{aligned} \tag{2.186}$$

Again, taking the pixelwise product of the mask (where Ω' is the pixelwise product of Ω_1 and Ω_2, and Ω'' is the pixelwise product of Ω_3 and Ω_4) and then decomposing it into harmonics

$$W^{ABCD}(\Omega', \Omega'') \equiv W^{AB}(\Omega_1, \Omega_2) W^{CD}(\Omega_3, \Omega_4) = \sum_{l_1' l_2' L' M'} W_{l_1' l_2'}^{L'M'} \Upsilon_{LM}^{l_1' l_2'}(\Omega', \Omega'') \tag{2.187}$$

allows one to separate out the mask term by integrating the harmonics using the Clebsch-Gordon series for bipolar harmonics:

$$\Upsilon_{L'M'}^{l_1' l_2'}(\Omega_1, \Omega_2) \Upsilon_{L''M''}^{l_1'' l_2''}(\Omega_1, \Omega_2) = \sum_{LM} C_{L'M'L''M''}^{LM} \sum_{l_1 l_2} B_{l_1' l_2' L' l_1'' l_2'' L''}^{l_1 l_2 L} \Upsilon_{LM}^{l_1 l_2}(\Omega_1, \Omega_2) \tag{2.188}$$

with

$$B^{l_1 l_2 L}_{l_1' l_2' L' l_1'' l_2'' L''} = \sqrt{\frac{(2l_1'+1)(2l_2'+1)(2l_1''+1)(2l_2''+1)}{(4\pi)^2}} \times \sqrt{(2L'+1)(2L''+1)} C^{l_1 0}_{l_1' 0 l_1'' 0} C^{l_2 0}_{l_2' 0 l_2'' 0} \left\{ \begin{array}{ccc} l_1' & l_1'' & l_1 \\ l_2' & l_2'' & l_2 \\ L' & L'' & L \end{array} \right\}, \tag{2.189}$$

where use has been made use of the Wigner $9j$-symbol. The multipolar harmonics are formed from the nested irreducible tensor product

$$\{Y_{l_1}(\Omega_1) \otimes \{\cdots \otimes Y_{l_p}(\Omega_p)\}_{l_{p-1,p}}\}_{LM} = \sum_{m_i} C^{LM}_{l_1 m_1 l_X m_X} \cdots C^{l_X l_X}_{l_{p-1} m_{p-1} l_p m_p} Y_{l_1 m_1}(\Omega_1) \cdots Y_{l_p m_p}(\Omega_p) \tag{2.190}$$

and allow a variety of coupling schemes; these have not yet found a use within cosmology but could be used for enumerating the violation of statistical anisotropy within each non-Gaussian term, and are included for completeness. The construction of coupling matrices is identical to that of the bispectrum, with the decomposition requiring only larger products of $9j$-symbols. For example, for the tripolar harmonics $\Upsilon^{l_1 l_2 l_3}_{\Lambda L M}(\Omega_1, \Omega_2, \Omega_3) \equiv \{Y_{l_1}(\Omega_1) \otimes \{Y_{l_2}(\Omega_2) \otimes Y_{l_3}(\Omega_3)\}_\Lambda\}_{LM}$the decomposition is

$$\Upsilon^{l_1' l_2' l_3'}_{\Lambda' L' M'}(\Omega_1, \Omega_2, \Omega_3) \Upsilon^{l_1'' l_2'' l_3''}_{\Lambda'' L'' M''}(\Omega_1, \Omega_2, \Omega_3) = \sum_{LM} C^{LM}_{L' M' L'' M''} \sum_{l_1 l_2 l_3 \Lambda} B^{l_1 l_2 l_3 \Lambda L}_{l_1' l_2' l_3' \Lambda' L' l_1'' l_2'' l_3'' \Lambda'' L''} \Upsilon^{l_1 l_2 l_3}_{\Lambda L M}(\Omega_1, \Omega_2, \Omega_3) \tag{2.191}$$

with

$$B^{l_1 l_2 l_3 \Lambda L}_{l_1' l_2' l_3' \Lambda' L' l_1'' l_2'' l_3'' \Lambda'' L''} = (4\pi)^{-3/2} \sqrt{(2l_1'+1)(2l_2'+1)(2l_1''+1)(2l_2''+1)(2l_3''+1)} \times \sqrt{(2l_3''+1)(2L'+1)(2L''+1)(2\Lambda+1)(2\Lambda'+1)(2\Lambda''+1)} \times C^{l_1 0}_{l_1' 0 l_1'' 0} C^{l_2 0}_{l_2' 0 l_2'' 0} C^{l_3 0}_{l_3' 0 l_3'' 0} \left\{ \begin{array}{ccc} l_1' & l_1'' & l_1 \\ \Lambda' & \Lambda'' & \Lambda \\ L' & L'' & L \end{array} \right\} \left\{ \begin{array}{ccc} l_2' & l_2'' & l_2 \\ l_3' & l_3'' & l_3 \\ \Lambda' & \Lambda'' & \Lambda \end{array} \right\}. \tag{2.192}$$

It should also be clear how coupling matrices for the variety of possible nestings and compactifications of all of the spectra summarised thus far could be constructed.

2.5 Where are the Defects?

In discussing the elegant symmetry-breaking phenomena ubiquitous in quantum fields, short work was made of the appearance of cosmic defects. If spontaneous symmetry-breaking really is the driving force behind the observed cosmology then all of its consequences must be expected. In this sense it can be viewed as surprising that, to date, nothing bar some tentative claims of defect detection have been made [88]. In the following a new method shall be presented with which one may attempt to detect such defects, complementary to the methods in the previous section for studying non-Gaussianity in maps.

2.5.1 The Laplacian-Difference Method for Detecting Defects

In chapter 1, it was discussed how defects were seen initially as a viable agent for cosmic structure; the crucial difference between defect-dominated structure formation and inflation-dominated structure formation is in the difference between adiabatic and isocurvature modes in the fluctuation spectrum. The WMAP-measured TE spectrum (Fig. 1.1) essentially rules out defects as the key component of structure formation, favouring inflation. Ignoring the caveats in reheating, inflation is an excellent mechanism for why no defects have been detected at all, by diluting them away. Despite dilution by inflation it is not unreasonable to expect to be able to detect at least one defect, such as a cosmic string, if they exist. The various phenomena which contribute to the formulation of detection methods are recounted; the focus is on those provided by cosmic strings.
First, defects could be revealed in the gravitational wave spectra as they radiate away their energy. This is a task for E/B decomposition at high-l, and will be coupled to the lensing properties of the strings. Since it was previously mentioned that for polarization scalar modes only generate E-modes, vector fluctuations create a strong B field and tensor fluctuations create E- and B-modes of a similar magnitude, it can be seen that small-scale B-modes from strings would be much larger than those from inflationary models. Second, strings should contribute to non-Gaussianity in the microwave sky via the *Kaiser-Stebbins* effect. The Kaiser-Stebbins effect [92], the cosmological manifestation of a discontinuous temperature gradient, is a well-known result of the presence of defects in the CMB such as cosmic strings; line discontinuities in the CMB temperature anisotropy field form from photons passing on opposite sides of a moving long string (Fig. 2.4). On sufficiently small scales the signal from string networks would be non-Gaussian, but on scales larger than the characteristic inter-string separation at radiation-matter

equality, those CMB temperature perturbations resulting from superposition of effects of many strings would be Gaussian.
For cosmic strings, the Kaiser-Stebbins temperature decrement is given by

$$\frac{\delta T}{T} = 8\pi G\mu\gamma_s \mathbf{v}_s \cdot (\mathbf{s} \times \mathbf{k}) \tag{2.193}$$

where γ_s is the Lorentz factor for the string segment, $\mathbf{v}_s$ is the string segment velocity, $\mathbf{s}$ the segment orientation and $\mathbf{k}$ the line of sight vector. The string tension is described by the dimensionless term $G\mu$, which encodes much of the interesting string physics.

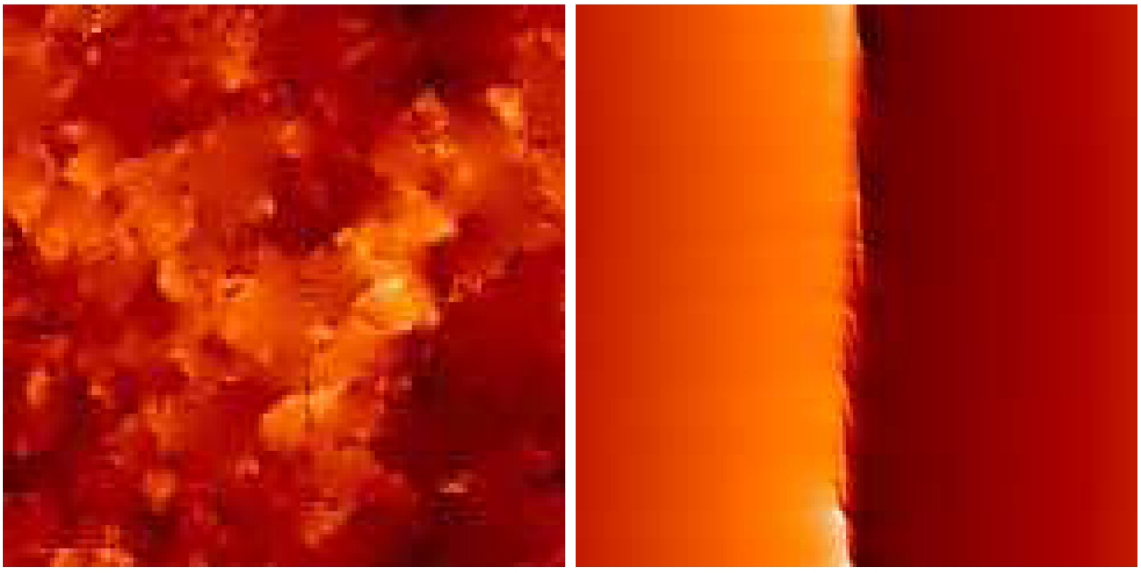

Figure 2.4: The Kaiser-Stebbins decrement [85]; a discontinuity in the microwave sky (left-hand diagram, discontinuous patch scaled up in the right-hand diagram) can be created by the redshift effect of a cosmic string.

One method of detecting such a discontinuity is by looking for characteristic signals in the derivatives of the CMB temperature field. Discontinuities have a characteristic delta-gradient. Recall that the finite-difference method is designed to calculate derivatives, i.e., gradients; due to Runge's phenomenon [228] it performs poorly for discontinuities and pathologies (anything that cannot be well-modelled by a polynomial). Runge's phenomenon is the observation of polynomial oscillation at an edge interval. Specifically, if a discontinuous function is interpolated with a polynomial P_n at n points, it can be shown that [228]

$$\lim_{n\to\infty} (\max |f(x) - P_n(x)|) = \infty. \tag{2.194}$$

The errors for a discontinuous function are related to the validity of Taylor expanding such a function; Taylor expansions are only valid for an infinitely differentiable function, i.e., the series is convergent only if the function is analytic. It is necessary to ask what really defines a discontinuity in the context of a 2d pixelized map (since any pixelized map can be viewed as a collection of discontinuities) and confirm the phenomenology of finite differences in their vicinity. In order to answer this question, the derivatives of a step function are studied. Figure 2.5 shows the error for differencing on a unit step function; the crucial difference between this discontinuity and the standard pixelized analysis is that in the unit step scheme, the regions outside the step are relatively flat; for the 2d pixelized maps this behaviour does not necessarily occur.

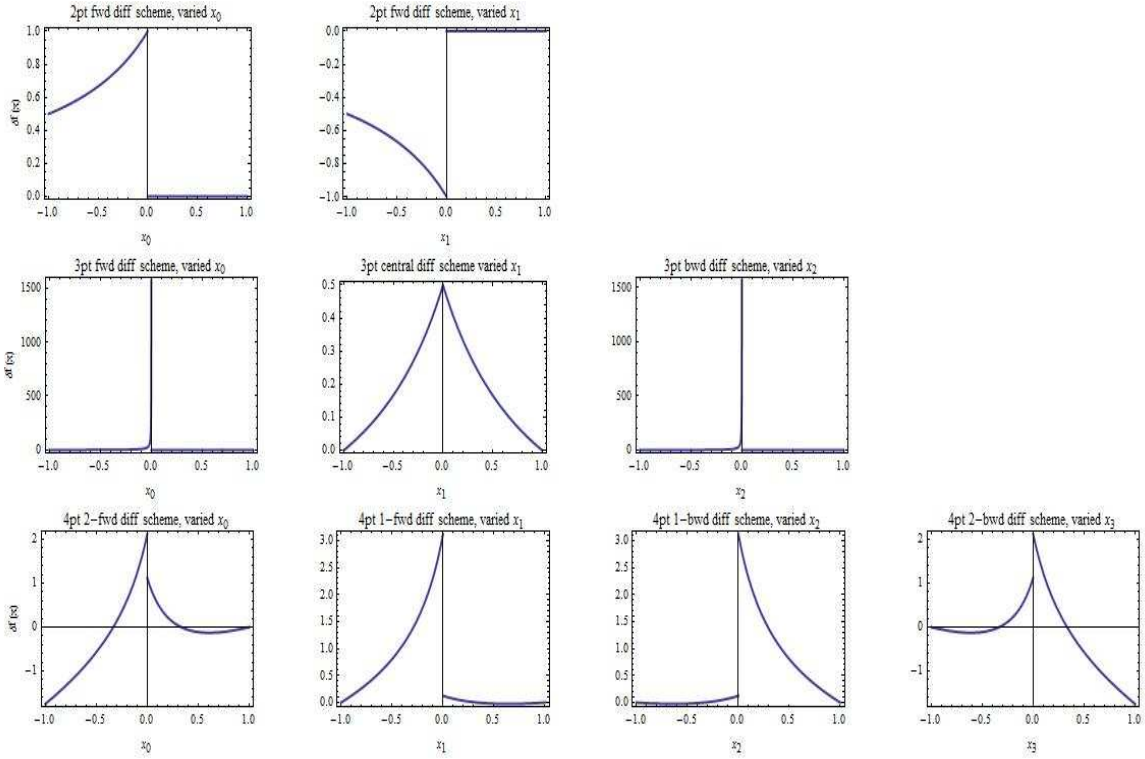

Figure 2.5: Errors $\delta f(x)$ for the derivatives of the Heaviside step function $U(x)$. Analytically, the derivative is defined as

$$U'(x) = \begin{cases} \text{Indeterminate} & x = 0 \\ 0 & \text{otherwise} \end{cases}$$

The above considerations suggest it might be possible to use the errors of an interpolation-based finite-difference scheme as a crude discontinuity detector. This shall be referred to as the 'Laplacian-difference' method, which shall be developed in a slightly more refined form. In particular the method to be used is the following: calculate the Laplacian map reconstructed from a spectral decompo-

sition, and the finite-differenced Laplacian map. The spectral map is constructed by calculating

$$\nabla^2 F = \sum_{lm} -l(l+1) f_{lm} Y_{lm} \tag{2.195}$$

where f_{lm} are the harmonic coefficients of the original map F, or using the equivalent harmonic basis and coefficients in a coordinate basis $\hat{n}$ if one wishes to extend the method to a non-spherical analysis. The construction of the finite-differenced map can be achieved by recalling that the Laplace-Beltrami theorem shows that the Laplacian of a scalar field on a given metric can be calculated from

$$\nabla^2 F = \frac{1}{\sqrt{g}} \partial_i \left(\sqrt{g} g^{ij} \partial_j F \right) \tag{2.196}$$

which can be generalized to operations on higher-rank (rank greater than zero) tensors using the spin-weighted operators $\eth$

$${}_s\nabla^2{}_s F = \bar{\eth}_{s+1} \eth_s \, {}_s F \tag{2.197}$$

and thus to Laplacians of order n by

$${}_s\nabla^{2n}{}_s F = \bar{\eth}_{s+1} \cdots \bar{\eth}_{s+2n} \eth_{s+2n-1} \cdots \eth_s \, {}_s F, \tag{2.198}$$

or in harmonic space

$$\begin{aligned} {}_s\nabla^{2n} &\leftrightharpoons (-1)^n \prod_{i=0}^{2n-1} (l-s-i)(l+s+i+1) \\ &\leftrightharpoons -(l-s)(1+l+s) \frac{\Gamma(s-l+2n)\Gamma(1+s+l+2n)}{\Gamma(1+s-l)\Gamma(2+s+l)}. \end{aligned} \tag{2.199}$$

Since the interpolating polynomial and the spherical harmonic bases are not identical, the discontinuity should be enhanced compared to smooth regions by calculating the map of differences between the finite-difference Laplacian and the spectrally-reconstructed Laplacian. This is then particularly useful when the discontinuity is subtle compared with the continuous signal. In order to estimate the results of this calculation, it can be noted that the differencing error for a function $F(\Omega_i)$ at pixel i given in equation (2.111) yields for the full scalar Laplacian

$$\delta(\nabla^2 F)_{\text{diff},i} \sim \left(\csc^2\theta \frac{F^{(1,3)}(\zeta)}{3!} + \cot\theta \frac{F^{(2,1)}(\zeta)}{2!} + \frac{F^{(3,1)}(\zeta)}{3!} \right) \text{Det}[v'] \tag{2.200}$$

where ζ is some position in the sampling region. Meanwhile, the function reconstruction error from the Gibbs' phenomenon receives contributions from two sources: First, if the function is pathological (i.e., not defined everywhere) then the harmonic sum in the limit of $l \to \infty$ will reconstruct the signal everywhere except at the discontinuity (regularization). Secondly (and more relevantly), truncation creates overshoot (ringing, Fig. 2.6) in the vicinity of the discontinuity, which approaches a finite limit.

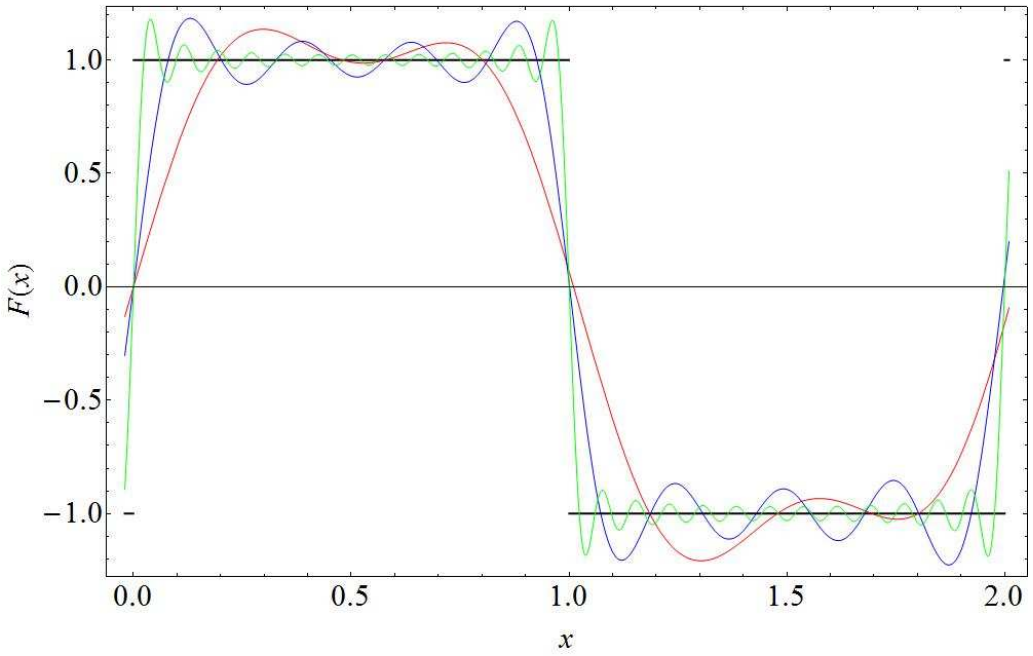

Figure 2.6: Gibbs' phenomenon: the incremental summation of harmonic terms for a discontinuous signal leads to increased convergence away from the step region but increased overshoot near to the step as the harmonic summation accumulates.

Three contributors of the numerical error to a harmonic reconstruction of a map can then be specified: truncation error (due to frequency limits):

$$\delta F_{\mathrm{trunc},i} = \left| \sum_{lm}^{n} (a^f_{lm} - a^g_{lm}) Y_{lm}(\theta, \phi)) \right|, \tag{2.201}$$

convergence error

$$\delta F_{\mathrm{conv},i} = \left| F(\theta, \phi) - \sum_{lm}^{\infty} a^F_{lm} Y_{lm}(\theta, \phi) \right|, \tag{2.202}$$

and the numerical error $\delta F_{\mathrm{num},i}$ implicit in any software package used. For a more detailed understanding of Gibbs' phenomenon in flat harmonic space, one can follow Carslaw [229]; an analysis of this type on the sphere has been implemented for longitudinal ringing via the Gegenbauer polynomials in Gelb [230].
Since the harmonic and interpolating bases are non-identical, one can show that the differences between the two reconstructions are largest where there exists a discontinuity — this is implicit in the differences between equation (2.111) and (2.194). For practical purposes, one may want to enhance this difference in order to isolate any particularly subtle signals. More generally, since the n-harmonic operators correspond to boosting the harmonic power by a factor

$$\nabla^{2n} \leftrightharpoons l^{2n}, \tag{2.203}$$

one should calculate the n-Laplacian-difference maps to pull out such a signal. Specifically, in the present case the calculations shall be limited to the spherical surface Laplacian-difference and bi-Laplacian-difference, using

$$\begin{aligned}\nabla^2 &= \csc\theta\partial_\theta(\sin\theta\partial_\theta) + \csc^2\theta\partial_{\phi\phi} \\ \nabla^4 &= 4\csc^4\theta\partial_{\phi\phi} + \csc^4\theta\partial_{\phi^4} + (2\cot\theta + \cot\theta\csc^2\theta)\partial_\theta - 2\cot\theta\csc^2\theta\partial_{\theta\phi\phi} \\ &\quad -\partial_{\theta\theta} + (\csc^2\theta - 2\cot^2\theta)\partial_{\theta\theta} + 2\csc^2\theta\partial_{\theta\theta\phi\phi} + 2\cot\theta\partial_{\theta^3} + \partial_{\theta^4}.\end{aligned} \tag{2.204}$$

One should also note that there is a minimum number of pixel samplings required for calculating these quantities, which increases with n, making the calculation of higher-order Laplacians more costly; furthermore, numerical noise will append a limit on the usefulness of scaling n to large values. The full error from this map can be estimated as:

$$\delta(\nabla^{2n}F)_i \sim \delta(\nabla^{2n}F)_{\mathrm{diff},i} - \nabla^{2n}\left(\delta F_{\mathrm{conv},i} + \delta F_{\mathrm{trunc},i} + \delta F_{\mathrm{num},i}\right). \tag{2.205}$$

One might also wish to calculate the gradient map

$$\nabla = (\partial_\theta, \csc\theta\partial_\phi) \tag{2.206}$$

in order to look for directional anomalies. By use of the spin-weighted harmonics, the harmonic decomposition of each term in the gradient can be found

$$\nabla F = \sum_{lm} -\sqrt{l(l+1)}f_{lm\,1}Y_{lm}. \tag{2.207}$$

Other useful derivatives and their harmonic expansions can be calculated via [225]

$$\begin{aligned} \partial_\theta &= \frac{1}{2}\left(e^{-i\phi}L_+ - e^{i\phi}L_-\right) \\ L_\pm Y_{lm} &= \sqrt{(l \pm m + 1)(l \mp m)}Y_{l,m\pm 1} \\ \partial_\phi &= 2L_z \qquad\qquad L_z Y_{lm} = mY_{lm} \end{aligned} \tag{2.208}$$

and the relations

$$\begin{aligned} e^{-i\phi}\sin\theta Y_{l,m+1} &= \sqrt{\frac{(l-m)(l-m+1)}{(2l+1)(2l+3)}}Y_{l+1,m} - \sqrt{\frac{(l+m)(l+m+1)}{(2l-1)(2l+3)}}Y_{l-1,m} \\ e^{i\phi}\sin\theta Y_{l,m-1} &= \sqrt{\frac{(l+m)(l+m+1)}{(2l+1)(2l+3)}}Y_{l+1,m} - \sqrt{\frac{(l-m)(l-m+1)}{(2l-1)(2l+3)}}Y_{l-1,m} \\ \cos\theta Y_{lm} &= \sqrt{\frac{(l-m+1)(l+m+1)}{(2l+1)(2l+3)}}Y_{l+1,m} + \sqrt{\frac{(l+m)(l-m)}{(2l+1)(2l-1)}}Y_{l-1,m}. \end{aligned} \tag{2.209}$$

The importance of the gradient terms is that they allow one to probe the question of error cancellation.

For firm statistical analysis (eschewing any by-eye method), the *needlet* approach [231] is particularly suitable to decomposing a discontinuity into power. Alternatively, one might utilize an edge-detection mechanism such as the Canny algorithm [232, 233]. The Canny algorithm is an edge-detection method that proceeds by the following:

- Convolve the map with a Gaussian filter to reduce pixel-scale noise.
- Determine the gradient and directional derivatives of the map.
- Isolate local maxima in the gradient maps.
- Trace the edges using hysteresis thresholding.

For the Laplacian-difference method, one might ask whether the harmonic basis is the optimal comparison basis for performing the map differencing. A basis with better localization properties, like the needlet approach, might enhance the discontinuity power more effectively; by contrast, since there is a small trade-off with global properties it may be more difficult to detect a subtle discontinuity against a smooth background. In any case, the harmonic method is both quick and simple to implement, making it an excellent choice of basis with which to

get a handle on how the method performs in practice. Further, it should be noted that there may be correlations with the Stokes Q and U parameters at the anomaly boundary, since cosmic strings have a vector B-mode signal [234] in real space analogous to the Kaiser-Stebbins effect in the temperature case.

Behaviour of the Laplacian-Difference Maps

It is important to estimate the expected behaviour of the Laplacian-differenced maps. The full field being operated on (making no statements about underlying discontinuities) can be denoted as

$$F(\theta,\phi) = \tilde{F}_{\rm sh}(\theta,\phi) + \delta_{\rm sh}(\theta,\phi) = \tilde{F}_{\rm ip}(\theta,\phi) + \delta_{\rm ip}(\theta,\phi) \tag{2.210}$$

where $\tilde{F}$ denotes the spherical harmonic (sh) or interpolating polynomial (ip) reconstructions of the original data, and δ corresponds to the error in the reconstruction. By linearity, the field being calculated is

$$\nabla^{2n}\lambda(\theta,\phi) \equiv |\nabla^{2n}(\tilde{F}_{\rm sh}(\theta,\phi) - \tilde{F}_{\rm ip}(\theta,\phi))| = |\nabla^{2n}(\delta_{\rm ip}(\theta,\phi) - \delta_{\rm sh}(\theta,\phi))|. \tag{2.211}$$

Since the polynomials overshoot in the region of a discontinuity it can be stated that, in the coordinates $(\zeta_1,\zeta_2) \in (\theta,\phi)$ covering any discontinuity

$$\lambda(\zeta_1,\zeta_2) = \max[\lambda(\theta,\phi)]. \tag{2.212}$$

If λ is then separated into two regions

$$\lambda(\theta,\phi) = \lambda(\theta-\zeta_1,\phi-\zeta_2) + \lambda(\zeta_1,\zeta_2) \tag{2.213}$$

and defining the harmonic expansions

$$\begin{aligned} A_{lm} &= \int \lambda(\theta-\zeta_1,\phi-\zeta_2)Y^*_{lm}(\theta,\phi)d\Omega \\ B_{lm} &= \int \lambda(\zeta_1,\zeta_2)Y^*_{lm}(\theta,\phi)d\Omega, \end{aligned} \tag{2.214}$$

then since $\sum_m B_{lm} > \sum_m A_{lm}$ over some bandwidth $\beta \in l$ corresponding to the discontinuity scale, the n-Laplacian-difference maps correspond to

$$\nabla^{2n}\lambda(\theta,\phi) = \sum_{lm}(l^{2n}A_{lm} + l^{2n}B_{lm})Y_{lm}. \tag{2.215}$$

If λ increases with stencil size, then the power of B_{lm} in the bandwidth β will scale up accordingly, leaving a more prominent discontinuity signal. Secondly, as one moves up the n-Laplacia, the smaller scales will receive larger and larger boosts in power. This implies that there is a nearest-to-equilibrium n-Laplacian-difference map, wherein 'equilibrium' refers to equal real-space contributions from the n-Laplacian-difference maps of $\lambda(\theta - \zeta_1, \phi - \zeta_2)$ and $\lambda(\zeta_1, \zeta_2)$. Away from this value of n, the difference maps should yield either a more conspicuous dominance of the discontinuous region or a more conspicuous absence of the discontinuous region as one evaluates to more extremal values of n (toward 0 or ∞). A natural corollary of this is that the $n = 0$ calculation is special — not merely since for $n = 0$ one need not construct any derivatives at all, utilizing just the standard geometric array to reconstruct the map — but also since the original map as given can be taken as the comparison map, rather than using a reconstruction. In the limit of large n one also expects floating-point noise to begin to dominate. It will later be seen that performing derivatives on the HEALPix sphere yields a polar signal blow-up related to the existence of $\csc$-type terms in the Laplacian. In this case, the standard Laplacian minimizes that problem, since its terms have a maximum power of 2 in the $\csc$ terms.

2.5.2 Wavelet Types

Analysis of enhanced-discontinuity maps requires the use of methods which can highlight the discontinuity, such as the edge-detection methods of the Canny algorithm, or the localized-power decomposition typical of wavelet schemes. Wavelets are important tools for signal analysis; as an alternative, more localized, set of transforms to the standard harmonic transforms, they have found a range of applications for CMB data analyses. Wavelets allow for a mixture of the advantages of frequency-type analysis (isolated multipole behaviour) and the contrasted real-space issues (partial sky coverage). As yet, there is no widely agreed-upon standard or optimal wavelet basis for CMB analysis.

The wavelet transform decomposes a signal into combinations of scalings of a template (or 'Mother') wavelet ψ. In flat space, the wavelet transform $\mathcal{F}_w$ of a function F at a frequency ω is defined by the shift b and scaling a parameters

$$\mathcal{F}_w(a, b) = \frac{1}{\sqrt{a}} \int_{-\infty}^{\infty} F(x) \psi^* \left(\frac{x - b}{a} \right) dx \tag{2.216}$$

with an inverse procedure

$$F(x) = \int_0^\infty \int_{-\infty}^\infty \frac{\mathcal{F}_w(a,b)}{a^2} \frac{1}{\sqrt{|a|}} \psi\left(\frac{x-b}{a}\right) dbda. \tag{2.217}$$

For example, the Mexican hat wavelet is defined by [235]

$$\psi(x,R) = \frac{1}{\sqrt{2\pi}R}\left(2 - \frac{x^2}{R^2}\right) e^{-\frac{x^2}{2R^2}}. \tag{2.218}$$

Working on the sphere makes it necessary to use a spherical analogue, given by the more general wavelet transform

$$\mathcal{F}_w(R,b) = \int f(\Omega)\psi(R,b)d\Omega \tag{2.219}$$

where w is the wavelet coefficient associated to the scale R at the point with coordinates b. One can in fact go a step better in localization than the Mexican hat wavelet by using a wavelet type referred to as a needlet; the spin-weighted spherical needlets are given by

$${}_s\beta_{jk} = \int_{\mathbb{S}^2} {}_sF(\Omega)\,{}_s\psi^*_{jk}(\Omega)d\Omega \qquad {}_sF(\Omega) = \sum_{jk} {}_s\beta_{jk}\,{}_s\psi_{jk}(\Omega), \tag{2.220}$$

where the needlet function is defined for each pixel k in a map of resolution j by

$${}_s\psi_{jk}(\Omega) = \sqrt{\lambda_{jk}} \sum_l W\left[\frac{l}{B^j}\right] \sum_m {}_sY_{lm}(\Omega)\,{}_sY^*_{lm}(\zeta_{jk}), \tag{2.221}$$

where λ_{jk} is a weight term and the needlet coefficients are

$${}_s\beta_{jk} = \sqrt{\lambda_{jk}} \sum_l W\left[\frac{l}{B^j}\right] \sum_m {}_sa_{lm}\,{}_sY^*_{lm}(\zeta_{jk}) \tag{2.222}$$

with flexibility in the choice of the window function $W[x]$; by considering the wavelengths of interest, an appropriate choice of the frequency-band term B and resolution scaling j can produce an optimal shape for $W[x]$.
The transform rules are much the same as for the harmonics; for example, the rotation of these coefficients can be formulated — for spherical harmonics this is given by

$$\mathcal{R}(\delta\Omega)F(\Omega) = \sum_{lm} f_{lm} \sum_{m'} D^l_{m'm}(\delta\Omega)Y_{lm'}(\Omega) \tag{2.223}$$

where the $D^l_{m'm}$ is the Wigner D-function (the harmonic basis for rotations in SO(3)), whilst for the needlets this is

$$\mathcal{R}(\delta\Omega)F(\Omega) = \sum_{jk} \beta_{jk}\sqrt{\lambda_{jk}} \sum_{l} W\left[\frac{l}{B^j}\right] \sum_{mm'} D^l_{m'm}(\delta\Omega) a^F_{lm'}(\Omega) Y^*_{lm}(\zeta_{jk}). \quad (2.224)$$

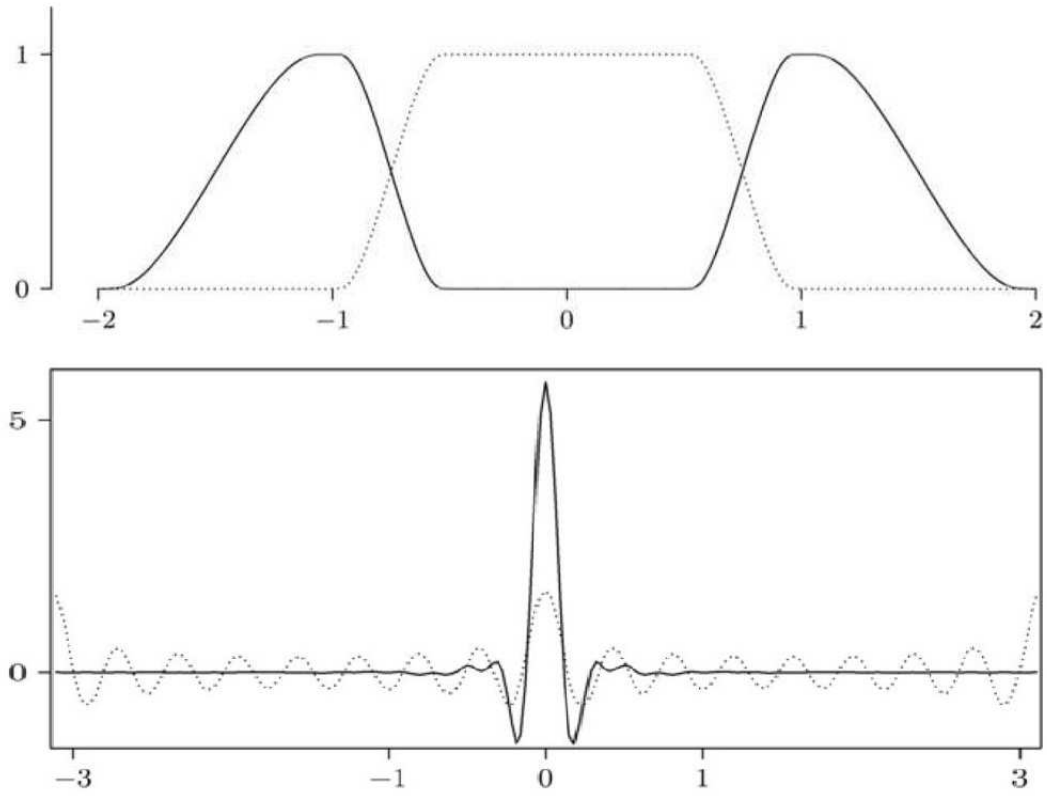

Figure 2.7: Construction functions (top diagram - the dotted line is ϕ and the thick line is W^2, for $B = 2$) and resulting needlets (bottom diagram - the dotted line is a Fourier wave for comparison of localization properties.), from Baldi et al [236]

A number of other interesting transforms such as ridgelets [237] and curvelets exist in the literature; these were developed specifically for dealing with smooth images with edges i.e., singularities along smooth curves. These retain the required localization properties of standard wavelets whilst incorporating direction-sensitivity. The transforms mentioned are then amongst the only widely used transforms, other than the harmonic transforms, in cosmology. However, one can of course construct a given transform for a given task. The needlet approach has a number of useful qualities [231] that single their use out for the purposes of this thesis:

- Not reliant on any plane wave approximations, unlike many wavelet trans-

forms on the sphere.

- Computationally convenient and can be incorporated easily into the HEALPix software package, which is used in the next chapter.
- The reconstruction formula in equation (2.220) is designed such that one need only compute the needlet function at each resolution once, with coefficients stored for later use.
- They are quasi-exponentially localized; this localization is described by

$$|\psi_{jk}(\hat{\gamma})| \leq \frac{c_k B^j}{(1 + B^j \arccos(\langle \hat{\gamma}, \zeta_{jk} \rangle)^k)}$$

  where c_k is a positive constant. Since $\arccos(\langle \hat{\gamma}, \zeta_{jk} \rangle)$ is the distance between two points on the sphere, it can be seen that for a fixed angular distance ψ goes to zero in the parameter B. The multipole support can be exactly calculated, allowing a decrease in computations.
- Random needlet coefficients are asymptotically uncorrelated.

The needlets shall be used in the discontinuity analysis due to their localization properties. The recipe in Marinucci [231] to construct the needlets (Fig. 2.7) is followed:

- Construct the function

$$f(t) = \begin{cases} \exp\left(-\frac{1}{1-t^2}\right) & -1 \leq t \leq 1 \\ 0 & \text{otherwise} \end{cases}$$

  which imports the quasi-exponentiality into the needlet structure.
- Then construct

$$\Psi(u) = \frac{\int_{-1}^{u} f(t)dt}{\int_{-1}^{1} f(t)dt}$$

  which is normalized such that $\Psi(-1) = 0$ and $\Psi(1) = 1$.
- Construct next the frequency-dependence:

$$\phi = \begin{cases} 1 & \text{if} \quad 0 \leq t \leq \frac{1}{B} \\ \Psi\left(1 - \frac{2B}{B-1}\left(1 - \frac{1}{B}\right)\right) & \text{if} \quad \frac{1}{B} \leq t \leq 1 \\ 0 & \text{if} \quad t > 1 \end{cases} .$$

- Finally, construct
$$W^2[\zeta] = \phi\left(\frac{\zeta}{B}\right) - \phi(\zeta)$$
yielding the window function of the transform.

The needlet basis is *not* orthonormal. However it is the next best thing, called a *tight frame*; a tight frame is a norm-preserving set of functions, i.e.,

$$\sum_j \langle f, e_j\rangle^2 \equiv \int_{\mathbb{S}^2} f(\hat{\gamma})^2 d\Omega \tag{2.225}$$

but does not qualify as a basis since there exist redundant elements within the set. How does this then affect the statistics of a needlet decomposition? Following Baldi et al [236, 238], one can analyse the needlet expansion of an isotropic field and prove that the needlet coefficients at any finite distance are asymptotically uncorrelated. By extension, one can construct a central limit theorem for needlet statistics — this is absolutely vital if one wishes to perform CMB analysis using needlets.
As previously mentioned, it might be wondered whether the needlet approach does not provide a better basis for comparison with the interpolation basis in the method of differencing Laplacian fields. After all, using wavelet-type approaches among others (i.e., Fejér summation, Riesz summation or via the Lanczos sigma factor) is one way of ameliorating the Gibbs' phenomenon. This is a valid proposal and it would be interesting to see how the statistics of such a field change compared to the harmonic approach, both local to the discontinuity and globally. In the present case the speed and general ease of utility of harmonic transforms demands their primacy.

2.6 A Finite-Resolution CMB?

This chapter ends with a speculative idea which seems like a natural extension to the defect-detection formalism: what if the CMB has a finite resolution? It appears that there is little literature on such a scenario, most likely because no non-contrived theory predicts such bizarre phenomenology. One can also imagine that, were any primordial, fundamental 'blockiness' to be imprinted in the CMB photons, it might very easily be washed out with further interactions en route to the observer. However, it is emphasized that this model provides a toy example of how one $might$ determine exotic CMB phenomena in real space. Ac-

tual real-space phenomena from, say, an underlying lattice spacetime blown-up by inflation would be model-dependent and may not result in this manifestation. The concept of finite resolutions certainly already exists as applied to spacetime in the context of quantum gravity, having arisen almost ubiquitously. Perhaps the earliest modern call for such quanta came from Pauli (1938, [239]) in correspondence with Heisenberg, despairing at the problem of regularizing QED — now known to be soluble using the path integral of Feynman, Tomonaga and Schwinger. This was followed by the program proposed by Regge [240] in an early attempt at numerical GR; by decomposing the metric into triangulations it was possible to perform calculations which evaded analytical approaches. This approach and the Cartan formalism of GR seeded the foundation for some of the modern attempts at a theory of quantum gravity. In modern terms, quanta of spacetime appear from various sources: the volume quanta in Loop Quantum Gravity [202], in the string uncertainty principle [241, 242], in noncommutative geometries [243, 244], in causal set universes [245] and even in deformed spacetime symmetries such as the κ-Minkowski space utilized in deformed special relativity [246]. In many, if not most, modern theoretical constructs the spacetime quanta are not of the rigid lattice sort; rather, they often arise from position uncertainty relations such as that from the work of Snyder [247], often calling into question whether the notion of spatial point has any operational meaning on such tiny scales. In the presence of an inflaton, it may be possible that quantum regions of spacetime are inflated to observable scales; certainly a generic phenomenon of altering the underlying spacetime is that the dispersion relations for particles is modified. Such trans-Planckian phenomena have been investigated along with the effect of an ultraviolet cut-off (defined by a lower bound in position uncertainty) in a number of papers [248, 249, 250, 251, 252].

Before speculations about potential real-space signals from a finite resolution CMB are made, a different example shall be explored for inspiration as to how the CMB can be affected by the phenomena of spacetime, from holographic considerations. The holographic principle [253, 254] defines a limit on the information content of spacetime regions; the number of fundamental degrees of freedom is related to the area of surfaces in spacetime. This information has been mentioned before, in the context of Bayesianism; it is no coincidence that Shannon information and physical (Boltzmann) information share the same nomenclature. The first suggestions of a holographic principle came from classical black hole entropy bounds. The following observations are due to the insights of Hawking, Bardeen, Bekenstein and others [255, 256]:

- The area theorem: *the area of a black hole event horizon never decreases with time* — analogous to the second law of standard thermodynamics

$$\frac{dA}{dt} \geq 0.$$

- The no-hair theorem:
  A full description of a stationary black hole can be arranged from its mass, angular momentum and electric charge.

In order to avoid breaking the second law of thermodynamics via the no-hair theorem, Bekenstein & Hawking were led to the Bekenstein entropy

$$S_{BH} \propto \frac{A}{4}, \qquad A = 16\pi M^2 \tag{2.226}$$

with a proposal that the second law of thermodynamics holds only for the full black hole-plus-matter system:

$$dS_{\text{total}} \geq 0. \tag{2.227}$$

The Hilbert space of a quantum-mechanical system is compatible with e^S independent states. In order to get a better understanding of black hole entropy one takes the analogy seriously, with a 'temperature' (the surface gravity κ) related to the thermal spectrum T of the particles 'emitted' by the black hole:

$$\kappa \propto \frac{dM}{dS_{BH}}. \tag{2.228}$$

In fact, this is an aspect of a more general phenomena whereby an accelerating observer experiences a shower of particles. More generally, in a d-dimensional spacetime the generalized second law implies that for any weakly gravitating system in an asymptotically flat space the inequality $S_{\text{matter}} \leq 2\pi ER$ holds, where E is the total mass-energy and R the circumferential radius of the system.
In order to make the full leap to holography, it is necessary to specify how many fundamental degrees of freedom a system may have. N is defined as the number of degrees of freedom in terms of the dimensions $\mathcal{N}$ of a Hilbert space $\mathcal{H}$

$$N = \ln \mathcal{N} = \ln \dim \mathcal{H}. \tag{2.229}$$

This is equal to the number of bits of information (number of spins) required to describe a state. Now recall that the Planck scale imposes an observational cut-off

point when probing regions of a certain scale:

$$l_{\rm Pl} = \sqrt{\frac{\hbar G}{c^3}} \qquad t_{\rm Pl} = \frac{l_{\rm Pl}}{c}. \tag{2.230}$$

Naively, discretizing space into a Planck grid with one oscillator per Planck region yields a discrete, bounded-from-below oscillator spectrum, giving

$$N \sim V \ln n \geq V \tag{2.231}$$

where V is the number of oscillators and n the number of states per oscillator. This contrasts with the $N = A/4$ result from field theory; the field theory approach fails because it discounts gravity. To generalize further, one must use the *covariant entropy bound*: The entropy of any light-sheet of a surface B will not exceed the area of B

$$S[L(B)] \leq \frac{A(B)}{4}. \tag{2.232}$$

Since a black hole is the highest entropy state attainable by any mass-energy, there is an absolute entropy bound for a region. Following the lead from information theory, entropy is a direct measure of information

$$S_{\rm Boltzmann} = -k \sum_i p_i \ln p_i \qquad S_{\rm Shannon} = -\sum_i p_i \ln p_i \tag{2.233}$$

where p_i is the probability of the microstate i in an equilibrium ensemble or the probability of the message i taken from the message space, respectively. Thus, as the degrees of freedom of a particle are the product of all the degrees of freedom of its sub-particles, then a maximal volume implies a minimal unit of information. For the cosmos, it can be shown [257] that the observable entropy bound is $S_{\rm max} = 3\pi/\Lambda$. Specifically, since inflation is equivalent to a de Sitter space, one gains a bound on the observable entropy of all quantum fields during inflation: $S_{\rm max} = \pi/H^2$, yielding $\pi \ln(2/H^2)$ binary spins. One is reminded that a detection of B-modes will set a direct limit on the value of H during inflation. More generally, this apparent holography has roots in the AdS/CFT correspondence — an insight which has had substantial influence on the direction of research within M-theory — which conjectures that a string theory with gravity defined in an anti-deSitter space can be described completely by the conformal field theory living on its boundary.

From Hogan's analysis [258], working in Euclidean space, it can be shown that a

correlation

$$f(y) = \langle \Psi(x)\Psi^*(x+y)\rangle_x = \int e^{-iky}\Psi_k\Psi_k^* dk \tag{2.234}$$

when spatially bounded implies a discrete spectrum

$$f(y) = \sum_{n=1}^{N} e^{-k_n y} f_{k_n} \tag{2.235}$$

in just the same sense that bound quantum mechanical states have a discrete energy spectrum. By continuation of this line of thought, modes frozen into the CMB should, by virtue of the horizon-scale correlation cut-off, exhibit a discrete spectrum. This is used to derive a bound on the information density

$$\mathcal{I} = \frac{9}{16\pi}\mathcal{F}M_{\rm Pl}^2 H^{-2}. \tag{2.236}$$

In Hogan's words, "there are absolute limits on how many different things can happen within the confines of any given region". In reality, horizon scale modes would be unlikely to carry anything other than a fraction of the information bound. Hogan [259] continues to set up a simplistic toy model for this effect, but then illustrates the observability of discreteness by interchanging discreteness in spectra for discreteness in pixellization. This is taken as a cue to look at potential signals for any such discrete spacetime. This can be naively considered from two angles: an information bound per area, with the area presumably bounded by the Planck scale; and Planck scale spacetime lattices, leading to the question: given that inflation expands regions by 10s of orders of magnitude, what observable consequences does an inherently pixellated CMB sky have?

Specifically, one may be able to take advantage of spherical pixelization schemes and the discontinuity-exposing method previously proposed to produce a simple and naive model of a finite-resolution CMB, wherein upgrading the resolution of such a map should lead to more obvious discontinuities. As previously stated, even if in reality the CMB contrived to have a fundamental blockiness at last-scattering, such a feature would be smeared out by the optical and acoustic effects at last-scattering, and by further interactions en route to the observer. Nonetheless, in order to make such a unusual detection one would want to cross-correlate results of the discontinuity-detecting software with the power spectrum. The reason being that whilst the signal for fundamental blockiness would be characteristic, it might not be so very different from that of an underlying string network. Further, whilst one would expect a drop to zero in power beneath the Nyquist

scale for the map, this could be confused with other contrived cosmological models. A combination of the two observations would be compelling evidence for blockiness in the CMB, since this would remove the degeneracies with strings and other non-blocky CMB physics. A positive detection of such a strange scenario would provide a challenging departure from the predictions of continuum field theory.

2.7 Summary

Cosmological data analyses occur within one of two paradigms — either the frequentist or the Bayesian approaches to statistics. While the Bayesian approach is fully rigorous, it can be computationally expensive. These analyses are usually considered only in harmonic-space, which requires global sampling for its full effectiveness, as opposed to local real-space approaches. CMB polarization analyses suffer from mixing between E- and B-modes due to obscuration by foregrounds, which can be dealt with by reparameterizing in terms of scalar field analogues of the E- and B-modes, constructed by performing derivative operations on the Stokes polarization data. The method used in this thesis for performing such operations is the finite-difference method, which samples locally.

One quick frequentist approach to measuring cosmological parameters is in the use of estimators. It is possible to construct mode-transfer arrays which describe the relation between the observed and the theoretical power spectrum in the mean. The advantage of utilizing scalar field analogues is that the transfer tensors for the self-coupled and cross-coupled spectra n-point spectra then all correspond to those of the temperature anisotropy spectra, which is considerably easier to compute when compared to the transfer tensors of direct E- and B-coupled spectra. Since the n-point spectra are related to the standard f_{NL}-type parameters which describe non-Gaussianity, the scalar field approach is useful following calculating non-Gaussianity in the polarization of the CMB.

The use of local methods can also be combined with harmonic methods in order to detect unusual signals, such as the discontinuous effects from the presence of cosmic strings from spontaneous symmetry-breaking or more unusual possibilities such as a finite-resolution sky. The Laplacian-difference technique constructed for this purpose had the novelty of utilizing errors in the finite-difference methodology in order to reveal any such signal.

Chapter 3

MasQU - Masked Stokes Q, U Analysis

The previous chapter saw the development of techniques that will be used to resolve the CMB polarization modes, amongst other CMB problems. These techniques were based on the utility of local methods such as the finite-difference scheme for calculating derivatives on a pixellated grid and the needlet decomposition for quantifying localized power. In the current chapter, the technical implementation of the finite-differencing algorithm on the popular HEALPix sphere is described — this is not without its own problems, as will be seen. The developments of the LR, QU and SVD decompositions can be found in standard textbooks on numerical methods [174, 260].

3.1 HEALPix

HEALPix [261], a *Hierarchical Equal Area isoLatitude Pixelisation* scheme for the sphere, is the most widely used software for construction and analysis of full-sky CMB maps. The lowest-resolution partitioning is into 12 equal area pixels. Each pixel is assigned a unique identification number (in either a 'nested' or 'ringed' numbering scheme — suited for nearest-neighbours searches and fast Fourier transforms respectively), and is surrounded by 8 other pixels, except in the polar cap where some of the pixels are surrounded by 6 or 7. Details can be found on the HEALPix website[1]. The map resolution is specified by the parameter

$$N_{\rm side} = 2^{N_{\rm order}} \qquad N_{\rm order} \in |\mathbb{Z}| \tag{3.1}$$

[1] `http://healpix.jpl.nasa.gov/index.shtml`

with each map of $12N_{\rm side}^2$ pixels composed of $4N_{\rm side}-1$ isolatitude rings; at each level higher in resolution, the pixels are subdivided into 4 equal area pixels in the higher-resolution map. The rings immediately by either pole consist of 4 pixels (independent of resolution), increasing by 4 pixels per ring for each ring increment toward the equator, up to a maximum $4N_{\rm side}$ pixels in the equatorial rings.

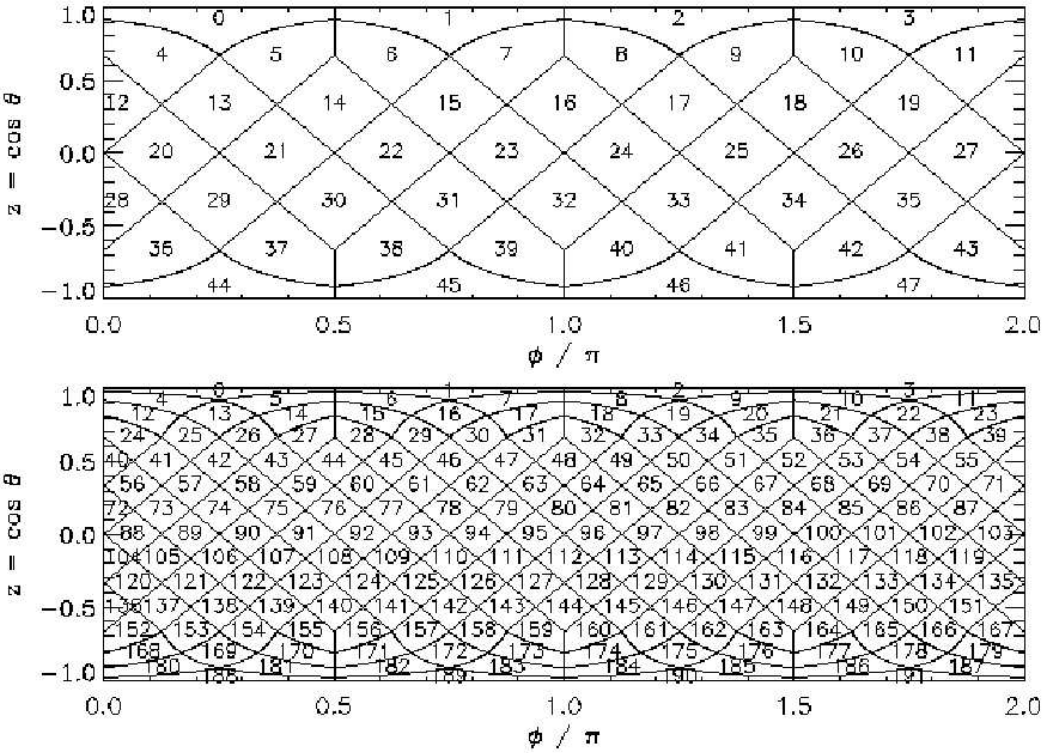

Figure 3.1: The Healpix sphere and pixel numbering in the ringed scheme, from Gorski et al [262]. The top diagram is an $N_{\rm side}=2$ resolution grid, while the bottom diagram has $N_{\rm side}=4$. The nested scheme at $N_{\rm side}=2$ splits each of the 12 lowest-resolution ($N_{\rm side}=1$) regions r into numberings $4r+{\rm pix}$, where ${\rm pix}\in[0,3]$ is the integer pixel number within the region. This procedure repeats iteratively on each pixel for higher resolutions.

The structure of HEALPix is designed to facilitate the quick calculation of methods such as spherical convolution, harmonic and wavelet analysis, computing Minkowski functionals and so on; the pixels follow a hierarchical quadratic pixel numbering (see Fig. 3.1), hence many functional properties are computed at an optimal RAM cost; this is important when dealing with large datasets, and the scalability of this set-up allows for quick map recalibration at different resolutions. Secondly, the grid is split into pixels of equal area hence white noise from the signal receiver does not receive a bias in pixel space. Finally, the iso-latitudinal

property of pixel rings allows quick computation of the likes of fast Fourier transforms (FFTs) and Legendre polynomials. The HEALPix structure is unique in offering all these facilities in one package; it has now appeared to have fought off competition from such alternatives as QuadCube [263] and GLESP [264], which can only offer a selection of the scaling and computation properties inherent in the grid geometry.
It will be useful to describe some of the utilities provided by HEALPix:

- The $anafast$ subroutine calculates power spectra from input temperature and polarization maps.
- $synfast$ is the inverse of $anafast$, synthesizing CMB maps from input spectra or harmonic coefficients.
- $alteralm$ rotates the input harmonic coefficients or deconvolves a specified beam window function from the same coefficients.
- $smoothing$ convolves the input map with a Gaussian beam.
- $udgrade$ upgrades or downgrades the resolution of a HEALPix map, averaging the higher-resolution pixel values in the process of downgrading.

The lowest-order estimator for the power spectrum calculated via the *anafast* subroutine is

$$\hat{C}_l = \frac{1}{2l+1}\left(\hat{a}_{l0} + 2\sum_{m=1}^{l}|\hat{a}_{lm}|^2\right), \tag{3.2}$$

where the harmonic coefficients can be computed from

$$\hat{a}_{lm} = \frac{4\pi}{N_{\rm pix}}\sum_{i=0}^{N_{\rm pix}-1} Y^*_{lm}(\Omega_i)F(\Omega_i), \qquad {}_{\pm2}\hat{a}_{lm} = \frac{4\pi}{N_{\rm pix}}\sum_{i=0}^{N_{\rm pix}-1} {}_{\pm2}Y^*_{lm}(\Omega_i){}_{\pm2}F(\Omega_i) \tag{3.3}$$

due to the equal-area pixellization of the HEALPix grid. The calculation of the E and B harmonics is then performed by summing the spin-weight $s = \pm2$ harmonics in the manner described in section 2.2. For the Stokes parameters, the

synfast subroutine calculates

$$\begin{aligned} T &= \mathrm{Re}\left[\sum_{lm} a^T_{lm} Y_{lm}\right] \\ Q &= \mathrm{Re}\left[-\sum_{lm} a^E_{lm} X_{1,lm} + i a^B_{lm} X_{2,lm}\right] \\ U &= \mathrm{Re}\left[-\sum_{lm} a^B_{lm} X_{1,lm} - i a^E_{lm} X_{2,lm}\right] \end{aligned} \tag{3.4}$$

where $m \geq 0$ and

$$\begin{aligned} X_{1,lm} &= \sqrt{\frac{2l+1}{4\pi}} F_{1,lm}(\theta) e^{im\phi} \\ X_{2,lm} &= \sqrt{\frac{2l+1}{4\pi}} F_{2,lm}(\theta) e^{im\phi} \\ F_{1,lm} &= N_{lm}[-((l-m^2)\csc^2\theta + \frac{l(l-1)}{2}) P_{lm}(\cos\theta) \\ &\quad + (l+m)\cos\theta \csc^2\theta P_{l-1,m}(\cos\theta)] \\ F_{2,lm} &= N_{lm} m \csc^2\theta \\ &\quad \times[-(l-1)\cos\theta P_{lm}(\cos\theta) + (l+m) P_{l-1,m}(\cos\theta)] \end{aligned} \tag{3.5}$$

with $N_{lm} = 2\sqrt{(l-2)!(l-m)!/[(l+2)!(l+m)!]}$.

3.2 Differencing on the HEALPix Sphere

The HEALPix sphere is an interesting case study, since it is a semi-regular distribution on a coordinate system with a pathology: the multi-valuedness of ϕ at the poles — hence differences in (θ, ϕ) across the pole are ill-defined. It does not matter if the pole point itself is not directly sampled — merely crossing the pole with a differencing stencil is enough to complicate the calculations, since the interpolating polynomial covers the whole region. Similarly, one must be careful at the $\phi = 0/2\pi$ boundary. However, at such a boundary here one can simply reassign the differences to the smallest of the two possible paths across the sphere between the points that are being differenced.

To test the software, the derivatives of harmonic functions on the sphere are computed, since primordial cosmological point signals are not expected. This implementation uses LAPACK [265] at double precision and the truncated SVD technique [174] for ill-conditioned matrices (in the limit of large stencils and irregu-

lar geometries). The geometry for each pixel stencil taken is given by a square-geometry differenced geometric array

$$V = \begin{pmatrix} 1 & \cdots & \cdots & 1 \\ \Delta x_1 & \cdots & \cdots & \Delta x_n \\ \Delta y_1 & \cdots & \cdots & \Delta y_n \\ \Delta x_1 \Delta y_1 & \cdots & \cdots & \Delta x_n \Delta y_n \\ \vdots & \cdots & \cdots & \vdots \\ \Delta x_1^{n-1} \Delta y_1^{n-1} & \cdots & \cdots & \Delta x_n^{n-1} \Delta y_n^{n-1} \end{pmatrix}, \tag{3.6}$$

where the (θ, ϕ) basis has been chosen to work in for computational convenience (one does not expect the Stokes fields to necessarily be a polynomial in this basis). This choice is determined by issues arising from analysis at the pole; whilst the analytic operators are necessarily covariant, discretization complicates matters at the pole. Consider a function $f(\theta, \phi)$ which is smooth in (θ, ϕ); at the pole there is a coordinate singularity in (θ, ϕ), forbidding the use of finite differences in this region. A change to Cartesian coordinates (x, y) would swallow the coordinate pathology; however it can be shown that $g(x, y)$, the Cartesian-space description of $f(\theta, \phi)$, will exhibit a functional pathology at the origin (i.e., $g(0, 0)$ may be a delta function or similar). This phenomenon is general for coordinate transforms which remove the polar coordinate singularity. Since the function is being approximated with a polynomial, any functional discontinuity or pathology will be poorly modelled by such a finite-difference scheme. The utilized alternative is choosing the pixel stencils in (θ, ϕ) such that they do not cross the pole at all, but instead progress toward an outer-difference scheme around the pole.
In the particular case of extracting E and B-modes, the pole also presents other numerical problems; one way to deal with these problems is by 'rotated oversampling' around the pole. This will be discussed briefly after the next subsection.

3.2.1 Structure of the Algorithm

The algorithm is as follows (see Fig. 3.2 for some visual examples):

- Construct an approximately square stencil of nearest-neighbour pixels, one for each pixel. This is achieved by taking the unique set of nearest neighbour pixels for the focal pixel, and then repeating recursively for the neighbour pixels until the specified stencil radius is satisfied. If the array cannot be filled with corresponding pixel numbers (such as in the case that a

pixel has less than 8 neighbouring pixel), then the remaining elements are assigned an identification value of -1. Note that since the HEALPix nearest-neighbours-finding routine always calls the neighbour pixels in the same geographic order, then pixels with identical surrounding geometries will necessarily have identical stencil arrays. In other words, the code is structured in such a way that the symmetries of the HEALPix grid are preserved also in the stack of pixel stencils taken. The notation for the stencils is as follows: a stencil of order O_n contains at most (existence and masking pending) precisely $(n+1)^2$ pixels. Since it is desirable to bias toward central differences, each n is even, corresponding to a radius of $n/2$ pixels about the central focus pixel. The stencil order n is initially the same for all pixels.

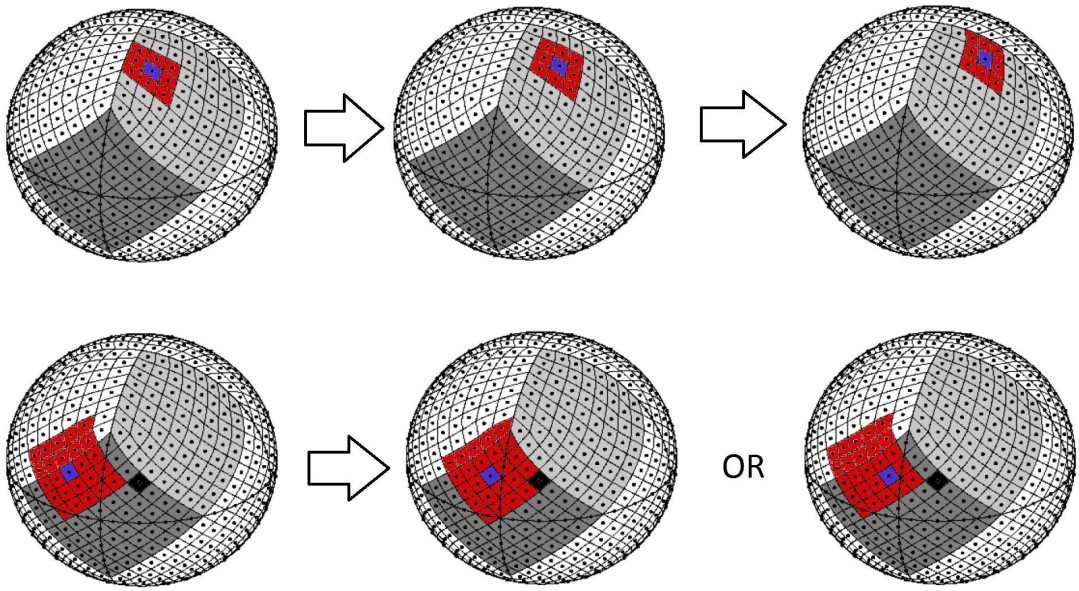

Figure 3.2: Standard sampling method, across orders, across the sphere. Top row: iteration of the O_2 calculation across a ring on the maskless sphere. The coloured pixels populate the pixel stencil whose geometry is used in calculating the pixel weights, which are used for approximating the value of a derivative at the blue focal pixel. Bottom row: for a sphere with a masked pixel (in black), an example is made of the O_4 calculation. The left diagram shows the scheme when the masked pixel is not within the pixel stencil. The centre and right diagrams are central and outer-difference schemes; the outer-differenced scheme contains more information than the central-differenced scheme in the case shown.

- Perform 're-mapping' for pixels p_i surrounded by one or more masked pixels — search amongst the stencils of the surrounding pixels p_j for the 'optimum' stencil (the stencil with the most available pixels and closest to the

central focus). A weight system of

$$W = \begin{cases} 0 & \text{Pixel is missing or in a cut region} \\ 1 & \text{Otherwise} \end{cases}$$

is applied. Pixels without enough information in their stencil to perform the requisite derivatives (three available pixels with a unique position θ, and the same for ϕ) are discarded.

- Analyse the mapped difference geometries to single out a smaller number of unique stencil geometries — these characterize a unique set of stencils which provide all the necessary weights for calculation across the sphere, saving computation time. In the unmasked case, there are also symmetries between the north and south polar regions and also the quarters of each hemisphere which can be taken advantage of to cut down computation time.

- Find solutions to the linear equation

$$v'w = \delta, \tag{3.7}$$

whose 1d analogue is equation (2.92), corresponding to each of the derivatives required — each set of weights is unique for a given stencil geometry and derivative order (except in trivial cases). The geometric array is by default that for a regular square array. In the case that there is not a full square stencil available, rows (starting from the lowest row/largest difference powers) and the corresponding columns of the geometric array are removed such that the array remains square. It is probably more rigorous to remove rows using geometric considerations instead (i.e., an analysis of which derivatives can be calculated from the stencil), but this has yet to be implemented and does not significantly affect the rest of the analysis since only the derivatives up to second order in (θ, ϕ) are calculated. Furthermore, the additional time cost for such a procedure might not be a good trade-off. Solutions to the linear equations are found using LAPACK and, depending on how deformed the stencil is, the QR decomposition or SVD technique, depending on the pixel sample.

- Repeat until all the calculations are finished and form the bi-Laplacians. Compute the power spectra of the corresponding $\nabla^4 e$ and $\nabla^4 b$ maps and remove the power contributed by the bi-Laplacian operator.

- In the presence of a mask, one should apodize the signal since masking redistributes signal power. An apodization subroutine is available with the software, whilst there is an optimal method for CMB studies due to Smith & Zaldarriaga [217].

- Output the derivative maps, the power spectra, and the weights used (these can be recycled once calculated for the first time) in FITS format.

The above methods are very easily tweaked in the software for a given geometric scheme (be it for alternative pixellization scheme on $\mathbb{S}^2$ such as GLESP, or non-spherical schemes) and a given desired derivative. Higher-dimensional generalizations have not been implemented but would be trivial. Testing the software for accuracy follows the process of taking pre-specified E- and B-mode harmonic coefficients, calculating the full-sky Q and U maps from these coefficients, operating on the sky maps to produce the bi-Laplacians, and then converting the power spectra of the $\nabla^4 e$ and $\nabla^4 b$ fields to that of the E- and B-modes for comparison with the original input spectra:

$$a_{lm}^{E,B} \rightarrow C_l^{E,B} \rightarrow Q, U \overset{\partial Q, \partial U}{\rightarrow} \nabla^4 e, \nabla^4 b \rightarrow C_l^{E,B}$$

where the full scalar field maps $\nabla^4 e$, $\nabla^4 b$ are also compared, using the sum of the original harmonic coefficients as in equation (2.29). The results of this testing will be discussed after some further discussion of the techniques used for calculation. Some further subroutines have also been left in the software package for their usefulness: a number of quadrature schemes of varying accuracy and time-complexity; a subroutine for constructing larger stencils than the base specification, in a given region (such as the spherical pole); a RAM-economising mode (although this increases the time complexity of each run); test modes (for comparing numerical and analytic results); pixel ring removal pre- or post-calculation (this is specific to the spherical pole problem discussed later). The inverse (integration) calculation using the weights found has not been implemented, but only requires inverting a sparse matrix.

Methods for Matrix Equations

For standard regular-geometry and low order calculations one might choose a decomposition of the type LU or QR. The former decomposes a matrix A into

$$A = \Lambda \Upsilon \tag{3.8}$$

where Λ is a lower triangular matrix and Υ an upper triangular matrix:

$$\begin{pmatrix} A_{11} & A_{12} & A_{13} & \dots \\ A_{21} & A_{22} & A_{23} & \dots \\ A_{31} & A_{32} & A_{33} & \dots \\ \vdots & \vdots & \vdots & \ddots \end{pmatrix} = \begin{pmatrix} \Lambda_{11} & 0 & 0 & \dots \\ \Lambda_{21} & \Lambda_{22} & 0 & \dots \\ \Lambda_{31} & \Lambda_{32} & \Lambda_{33} & \dots \\ \vdots & \vdots & \vdots & \ddots \end{pmatrix} \begin{pmatrix} \Upsilon_{11} & \Upsilon_{12} & \Upsilon_{13} & \dots \\ 0 & \Upsilon_{22} & \Upsilon_{23} & \dots \\ 0 & 0 & \Upsilon_{33} & \dots \\ \vdots & \vdots & \vdots & \ddots \end{pmatrix} \tag{3.9}$$

thus the linear equation $Ax = b$ becomes

$$Ax = (\Lambda\Upsilon)x = \Lambda(\Upsilon x) = b \tag{3.10}$$

where one calculates

$$\Lambda y = b, \qquad \Upsilon x = y \tag{3.11}$$

using forward substitution as follows:

$$y_1 = \frac{b_1}{\Lambda_{11}}, \qquad y_i = \frac{1}{\Lambda_{ii}} \left[b_i - \sum_{j=1}^{i} \Lambda_{ij} y_j \right] \tag{3.12}$$

and then backsubstitution,

$$x_n = \frac{y_n}{\Upsilon_{nn}}, \qquad x_i = \frac{1}{\Upsilon_{ii}} \left[y_i - \sum_{j=i}^{n} \Upsilon_{ij} x_j \right]. \tag{3.13}$$

This has a computation time of order $\sim \mathcal{O}(n^3/6)$ compared with $\sim \mathcal{O}(n^3/2)$ for elimination methods; for a given matrix one needs only decompose once, store the Λ and Υ elements, and then apply to a given vector b.
In order to generate the triangular matrices, one can write out the components i, j of A in terms of a summation

$$\text{For} \quad \begin{cases} i < j: & \Lambda_{i1}\Upsilon_{1j} + \cdots \Lambda_{ii}\Upsilon_{ij} = A_{ij} \\ i = j: & \Lambda_{i1}\Upsilon_{1j} + \cdots \Lambda_{ii}\Upsilon_{jj} = A_{ij} \\ i > j: & \Lambda_{i1}\Upsilon_{1j} + \cdots \Lambda_{ij}\Upsilon_{jj} = A_{ij} \end{cases} \tag{3.14}$$

normalized by $\Lambda_{ii} = 1$. The coefficients are then solved for using Crout's algorithm:

- Iterating over i, set $\Lambda_{ii} = 1$.

- Iterating over j and then i, solve for Υ_{ij}:

$$\Upsilon_{ij} = A_{ij} - \sum_{k=1}^{i} \Lambda_{ik}\Upsilon_{kj}$$

and then solve for Λ_{ij}:

$$\Lambda_{ij} = \frac{1}{\Upsilon_{ij}}\left(A_{ij} - \sum_{k=1}^{j} \Lambda_{ik}\Upsilon_{kj}\right).$$

For stability, partial pivoting — the interchange of rows (this amounts to a decomposition of a permutation of A rather than the original LU) — is often required. One can also construct the determinant of a matrix by the product

$$\text{Det}[A] = \prod_{j=1}^{n} \Upsilon_{jj}. \tag{3.15}$$

The other standard decomposition method for solving systems of linear equations is the QR decomposition

$$A = QR \tag{3.16}$$

where R is an upper triangular matrix, while Q is instead an orthogonal matrix ($Q^TQ = 1$). In order to solve the linear system $Ax = b$, one solves instead

$$Rx = Q^Tb \tag{3.17}$$

by backsubstitution. The computation requires iterating the sum of the inner product

$$u_k = \sum_{j=1}^{k-1} \frac{\langle \mathbf{e}_j \mathbf{a}_k \rangle}{\langle \mathbf{e}_j \mathbf{e}_j \rangle}, \qquad \mathbf{e}_k = \frac{\mathbf{u}_k}{|\mathbf{u}_k|} \tag{3.18}$$

where the vectors $\mathbf{a}$ are columns of the matrix A, yielding for Q and R

$$Q_{ij} = \mathbf{e}_{ij}, \qquad R_{ij} = \langle \mathbf{e}_i \mathbf{a}_j \rangle \, \delta_{i \le j}. \tag{3.19}$$

This method is approximately twice as computationally expensive as the LU decomposition, but is of greater utility in certain situations — such as when solving a succession of linear systems where each system differs only slightly from its predecessor. In the QR method, one can then easily update the matrix factorization in $O(n^2)$ operations in order to solve the next linear system, unlike the LU

case wherein complications in updating arise from pivoting.
When solving problematic linear equations, the Singular Value Decomposition (SVD) is often useful. The SVD technique separates a matrix A into

$$A = \alpha^{\dagger}\Sigma\beta \tag{3.20}$$

(where Σ is the diagonal array of singular values and α and β are unitary matrices consisting of basis vectors) and is known for yielding optimal linear solutions in the presence of near-singular matrices; by calculating the pseudo-inverse of A one yields the least-squares solution (i.e., with minimized norm $||Ax - b||$) in the absence of a unique solution to the linear system involving A. Near-singular arrays can be diagnosed by use of a *condition number* $||A||||A^{+}||$ calculated from the product of the norms of A and A^{+}, where A^{+} is the pseudo-inverse of A. A large condition number implies that round-off error will cause large fluctuations in the solution to the linear equation.
The efficacy of the SVD technique is related to the fact that it provides a representation of the range (the set of all linear combinations of columns) and null space (the set of all vectors which satisfy the condition $Ax = 0$) of A. In the near-singular case, the smaller singular values can be dominated by round-off error leading to dramatic errors in the solution. For large geometric arrays, the bottom-row elements are most likely to suffer from round-off error since they are large powers of small numbers. This means the singular value array must be truncated below some numerical threshold in order to yield reasonable numerical results, equivalent to calculating an effective rank for A, achieved by replacing the corresponding inverted elements in the inverted singular value array with zero; truncation error will contribute to any inaccuracy of the calculation. If A is a square matrix, the singular values are related to the eigenvalues of the matrix by

$$A^{*}A = V(\Sigma^{*}\Sigma)V^{*}, \qquad AA^{*} = U(\Sigma\Sigma^{*})U^{*}, \tag{3.21}$$

implying that the singular array has in fact a left- and right-inverse.
Since the different resolutions correspond to a mere scaling of geometries on the HEALPix sphere, the truncation threshold should be defined by the ratio Σ_{ii}/Σ_{11}. Below this truncation threshold one discards the degenerate solutions, potentially losing information. However, most of the information (i.e., the best-determined/most influential) is retained in the first diagonal elements of the decomposition, minimizing information loss through truncation. Figure 3.3 shows the implementation of the SVD technique on the HEALPix sphere.

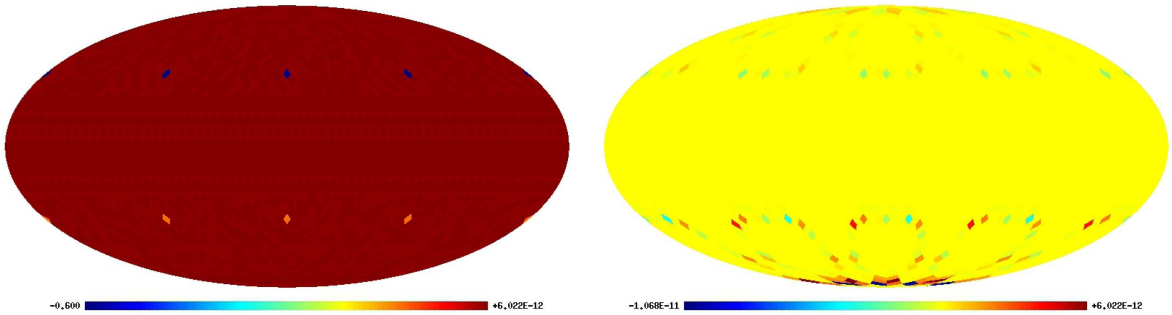

Figure 3.3: O_6 bi-Laplacian of an $N_{\rm side} = 16$ test harmonic function generated from $a^E_{lm} = \delta_{l2}\delta_{m0}$, $a^B_{lm} = 0$ for the raw inversion of the geometric array (left diagram) and SVD-calculated (pseudo-) inversion of the geometric array (right diagram). The large error values in the raw map coincide with the most irregular stencil geometry on the HEALPix sphere.

Optimal truncation may depend on some non-machine aspects: array size and geometry. Whilst this problem has not been solved generally, empirically-derived truncation thresholds for the unmasked sphere as-a-whole (i.e., individual stencil geometries have not been studied) which maximize the accuracy of the calculations have been implemented for the first few stencil sizes. Masking has not been fully SVD-optimised (the same thresholds are used as for unmasked maps) since this study requires generalization of the thresholds to any number of pixels in a range of distributions. Some limited analysis of the error properties in the SVD technique can be found in Wedin et al [266].

Performance Considerations

For performance considerations beside the question of accuracy, it is necessary to consider time complexity. While it can be seen that a first-time implementation of the code is out-performed by the standard HEALPix methods in terms of speed, one need calculate the weights only once. Web resources for calculated weights across a range of resolutions, geometries and masks would not be difficult to maintain. For a survey like *Planck*, with up to 5×10^7 pixels per map, the maximum HEALPix resolution is $N_{\rm side} = 2048$. For the corresponding O_2 calculation, an interpolating function is used to extrapolate a timescale of 1440 seconds on a low-end machine (Fig. 3.4). Further reductions in time complexity could be achieved by an implementation of the MPI (Message Passing Interface) procedure for parallel computations.

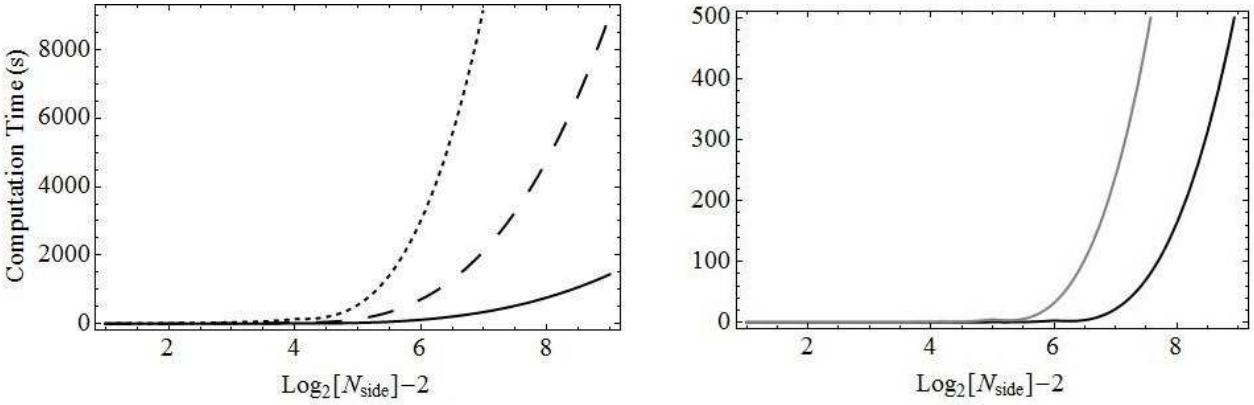

Figure 3.4: Left diagram: Time complexity for a maskless calculation across $N_{\rm side}$. The diagram key is (O_2, O_4, O_6) = (thick line, long-dashed line, short-dashed line). Due to RAM limitations interpolation and extrapolation are used for the *Planck* resolution timescale, $t_{O_2,\rm Planck} = 1440$ s, $t_{O_4,\rm Planck} = 9024$ s, $t_{O_6,\rm Planck} = 39946$ s. Masked calculations are only very marginally slower (and the time costs display some small mask-dependency). Right diagram: By comparison, HEALPix calculations with default parameters. The black line is the zeroth order calculation, with the grey line for 4 iterations of the $map2alm$ subroutine. For a *Planck* resolution map the timescales are 534.7 s and 1823.36 s respectively.

Finally, one might wonder what the effect of scaling the input map by some order of magnitude has on the computations; at a certain scaling of the pixel values for a given map the results might be effected by numerical fluctuations in the underlying computations. As an example, the difference between the $\nabla^4 b$-field calculated from a CMBFAST simulation (Tensorless, $N_{\rm side} = 128$, with Q and U maps defined on a K scale) and scaled up by 10^6 to match a comparison map — the $\nabla^4 b$-field calculated from an identical CMBFAST simulation defined at the μK scale — is calculated. The resultant map of differences between the two $\nabla^4 b$-fields has fluctuations of order 10^{-11}, which is more than acceptable. However, for safety one would ideally calculate at the micro-Kelvin scale.

3.2.2 The 'Pole Problem' and Rotated Sampling

For polar pixels, the algorithm is amended as follows (Fig. 3.5):

- Define polar pixel 're-mappings': for each pole-crossing pixel (referred to as $p_{\rm pol}$), perform a search among its stencil pixels for the set of pixels whose stencils do not cross the pole. Then select from this set the subset of pixels that satisfies the requirements that minimize their distance on the sphere from $p_{\rm pol}$ in order that the new calculation scheme is as close to a central-

difference scheme as possible, and from this subset choose the pixel which is closest to the pole (referred to as $p_{\rm npol}$). The stencil of $p_{\rm pol}$ is then reassigned from a central-difference in the $p_{\rm pol}$ stencil basis to an outer-difference in the chosen $p_{\rm npol}$ basis.

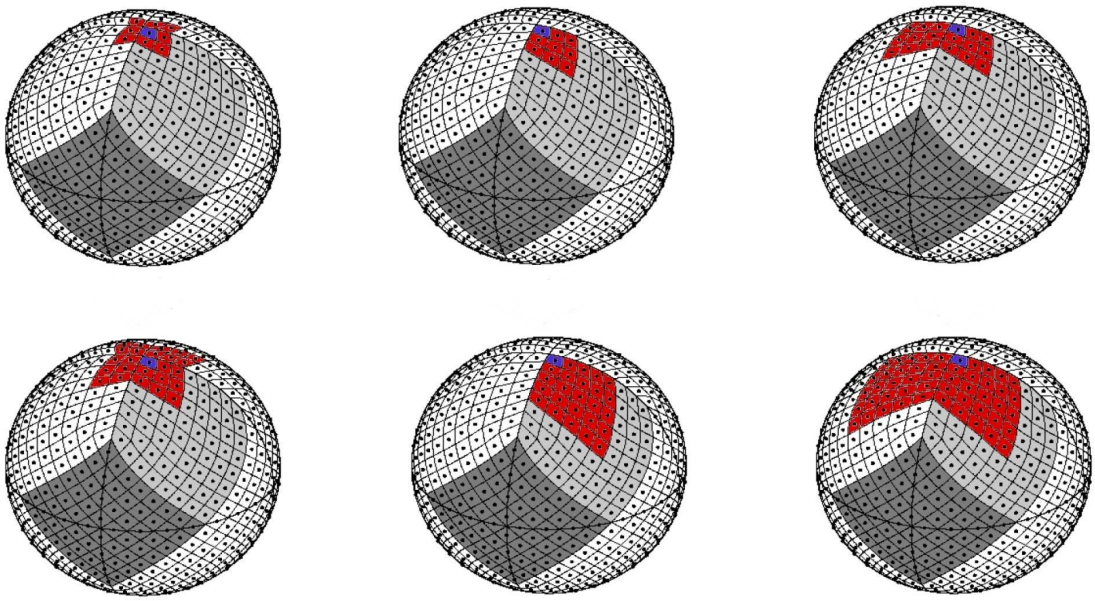

Figure 3.5: Various polar sampling methods. Left diagram: standard pole-crossing stencils. Middle: outer-differenced stencils. Right diagram: 'Doubled' sampling, equivalent to ϕ-rotated sampling with $\delta\phi = \pi/2$. The top and bottom rows correspond to O_2 and O_4 sampling respectively.

The full array of pole problems for schemes not crossing the pole are as follows. Firstly, it can be seen from the 1-dimensional tests (Fig. 2.3) that while the forward- and backward-difference schemes are of the same magnitude error as the central schemes, they generally perform slightly worse than the equivalent central-difference scheme. The same is true for comparisons of higher- to lower-order derivatives. This is because higher-order derivatives require more sampling pixels, and hence a larger basic stencil size, than lower orders. This can also be seen in the HEALPix scheme for derivatives of the $s = 0$ spherical harmonics (Fig. 3.6), where the accuracy of the software has been tested, hence the higher errors at the poles. This is referred to as 'outer-differencing' error.
Secondly, the $\Delta\phi$ values between sampled pixels increase toward the pole due to the lower pixel sampling per HEALPix ring toward the pole. At its most extreme, the pixel rings immediately surrounding either pole have only 4 pixels each, with a separation $\pi/2$. Since the errors in the differencing scheme depend on powers of $\Delta\phi$, then a lower accuracy is expected around the pole. This is referred to as

the 'polar $\Delta\phi$' problem. It is apparent in all cases that (i) second-order derivatives perform slightly worse than first-order derivatives; (ii) $\partial_{\theta\theta}$ performs worst. This is no surprise given that the polar cap pixels are only central in ϕ; (iii) large-magnitude functional variation in ϕ about the pole seems to correlate with large polar errors (Fig. 3.6).

A third, more drastic problem comes from the construction of the terms to be calculated. In the continuum limit, these are

$$\begin{aligned}\nabla^4 e &= -(-2 - \csc^2\theta\partial_{\phi\phi} + 3\cot\theta\partial_\theta + \partial_{\theta\theta})Q - 2\csc\theta(\cot\theta\partial_\phi + \partial_{\theta\phi})U \\ \nabla^4 b &= 2\csc\theta(\cot\theta\partial_\phi + \partial_{\theta\phi})Q - (-2 - \csc^2\theta\partial_{\phi\phi} + 3\cot\theta\partial_\theta + \partial_{\theta\theta})U.\end{aligned} \tag{3.22}$$

This is quite a delicate combination due to a number of $\csc\theta$ and $\cot\theta$ terms, which clearly blow up as the pole is approached. The contributor of the largest error is then the $\csc^2\theta\partial_{\phi\phi}$ term, which will blow up any errors in the discrete approximation to $\partial_{\phi\phi}$. This is referred to as the 'blow-up' problem, and accentuates the first two problems.

Taking derivatives using larger stencils is not always advantageous. Instead, a method for dealing with the pole is by rotated sampling; the sphere is rotated by some small amount $\delta\phi < \Delta\phi$ and derivatives calculated on a 'doubled' stencil. Figure 3.8 shows that the error is greatly reduced in this manner. There is though the caveat that it is necessary to sample the harmonic coefficients accurately in order to effectively remove the pole problem. The polar $\Delta\phi$ problem ensures that taking 'discrete' doubled sampling (calculating over a stencil which includes the next-neighbour-in-ϕ's stencil) is not nearly effective enough. Of course, for the rotated sampling case one can always perform the rotation more than once in order to improve the accuracy. In the case of discrete doubling, one is limited to using $N_{\mathrm{pix-in-ring}}/2$ adjacent stencils, so as not to have a pole-crossing calculation.

The combination of these polar effects leads to dramatic problems at the pole for realistic (CMBFAST-generated, see Table 3.1 for maps used) sky maps: in Fig. 3.9 the operation on realistic B-mode-free maps can be seen. Even for a large stencil the error swamps the $\nabla^4 e$ signal; for a non-zero $\nabla^4 b$ signal the problem is then more drastic due to the $\nabla^4 b$ signal's small magnitude.

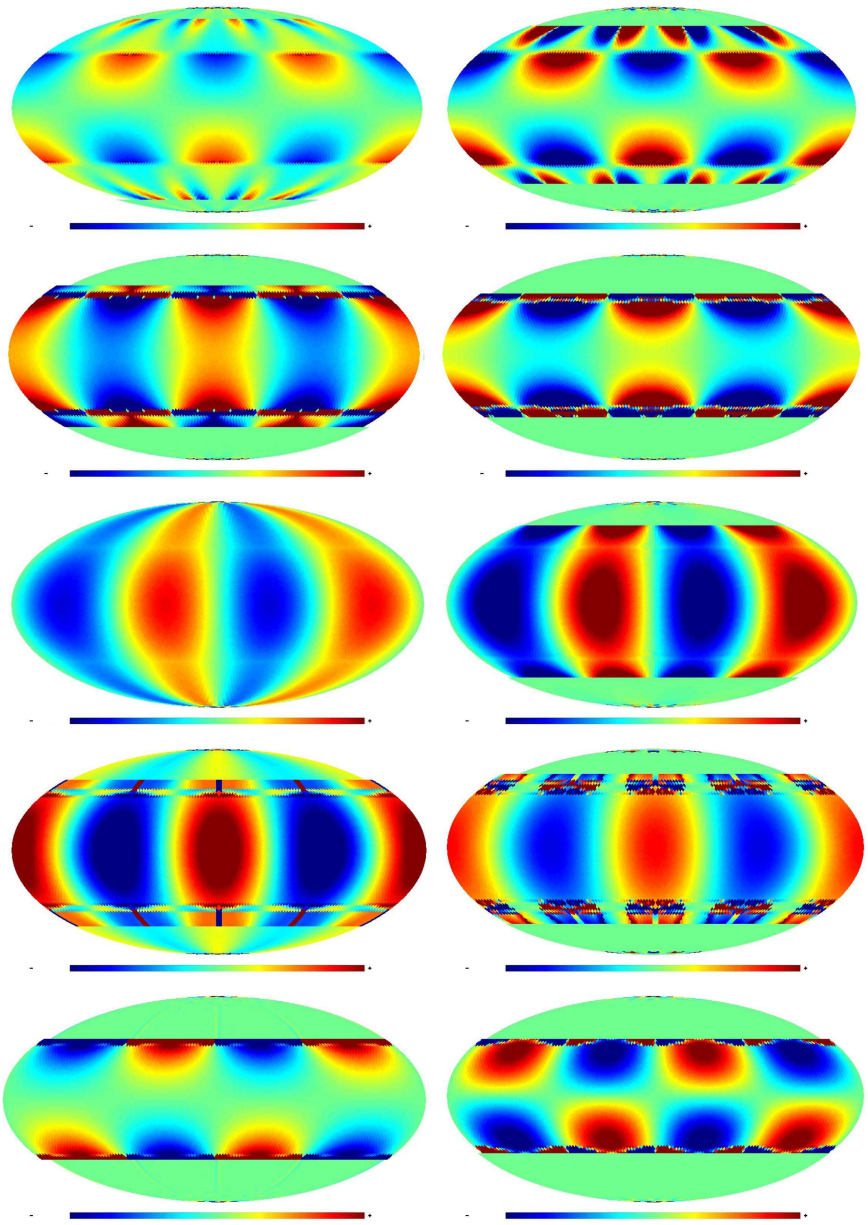

Figure 3.6: O_2 and O_4 accuracy (across rows) at $N_{\text{side}} = 128$ for derivatives $\partial_\theta, \partial_{\theta\theta}, \partial_\phi, \partial_{\phi\phi}, \partial_{\theta\phi}$ (down columns) of $Y_{22}(\theta, \phi)$, with absolute maximum values of $\sim \begin{pmatrix} 1.5 \times 10^{-3} & 0.1 & 4.5 \times 10^{-4} & 2.6 \times 10^{-3} & 3.1 \times 10^{-2} \\ 1.5 \times 10^{-2} & 0.8 & 1.5 \times 10^{-3} & 3.1 \times 10^{-3} & 9.0 \times 10^{-2} \end{pmatrix}^T$. Since the error in the polar cap is much larger than the equatorial region for all maps bar ∂_ϕ, the values in the equatorial regions in these maps has been limited to $\begin{pmatrix} \pm 10^{-6} & \pm 2 \times 10^{-6} & \pm 2 \times 10^{-6} & \pm 2 \times 10^{-6} & \pm 10^{-6} \\ \pm 10^{-3} & \pm 10^{-3} & \text{n/a} & \pm 10^{-3} & \pm 2 \times 10^{-4} \end{pmatrix}^T$, resulting in the observed discontinuous 'bands' at the polar cap boundaries. The figure shows that the accuracy improves with stencil size, and is worst at the pole (due to a combination of outer-differencing error (for ∂_θ and $\partial_{\theta\theta}$) and increased position differences Δ). However, it is not reasonable to simply increase the stencil order with the aim of achieving some threshold accuracy, for three reasons: 1) The time complexity for matrix inversion goes as $\mathcal{O}(n^3)$, where n is the number of pixels in the matrix [174]; 2) The maximum stencil size is limited to $(2N_{\text{side}} + 1)^2$. (3) The example (l, m) given has a relatively small magnitude pole problem error for harmonic functions (See Fig. 3.7). Thus the convergence rate with stencil size is too slow.

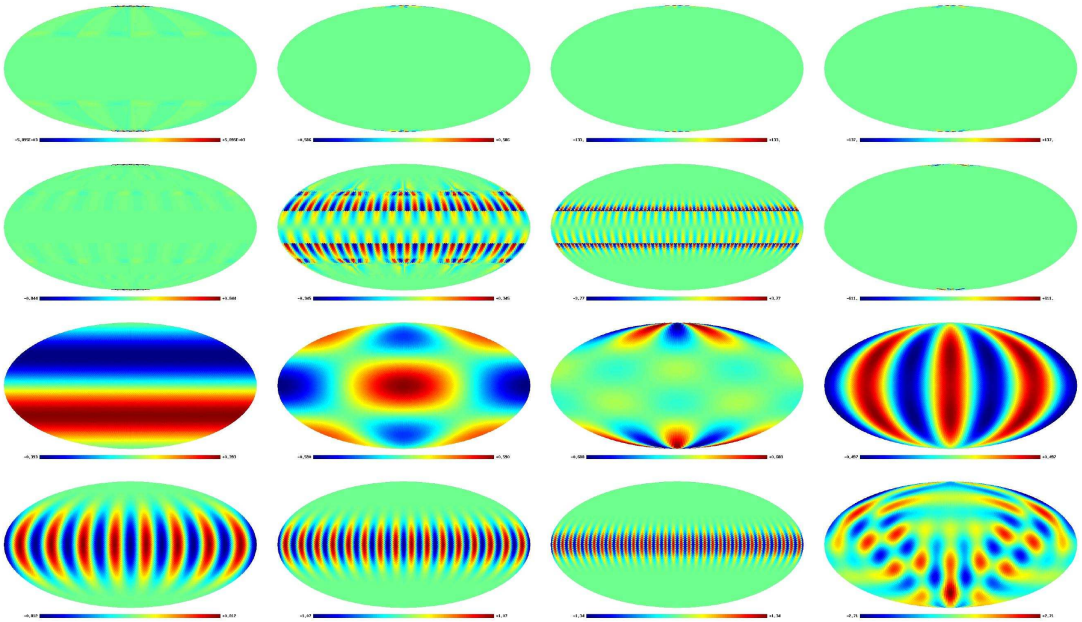

Figure 3.7: Top 2 rows: O_4 accuracy maps of $\nabla^4 b$-fields with $N_{\rm side} = 32$ for a range of unit-a^E_{lm} sources, with maximum absolute values of $\begin{pmatrix} 5.9\times10^{-3} & 0.6 & 133 & 137 \\ 0.8 & 0.3 & 3.8 & 611 \end{pmatrix}$. Bottom 2 rows: Q maps corresponding to the sources given:
$a^E_{lm} = \begin{pmatrix} \delta_{l3}\delta_{m0} & \delta_{l3}\delta_{m1} & \delta_{l3}\delta_{m2} & \delta_{l3}\delta_{m3} \\ \delta_{l8}\delta_{m8} & \delta_{l16}\delta_{m16} & \delta_{l32}\delta_{m32} & \sum_{l'=0}^{9}\sum_{m'}\delta_{ll'}\delta_{mm'} \end{pmatrix}$.
Whilst the absolute maximum values are of order $\sim \mathcal{O}(1)$ for each Q map, the polar errors peak for $m = 2$ and $m = 3$, and the magnitude of the polar errors at fixed m increases with l. (l, m) = (32, 32) maps have been included to show how error can propagate at the equator, due to variation in ϕ greater than that modellable by the stencil.

Table 3.1: CMB source maps, calculated using the online CMBFAST interface. The source spectra were generated using the online javascript form with default inputs unless otherwise stated, including $K(\eta)_{\rm max} = 3000$, a cosmological constant, Peebles recombination and no 5th dimension. See the online documentation (`http://lambda.gsfc.nasa.gov/`) for a discussion of these terms and their implementation.

Resolutions $N_{\rm side}$ generated	Ω_b, Ω_Λ, $\Omega_{\rm cdm}$, $\Omega_{\rm hdm}$, $T_{\rm cmb}$ (K), $g^*_{\rm massive}$, H_0 (kms^{-1}Mpc^{-1}), $Y_{\rm He}$, n_s	$N_{\nu,\rm massless}$, $N_{\nu,\rm massive}$	Tensors?
32, 128	0.046, 0.73, 0.224, 0, 2.725, 0, 70, 0.24, 0.96	3.04, 0	No
32, 128	0.046, 0.73, 0.224, 0, 2.725, 0, 70, 0.24, 0.96	3.04, 0	Yes, $n_t = n_s - 1$

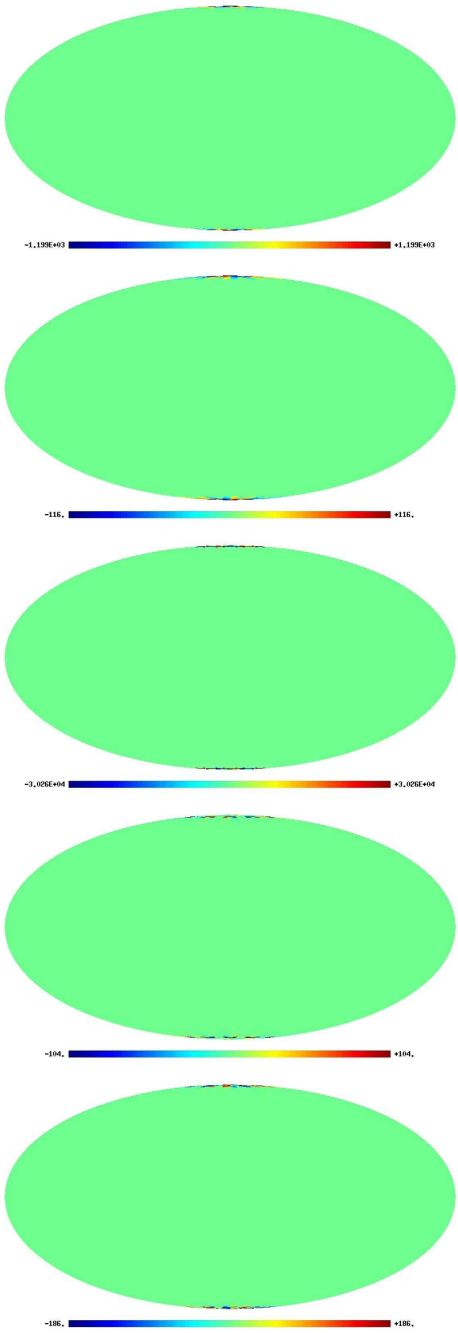

Figure 3.8: O_2 $\nabla^4 b$-fields, with $N_{\mathrm{side}} = 32$: various oversampling techniques; only the polar values are of interest here. From top to bottom: (i) Original results for the source $a^E_{lm} = \delta_{l2}\delta_{m2}$, $a^B_{lm} = 0$, (ii) with an O_4 stencil about the pole, (iii) $\delta\phi = 0.01$ HEALPix-reconstructed ($l_{\max} = 2N_{\mathrm{side}}$) rotated doubled sampling, (iv) $\delta\phi = 0.01$ analytic rotated doubled sampling, (v) discrete doubled sampling. The absolute maximum values for each map are $\begin{pmatrix} 1.2 \times 10^3 & 116 & 3.0 \times 10^4 & 104 & 186 \end{pmatrix}^T$. The discrete doubled sampling mode performs better than the standard O_2 but falls short of the rotated sampling; with an accurate map reconstruction method there is nothing in principle to forbid an n-tupled rotation sampling, which would bring the pole error down quickly.

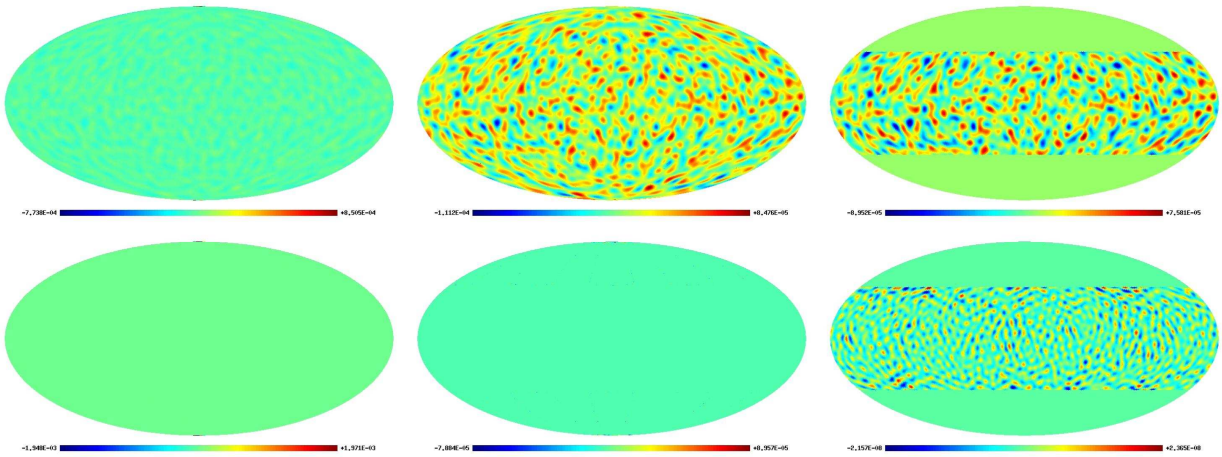

Figure 3.9: Top row: $O_4\ \nabla^4 b$ map generated from CMBFAST Q and U maps, with tensors. Bottom row: $O_4\ \nabla^4 b$ map generated from CMBFAST Q and U maps, no tensors. The map resolution is $N_{\rm side} = 128$, and all the other parameters are the defaults from the LAMBDA (`http://lambda.gsfc.nasa.gov/`) online tool page (see Table 3.1). Columns, left-to-right: No ring removal, 1st north & south polar rings removed, equatorial region only. In the no-tensors scenario, at the power spectrum level the pole problem could provide a false-positive detection; at the level of the map, these can be distinguished by eye — inconsistency between polar and equatorial regions in a given map, as seen in the middle and right-hand images, is a result of the differencing error dominating the calculated map. This then amounts to a consistency criteria by which to check for a false positive detection. The irregular geometries outside the equator induce a larger error than at the equatorial region. For the equator, the cut-off length is defined by the ring at which the stencil geometries become irregular, and is hence O_n-dependent.

3.2.3 The 'Pole Problem' and Accurate Reconstruction of the Harmonic Coefficients

It is known now that the construction of the bi-Laplacians is highly sensitive at the pole to error in the underlying derivatives, and that rotated sampling can solve this problem. In order to produce an adequate rotated map, one must accurately calculate the harmonic coefficients a_{lm} of the map, apply the Wigner rotation functions, and then sum over the new coefficients.

The HEALPix method of reconstructing the harmonic coefficients of a scalar field is an iterative procedure [262]: one starts with a zeroth-order estimator

$$a_{lm}^{T,(0)} = \frac{4\pi}{N_{\rm pix}} \sum_{i}^{N_{\rm pix}} T(\Omega_i) Y_{lm}^{*}(\Omega_i) \tag{3.23}$$

and resums the coefficients to form a map $T^{(0)}$. The next step is to take the difference map $\delta T^{(0)} = T - T^{(0)}$ and compute the zeroth order harmonic coefficients of $\delta T^{(0)}$ in the same manner as the zeroth order of T, then iterate and sum over coefficients to form the n^{th}-order approximation:

$$a_{lm}^{T} \approx \frac{4\pi}{N_{\text{pix}}} \left[\sum_{i}^{N_{\text{pix}}} T(\Omega_i) Y_{lm}^{*}(\Omega_i) + \sum_{j=0}^{n-1} \sum_{i}^{N_{\text{pix}}} \delta T^{(j)}(\Omega_i) Y_{lm}^{*}(\Omega_i) \right]. \tag{3.24}$$

The optimal a_{lm} sampling scale for map reconstruction is $l_{\max} = 2N_{\text{side}}$, with the optimal number of iterations being 3 according to the HEALPix software recommendations. While this is a quick and reasonable approximation, a numerical analysis finds that the convergence of the limit as iterations increase is not suitable for the rotated sampling method.

Further, the calculation of the spherical harmonic coefficients in the HEALPix method relies on the following algorithm (which can be found in Press et al [174]):

$$\begin{aligned} f_{lm}(x) &= \sqrt{\frac{2l+1}{2}\frac{(l-m)!}{(l+m)!}} P_{lm}(x) \\ f_{mm}(x) &= \frac{(-1)^m}{\sqrt{2}} \sqrt{\frac{(2m+1)!!}{(2m-1)!!}} (1-x^2)^{m/2} \\ f_{m,m+1}(x) &= x\sqrt{2m+3} f_{mm}(x) \\ f_{lm}(x) &= x\sqrt{\frac{4l^2-1}{l^2-m^2}} f_{l-1,m}(x) - \sqrt{\frac{2l+1}{2l-3}\frac{(l-1)^2-m^2}{l^2-m^2}} f_{l-2,m}(x) \end{aligned} \tag{3.25}$$

where the last of the relations is only quasi-stable.

GLESP is known to improve on this by (1) using Gauss-Legendre integration for quick, accurate integrals over $d\theta$ and (2) by using also a further recurrence relation which is stable for all (l, m), for $m \leq l$:

$$\begin{aligned} \sqrt{(l-m-1)(l+m+2)} f_{l,m+2}(x) + \frac{2x(m+1)}{\sqrt{(1-x^2)}} f_{l,m+1}(x) \\ + \sqrt{(l-m)(l+m+1)} f_{lm}(x) = 0. \end{aligned} \tag{3.26}$$

The HEALPix pixellization, although distributed in azimuthal rings, does not sample at the correct points to use the Gauss-Legendre scheme. An accurate calculation of the integral equation (1.15) is desired. For the HEALPix grid, the

points in θ are described by [261]

$$\begin{aligned} \cos\theta &= \frac{4}{3} - \frac{2i}{3N_{\text{side}}} && \text{North equatorial belt, } N_{\text{side}} \leq i \leq 2N_{\text{side}} \\ \cos\theta &= 1 - \frac{i^2}{3N_{\text{side}}^2} && \text{North polar cap,} \qquad 1 \leq i \leq N_{\text{side}} \end{aligned} \tag{3.27}$$

with corresponding symmetry in the southern hemisphere. Although this is globally irregular, the HEALPix θ points may be split into regular (equatorial) and irregular (polar cap) parts. Specifically then, one should Fourier transform across rings in ϕ and then integrate up the poles.
The standard tool for Fourier transforming on a discretized grid is the FFT [174]. The Nyquist rate

$$f_c = \frac{1}{2\Delta} \tag{3.28}$$

describes the fact that if a continuous function $h(t)$, sampled at an interval Δ, happens to be bandwidth limited to frequencies smaller in magnitude than f_c then the function $h(t)$ is completely determined by its samples h_n, described by

$$h(t) = \Delta \sum_{n=-\infty}^{\infty} h_n \frac{\sin[2\pi f_c(t - n\Delta)]}{\pi(t - n\Delta)}. \tag{3.29}$$

For sampling a continuous function that is not bandwidth limited to less than the Nyquist critical frequency, any frequency component outside of the frequency range $(-f_c,\ f_c)$ is aliased into that range by the discrete sampling. This information allows one to estimate the discrete Fourier transform of a function by a discrete sum:

$$H(f_j) \approx \Delta \sum_{k=0}^{n-1} h_k e^{2\pi i k j/n} \tag{3.30}$$

with discrete inverse

$$h_k = \frac{1}{n} \sum_{j=0}^{n-1} H_j e^{-2\pi i k j/n}. \tag{3.31}$$

Similarly, a discrete form of Parseval's theorem is obeyed:

$$\sum_{k=0}^{n-1} |h_k|^2 = \frac{1}{n} \sum_{j=0}^{n-1} |H_j|^2. \tag{3.32}$$

The discrete Fourier transform can be computed in $\mathcal{O}(n \log_2 n)$ operations by the FFT algorithm. The algorithm splits a discrete Fourier transform into the sum

of two discrete Fourier transforms, formed from the even numbered points and odd-numbered points of the original distribution:

$$F_k^e + W^k F_k^o \tag{3.33}$$

where W relates H_j to h_k by

$$H_j = \sum_{k=0}^{n-1} W^{jk} h_k. \tag{3.34}$$

This construction then allows for a recursively-scaled computation of any data grid of length 2^n, such as that provided by the FFTW package[2].
Having defined a Fourier transform across ϕ, one is left with a 2d partial-transform field; in order to compute the accurate harmonic coefficients, it is necessary to integrate up θ. For the semi-regular distribution of points, a first guess might be to utilize the composite trapezoid method. The trapezoid rule approximates an integral by

$$\int_a^b f(x)dx \approx (b-a)\frac{f(a)+f(b)}{2}. \tag{3.35}$$

To integrate over the entire point distribution one can decompose the full integral into a summation of smaller integrals via the composite trapezoidal rule:

$$\int_a^b f(x)dx \approx \frac{b-a}{n}\left[\frac{f(a)+f(b)}{2} + \sum_{k=1}^{n-1} f\left(a + k\frac{b-a}{n}\right)\right], \tag{3.36}$$

which for non-uniform intervals is

$$\int_a^b f(x)dx \approx \frac{1}{2}\sum_{i=2}^{n}(x_i - x_{i-1})(f(x_i) + f(x_{i-1})). \tag{3.37}$$

The trapezoid rule is the 2-point Newton-Cotes (NC) formula; using the residue calculus, the leading error of the composite trapezoidal rule is

$$\text{Err} \sim -\frac{(b-a)^3}{12n^2} f''(\zeta) \tag{3.38}$$

with ζ some point between a and b. The accuracy of the integrals can be improved; for the regular grid part one might choose a more general Newton-

[2]Available at `http://www.fftw.org/`

Cotes method. Since the equatorial region is equally spaced, use can be made of the composite trapezoid rule for the poles, summed with a single n_{equator}-point Newton-Cotes approximation at the equator.
If an integral is approximated by

$$\int f dx = \sum_i w_i f_i \Delta x \tag{3.39}$$

where the nodes are equally spaced, then it can be shown that the n-point Newton-Cotes weights can be found by solving

$$\begin{pmatrix} x_1^0 & \cdots & x_n^0 \\ \vdots & \ddots & \vdots \\ x_1^n & \cdots & x_n^n \end{pmatrix} \begin{pmatrix} w_1 \\ \vdots \\ w_n \end{pmatrix} = \begin{pmatrix} \frac{x_n - x_1}{2} \\ \vdots \\ \frac{x_n^{n+1} - x_1^{n+1}}{2^{n+1}} \end{pmatrix}. \tag{3.40}$$

Starting with a Lagrange basis interpolation polynomial

$$P(x) = \sum_j f_j L_j(x) \qquad L_j = \prod_{i \neq j} \frac{x - x_i}{x_j - x_i} \tag{3.41}$$

then one can integrate this

$$I = \int_{x_0}^{x_n} P(x) dx \tag{3.42}$$

to form the polynomial approximation of the integral. By separating out the factors into a sum

$$I = \sum_i^n \alpha_i(x) f(x_i), \tag{3.43}$$

$w_i = \alpha_i$ can be assigned and the linear system solved

$$\begin{pmatrix} x_1^0 & \cdots & x_n^0 \\ \vdots & \ddots & \vdots \\ x_1^n & \cdots & x_n^n \end{pmatrix}^{-1} \begin{pmatrix} c_1 \\ \vdots \\ c_n \end{pmatrix} = \begin{pmatrix} w_1 \\ \vdots \\ w_n \end{pmatrix} \tag{3.44}$$

where the solution vector to this system, c, is exactly that given in equation (3.40). Table 3.2 shows the results for this method on a regular grid, and Table 3.3 a comparison with Gaussian methods. While this works well for even spacing, it does not work as well for uneven spacing due to the $x_n - x_{n-1}$ terms; unfortunately, this fails to produce maps of the required accuracy even if a HEALPix-like recursive scheme is invoked.

Table 3.2: Numerical test of the NC scheme; a Mathematica calculation gives $\int_{-1}^{1} f(x)dx \approx 1.71125; \Delta = b - a$.

No. of nodes	x	NC scheme	result
2	-1,1	$\frac{\Delta}{2}(f_1 + f_2)$	1.21306
3	-1,0,1	$\frac{\Delta}{2}(f_1 + 4f_2 + f_3)$	2.60653
4	-1,-1/3,1/3,1	$\frac{3\Delta}{8}(f_1 + 3f_2 + 3f_3 + 4f_4)$	2.1771
5	-1,-1/20,1/2,1	$\frac{2\Delta}{45}(7f_1 + 32f_2 + 12f_3 + 32f_4 + 7f_5)$	1.71047
6	-1,-3/5,-1/5, 1/5,3/5,1	$\frac{5\Delta}{288}(19f_1 + 75f_2 + 50f_3 + 50f_4 + 75f_5 + 19f_6)$	1.71082
7	-1,-4/6,-2/6,0, 2/6,4/6,1	$\frac{\Delta}{140}(41f_1 + 216f_2 + 27f_3 + 272f_4 + 27f_5 + 216f_6 + 41f_7)$	1.71128

Table 3.3: 4-point results summary for various methods, for the same integral as in Table 3.2. The Gaussian methods perform better than the Newton-Cotes methods, but vary in their accuracy depending on the grid geometry.

Method	value
Exact	1.71125
Gauss-Legendre	1.71122
Newton-Cotes (regular)	2.1771
General Gauss Method (regular)	1.7222
General Gauss Method (irregular)	1.67456

Since it is known how the regular and irregular HEALPix θ grid parts are constructed, then for better accuracy one can attempt a mixed NC-and-Gaussian scheme for the regular and irregular parts respectively, or even a Gaussian scheme for the whole sphere. Gaussian quadrature schemes approximate the integral by the sum of certain weights at particular points which are specified by a weight function $W(x)$ [215]

$$I = \int_a^b f(x)W(x)dx \approx \sum_{j=1}^{n} w_j f(x_j); \tag{3.45}$$

the freedom of choosing points allows one to attain in principal higher accuracy for higher order calculations. This is anchored by a choice of weight function, which is in a polynomial basis with roots at the particular points — evaluating the integrand using those root points leads to much-improved accuracy. Given a scalar product

$$\langle f|g\rangle = \int_a^b W(x)f(x)g(x)dx, \tag{3.46}$$

one can find a set of polynomials (i) that includes exactly one polynomial of order

j , called $p_j(x)$, and (ii) all of which are mutually orthogonal over $W(x)$ via the recurrence relation

$$\begin{aligned} p_{-1}(x) &= 0 \qquad p_0(x) = 1 \\ p_{j+1}(x) &= (x - a_j)p_j(x) - b_j p_{j-1}(x) \end{aligned} \tag{3.47}$$

where

$$a_j = \frac{\langle x p_j | p_j \rangle}{\langle p_j | p_j \rangle}, \qquad b_j = \frac{\langle p_j | p_j \rangle}{\langle p_{j-1} | p_{j-1} \rangle} \tag{3.48}$$

and $p_j(x)$ has j distinct roots in the interval (a, b) — the abscissas of the Gaussian quadrature formulae are the roots of the orthogonal polynomial $p_n(x)$ for the same interval and weighting function. Once the abscissas are determined, weights can be determined by solving

$$\begin{pmatrix} p_0(x_0) & \cdots & p_0(x_{n-1}) \\ \vdots & \ddots & \vdots \\ p_{N-1}(x_0) & \cdots & p_{n-1}(x_{n-1}) \end{pmatrix} \begin{pmatrix} w_0 \\ \vdots \\ w_{n-1} \end{pmatrix} = \begin{pmatrix} \int_a^b W(x) p_0(x) dx \\ 0 \\ \vdots \end{pmatrix} \tag{3.49}$$

or via

$$w_j = \frac{\langle p_{n-1} | p_{n-1} \rangle}{p_{n-1}(x_j) p'_n(x_j)}. \tag{3.50}$$

Gaussian quadrature (in particular Gauss-Legendre quadrature) is used in GLESP to yield fast and highly accurate harmonic coefficients without recourse to iterative methods. The HEALPix points do not follow the abscissas of the Gauss-Legendre scheme, so it is necessary to derive the general Gaussian scheme first. Starting from the integral (3.45) and using an interpolating polynomial L_j, one finds

$$w_j = \int_a^b \frac{L_j(x) W(x)}{x - x_j} dx \tag{3.51}$$

such that the relevant integral to solve is

$$I = \int_a^b \frac{\prod_{j=1}^m (x - x_j) W(x)}{x - x_j} dx. \tag{3.52}$$

Using Mathematica, a general solution to the above integral with $W(x) = 1$ over

n points is found to be

$$\begin{aligned} I_n &= \ln(x - x_j) \prod_{i=1}^{n} (x_j - x_i) + \sum_{z=1}^{n-1} x_j^z \left[\sum_{\alpha=0}^{z} (-1)^\alpha \frac{x^{z-\alpha}}{\alpha} S_\alpha \right] \\ S_\alpha &= \sum_{y_0 \neq \cdots \neq y_\alpha}^{\text{combins}} x_{y_0} \cdots x_{y_\alpha}, \end{aligned} \tag{3.53}$$

giving for example a 3-point solution

$$I_3 = \frac{x^3}{3} + \frac{x^2}{2} \left(x_j - \sum_{i=1}^{3} x_i \right) + x \left(x_1 x_2 + x_1 x_3 + x_2 x_3 + x_j^2 - x_j \sum_{i=1}^{3} x_i \right) \tag{3.54}$$

where the log term disappears since one can only realistically sample at the pixel positions i. Under certain conditions (such as $f'(x) \neq 0$ in the vicinity of the nodes), this reduces to the form given in Yakimiw [267]:

$$w_j = -\frac{k_{n+1}}{k_n} \frac{1}{p_{n+1}(x_j) p'_n(x_j)} \tag{3.55}$$

where the polynomials p are components of the interpolating polynomial:

$$p_n(x) = \prod_{j=1}^{n} (x - x_j) \qquad p'_n(x_j) = \left[\frac{dp_n(x)}{dx} \right]_{x=x_j}. \tag{3.56}$$

The performance of this method is better than the NC method, and almost competitive with Gauss-Legendre (see Table 3.3) — it can be shown that the general Gaussian scheme reduces to Gauss-Legendre at those nodes.

There does however remain an important problem with this scheme: the number of combinations to calculate for, say, an $N_{\text{side}} = 32$ HEALPix map for a mixed Gauss-and-NC (Gaussian at the polar caps) and full Gaussian scheme respectively are $\sum_{\alpha=1}^{30} 31![(31-\alpha)!\alpha!]^{-1}$ and $\sum_{\alpha=1}^{126} 127![(127-\alpha)!\alpha!]^{-1}$ which have prohibitively large time complexities.

A final alternative is to rotate the underlying grid geometry by $\delta\theta = \pi/2$ which rotates the pole to the equator of a new coordinate system. This allows one to calculate the rotated scalar and pseudo-scalar field pole pixels using a central-difference scheme whilst avoiding the pole issues of the $\csc\theta$-type terms. Specifically one transforms the pixel coordinates from $\mathbb{S}^2$ to $\mathbb{R}^3$, performs the rotation $\mathcal{R}$ in its matrix form, calculates the derivatives in the basis elements of $\mathcal{R}$ and utilizes the Jacobian $\mathcal{J} = X^a_{,b}$ to convert back to polar form. Rotating the resulting calcu-

lations back to the pole results in ringing from the pixel boundary, which can be tempered by calculating a larger region of rotated pixels since ringing dies down further from a discontinuous boundary. Performing such a method essentially doubles the computation time of the full field calculations, but is recommended if the polar pixels are needed. This might be ameliorable via the method of approximating the ringing response from a unit pixel; such a method is not pursued here.

In the absence of a quick, accurate method for performing rotated sampling, one is reduced to simply removing the offending pixel rings; for most calculations this is recommended since the polar pixel region is negligible for large (i.e., $Planck$-type) maps. This can be compared with the various oversampling techniques (Fig. 3.8).

On a masked sphere, the methods to deal with the pole problem are more limited. Boundary effects will contaminate the results of any harmonic transformation, so one may have to resort to wavelet-type analysis instead for accurate enough map reconstructions in order to control the sensitive polar $\nabla^4 b$ calculations.

It has been found that a pole problem exists for separating the polarization modes; furthermore one can solve the problem of accurate reconstruction of the harmonic coefficients on the HEALPix sphere. All this was done on an unmasked sphere. For a sphere with masking, it is necessary to look at transform types with better real-space localization properties. Wavelets are the canonical example; indeed, it is not impossible that harmonic and wavelet techniques could be combined to engineer a more accurate map reconstruction. However, as can be seen from the previous chapter, rotation of needlets relies on accurate integration, so is out of the question around the pole using the standard HEALPix approach.

3.3 Estimators

For cosmology, it is necessary to calculate the errors on the scalar fields in harmonic space such that one can define the accuracy of the power spectral estimators. For example, on a flat 1d space one can compute the estimator for the transform of a first-order derivative,

$$F(x) = \sum_k \hat{f}_k e^{ikx} \qquad \Rightarrow \qquad \partial_x F = \sum_k ik\hat{f}_k e^{ikx} \tag{3.57}$$

where $\hat{f}_k$ is the Fourier power in F for mode k. On a discrete grid, there is instead the 1-point forward difference equation

$$\tilde{\partial}_x F = \sum_k \hat{f}_k \frac{i \sin(k\Delta) e^{ikx}}{\Delta} \tag{3.58}$$

where the $\sim$ over the derivative operator denotes a discrete derivative, hence the finite-differenced spectrum $\tilde{\mathcal{P}}_k$ always underestimates the true spectrum $\mathcal{P}_k$:

$$\tilde{\mathcal{P}}_k = \text{sinc}^2(k\Delta)\mathcal{P}_k. \tag{3.59}$$

This is illustrated with a calculation of the signal and leakage of the Laplacian of a signal, using a 3-point difference equation on a regular grid (Fig. 3.10). The reader is reminded that an *n-point stencil* is a collection of n pixels over which the finite-difference calculation in equation (2.68) for a given point on a grid is made. The full flat-sky operators on a regular grid with 3-point stencils are then, for $\mathbf{k} = (k_1, k_2)$, given by

$$\begin{aligned} \tilde{D}_0^+ F &= -\sum_k \frac{2}{\Delta^2}(\cos(k_2\Delta) - \cos(k_1\Delta))\hat{f}_k e^{i\mathbf{k}\cdot\mathbf{n}} \\ \tilde{D}_0^- F &= -\sum_k \frac{2}{\Delta^2}(\sin(k_1\Delta)\sin(k_2\Delta))\hat{f}_k e^{i\mathbf{k}\cdot\mathbf{n}}. \end{aligned} \tag{3.60}$$

For more general 1d derivatives, one has to start from

$$\tilde{\partial}_x F_{j'} = \sum_k \hat{f}_k e^{ikx} \sum_j w_j e^{ik\Delta_{j,j'}} \tag{3.61}$$

and induce simplifications at this point using grid symmetries. There is then no simple sinusoidal statement for general irregular grids but the estimator is not difficult to calculate. The first-order derivative spectral estimator is then proportional to

$$\mathcal{P}_k \propto \left(\sum_j w_j e^{ik\Delta_{j,j'}} \right)^2, \tag{3.62}$$

where the full irregular flat sky discrete operators correspond to the general solution for w discussed in section 2.3, which could be used to compute the leakage. The 2d solution is generally more difficult since solving the geometric matrices is much more involved, even for the case of an approximately-square stencil geometry. A more general full correction in terms of irregular 2d grids on a sphere can be given in a sinusoidal form only with a relation between the flat space har-

monic coefficients and the Legendre coefficients.
For the full-sky discrete estimator, whilst one can simply separate out the $\Delta\phi$ from the underlying harmonic field expansion (as in equation (3.61)), the derivative operators in the definition of the associated Legendre terms mean that one cannot do the same with the $\Delta\theta$ term, since the rotation is

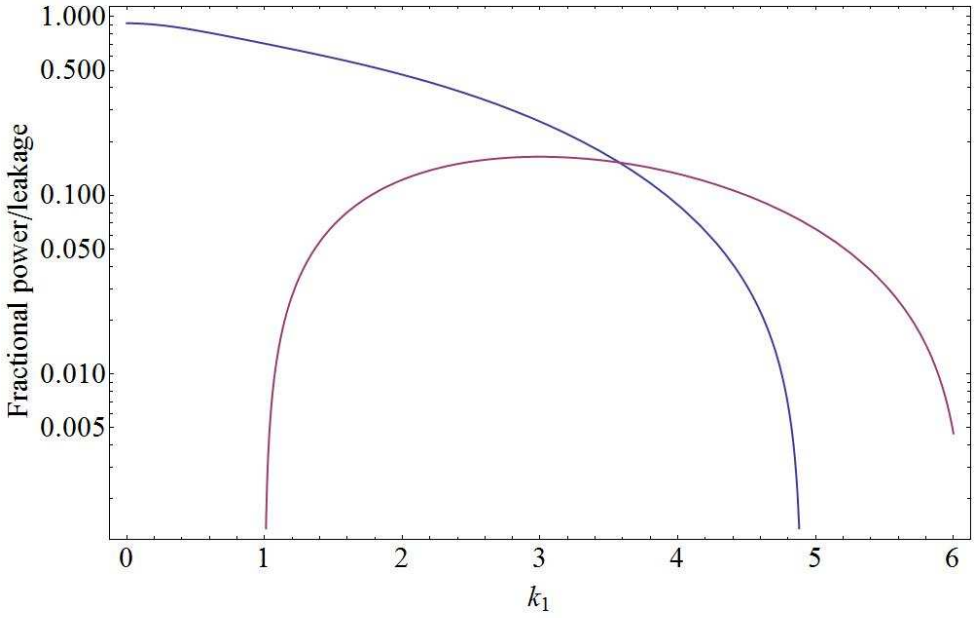

Figure 3.10: 1d Laplacian accuracy (blue line) and residual (purple line); here $\Delta = 1$, $k_2 = 1$ has been used.

$$\begin{aligned} \mathcal{R}(0, \Delta\theta, 0) P_{lm}(\cos\theta) &= \sum_{m'} d^l_{m',m}(\Delta\theta) P_{lm'}(\cos\theta) \\ P_{lm}(x) &= (-1)^m (1-x^2)^{m/2} \frac{d^m}{dx^m} P_l(x). \end{aligned} \tag{3.63}$$

This is made more explicit from the fact that the derivative of the Legendre term has contributions between modes [268]

$$\partial_\theta P_{lm}(\cos\theta) = \frac{1}{\sqrt{1-\cos^2\theta}} \left(l \cos\theta P_{lm}(\cos\theta) - (l+m) P_{l-1,m}(\cos\theta) \right), \tag{3.64}$$

although the estimator can be approximated by performing low-order Taylor expansions. Instead, one can compute (by brute force) the numerical power contributions for each derivative term via the Wigner 3lm-symbol by treating the w_j

elements as part of $(n+1)^2$ separate fields (for the case of using square 2d grids):

$$(\partial_n)_{lm} = \sum_{j,l',m'} \frac{4\pi}{N_{pix}} \sum_i w_j^{(n)}(\Omega_i) Y_{l',m'}(\delta\Omega_{j,i}) Y^*_{lm}(\Omega_i) \tag{3.65}$$

where the $\Omega_{j,i}$ refers to the rotations between the focal pixel i's position on the sphere and that of the given neighbouring pixel j. It is then possible to calculate the accuracy of the power contribution by measuring the bi-Laplacian (the 'signal' generated by the derivatives) and the commutator (the 'residual' generated by the derivatives):

$$\text{Sig} \leftrightharpoons \nabla^4 = D^+_{\mp 2} D^+_0 + D^-_{\mp 2} D^-_0 \qquad \text{Res} \leftrightharpoons D^+_{\mp 2} D^-_0 - D^-_{\mp 2} D^+_0 \tag{3.66}$$

using

$$\begin{aligned}(D^\pm_0)_{lm} \leftrightharpoons & \frac{1}{2(i)} \sum_{l'm'} \sqrt{(l'-1)l'(l'+1)(l'+2)} \\ & \times \sum_{l''} \sqrt{4\pi(2l''+1)} \begin{pmatrix} l' & l & l'' \\ m & -m & 0 \end{pmatrix} \begin{pmatrix} l' & l & l'' \\ -2 & 0 & 2 \end{pmatrix} \\ & \times \int {}_2Y_{l'',m'-m}(\Omega) \pm (-1)^{l+l'+l''} {}_{-2}Y_{l'',m'-m}(\Omega) d\Omega.\end{aligned} \tag{3.67}$$

The spin-2 harmonic integrals are only non-zero for $n = 0$, hence $m = m'$, simplifying to

$$\begin{aligned}\int {}_{\pm 2}Y_{lm}(\Omega) d\Omega = & \frac{1}{2(i)} \sum_{l'} f_{l'm} \sqrt{(l'-1)l'(l'+1)(l'+2)} (-1)^{-m} \sum_{l''} \begin{pmatrix} l' & l & l'' \\ m & -m & 0 \end{pmatrix} \\ & \times \begin{pmatrix} l' & l & l'' \\ -2 & 0 & 2 \end{pmatrix} \sqrt{\frac{(2l+1)(2l'+1)}{4\pi}} \int \left[{}_2Y_{l'',0}(\Omega) \pm (-1)^{l+l'+l''} {}_{-2}Y_{l'',0}(\Omega) \right] d\Omega.\end{aligned} \tag{3.68}$$

Finally, one can utilize

$$\begin{aligned}\int {}_{\pm 2}Y_{l,0}(\Omega) d\Omega = & 2 \sqrt{\frac{\pi (l!)^2 (2l+1)}{(l+2)!(l-2)!}} \sum_{r=0}^{l-2} \begin{pmatrix} l-2 \\ r \end{pmatrix} \\ & \times \begin{pmatrix} l+2 \\ r+2 \end{pmatrix} (-1)^{l-r-2} \frac{\Gamma(l-r)\Gamma(2+r)}{\Gamma(2+l)},\end{aligned} \tag{3.69}$$

which is only non-zero for l a multiple of 2, allowing a reduction in computations. Further speed-up is achieved by recognising that the D_s^- operators are full imaginary while the D_s^+ operators are real.
Since equation (2.30) can be written in pixel space as

$$\begin{aligned}\nabla^4 e &= \left(\tilde{D}^+_{\mp 2} D^+_0 + \tilde{D}^+_{\mp 2} D^-_0\right) e + \mathrm{Err}(e) - \left(\tilde{D}^+_{\mp 2} D^-_0 - \tilde{D}^-_{\mp 2} D^+_0\right) b \\ \nabla^4 b &= \left(\tilde{D}^+_{\mp 2} D^+_0 + \tilde{D}^+_{\mp 2} D^-_0\right) b + \mathrm{Err}(b) + \left(\tilde{D}^+_{\mp 2} D^-_0 - \tilde{D}^-_{\mp 2} D^+_0\right) e\end{aligned} \tag{3.70}$$

where Err represents remaining error in the calculation from the summation of the 'signal' and 'residual' parts, the leakage can be approximated. Whilst a simple approximation can be taken by assuming leakage into e from b is negligible the full calculation is clearly coupled. A calculation for the residual estimator, using the scheme described in the next section, can be seen in Fig. 3.11. This calculation is then equivalent to defining the pixelization leakage in terms of a convolution operator

$$(\partial_{\hat{n}})_{lm} = \sum_{l'm'} \mathcal{W}_{ll'mm'} Y_{l'm'} \tag{3.71}$$

where

$$\mathcal{W}_{ll'mm'} = \int \left(\sum_j w_j(\Omega)\right) Y_{l'm'}(\Omega) Y_{lm}(\Omega) d\Omega, \tag{3.72}$$

with which one can deconvolve out the pixellization leakage. When calculating the residual for operation of discrete derivatives in different frames (such as the Stokes tensor frame), or even for different spin-weight fields (such as if one has a vector field) it is useful to look at the more general convolution operator

$${}_{ss'}\mathcal{W}_{ll'mm'} = \int \partial_{\hat{n}} \left[{}_{s'}Y_{l'm'}(\Omega)\right] {}_sY_{lm}(\Omega) d\Omega. \tag{3.73}$$

Some of the techniques available for such a calculation are briefly expounded on, without carrying out an in-depth example. One can first calculate the convolution operator for the derivatives in the analytic case by utilizing the relation between the spin-weighted harmonics and the Wigner D-functions

$$D^l_{-m,s}(\phi,\theta,\psi) = e^{im\phi} d^l_{-m,s}(\theta) e^{-is\psi} = (-1)^m \sqrt{\frac{4\pi}{2l+1}}\, {}_sY_{lm}(\theta,\phi) e^{is\psi} \tag{3.74}$$

where the Wigner 'little-d' function is

$$d^l_{mm'}(\theta) = \sum_{r=m'-m}^{l+m} \frac{(-1)^r \sqrt{(l+m')!(l-m')!(l+m)!(l-m)!}}{(l+m-r)!r!(m'-m+r)!(l-m'-r)!} \times \left(\cos\frac{\theta}{2}\right)^{2l+m-m'-2r} \left(\sin\frac{\theta}{2}\right)^{m'-m+2r} \tag{3.75}$$

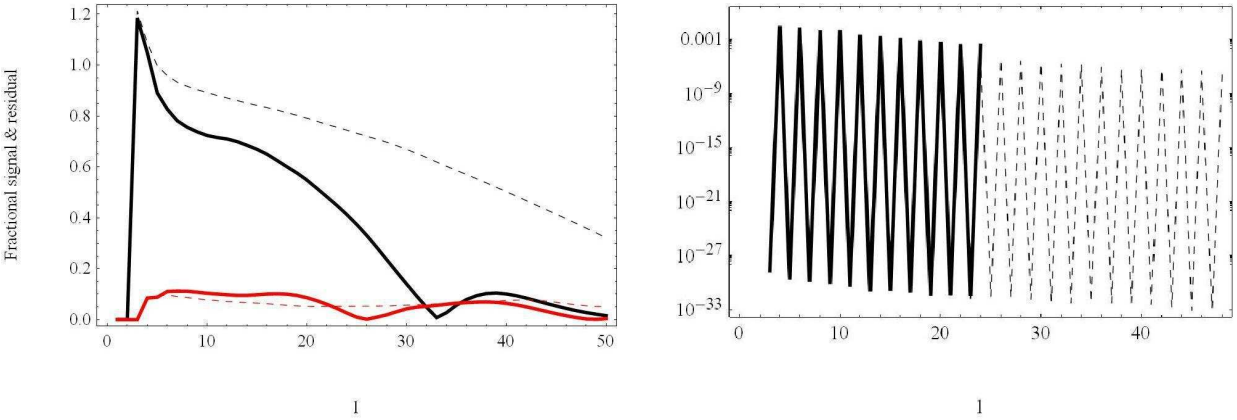

Figure 3.11: Left diagram: Fractional signal (black lines) and residual leakage (red lines) of the finite-difference scheme on the HEALPix sphere at O_2 calculate from equation (3.65); the (thick lines, dashed lines) correspond to $N_{\rm side} = (8, 16)$. There is a characteristic high point at the very low-l scale, followed by an immediate dip in leakage. The first phenomenon is related to the pole problem in the formalism on the HEALPix sphere; the signal starts to peak again at approximately the Nyquist frequency for the map ($\sim 2N_{\rm side}$). Right diagram: Residuals from individual point C_l map generated from $a^E_{lm} = \delta_{ll'}$ where l' specifies the point l-range. In this case, $l' = 10$ for maps with $N_{\rm side} = (8, 16)$ corresponding to (thick line, dashed line). The leakage has a steep downward gradient across l with the leakage contribution to each multipole oscillating rapidly, the oscillation rate scaling with resolution.

and the angular momentum operators on $\mathbb{S}^2$ [225] are

$$\begin{aligned} \hat{L}^2 &= -\left[\partial^2_\theta + \cot\theta\partial_\theta + \csc^2\theta(\partial^2_\phi - 2\cos\theta\partial_{\psi\theta} + \partial_\psi)\right] \\ \hat{L}_z &= -i\partial_\phi \qquad \hat{L}_{z'} = -i\partial_\psi \\ \hat{L}_\pm &= -\frac{1}{\sqrt{2}} e^{\pm i\phi}\left(\partial_\theta \pm i\cot\theta\partial_\phi\right), \end{aligned} \tag{3.76}$$

where it should be noticed that on $\mathbb{S}^2$ the operator $\hat{L}^2$ is equivalent to D^+_0. These

operators have the power contributions

$$\begin{aligned}
\hat{L}^2 D^l_{mm'}(\phi,\theta,\psi) &= l(l+1) D^l_{mm'}(\phi,\theta,\psi) \\
\hat{L}_z D^l_{mm'}(\phi,\theta,\psi) &= -m D^l_{mm'}(\phi,\theta,\psi) \\
\hat{L}_{z'} D^l_{mm'}(\phi,\theta,\psi) &= -m' D^l_{mm'}(\phi,\theta,\psi) \\
\hat{L}_{\pm} D^l_{mm'}(\phi,\theta,\psi) &= \pm\sqrt{\frac{l(l+1)-m(m\mp 1)}{2}} D^l_{m\mp 1,m'}(\phi,\theta,\psi)
\end{aligned} \tag{3.77}$$

which allows one to construct the analytic derivatives of the spin-harmonics using the recurrence relations of the Wigner terms (p.90 of Varshalovich et al [225]). As an illustrative example, the recurrence relation

$$\begin{aligned}
\sin\theta e^{\pm i\phi} D^l_{m\pm 1,m'}(\phi,\theta,\psi) = &\mp \frac{\sqrt{(l\pm m)(l\pm m+1)(l^2-m'^2)}}{l(2l+1)} D^{l-1}_{mm'}(\phi,\theta,\psi) \\
&+ \frac{m'\sqrt{(l\pm m)(l\pm m+1)}}{l(l+1)} D^l_{mm'}(\phi,\theta,\psi) \\
&\pm \frac{\sqrt{(l\pm m)(l\pm m+1)[(l+1)^2-m'^2]}}{(l+1)(2l+1)} D^{l+1}_{mm'}(\phi,\theta,\psi)
\end{aligned} \tag{3.78}$$

shows that the ∂_θ operator redistributes power across multipoles l. To finish the evaluation of the analytic convolution operators, it is necessary to evaluate the integral

$$I = \int {}_{s'}Y_{l'm'}(\Omega)\, {}_{s}Y_{lm}(\Omega) d\Omega. \tag{3.79}$$

This can be achieved by utilizing the orthogonality relations of the little-d functions

$$\int_0^\pi d^l_{mm'}(\theta) d^{l'}_{mm'}(\theta) \sin\theta d\theta = \frac{2}{2l+1}\delta_{ll'} \tag{3.80}$$

and those of the Jacobi polynomials $P_l^{(\alpha,\beta)}$ (Gradshteyn & Ryzhik [268], p.806), since

$$d^l_{mm'}(\theta) = \sqrt{\frac{(l+m)!(l-m)!}{(l+m')!(l-m')!}} \left(\sin\frac{\theta}{2}\right)^{m-m'} \left(\cos\frac{\theta}{2}\right)^{m+m'} P_{l-m}^{(m-m',m+m')}(\cos\theta). \tag{3.81}$$

For discrete derivatives on a regular grid with sampling points separated by a length Δ, the generalized convolution operator for derivatives in ϕ is trivial to compute. For the analysis of derivatives in θ, a perturbation expansion in the

little-d functions, $d^l_{mm'}(\cos(\theta+\Delta))$, can be used; by isolating the lowest order expansions in the sinusoidal terms in equation (3.81)

$$\begin{aligned}\left(\cos\left[\frac{\theta+\Delta}{2}\right]\right)^{2l+m-m'-2r}\left(\sin\left[\frac{\theta+\Delta}{2}\right]\right)^{m'-m+2r}&\\ \approx\left(\cos\frac{\theta}{2}\right)^{2l+m-m'-2r}\left(\sin\frac{\theta}{2}\right)^{m'-m+2r}&\\ \times(1+(m'-l-m+2r+l\cos\theta)\Delta\csc\theta)+\mathcal{O}(\Delta^2)&\end{aligned} \tag{3.82}$$

it can be seen that the discrete derivatives in θ mix power across multipoles s, l and m.

Returning from these more general considerations, the residual in the Stokes tensor frame can be approximated by calculating the operators

$$\begin{aligned}\eth_{-1}\eth_{-2}&=\partial_{\theta\theta}-\csc^2\theta\partial_{\phi\phi}+2i\csc\theta\partial_{\theta\phi}+3\cos\theta\csc\theta\partial_\theta+2i\cos\theta\csc^2\theta\partial_\phi-2\\ \bar{\eth}_1\bar{\eth}_2&=\partial_{\theta\theta}-\csc^2\theta\partial_{\phi\phi}-2i\csc\theta\partial_{\theta\phi}+3\cos\theta\csc\theta\partial_\theta-2i\cos\theta\csc^2\theta\partial_\phi-2\end{aligned} \tag{3.83}$$

which are spin-weighted in correspondence with operation on the Stokes tensor instead of the individual Q and U fields, and their discrete analogues, given by

$$\tilde{\eth}_{-1}\tilde{\eth}_{-2}f(\Omega)=\eth_{-1}\eth_{-2}f(\Omega)+R^+f(\Omega)\qquad\tilde{\bar{\eth}}_{-1}\tilde{\bar{\eth}}_{-2}f(\Omega)=\bar{\eth}_{-1}\bar{\eth}_{-2}f(\Omega)+R^-f(\Omega) \tag{3.84}$$

where the operators $R^\pm$ are the quantities that will be approximated. By taking the lowest order errors in the Taylor series derivation of the first and second order derivatives in 1d

$$\begin{aligned}\frac{f^{j+1}-2f^j+f^{j-1}}{\Delta_x^2}&\approx\partial_{xx}f^j+\frac{\Delta_x^2}{12}\partial_{x^4}f^j\\ \frac{f^{j+1}-f^{j-1}}{2\Delta_x}&\approx\partial_xf^j+\frac{\Delta_x^2}{6}\partial_{x^3}f^j\\ \frac{f^{j+1}_{i+1}+f^{j-1}_{i-1}-f^{j+1}_{i-1}-f^{j-1}_{i+1}}{4\Delta_x\Delta_y}&\approx\partial_{xy}f^j_i+\frac{2}{3}\left(\Delta_x^2\partial_{x^3y}f^j_i+\Delta_y^2\partial_{xy^3}f^j_i\right),\end{aligned} \tag{3.85}$$

the residual operators $R^\pm$ are

$$\begin{aligned}R^\pm=\Delta_\theta^2\left(\frac{1}{12}\partial_{\theta^4}\pm i\frac{\csc\theta}{3}\partial_{\theta^3\phi}+\frac{\cot\theta}{2}\partial_{\theta^3}\right)&\\ -\Delta_\phi^2\left(\frac{\csc^2\theta}{12}\partial_{\phi^4}\mp\frac{\csc\theta}{3}\partial_{\theta\phi^3}\mp2i\cos\theta\csc^2\theta\partial_{\phi^3}\right),&\end{aligned} \tag{3.86}$$

and by substitution into

$$\begin{aligned}\tilde{\nabla}^4 e &= \nabla^4 e - \sum_{lm} a^E_{lm}\left[R^+{}_{-2}Y_{lm} + R^-{}_2Y_{lm}\right] + i\sum_{lm} a^B_{lm}\left[R^+{}_{-2}Y_{lm} - R^-{}_2Y_{lm}\right] \\ \tilde{\nabla}^4 b &= \nabla^4 b - \sum_{lm} a^E_{lm}\left[R^+{}_{-2}Y_{lm} - R^-{}_2Y_{lm}\right] + i\sum_{lm} a^B_{lm}\left[R^+{}_{-2}Y_{lm} + R^-{}_2Y_{lm}\right]\end{aligned} \tag{3.87}$$

the residual approximation is calculated[3]. For the case of HEALPix, one has $\Delta_\phi(\theta,\phi) \approx \Delta_\theta(\theta,\phi)/\sin\theta$, yielding the contribution at each point in θ:

$$\begin{aligned}\tilde{\nabla}^4 e &= \nabla^4 e - \sum_{lm}\sqrt{\frac{(l+4)!}{(l-4)!}}\left[a^E_{lm}\left(1+\frac{\csc\theta}{6}\right)Y_{lm} + ia^B_{lm}\left(1-\frac{\csc\theta}{6}\right)Y_{lm}\right]\Delta^2_\theta \\ \tilde{\nabla}^4 b &= \nabla^4 b - \sum_{lm}\sqrt{\frac{(l+4)!}{(l-4)!}}\left[a^E_{lm}\left(1-\frac{\csc\theta}{6}\right)Y_{lm} + ia^B_{lm}\left(1+\frac{\csc\theta}{6}\right)Y_{lm}\right]\Delta^2_\theta.\end{aligned} \tag{3.88}$$

Alternatively, one might simply reconstruct the Q and U fields solely from the underlying E spectra and perform the real-space commutator derivatives. The HEALPix geometry also provides a consistency criterion for calculating $\nabla^4 b$-fields on the real-space HEALPix sphere which can help to expose whether the calculated signal is predominantly numerical noise; since there is a significant change in geometry and position differences between the equatorial and polar HEALPix regions, a jump in the computed values of $\nabla^4 b$ across the equator-polar cap boundary implies that the calculations are dominated by numerical error.

3.4 Masking & Noise Performance

Our analysis so far has been limited to an ideal unmasked sphere; however the real sky is obscured by the galactic plane amongst other foreground sources and will have various contributions of noise to it. This section is used to note the performance of the software on a maskless sky against the standard methods, i.e., pure pixellization and finite-difference error and then show the efficacy of the software in the presence of masking and noise. Of course, while testing against standard methods shows that the proposed method works as required, the real test of the software will be against alternative proposals for clean subtraction of the B-mode leakage. In this section, unless otherwise stated the HEALPix

[3]This calculation is due to D. I. Novikov.

methods shall be utilized at their optimal values for $l_{\max}$ and $map2alm$ iterations: $l_{\max} = 2N_{\text{side}}$ and 3 iterations. The CMB models used for calculation are those appearing in Table 3.1.

Figure 3.12 compares MasQU calculations on the full unmasked sky to similar HEALPix calculations; on the unmasked sky the harmonic space separation is superior to calculations using the first few stencil sizes; with large sky masking the MasQU method features significantly less leakage. There should exist an intermediate masked area, for a given MasQU calculation order and map resolution, wherein the difference between the HEALPix leakage and MasQU error is minimized. This interesting calculation is left to future work, since for realistic experiments the masking volume will likely exceed such an intermediate value.

Pole removal (Fig. 3.13) has the effect of lowering power across scales, with the decrement most noticeable at low l. This was implemented by removing the $(O_n + 1)$ rings immediately outside each pole. For completeness, the difference between operating in the full-sky and flat-sky formalisms is shown; it should not be surprising that the errors in the flat-sky approximation are at their largest at low l.

3.4.1 Masking

In the case of masking, analysis was performed using 3 basic types of mask (Fig. 3.14): equatorial, polar and random masks. In the masked case differences between the MasQU method and the raw (not apodized) HEALPix $map2alm$ calculations are found as expected; the pole problem particularly affects the power at around $l = 2$ by boosting it significantly. Focussing on the no-tensors maps, at multipoles higher than $l \sim 10$ MasQU performs considerably better than the raw pseudo-C_l calculations for masked HEALPix schemes, by about 1 to 3 orders of magnitude; in most models gravitational lensing rather than primordial modes dominate the foreground polarization from $l \sim 150$, meaning there is a large l-range where MasQU is advantageous for calculating B-modes. The smoothness of the masked calculations is in contrast to that of underlying functional discontinuities. The effect of a shelf discontinuity itself under the operation of the full-sky MasQU calculations is shown in Fig. 3.15. As can be expected (since the underlying approximation to the signal is an interpolating polynomial), the software actually performs worse with a larger stencil when in the presence of a discontinuity. For the CMB, discontinuities will mostly be contibuted by point sources on the sky; these will need to be masked away using a source catalogue.

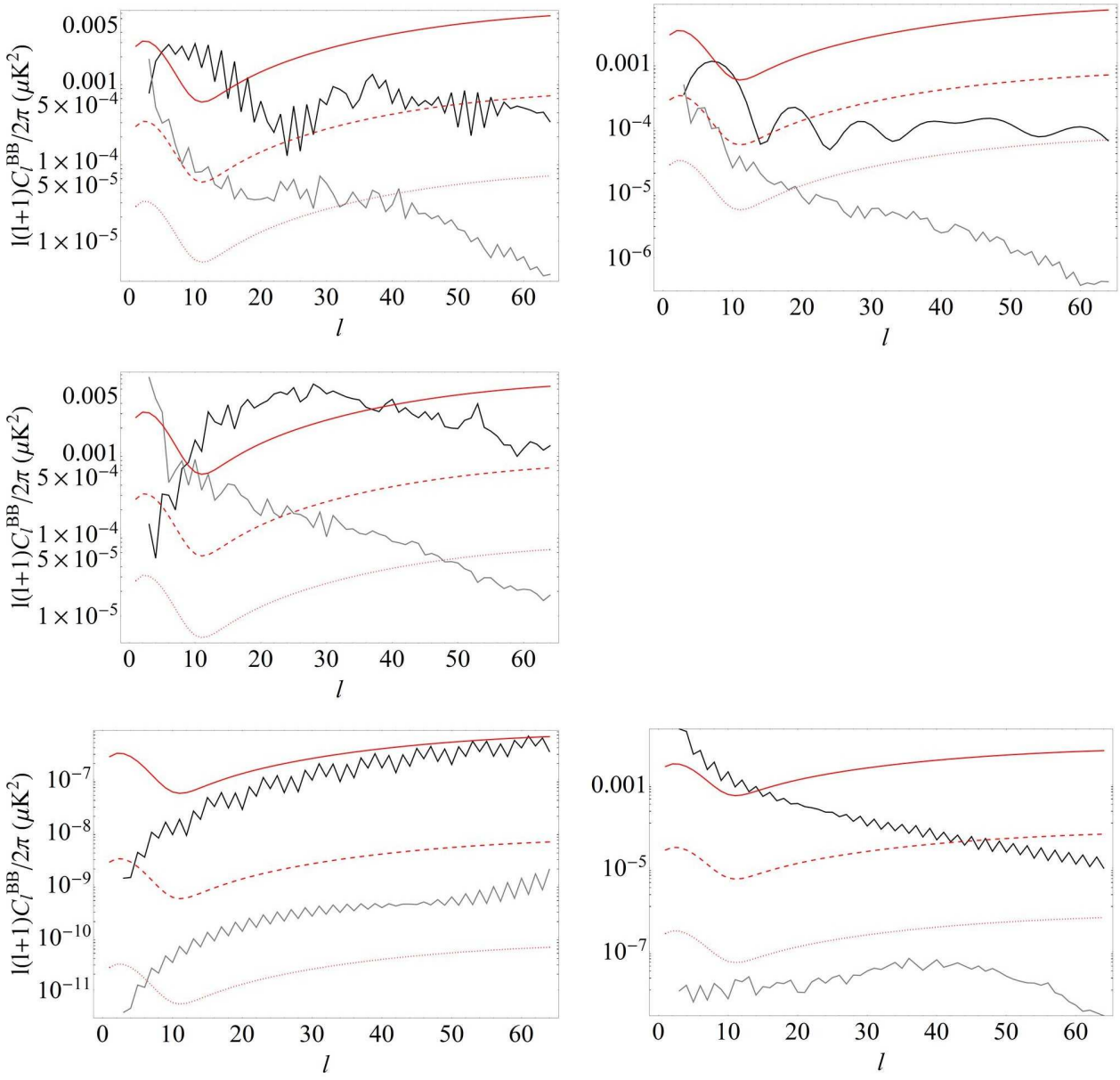

Figure 3.12: Top 2 rows: B-mode C_ls from the fiducial $N_{\rm side} = 32$ B-mode-free maps as reconstructed by the 3-iterations HEALPix method (black) or an O_2 MasQU calculation (grey), for equatorial (top-left), polar (top-right) and random (middle) masks. Further details of these masks can be found from Figure 3.14. In all these plots, the red lines are B-mode spectra from tensor modes corresponding to $r = 10^{-1}$, 10^{-2}, 10^{-3}. Bottom row: Maskless calculations, with raw HEALPix (i.e., no special apodization used) on the left and O_2 MasQU on the right. For the HEALPix calculations, the black line is for 0 iterations while the grey line is for 3 iterations. For the MasQU calculations, the grey line is for a standard calculation, with the pole removed for the black line. The corresponding $\nabla^4 e$ signal has an rms $\sim 2 \times 10^{-8}$K; the red lines are full-sky B-mode spectra from tensor modes corresponding to $r = 10^{-5}$, 10^{-7}, 10^{-9} (left-hand diagram) and $r = 10^{-1}$, 10^{-3}, 10^{-5} (right-hand diagram).

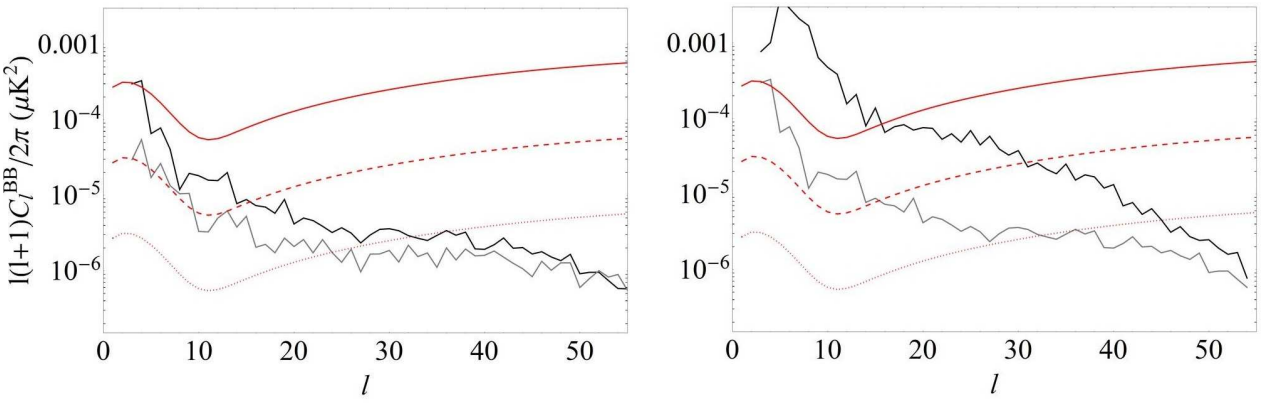

Figure 3.13: Left diagram: O_2 and O_4 (black, grey) maskless B-modes from the $N_{\rm side} = 32$, $r = 0$ map, with the pole removed. Right diagram: O_2 calculations with the flat-sky and full-sky operators (black, grey). In both plots, the red lines are B-mode spectra from tensor modes corresponding to $r = 10^{-2}, 10^{-3}, 10^{-4}$.

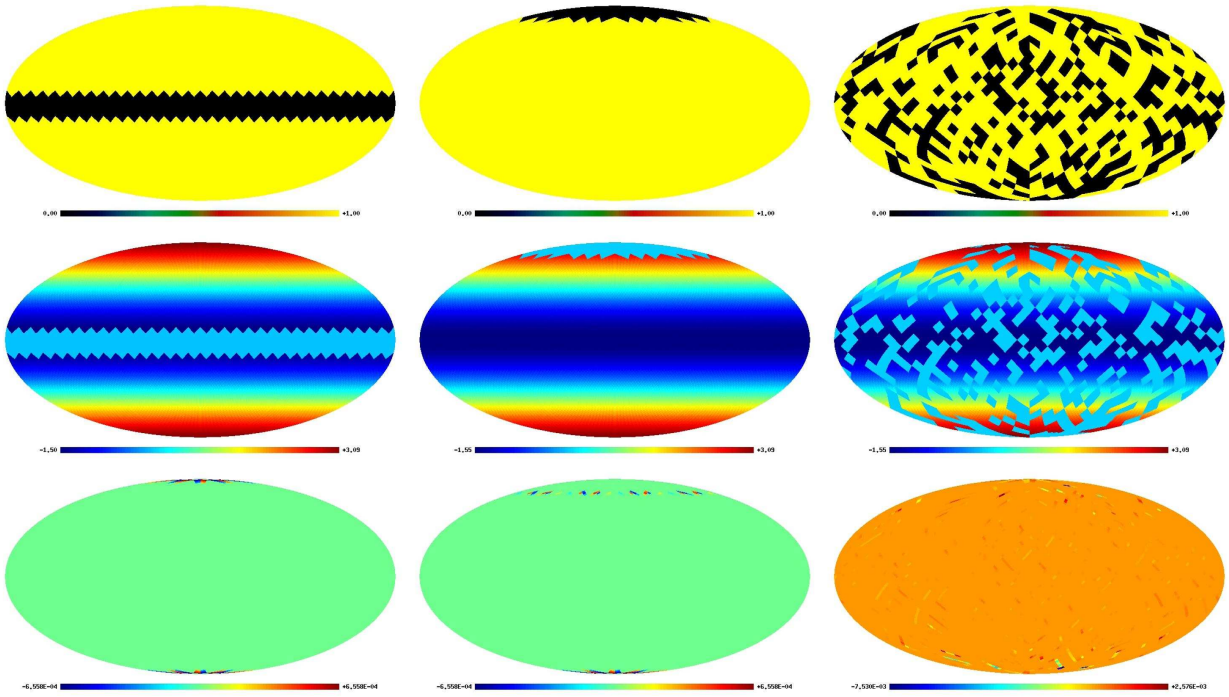

Figure 3.14: Rows, top-to-bottom: Masking schemes, $\nabla^4 e$ maps and $\nabla^4 b$ maps, at O_6 and $N_{\rm side} = 32$ for $a^E_{lm} = \delta_{l2}\delta_{m0}$, $a^B_{lm} = 0$. Left to right: the equatorial mask ($f_{\rm sky} \approx 0.83$), polar mask ($f_{\rm sky} \approx 0.96$) and random mask ($f_{\rm sky} \approx 0.64$). The source function was chosen for the smallness of the pole problem errors, but nonetheless the masking errors are generally smaller than the errors contributed by the pole problem; specifically, the absolute maximum values in the $\nabla^4 b$ maps are, from left to right, ($\sim 6.6 \times 10^{-4}, \sim 6.6 \times 10^{-4}, \sim 7.5 \times 10^{-3}$).

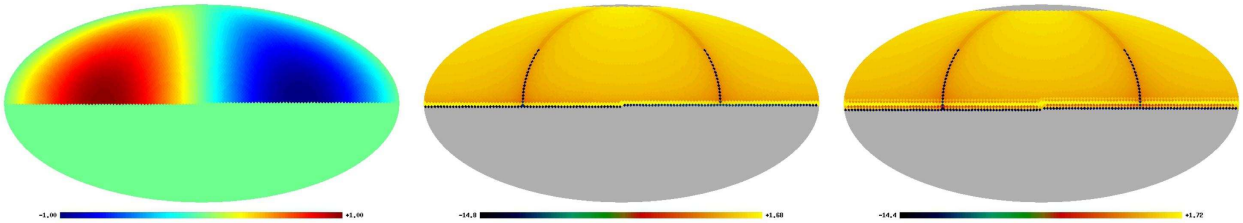

Figure 3.15: (Logarithmic) code performance in the presence of shelf discontinuities; the B-modes are calculated from a $Q = \sin\theta \sin\phi$, $U = 0$ pair of $N_{\text{side}} = 128$ maps with a cut-off to $Q = 0$ in the southern hemisphere at the equator. Without a U signal, one should have no B-modes. Left-to-right: Original Q map, O_2 and $O_4\nabla^4 b$ maps. The map value ranges for each image are $(-1, 1)$, $(-14.8, 1.68)$ and $(-14.4, 1.72)$ respectively. Notice that there is a blow-up in errors for calculations across the discontinuity, as expected; the error actually gets worse and effects a larger region for larger stencils, and also scales with the magnitude of the discontinuity. This general behaviour also follows for point discontinuities.

3.4.2 Noise Performance

A number of simple noise models (white Gaussian, anisotropic uncorrelated and pixel-to-pixel correlated) are also analysed. The Gaussian model was calculated using the HEALPix random number-generating subroutine *planck-rng* in harmonic space rather than pixel space, since one can then look at the effect of the dominant noise scale on the calculations. The crude anisotopic noise map was constructed from a pixel-level Gaussian noise map with a small functional direction-dependence imposed on it whilst the pixel-correlated signal was constructed from a pixel-level Gaussian noise map with reflection symmetry imposed between the north and south hemispheres. Figure 3.16 presents power spectra for the realistic B-mode-less CMB maps with Gaussian noise added, where variations have been made in the mean value of the noise (at 10%, 1% and 0.1% the mean signal values of the noiseless CMBFAST-generated Q and U maps, i.e., $\langle X_{\text{noise}}\rangle \propto \langle X_{\text{sig}}\rangle$ where $X \in \{Q, U\}$) and in the scaling of the noise (via a cut-off in the number of multipoles generated for the noise maps). At high magnitude and large l, since the noise translates to a collection of point discontinuities in real space, the sum of the derivatives of the summed signal and noise maps can be expected to feature more point source errors. The addition of the Gaussian noise models serves to boost B-mode power fairly consistently across l up to the l_{max} value that sets the smallest scale for noise; a lower-l noise mode cut-off l_{max} results in a drop in signal power boosting for $l > l_{\text{max}}$, but still with a significant contribution. The pixel-correlated power boost is almost indistin-

guishable from the pure Gaussian boost; in contrast, the anisotropic boost is dependent on the scaling of the direction-dependent noise. The MasQU method can then be seen to be very sensitive to noise; one would want a good understanding of the systematic and foreground noise properties in order to effectively purify the B-modes.

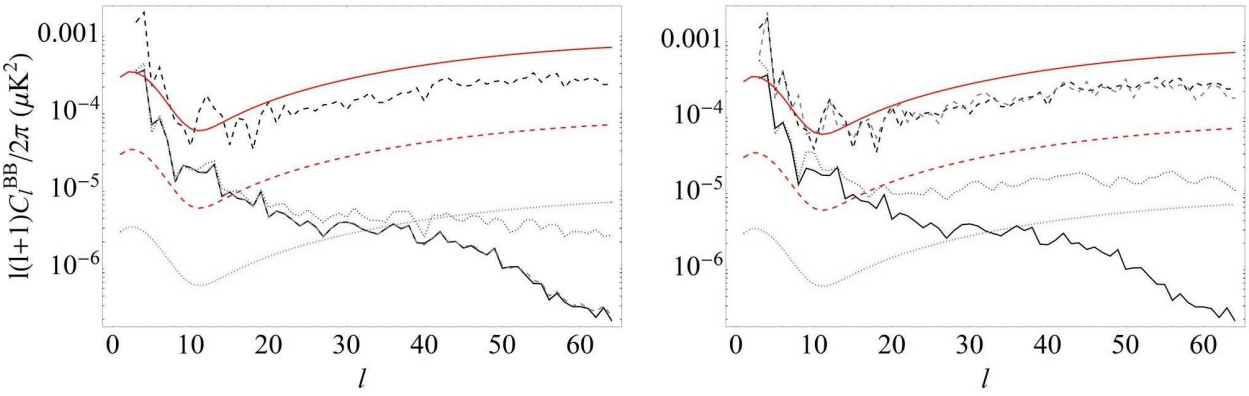

Figure 3.16: Left diagram: O_2 maskless B-modes from the $r = 0$ map with resolution $N_{\text{side}} = 32$, with Gaussian noise added to the underlying Q, U maps and the pole removed. The Gaussian noise models in Q and U are calculated from a Gaussian distribution of harmonic coefficients and normalized such that its mean is some proportion of the signal mean, i.e., $\langle N \rangle = \alpha \langle S \rangle$. The thick black line is the noiseless model, whilst the scaling for the dashed black, dotted black, and dashed grey lines are $\alpha = 0.1$, 0.01 and 0.001 respectively. Right diagram: The thick black line is the noiseless model, with the dashed black, dotted black, and dashed grey lines for Gaussian, anisotropic, and pixel-correlated noise models respectively, all with $\alpha = 0.1$. In both plots, the red lines are B-mode spectra from tensor modes corresponding to $r = 10^{-2}$, 10^{-3}, 10^{-4}.

3.4.3 Leakage from Realistic Surveys

In order to get a rough idea of the leakage improvement the software can bring to real data, the leakage for sky coverages in a simplified model of the *E and B Experiment* (EBEX, [269]) survey and the bounds that may be set on the tensor-to-scalar ratio r in these simplistic cases is calculated; the algorithm is also performed on a mask of similar area centred on the equator. In the past the signal-to-noise ratio S/N has been too low to perform differencing on the real sky, but such projects are designed to improve S/N, making such calculations plausible. The fiducial model is the same as the parameters set for the previous no-tensors analysis (Table 3.1).

The EBEX survey is a balloon-borne polarimeter for probing the sky with a resolution of less than 8 arcminutes at frequency bands centered at 150, 250, 350, and

450 GHz. The sky patch covered by the ∼1300-detector instrument corresponds to 350 square degrees. The EBEX region is an approximately square patch, corresponding to Fig. 9 in Stivoli et al [270]. In particular, MasQU calculations are performed that are equal roughly to the EBEX "sky"and "ground" coverages found in Stivoli et al, for the fiducial B-mode-free model adding uncorrelated Gaussian noise, at the levels 3.2 μK and 0.9 μK for the sky and ground coverages respectively[4], in both Q and U (i.e., $\langle X\rangle_{\mathrm{noise,\text{“}sky\text{”}}} = 3.2\mu\mathrm{K}$ and $\langle X\rangle_{\mathrm{noise,\text{“}ground\text{”}}} = 0.9\mu\mathrm{K}$ where $X = \{Q, U\}$). This is performed on an $N_{\mathrm{side}} = 128$ resolution HEALPix map — less than the resolution capable by EBEX, but more than enough to capture the essential low-l polarization information relevant to tensor modes. The procedure starts by smoothing the signal + noise map with a Gaussian kernel, and calculate the E- and B-mode spectra from the resulting smoothed map (Fig. 3.17); the noise model is approximated by performing the same derivatives on a smoothed Gaussian field. Since the convolution of the map with a Gaussian function smooths high-resolution variation, this amounts to a low-frequency pass filter. On the HEALPix sphere, the decreasing resolution per ring will serve to increase low-l power in the calculations. Since one is not using the full sky it is advantageous to rotate the survey region to the equator, which would ameliorate such a problem. This is because the pixel distributions in the polar cap and equatorial regions differ significantly.

Mock likelihoods for the tensor-to-scalar ratio r from Gaussian priors (centred on $r = 0$ with $(\min, \max) = (0, 0.33)$) are also computed, using CosmoMC and $\sim 200,000$ likelihood space samplings: all cosmological parameters are held constant[5] except for varying r, the scalar and tensor spectral indices n_s, n_t and the superhorizon power of the scalar perturbations $\log A_s$, centred on 0.95, 0 and 3 respectively. This of course assumes that quantities such as the reionization optical depth are known perfectly; for a realistic analysis one would have to perform the MCMC calculations over a higher-dimensional space that includes such parameters as variables. Thus if the noise model is well-known, then the MasQU method provides an excellent improvement in the mock surveys over standard harmonic methods. Specifically, since real-space derivatives obey linearity, one can in principle approximate the noiseless map by removing the E- and B-modes calculated by a full real-space noise model. Given that the noise models from projects such as WMAP are computed initially as sky maps, this would have the advantage of

[4]From correspondences with the EBEX team.

[5]Baryon density $\Omega_b h^2 = 0.0223$, dark matter density $\Omega_{dm} h^2 = 0.105$, optical depth $\tau = 0.09$, curvature $\Omega_k = 0$ and dark energy equation-of-state parameter $w = -1$.

separating out point sources before smoothing of the map is performed.

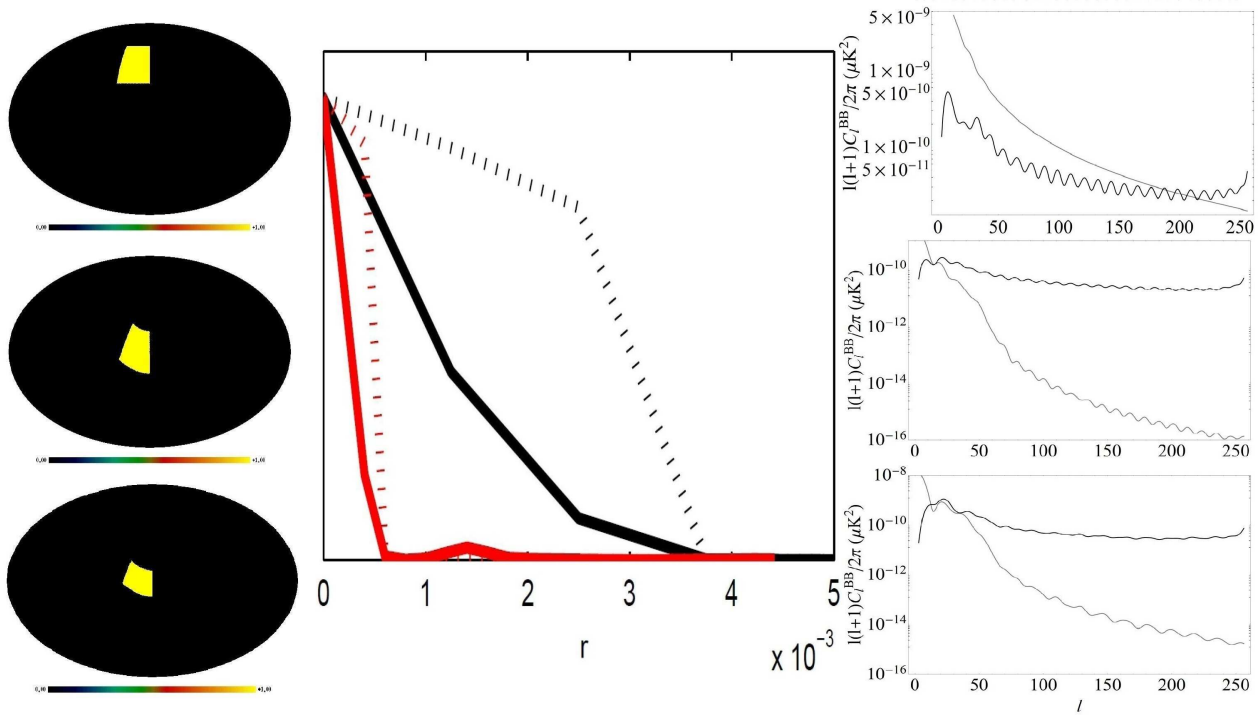

Figure 3.17: Left column, top-to-bottom: Mock EBEX ground survey, rotated ground survey, and the rotated sky survey masks. The ground and sky surveys are imposed with a 0.9 μK and 3.2 μK smoothed Gaussian noise component, representing detector error. Right column, B-mode spectra corresponding to the survey regions in the left column; the black line is a HEALPix calculation, the grey an O_2 MasQU calculation. These results compare favourably with the B-mode residual in more detailed EBEX analysis [270], although the noise model used in the analysis here is far more simplistic. Central column: Maximum likelihood calculations of r for the middle row mask according to the text; the black lines are the HEALPix calculations, with the MasQU calculations in red (solid lines are the fully marginalized posteriors, dotted lines the relative mean likelihoods).

3.5 Apodization & Signal Optimization

Leakage from E and B polarization modes into each other comes directly from two sources: sky pixellization and sky masking. Having dealt with signal leakage from the coupled polarization modes into each other due to masking by constructing pure scalar fields, one is then left with a remaining leakage problem: power also leaks between modes of the same scalar field when calculating the angular power spectrum on a masked sky. This is mostly due to the edge discontinuities present in a mask, although aliasing (the transference of power from

undersampled higher-resolution modes to lower modes) also has an effect. In practice one avoids aliasing by sampling the map at a higher resolution than the Nyquist frequency for the required l-range.

The edge discontinuities can be dealt with using apodization techniques; in the case of sky masking one can apodize the harmonic calculation by applying a weight function $W(\Omega) \in (0, 1)$ to each pixel element on the sphere during harmonic integration

$$\tilde{b}_{lm} = \frac{(l-2)!}{(l+2)!} \int W(\Omega) \nabla^4 b(\Omega) Y^*_{lm}(\Omega) d\Omega \tag{3.89}$$

where trivially one has $W(\Omega)$=0 in the masked regions. This allows one to smooth an edge at the cost of information loss. This information loss is also dependent on the length of the apodization function, which brings with it a variable sensitivity to different frequencies. Since the apodization term is a modified sky mask, this technique is related to the mode-coupling described in section 2.4.

The choice of kernel W usually requires careful consideration; many standard apodization schemes exist in the literature such as Gaussian, Hamming and others, which differ in their redistribution properties such as dynamic range against sensitivity. Specifically though, there are a few standard constraints one requires — that the kernel starts at a value $W = 1$ from some radius within the bounded region and smoothly evolves to $W = 0$ at the boundary. How far in the region this graduation starts affects how much power is lost versus how smooth the transition is. Smoothness is important in the same sense that the discontinuous mask cut-off is important; there are therefore a number of necessary trade-offs when choosing an apodization scheme.

Figure 3.18 shows the performances of apodizations on a unit-C_l temperature map for 3 classes of mask: equatorial, polar and random, for a Gaussian apodization scheme. This scheme is varied in length according to pixel radius of up to 3, providing a visual information on the effects of apodization; the information lost by apodization is in proportion with the summed perimeter of the masked regions in a given masking scheme.

Smith and Zaldarriaga [217] showed that apodizing the pure scalar fields is equivalent to finding the weights in the 'pseudo-C_l-with-counterterms' method

(from now on referred to merely as the 'counterterms' method)

$$\tilde{b}_{lm} = \frac{i}{2}\int d\Omega(Q+iU)\left(W\,{}_2Y^*_{lm} + \frac{2_1W^*\,{}_1Y^*_{lm}}{\sqrt{(l-1)(l+2)}} + \frac{{}_2W^*Y^*_{lm}}{\sqrt{(l-1)l(l+1)(l+2)}} + \text{c.c.}\right) \tag{3.90}$$

with an analogous expression for the e-field, where the conditions $W = 0$ and $\eth W = 0$ are assumed to be satisfied at the mask boundary. The spin-weighted apodization weights with $s > 0$ serve to purify the calculation, whilst the $s = 0$ weight acts in much the same way as the weight in equation (3.89).

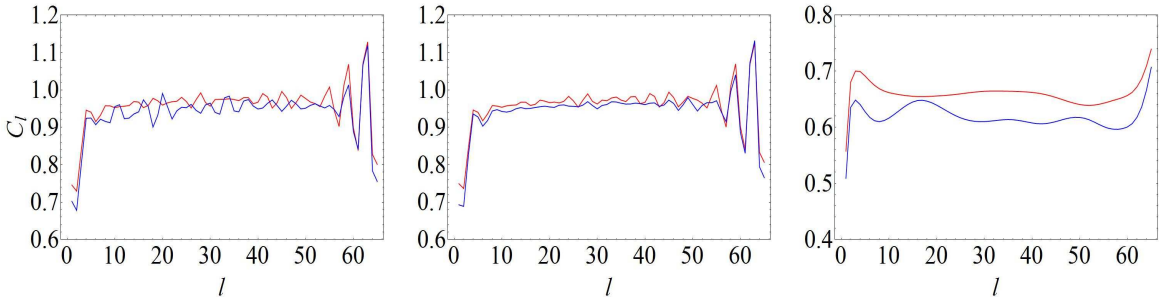

Figure 3.18: HEALPix scalar harmonic calculations with various masks and a Gaussian apodization scheme, from an underlying map constructed from a unit-step power spectrum $C_l = U(l-2)U(18-l)$ where $U(l)$ is a Heaviside step function. Left-to-right: equatorial, polar and random masks. Red corresponds to a 1-pixel apodization radius, blue to a 3-pixel apodization radius.

Further, one wishes to take account of the noise properties in a systematic way. The method provided by Smith and Zaldarriaga is just such a consistent, unified method. One wishes (as in the MASTER technique [216]) to solve for $C_l^{\nabla^4 b}$ in

$$\left\langle \hat{C}_l^{\nabla^4 b} \right\rangle = \int \frac{d^2l'}{4\pi^2} ||\tilde{W}(l-l')||^2 C_{l'}^{\nabla^4 b}. \tag{3.91}$$

By operating on the the apodization weights with the spin-weighted operators, one yields

$$\begin{aligned}
\tilde{e}_{lm} = \frac{1}{2}\int &(Q+iU)(N_l Y^*_{lm-2}W - N'_{l-1}Y^*_{lm-1}W + {}_2Y^*_{lm}W) \\
&+(Q-iU)(N_l Y^*_{lm\,2}W + N'_{l\,1}Y^*_{lm1}W + {}_2Y^*_{lm}W)d\Omega \\
\tilde{b}_{lm} = \frac{i}{2}\int &(Q+iU)(N_l Y^*_{lm-2}W - N'_{l-1}Y^*_{lm-1}W + {}_2Y^*_{lm}W) \\
&-(Q-iU)(N_l Y^*_{lm\,2}W + N'_{l\,1}Y^*_{lm1}W + {}_2Y^*_{lm}W)d\Omega
\end{aligned} \tag{3.92}$$

where

$$N_l = \frac{1}{\sqrt{(l-1)l(l+1)(l+2)}}, \qquad N'_l = \frac{2}{\sqrt{(l-1)(l+2)}} \tag{3.93}$$

with the conditions

$$\int W d\Omega = 4\pi, \qquad \sum_s {}_s W = 1. \tag{3.94}$$

The apodization, which is required for correcting for mask leakage, can be calculated optimally with a scheme given by

$$W_{\rm opt} = [C^\beta * C]^{-1}\mathbf{1} \tag{3.95}$$

where C is the $N_{\rm pix} \times N_{\rm pix}$ (signal-and-noise) covariance, C^β the $N_{\rm pix} \times N_{\rm pix}$ band-limited signal covariance

$$C^\beta = \frac{\partial C}{\partial C_{l(\beta)}}, \tag{3.96}$$

β the index over l bands and the $*$ operation signifies element-wise matrix multiplication. For the scalar and pseudo-scalar e and b fields, this relates to the signal/noise decomposition in the pixel (i, j) basis by

$$C_{ij} = S_{ij} + N_{ij} \qquad S_{ij} = \sum_l \frac{2l+1}{4\pi} C_l P_l \qquad \Rightarrow \qquad C_\beta = \frac{2l+1}{4\pi} P_{l(\beta)} \tag{3.97}$$

which could alternatively be analysed in the spin-2 field approach using

$$S_{ij}^{aa'} = \left\langle \begin{pmatrix} Q_i Q_j & Q_i U_j \\ U_i Q_j & U_i U_j \end{pmatrix} \right\rangle. \tag{3.98}$$

The sky mask is incorporated at this stage, by removing elements of the covariance matrix. The optimal weights scheme is derived by requiring W to minimize the expectation value

$$\left\langle \tilde{C}_\beta \right\rangle = \left\langle \sum_{ij} d_i W_i C_{ij}^\beta W_j d_j \right\rangle = \sum_{ij} W_i W_j C_{ij} C_{ij}^\beta \tag{3.99}$$

where d is a length-$N_{\rm pix}$ data vector. The normalization condition $\sum_i W_i = {\rm const.}$ comes from differentiating with respect to the weights:

$$\frac{d\left\langle \tilde{C}_\beta \right\rangle}{dW_i} = \sum_j C_{ij} C_{ij}^\beta W_j = 1 \qquad \Rightarrow \qquad W = (C * C^\beta)^{-1}\mathbf{1}. \tag{3.100}$$

As an analytic example, in the flat-sky approach on a disk of radius R with covariance C given by an l^2 spectrum, the covariance terms are

$$C_{ij} = -\nabla^2\delta^2(x-y), \qquad C_{\beta,ij} = j_0(l_0\|x-y\|) \tag{3.101}$$

which yields

$$(-\nabla^2 + l_0^2)W = 1 \qquad \Rightarrow \qquad W = 1 - \frac{I_0(l_0 r)}{I_0(l_0 R)} \tag{3.102}$$

where I_0 is a Bessel function, the stated Laplacian is just the radial part of the 2d circular Laplacian and the boundary conditions are $W'(0) = 0$, $W(R) = 0$. Similarly, for $C = \delta^2(x-y)$ one yields the expected uniform weights everywhere.
Since the counterterms method is equivalent to passing to b by taking finite differences, then while a pseudo-C_l method for calculating the spin-weighted minimum variance apodization weights exists it is only necessary to calculate the scalar weights for the scalar field. In some sense there is more information in the scalar field method than the counterterms method; one is not limited to taking the power spectrum of the field, but has the phase information available. On the other hand, the use of 5 different weights means that there are more degrees of freedom available in the counterterms method. The method is by construction pure; the counterterms method is (almost) pure but close to optimal, since the Dirichlet boundary conditions on the spin-weighted W terms are never fully satisfied. By recalling the transfer array in equation (2.134), one can calculate the unbiased estimator. One calculates the pseudo power spectrum and then the transfer matrix (using the same weights as in the pseudo spectrum); finally, the inversion is performed.
One can define an optimal estimator from Fisher analysis [59]; for a lossless quadratic method which is unbiased, one is lead to

$$E_l = \frac{1}{2F_{ll}} C^{-1} P_l C^{-1} \tag{3.103}$$

which can be rewritten in band-limited form as

$$E_\beta = d_i (C^{-1} C^\beta C^{-1})_{ij} d_j. \tag{3.104}$$

The ansatz for finding W is such that the pseudo-C_l estimator

$$\tilde{C}_\beta = \sum_{ij} d_i W_i C^\beta_{ij} W_j d_j \tag{3.105}$$

is as close to the optimal estimator as possible, where the $N_{\rm pix} \times N_{\rm pix}$ signal covariance in the bandpower that is being estimated is denoted C^β and the $N_{\rm pix} \times N_{\rm pix}$ matrix C represents the total covariance (signal plus noise). In other words, the optimized weight function minimizes the total expectation value $\left\langle \tilde{C}_\beta \right\rangle$.
Numerically, this can be achieved in the following way: since

$$\begin{aligned} \left\langle \tilde{C}^\beta \right\rangle &= \left\langle \tilde{C}^\beta \right\rangle_{\rm sig} + \left\langle \tilde{C}^\beta \right\rangle_{\rm noise} \\ &= w^T Q_s w + w^T Q_n w = \sum_{lm} a^{W*}_{lm} C_l^{WW} a^W_{lm} + a^{N*}_{lm} C_l^{NN} a^N_{lm} \end{aligned} \tag{3.106}$$

and the signal and noise contributions are computed from

$$\begin{aligned} \left\langle \tilde{C}^\beta \right\rangle_{\rm noise} &= \frac{1}{4\pi} \sum_{lx} W_l \sigma^2(x) W(x)^2 \\ C_l^{WW} &= \int_{-1}^{1} dz \sum_{l'l''} \left(\frac{2l''+1}{16\pi} \right) W_{l''} d^l_{00}(z) d^{l'}_{00}(z) d^{l''}_{00}(z) C^{TT}_{l'}, \end{aligned} \tag{3.107}$$

then one can calculate the weight spectra, perform the transform to the correlation matrix, and solve for the real-space weights using conjugate gradient inversion. In this set-up, the W_l term represents a band-limiting function valued at $l(l+1)/2\pi$ within the band and 0 outside it, whilst the masking is implicit in removing zero-element rows from the covariance matrix.
The standard Conjugate Gradient (CG) method [271] is a popular iterative method used to solve a linear system $Ax = b$ without having to directly invert the symmetric and positive-definite A; this makes it useful when the array size is large and the array is sparse, precisely the case for the correlation matrices in the apodization scenario presented. One can use this procedure to approximate A^{-1} quickly. The aim is to find the two non-zero vectors u and v where

$$u^T A v = 0. \tag{3.108}$$

This is simplified by expanding the solution to the linear equation as

$$x = \sum_{i=1}^{n} \alpha_i p_i \tag{3.109}$$

for some vector p; then one can utilize the summations

$$b = \sum_{i=1}^{n} \alpha_i A p_i, \qquad \alpha_i = \frac{p_i^T b}{p_i^T A p_i} \tag{3.110}$$

to construct an iterative method of finding x. The CG method can be applied to matrices thus:

$$A^T Ax = A^T b \tag{3.111}$$

where it can be seen that if

$$S = p^T Ap \qquad \Rightarrow \qquad A^{-1} = pS^{-1}p^T. \tag{3.112}$$

One can build intuition for this seemingly 'black-box'-type calculation by considering some of the geometry. By constructing a quadratic form

$$f(x) = \frac{1}{2}x^T Ax - b^T x + c \tag{3.113}$$

in terms of the linear system, then taking the gradient shows that the solution to the linear equation is a critical (saddle) point in $f(x)$, to be found by minimization. The iterative method is then equivalent to the method of steepest descent; if the error term is an eigenvector of the matrix A then the convergence is immediate.

Particularly, it is more useful to employ the biconjugate gradient method; this is a subtle modification using the residual vector r, which satisfies the biorthogonality and biconjugacy conditions

$$\bar{r}_i r_j = r_i \bar{r}_j = 0, \qquad \bar{p}_i A p_j = p_i A^T \bar{p}_j = 0 \tag{3.114}$$

wherein with modified recurrence relations one can solve for linear equations which are not necessarily symmetric positive-definite. The rate of convergence of these methods can be improved with the use of a preconditioning matrix, which allows one to set the initial state of the computation closer to the solution of the system. Of course, this requires some intuition about the kind of system that is being solved.

For the E/B-unmixing counterterms equivalent to apodizing e and b, the optimal apodization set-up is more involved. The transfer arrays are given in equation (2.143). In order to satisfy the optimization ansatz, the correlation function to be

inverted is

$$C(\theta) = F(x,x') = \sum_{lm} \begin{pmatrix} C_l^{WW} Y^*_{lm} Y'_{lm} & C_l^{WG} Y^*_{lm} Y'^{G}_{(lm)a'} & C_l^{WE} Y^*_{lm} Y'^{E}_{(lm)b'c'} \\ C_l^{WG} Y^{G*}_{(lm)a} Y'_{lm} & C_l^{GG} Y^{G*}_{(lm)a} Y'^{G}_{(lm)a'} & C_l^{GE} Y^{G*}_{(lm)a} Y'^{E}_{(lm)b'c'} \\ C_l^{WE} Y^{E*}_{(lm)bc} Y'_{lm} & C_l^{GE} Y^{E*}_{(lm)bc} Y'^{G}_{(lm)a'} & C_l^{EE} Y^{E*}_{(lm)bc} Y'^{E}_{(lm)b'c'} \end{pmatrix} + \begin{pmatrix} 0 & 0 & 0 \\ 0 & C_l^{CC} Y^{C*}_{(lm)a} Y'^{C}_{(lm)a'} & C_l^{CB} Y^{C*}_{(lm)a} Y'^{B}_{(lm)b'c'} \\ 0 & C_l^{CB} Y^{B*}_{(lm)bc} Y'^{C}_{(lm)a'} & C_l^{BB} Y^{B*}_{(lm)bc} Y'^{B}_{(lm)b'c'} \end{pmatrix} \tag{3.115}$$

which can be calculated using the spin-s Legendre functions

$$\begin{aligned} P_l^{ss'} &= \frac{4\pi}{2l+1} \sum_m {}_sY^*_{lms'} Y'_{lm} \\ Q_l^{ss'} &= \frac{P_l^{ss'} + (-1)^{s'} P_l^{s,-s'}}{2} \\ R_l^{ss'} &= \frac{P_l^{ss'} - (-1)^{s'} P_l^{s,-s'}}{2}, \end{aligned} \tag{3.116}$$

with summation relations for symmetric and antisymmetric tensors S of rank s

$$\begin{aligned} \sum_m Y^*_{lm} Y'^{S}_{(lm)b'_1\cdots b'_s} &= -\frac{2l+1}{4\pi} P_l^{0s} \mathcal{X}'_{b'_1\cdots b'_s} \\ \sum_m Y^{S*}_{(lm)b_1\cdots b_s} Y'^{S'}_{(lm)b'_1\cdots b'_{s'}} &= \frac{2l+1}{4\pi} (Q_l^{ss'} \mathcal{X}_{b_1\cdots b_s} \mathcal{X}'_{b'_1\cdots b'_s} + R_l^{ss'} \mathcal{Y}_{b_1\cdots b_s} \mathcal{Y}'_{b'_1\cdots b'_s}) \end{aligned} \tag{3.117}$$

where the $\mathcal{X}$ and $\mathcal{Y}$ tensor basis fields correspond to, for tensor ranks 1 and 2,

$$\begin{aligned} Q_{ab} &= \frac{X_a X_b - Y_a Y_b}{2} & U_{ab} &= \frac{X_a Y_b + Y_a X_b}{2} \\ X_a &= \begin{pmatrix} 1 & 0 \end{pmatrix} & Y_a &= \begin{pmatrix} 0 & \sin\theta \end{pmatrix} \end{aligned} \tag{3.118}$$

are tensor and vector basis fields, and similarly for antisymmetric tensors A of rank a. It will be useful to transfer between the tensor and spin-weighted formalisms; one can use the relation between spin- and tensor-harmonics via the null vectors m_a

$$Y^S_{(lm)b_1\cdots b_s} = {}_{-s}Y_{lm} m_{b_1} \cdots m_{b_s} - {}_sY_{lm} \bar{m}_{b_1} \cdots \bar{m}_{b_s}, \qquad m = \frac{\hat{e}_1 + i\hat{e}_2}{2} \tag{3.119}$$

with the correlation functions

$$\langle T\mathcal{X}\rangle = -\sum_l \frac{2l+1}{4\pi} C_l^{TS} P_l^{0s}, \qquad \langle T\mathcal{Y}\rangle = -\sum_l \frac{2l+1}{4\pi} C_l^{TA} P_l^{0a} \tag{3.120}$$

and

$$\begin{aligned}
\langle \mathcal{X}\mathcal{X}'\rangle &= \sum_l \frac{2l+1}{4\pi}(C_l^{SS'} Q_l^{ss'} + C_l^{AA'} R_l^{aa'}) \\
\langle \mathcal{Y}\mathcal{Y}'\rangle &= \sum_l \frac{2l+1}{4\pi}(C_l^{SS'} R_l^{ss'} + C_l^{AA'} Q_l^{aa'}) \\
\langle \mathcal{X}\mathcal{Y}'\rangle &= \sum_l \frac{2l+1}{4\pi}(C_l^{SA'} Q_l^{sa'} - C_l^{AS'} R_l^{sa'})
\end{aligned} \tag{3.121}$$

where the full polarization tensor correlation is

$$\left\langle P^{de} P^{d'e'} \right\rangle = \left(\frac{2l'+1}{4\pi}\right)(R_{l'}^{22} Q^{de} Q'^{d'e'} + Q_{l'}^{22} U^{de} U'^{d'e'}) \tag{3.122}$$

to yield, for the BB spectrum, the scalar weight power spectrum

$$C_l^{WW} = \int_{-1}^{1} dz \sum_{l'l''} \left(\frac{2l''+1}{16\pi}\right) W_{l''} d_{00}^{l}(z) \left[C_{l'}^{+} d_{22}^{l'}(z) d_{22}^{l''}(z) - C_{l'}^{-} d_{2,-2}^{l'}(z) d_{2,-2}^{l''}(z)\right] \tag{3.123}$$

and its corresponding self-coupled spin-mixing spectra

$$\begin{aligned}
C_l^{GG} &= \int_{-1}^{1} dz \sum_{l'l''} \beta_{l''} W_{l''} (N'_{l''})^2 \left[C_{l'}^{+} d_{11}^{l}(z) d_{22}^{l'}(z) d_{11}^{l''}(z) - C_{l'}^{-} d_{1,-1}^{l}(z) d_{2,-2}^{l'}(z) d_{1,-1}^{l''}(z)\right] \\
C_l^{CC} &= \int_{-1}^{1} dz \sum_{l'l''} \beta_{l''} W_{l''} (N'_{l''})^2 \left[C_{l'}^{+} d_{11}^{l}(z) d_{22}^{l'}(z) d_{11}^{l''}(z) + C_{l'}^{-} d_{1,-1}^{l}(z) d_{2,-2}^{l'}(z) d_{1,-1}^{l''}(z)\right] \\
C_l^{EE} &= \int_{-1}^{1} dz \sum_{l'l''} \beta_{l''} W_{l''} N_{l''}^2 \left[C_{l'}^{+} d_{22}^{l}(z) d_{22}^{l'}(z) - C_{l'}^{-} d_{2,-2}^{l}(z) d_{2,-2}^{l'}(z)\right] d_{00}^{l''}(z) \\
C_l^{BB} &= \int_{-1}^{1} dz \sum_{l'l''} \beta_{l''} W_{l''} N_{l''}^2 \left[C_{l'}^{+} d_{22}^{l}(z) d_{22}^{l'}(z) + C_{l'}^{-} d_{2,-2}^{l}(z) d_{2,-2}^{l'}(z)\right] d_{00}^{l''}(z)
\end{aligned} \tag{3.124}$$

and cross-coupled spectra

$$
\begin{aligned}
C_l^{WG} &= \int_{-1}^{1} dz \sum_{l'l''} \beta_{l''} W_{l''} N'_{l''} d^l_{01}(z) \left[-C^+_{l'} d^{l'}_{22}(z) d^{l''}_{12}(z) + C^-_{l'} d^{l'}_{2,-2}(z) d^{l''}_{1,-2}(z) \right] \\
C_l^{WE} &= \int_{-1}^{1} dz \sum_{l'l''} \beta_{l''} W_{l''} N_{l''} d^l_{02}(z) \left[-C^+_{l'} d^{l'}_{22}(z) d^{l''}_{02}(z) + C^-_{l'} d^{l'}_{2,-2}(z) d^{l''}_{02}(z) \right] \\
C_l^{GE} &= \int_{-1}^{1} dz \sum_{l'l''} \beta_{l''} \frac{W_{l''}}{2} (N'_{l''})^2 N_{l''} \left[C^+_{l'} d^l_{12}(z) d^{l'}_{22}(z) - C^-_{l'} d^l_{1,-2}(z) d^{l'}_{2,-2}(z) \right] d^{l''}_{01}(z) \\
C_l^{CB} &= \int_{-1}^{1} dz \sum_{l'l''} \beta_{l''} \frac{W_{l''}}{2} (N'_{l''})^2 N_{l''} \left[C^+_{l'} d^l_{12}(z) d^{l'}_{22}(z) + C^-_{l'} d^l_{1,-2}(z) d^{l'}_{2,-2}(z) \right] d^{l''}_{01}(z) \\
C_l^{CB} &= \int_{-1}^{1} dz \sum_{l'l''} \beta_{l''} \frac{W_{l''}}{2} (N'_{l''})^2 N_{l''} \left[C^+_{l'} d^l_{12}(z) d^{l'}_{22}(z) + C^-_{l'} d^l_{1,-2}(z) d^{l'}_{2,-2}(z) \right] d^{l''}_{01}(z)
\end{aligned}
\tag{3.125}
$$

where $\beta_l = (2l+1)/16\pi$, $C_l^{\pm} = C_l^{EE} \pm C_l^{BB}$ and noting that the superscript XY on the C_l in equation (3.125) refers not to the gradient- and curl-type parts of the cosmological signal but of the mode-unmixing weights, and

$$
\int_{-1}^{1} d^l_{s,\pm s'}(z) d^{l'}_{2,\pm 2}(z) d^{l''}_{2-s,\pm 2\mp s'}(z) = 2 \begin{pmatrix} l & l' & l'' \\ s & -2 & 2-s \end{pmatrix} \begin{pmatrix} l & l' & l'' \\ s' & \mp 2 & \pm 2 \mp s' \end{pmatrix}. \tag{3.126}
$$

The EE spectrum employs similar unmixing terms. As before, one should minimize $\left\langle \tilde{C}_\alpha \right\rangle = w^T Q w = a^T \tilde{Q} a$ which, from the ansatz given, means solving one of the linear systems

$$
Qw = v \qquad \tilde{Q}a = \tilde{v} \tag{3.127}
$$

since v is a unit spin-weight vector. The harmonic components of the weights are

$$
\begin{aligned}
a^W_{lm} &= \sum_x W(x) Y^*_{lm}(x) \\
a^S_{lm} &= -\sum_x W_s(x) \left(\frac{{}_sY^*_{lm}(x) - {}_{-s}Y^*_{lm}(x)}{2} \right) \\
a^A_{lm} &= i \sum_x W_a(x) \left(\frac{{}_aY^*_{lm}(x) + {}_{-a}Y^*_{lm}(x)}{2} \right)
\end{aligned}
\tag{3.128}
$$

so

$$C_l^{\rm full} = \begin{pmatrix} C_l^{WW} & C_l^{WG} & C_l^{WE} & 0 & 0 \\ C_l^{WG} & C_l^{GG} & C_l^{GE} & 0 & 0 \\ C_l^{WE} & C_l^{GE} & C_l^{EE} & 0 & 0 \\ 0 & 0 & 0 & C_l^{CC} & C_l^{CB} \\ 0 & 0 & 0 & C_l^{CB} & C_l^{BB} \end{pmatrix}. \tag{3.129}$$

The correlation matrix in the spin basis is then

$$C(\theta)^{\rm full} = \begin{pmatrix} C^{W_0W_0} & C^{W_0W_1} & C^{W_0W_2} & C^{W_0W_{-1}} & C^{W_0W_{-2}} \\ C^{W_1W_0} & C^{W_1W_1} & C^{W_1W_2} & C^{W_1W_{-1}} & C^{W_1W_{-2}} \\ C^{W_2W_0} & C^{W_2W_1} & C^{W_2W_2} & C^{W_2W_{-1}} & C^{W_2W_{-2}} \\ C^{W_{-1}W_0} & C^{W_{-1}W_1} & C^{W_{-1}W_2} & C^{W_{-1}W_{-1}} & C^{W_{-1}W_{-2}} \\ C^{W_{-2}W_0} & C^{W_{-2}W_1} & C^{W_{-2}W_2} & C^{W_{-2}W_{-1}} & C^{W_{-2}W_{-2}} \end{pmatrix} \tag{3.130}$$

where the harmonic transforms are given by

$$\begin{aligned} C^{W_0W_0} &= \sum_l \frac{2l+1}{4\pi} C_l^{WW} P_l(\cos\theta) \\ C^{W_0W_s} &= -\sum_{lm} \frac{2l+1}{4\pi} C_l^{WS} P_l^{s0}(\cos\theta) \\ C^{W_0W_{-s}} &= -\sum_{lm} \frac{2l+1}{4\pi} C_l^{WS} (-1)^{ls'} P_l^{-s,0}(\cos\theta) \\ C^{W_sW_{s'}} &= C^{W_{-s}W_{-s'}} = \sum_{lm} \frac{2l+1}{4\pi} (C_l^{SS'} + C_l^{AA'}) P_l^{s's}(\cos\theta) \\ C^{W_sW_{-s'}} &= \sum_{lm} \frac{2l+1}{4\pi} (C_l^{SS'} - C_l^{AA'}) (-1)^{l+s} P_l^{ss'}(\cos\theta) \end{aligned} \tag{3.131}$$

again assuming no correlation between parities. Similarly, one can take a quick look at optimality with the higher-order spectra. The full optimal estimator for f_{NL} from the bispectrum is given by

$$\begin{aligned} \hat{f}_{NL} = \frac{1}{N} \sum_{l_i m_i} &\begin{pmatrix} l_1 & l_2 & l_3 \\ m_1 & m_2 & m_3 \end{pmatrix} B_{l_1 l_2 l_3} \\ &\times \left[(C^{-1}a)_{l_1 m_1} (C^{-1}a)_{l_2 m_2} (C^{-1}a)_{l_3 m_3} + C^{-1}_{l_1 m_1, l_2 m_2} (C^{-1}a)_{l_3 m_3} \right] \end{aligned} \tag{3.132}$$

where $N = \sum_{l_i} B^2_{l_1 l_2 l_3} / (C_{l_1} C_{l_2} C_{l_3})$ for an isotropic survey. The optimal estimator for the non-Gaussianity from the two-to-one spectrum can be found in Munshi et al [100]. Since the Fisher matrix encodes the covariance and errors of the estimator, then one can utilize this to minimize the variance of the estimator. The use

of Fisher analysis then represents a robust and straightforward method of optimizing the higher-order spectra; it will be useful in the future to generalize the optimal estimators for the general spectra given in Chapter 2.
Alternatively, in the original power spectrum approach, the band-limited spectra are given by

$$C_\beta[d] = \sum_l^\beta \sum_m |\tilde{a}_{lm}|^2 = \sum_{ij} d_i W_i C_{ij}^\beta W_j d_j. \tag{3.133}$$

This was constructed by simply expanding the harmonic terms into integrals, and then following through the summation of multipoles in the limit of statistical isotropy. A similar calculation may be performed for the bispectrum, giving:

$$B_{\beta_1\beta_2\beta_3}[d] = \sum_{ijk} d_i d_j d_k W_i W_j W_k B_{ijk}^{\beta_1\beta_2\beta_3} \tag{3.134}$$

where $B^{\beta_1\beta_2\beta_3}$ is the bandwidth-limited 3-point real-space correlation function; in practice, the 3 band-limits would be taken as $\beta_1 = \beta_2 = \beta_3$. The general band-limited n-point spectrum is then giving by

$$N_{\beta_1\cdots\beta_n}[d] = \sum_{i_1\cdots i_n, j_1\cdots j_n} d_{i_1}\cdots d_{i_n} W_{i_1}\cdots W_{i_n} N_{i_1\cdots i_n j_1\cdots j_n}^{\beta_1\cdots\beta_n} W_{j_1}\cdots W_{j_n} d_{j_1}\cdots d_{j_n} \tag{3.135}$$

from which one solves

$$W_{i_1}^T \cdots W_{i_n}^T Q_{i_1\cdots i_n} W_{i_1}\cdots W_{i_n} \tag{3.136}$$

by stacking slices of the respective tensors into respective matrices and utilizing the conjugate gradient method as before. Obviously, this is computationally restrictive for all but the lowest-order cumulants. This method, whilst optimizing the higher-order spectra, is not very useful since the non-Gaussian signal is small, hence the summation into the single number f_{NL} is preferred.

3.6 Defect Detection

Previously, a method has been developed with which to detect discontinuities in the underlying CMB Stokes maps. This was motivated physically by the need to probe exotic physics such as topological defects. In chapter 4, its use as a check for systematics is shown, exposing a smoothing issue within the WMAP ILC temper-

ature map. In this section, the theoretical approach (section 2.5) is complemented with analysis of the defect detection method on the HEALPix sphere, in order to understand how useful the Laplacian-difference maps are for defects, and what geometric imprint the HEALPix sphere will have on them.
To perform this, various statistics of Gaussian CMB simulation maps and maps of CMB simulations with a range of toy defects imposed on them are computed. The toy defects are produced in the naive sense of merely adding a Heaviside unitstep $U(x)$ function multiplied by some visibility parameter g to a single CMB simulation; a more realistic method such as the evolution of a cosmic string network would require considerable computation resources. In this sense the calculations are 'proof-of-principle' calculations.
To analyze the produced maps, the localized needlet power is looked at, the power spectra of the Laplacian-difference maps and their skew-spectra, and a brief application of an edge-detection method. If discontinuities exist on all of the T, e and b maps, which might be expected if there were a cosmic string in the microwave sky, then in addition one might reasonably expect position-space correlations between the Laplacian-difference maps of T, Q, U, e and b. Further, since this is in a sense convolving a discontinuity with a polynomial and the form of the polynomial can be computed it may be possible to reconstruct the discontinuity. This would form the basis of a further analysis; the analysis in this thesis is limited mostly to temperature discontinuities using a range of toy models.

3.6.1 Toy Defects

In order to study the utility of the Laplacian-difference method, a number of toy defects will be created and imprinted on a simulated CMB map. The method is implemented by performing the difference of two maps: the spectrally-constructed Laplacian map, created by calculating the harmonic coefficients using the $map2alm$ facility, multiplying these coefficients by $-l(l+1)$ and then forming the harmonic sum via the $alm2map$ facility, and the finite-differenced Laplacian map created by MasQU. As has been seen, there will be overshoot caused by the use of an interpolating polynomial (Runge's phenomenon). Similarly, the limited l-sampling of the $map2alm$ subroutine will produce ringing in the region of any discontinuity (Gibbs' phenomenon). In both cases the exact error can only be calculated in the case that the underlying functional description of the discontinuity is known.
For the special cases such as the toy models, one can calculate the error in both

harmonic and polynomial approximations in order to give a rough estimate as to how noticable the discontinuity could be. This calculation is sketched only for the temperature case of an equatorial step rather than the more complicated polarization case, utilizing the analytic Fourier transform $\mathcal{F}$ of a unit step such as the 1d form

$$\mathcal{F}(U(x)) = \frac{i}{k\sqrt{2\pi}} + \sqrt{\frac{\pi}{2}}\delta(k). \tag{3.137}$$

This allows the construction of the exact Laplacian map of the scalar field (subject to summation truncation in l); by linearity, the effect of the discontinuous injection can be isolated

$$\mathcal{F}(A_{\rm cmb} + gA_{\rm dis}) = \mathcal{F}(A_{\rm cmb}) + g\mathcal{F}(A_{\rm dis}) \tag{3.138}$$

in terms of the visibility function g. Given the full analytic map and the analytic truncated harmonic reconstruction one can calculate the difference $\delta F_{\rm sh}$. By similarly constructing the finite-difference error and then applying the derivative operator to the difference of the two maps one can observe the effectiveness of different n-Laplacians for exposing a particular toy model; an analytic calculation could in principle yield an error bound on the difference map that must be saturated if one wishes to take an edge detection seriously.

There may also be interesting signals in the power spectra of such models. Particularly, one should try to get a handle on the scaling properties of noise. By looking at both the differences between the power spectra of the respective Laplacians and the power spectrum of the $\nabla^2\lambda$ map one can get a feel for the typical characteristics (Fig. 3.19). Note that these two are not the same since it can be shown that the power spectrum is not linear in addition:

$$C_l^A + C_l^B \neq C_l^{A+B} \tag{3.139}$$

specifically, comparison of the terms

$$\begin{aligned} C_l^A - C_l^B &= \frac{1}{2l+1}\sum_m a_{lm}^A a_{lm}^{A*} - a_{lm}^B a_{lm}^{B*} \\ C_l^{|A-B|} &= \frac{1}{2l+1}\sum_m |a_{lm}^A - a_{lm}^B||a_{lm}^A - a_{lm}^B|^* \end{aligned} \tag{3.140}$$

is being made.

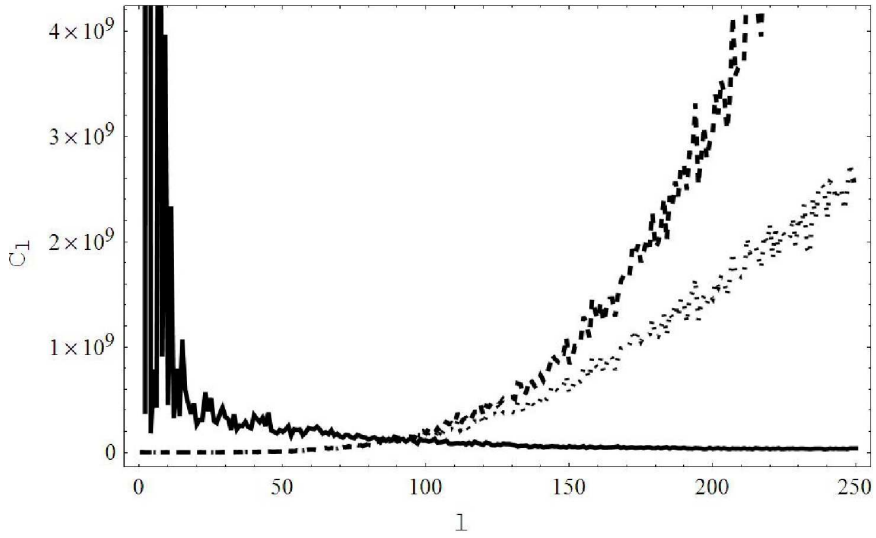

Figure 3.19: Thick line: power spectrum for the O_2 absolute difference map $|\nabla^2 T_{spec} - \nabla^2 T_{F.D.}|$ calculated over a map synthesized from a Gaussian random sample of harmonic coefficients provided by the ($\sigma = 1\mu$K) HEALPix random number generator facility. The dashed and dotted lines are the spectra for the spectrally-calculated and O_2 finite-differenced Laplacian maps respectively. The discrepancy between the dashed and dotted lines decreases with an increased number of sampling points in the finite-differencing calculations. The power spectrum $C_l^{|\nabla^2 T_{spec} - \nabla^2 T_{F.D.}|}$ of the map differences has a white spectrum on small-scales due to the strong correlation of noise between the maps and a boost on large scales due to the HEALPix geometry in the polar cap.

Starting the analysis with the equatorial step model, the equatorial step is defined by

$$F(\theta, \phi) = U(\theta - \pi/2) \tag{3.141}$$

with its harmonic coefficients nonzero only for (l, m)= $(0, 0)$ and (l, m)= $(\text{odd}, 0)$. The first few coefficients, calculated in Mathematica, are given by:

$$f_{00} = \sqrt{\pi} \qquad f_{10} = -\frac{\sqrt{3\pi}}{2} \qquad f_{30} = \frac{\sqrt{7\pi}}{8} \qquad f_{50} = -\frac{11\pi}{16} \tag{3.142}$$

This allows one to construct the ringing map analytically for the step function and then the harmonic error map. In HEALPix, this is only approximate since there will feature some errors from the following:

- The pixel borders are not at the pixel centres specified.
- The HEALPix border has a zigzag-type geometry rather than a flat line geometry.

- The use of the $map2alm$ and $alm2map$ subroutines introduces numerical errors.

To estimate the overshoot of the interpolating polynomial one can assume that the polynomial is exact outside a small radius of the discontinuity meaning that the full calculation is only performed in the discontinuity region. An estimation of the full Laplacian-difference map for the equatorial discontinuity can be seen in (Fig. 3.20).
Now, assuming linearity in the reconstructions, the Laplacian-difference map with $n = 0$ is

$$\nabla^0\lambda = \lambda = (T_{\mathrm{cmb,sh}} + T_{\mathrm{dis,sh}}) - (T_{\mathrm{cmb,ip}} + T_{\mathrm{dis,ip}}) \tag{3.143}$$

and if the difference between the polynomial expressions is small in the region outside the discontinuity, then the calculated Laplacian-difference map is approximately independent of the foreground polynomial-modelled CMB

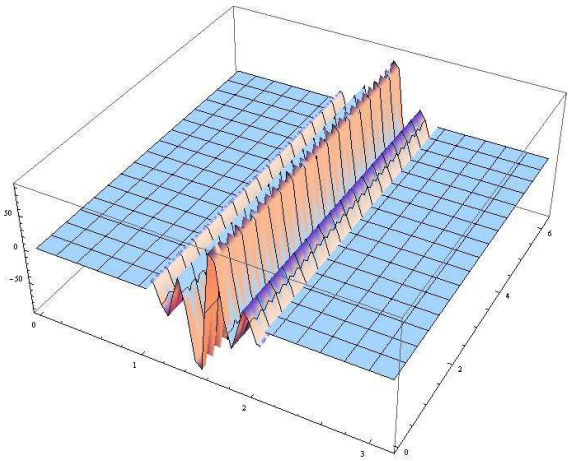

Figure 3.20: Analytically-calculated Laplacian-difference in the restricted discontinuity region from multipoles up to $l = 15$, approximately equivalent to the Laplacian-difference map of the step discontinuity.

$$\lambda \sim A_{\mathrm{dis,sh}} - A_{\mathrm{dis,ip}} \tag{3.144}$$

i.e., it is approximately a difference map for the discontinuity. The differences between the spectrally-constructed and finite-differenced maps will show greater localization of differences at lower order; one could use larger stencils about the discontinuity to optimise the combination of accuracy and locality. By corollary then, one could use the Kim method [197] to clean the ringing of the harmonic map and enhance the method further.

Figures 3.21, 3.22, 3.23 and 3.25 show a variety of results for the full MasQU discontinuity method; note that the best order of Laplacian-difference for enhancing the discontinuity is dependent on that discontinuity's geometry. By utilizing the Kaiser-Stebbins relation (2.193), and by setting the dynamical properties $\gamma_s \mathbf{v}_s \cdot (\mathbf{s} \times \mathbf{k}) = 1$ (such that the string is assumed to be oriented toward the observer), an approximation to the string tensions probed by the Laplacian-difference method can be made. This is reasonable for string velocities $0.2 \lesssim |\mathbf{v}_s| \lesssim 0.9$. These should be resolution-independent, since a physical discontinuity is infinitesimal in thickness. The by-eye limits are calculated as shown in Table 3.4; one can reconstruct δT, and hence $G\mu$ from the map by reverse-engineering, i.e., isolate a suspected discontinuity, throw an identically-shaped discontinuity into a Gaussian map of identical mean and variance to the signal map (corrected for the presence of the discontinuity), then measure what injection g achieves the same visibility for the detected discontinuity.

Table 3.4: By-eye detection limits for string tensions via MasQU temperature analysis.

Laplacian order	Stencil order	Injection limit (μK)	String tension $G\mu$ limit
2	2	40	$\sim 1.6 \times 10^{-6}$
2	4	15	$\sim 6 \times 10^{-7}$
2	6	10	$\sim 4 \times 10^{-7}$

One can also seek to expose the discontinuities using the needlet approach. One can isolate the contributions of each scale to the Laplacian-difference map by constructing

$$T_j(\Omega) = \sum_k \beta_{jk} \psi_{jk}(\Omega) \tag{3.145}$$

where the full map reconstruction is

$$T(\Omega) = \sum_j T_j(\Omega). \tag{3.146}$$

Since it is already known that the discontinuity scale is at the individual-pixel level, then the discontinuity signal should at least be apparent in the scale j corresponding to the pixel-level scale. Figure 3.24 shows the needlet maps for the diamond model with some very subtle values of g; the limits in Table 3.4 can correspondingly be reduced by $\sim 10\%$ when utilizing the needlet maps.

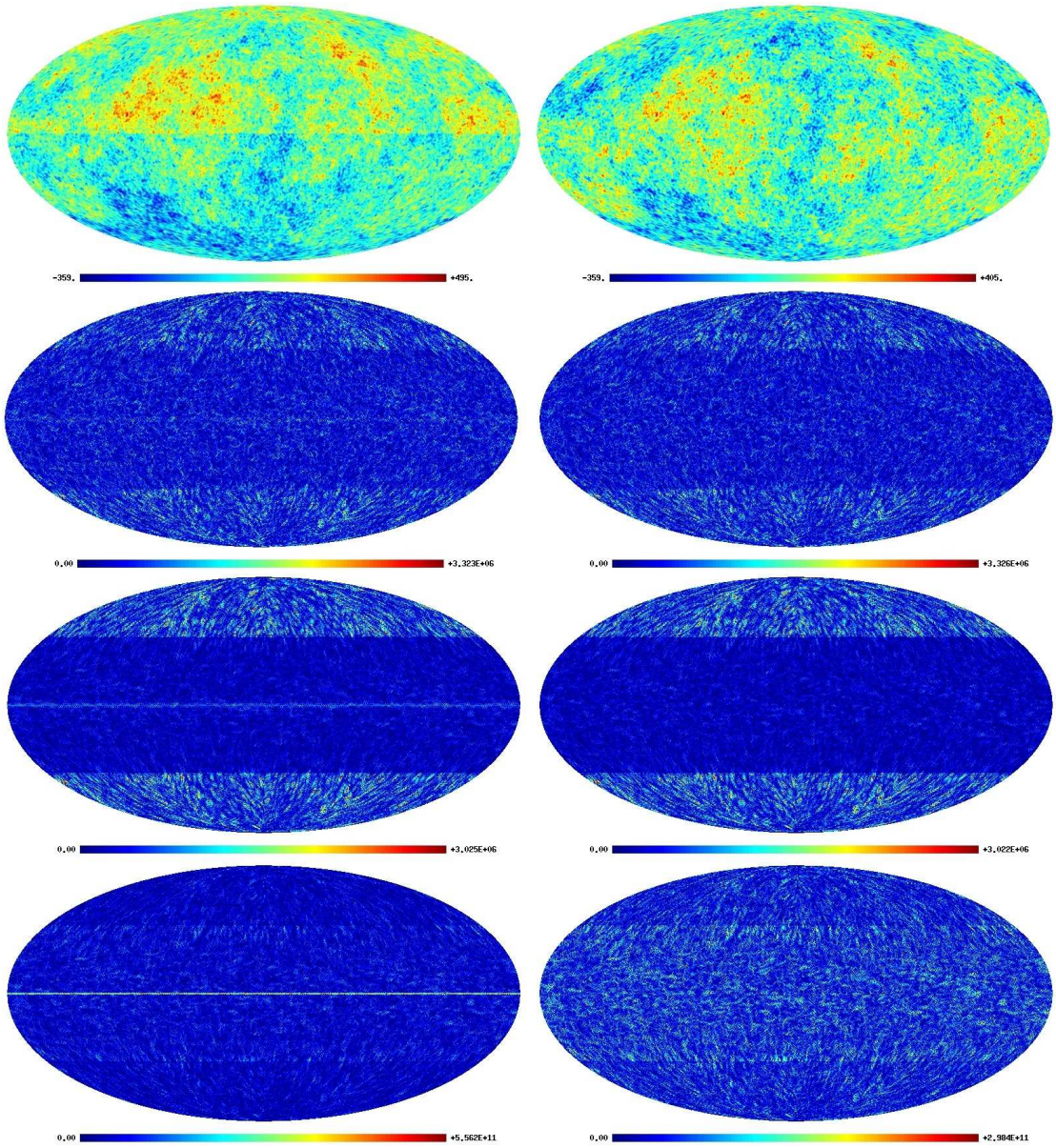

Figure 3.21: Left column: T + 100 μK discontinuity map, $\nabla^2\lambda^T$ at O_2, $\nabla^2\lambda^T$ and $\nabla^4\lambda^T$ both at O_4. Unlike the diamond case (Fig. 3.22), the line is even more enhanced by the bi-Laplacian-difference. Right column: T + 10 μK map, $\nabla^2\lambda^T$ at O_2, $\nabla^2\lambda^T$ and $\nabla^4\lambda^T$ both at O_4.

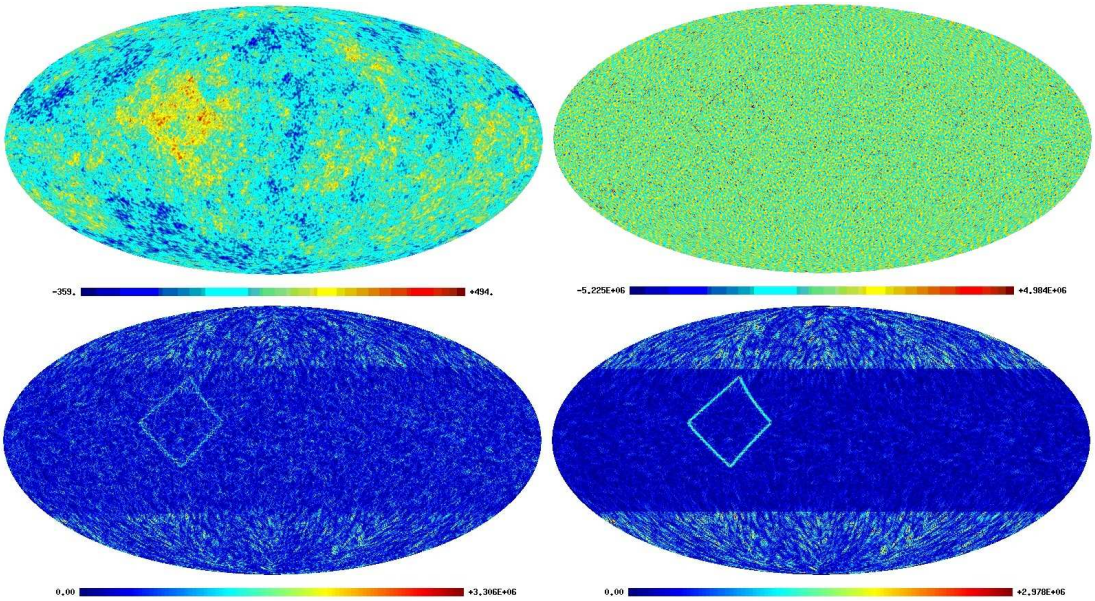

Figure 3.22: Top, left-to-right: standard CMB temperature map with a diamond-shaped anomaly added (+ 100 μK) and the map of the Laplacian; Bottom, left-to-right: enhanced temperature discontinuity in the Laplacian-difference map at O_2 (left) and O_4 (right). The higher order term is even more enhanced.

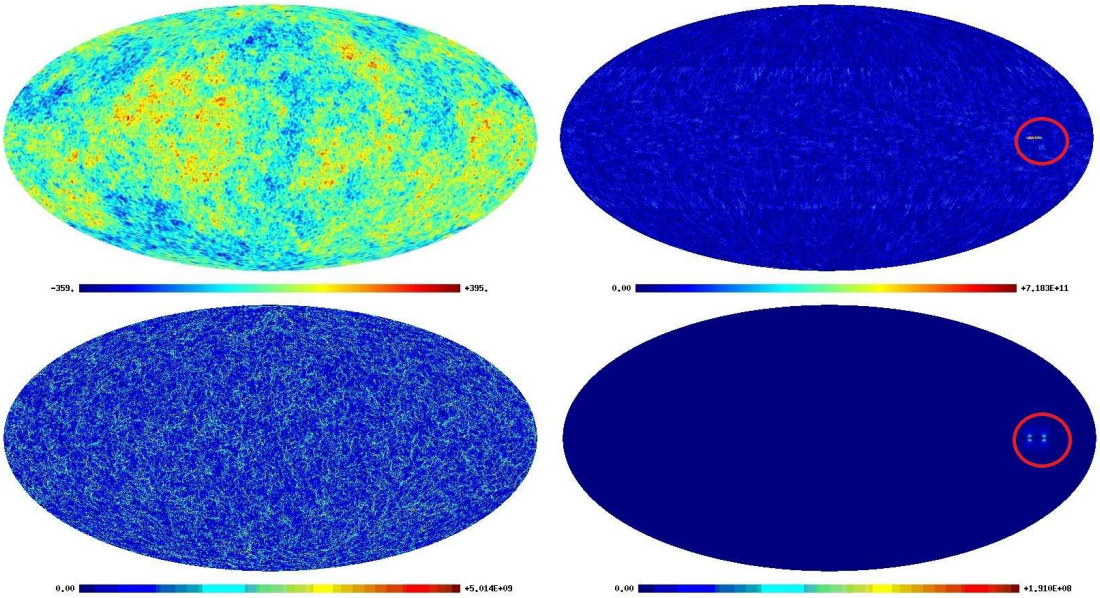

Figure 3.23: Top diagram: T map for a line-shaped anomaly and $\nabla^4\lambda^T$ at O_4. The anomaly has been ringed in red. Unlike the diamond case, the line is even more enhanced by the bi-Laplacian-difference. Bottom $\lambda^{\nabla^4 e}$ and $\lambda^{\nabla^4 b}$ at O_2 for the toy model imposed on the Q map.

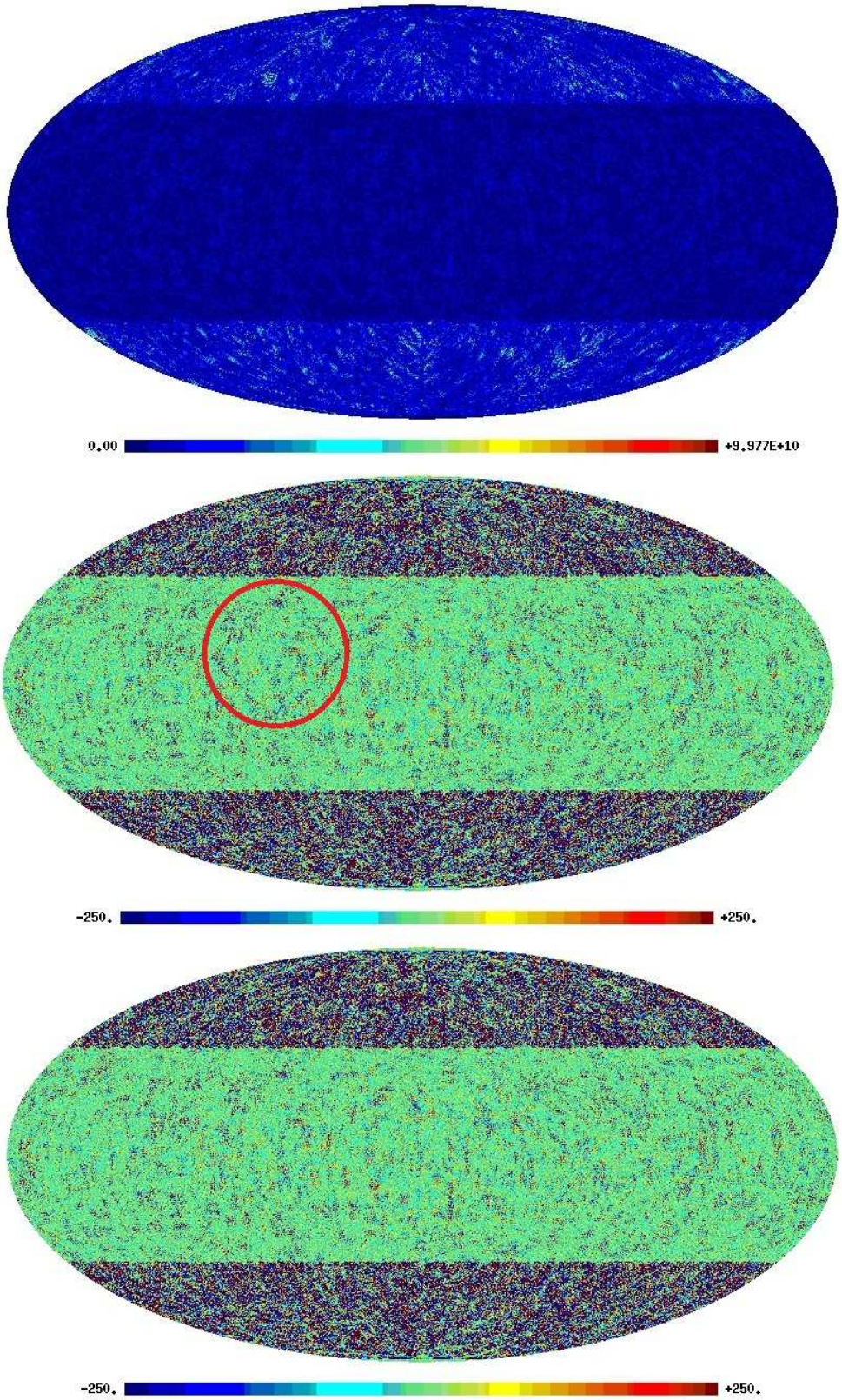

Figure 3.24: Top diagram: $O_6\ \nabla^2\lambda^T$ map with a diamond-shaped 10μK injection, at $N_{\rm side} = 128$ with needlet frequency band term $B = 2$; Central diagram: isolated $j = 8$ contribution of the top diagram. Whilst it is difficult to make out any imprint of the anomaly in the top diagram, the discontinuity can be seen here ringed in red. Bottom diagram: Isolated $j = 8$ contribution for an $O_6\ \nabla^2\lambda^T$ map with a 5 μK injection; this is beyond the limits of analyzing by-eye the needlet-decomposed Laplacian-difference maps.

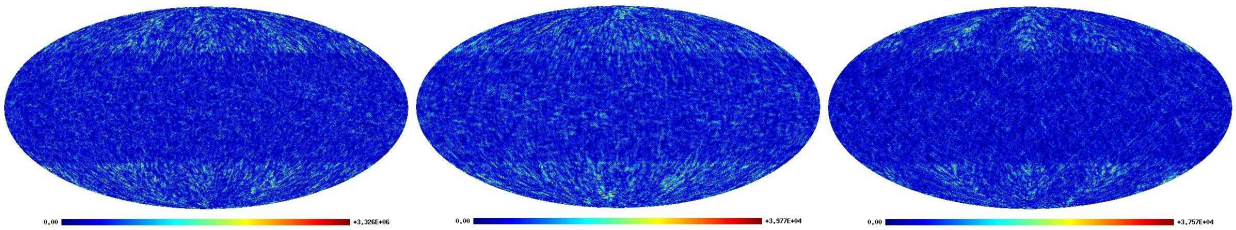

Figure 3.25: CMB simulation maps of $\nabla^2\lambda^T$, $\nabla^2\lambda^Q$ and $\nabla^2\lambda^U$. The large polar cap values are from higher pixelization errors from the deformed stencil geometries; these must be distinguished from any discontinuity or point signal, ideally by rotating the signal about the ϕ coordinate.

Figures 3.26 and 3.27 show power-spectral and skew-spectral calculations for the toy models; whilst it can be seen that the toy models inject a small amount of power into each, there is no characteristic signal for the existence, or geometry, of a discontinuity here. Rather, a small non-zero skew-spectrum might be a signal to check the discontinuity maps in the first place.
The standard statistic

$$\chi^2 = \frac{\langle (T_{i,\mathrm{map}} - T_{i,\mathrm{null}})^2 \rangle}{\langle T^2_{i,\mathrm{null}} \rangle} \tag{3.147}$$

does not give any particularly useful information, beyond a departure from Gaussianity already implicit in the nature of the maps. However, the pixel maps

$$\chi^2_i = \frac{(T_{i,\mathrm{map}} - T_{i,\mathrm{null}})^2}{T^2_{i,\mathrm{null}}} \tag{3.148}$$

show some measure of the correlation in the maps without having to perform the laborious $N_{\mathrm{pix}} \times N_{\mathrm{pix}}$ matrix analysis; indeed, this can be used to isolate the discontinuity more clearly (Fig. 3.28). In a real measurement, one does not have the null map to measure against; instead this confirms that the differenced Laplacian maps are better described as correlation-type maps than edge-type maps.
Such an observation has interesting corollaries for further developments of the MasQU software. An interesting enhancement of this software might be to utilize the Canny edge-detection algorithm developed in Danos & Brandenberger [233] not on the CMB temperature anisotropy maps, but rather on the Laplacian-difference maps that have been created here. This would have the advantage of much lower storage space requirements than the needlet approach coupled to the ease-of-use with constructing just one map to analyze. Figure 3.29 shows a first attempt at Canny analysis utilizing Mathematica's functionality; these results do not show any advantage in the employment of the Canny method on the differenced maps, although a more rigorous implementation might yield different

results.

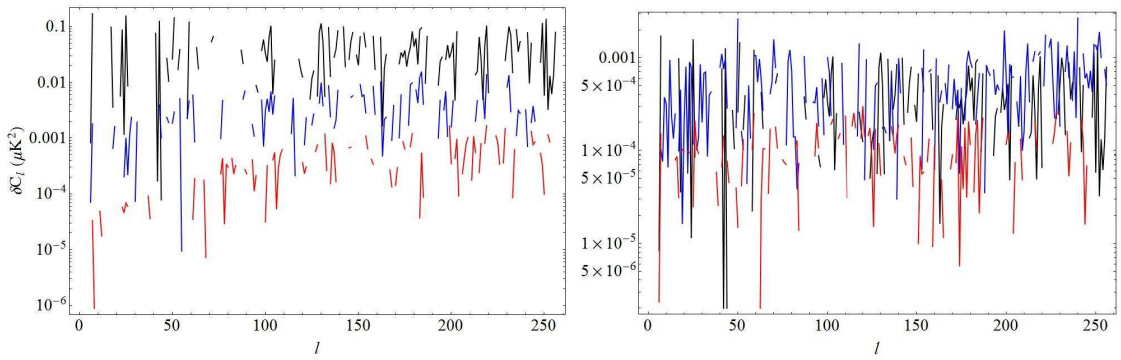

Figure 3.26: Fractional power-spectral differences in values of δC_l between the discontinuity and Gaussian CMB maps; Left: Equatorial step model for 100μK (black), 10μK (blue) and 1μK (red) injections, calculated at O_2. Right: 100μK equatorial step (black), diamond (blue) and line (red) models, calculated at O_2.

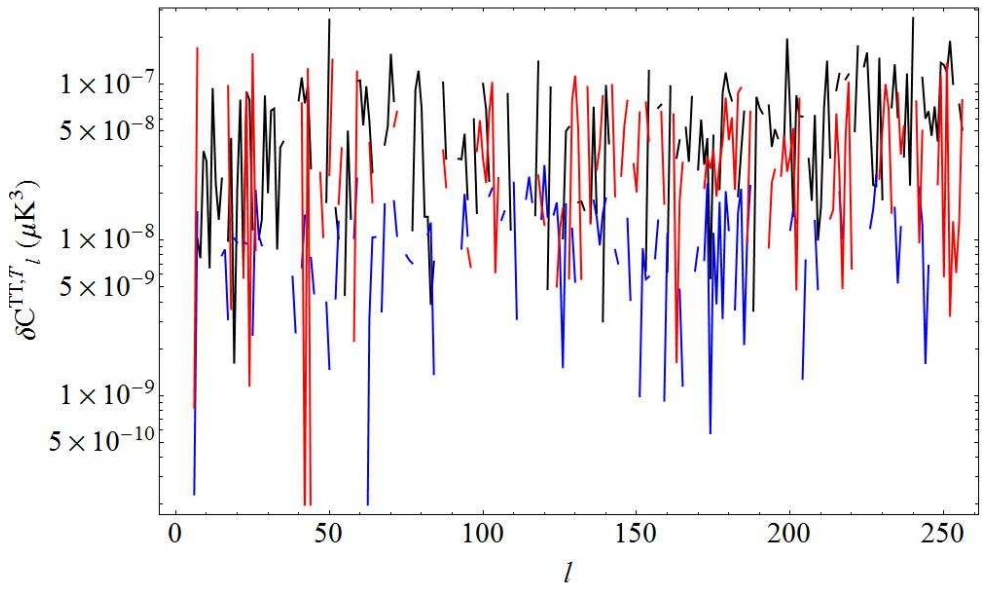

Figure 3.27: Skew-spectral differences in values of δC_l between the discontinuity and Gaussian CMB maps for the 100μK equatorial step (black), diamond (blue) and line (red) models, calculated at O_2.

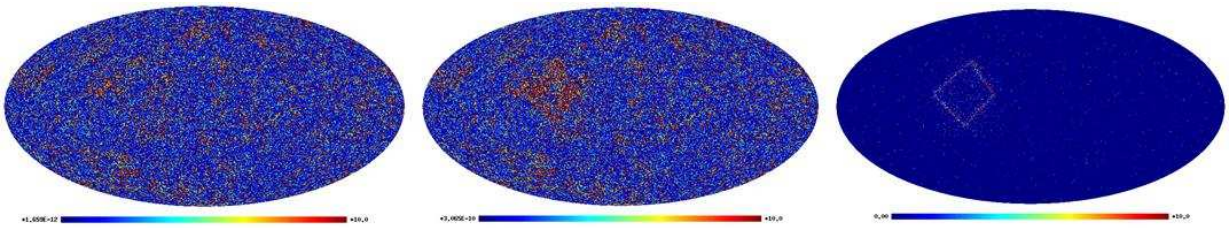

Figure 3.28: Left-to-right: CMB simulation, simulation + diamond model, O_2 $\nabla^2\lambda^T$ simulation + diamond. By definition of using a Gaussian null map to measure against, the discontinuous pattern can be separated for any given injection. However, the use of these maps is not in making inferences about real data; rather, it shows that the signal is not really of edge-type.

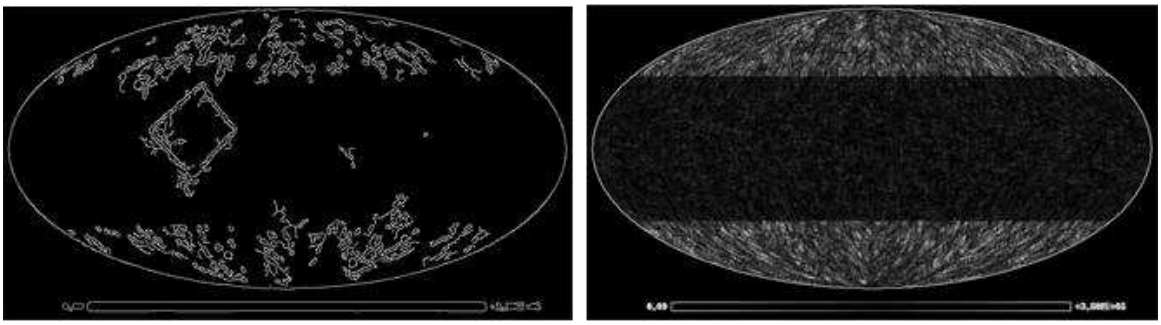

Figure 3.29: Canny edge maps determined using Mathematica; the left diagram is the O_2 100μK diamond, the right diagram the O_6 10μK diamond. This first attempt suggests that the Mathematica approach is not very effective, since it operates on an image of the data rather than the raw data; this result may change with a more in-depth custom implementation.

3.7 Signals of a Finite Resolution CMB

The final section of this chapter features an elaboration of potential signals of a finite resolution CMB. This is explored using a not unreasonable set of approximations. The first approximation used is the utility of the ud_grade HEALPix facility to simulate a finite-resolution map by upgrading the resolution of the input map to that of an output map denoted $T_{\mathrm{in}\to\mathrm{out}}$. The caveats here are that a local lattice-type resolution (as opposed to so-called 'fuzzy' structures) is being presumed and that the exact geometry of the lattice vertices is not very relevant to this study; the vertices corresponding to the HEALPix grid vertices can be used.

The second approximation is used in the set of comparison maps; a variety of discrete injection maps, like those used for the discontinuities previously explored,

are used to approximate a string network without having to resort to computationally expensive simulation. Since it is only the broad geometry of decrement that is of interest here, it is expected that this is a reasonable starting point.
Figures 3.30 and 3.31 show the MasQU results for both types of map, for the temperature case only. A quite characteristic signal of the finite-resolution maps can be seen. Whilst realistically one would want the mock string network maps to mimic the local structure of the finite-resolution maps, the variety of maps produced show (a) that this can in principle be achieved and (b) that they provide a reasonable approximation when calculating power spectra, since local structures are smoothed out in a harmonic transform.
It is precisely the further harmonic-type and Canny-type algorithms which can separate the two map types; Fig. 3.32 shows that the Canny maps, as operated on the CMB skies instead of the (not very effective) Canny analysis on the Laplacian-difference maps, are considerably more effective for finite-resolution maps than for the mock string networks — the finite maps unambiguously feature edge-like structures, by definition.
Meanwhile, it is the power spectral analysis which would really unambiguously expose the difference in the underlying physics of the maps; since there is no variation in the finite-resolution maps beyond the maximum resolution, one expects a large drop in power beyond the Nyquist scale of the maximum resolution (Fig. 3.33) for the power spectrum — in contrast to the mock string network maps. This simple physical result could be coupled with more exotic effects of an underlying lattice structure depending on the lattice physics, such as violations of statistical isotropy or local Lorentz invariance.
One might further expect interesting cross-correlation with the polarization sky maps that would further differentiate a finite CMB from a string network.

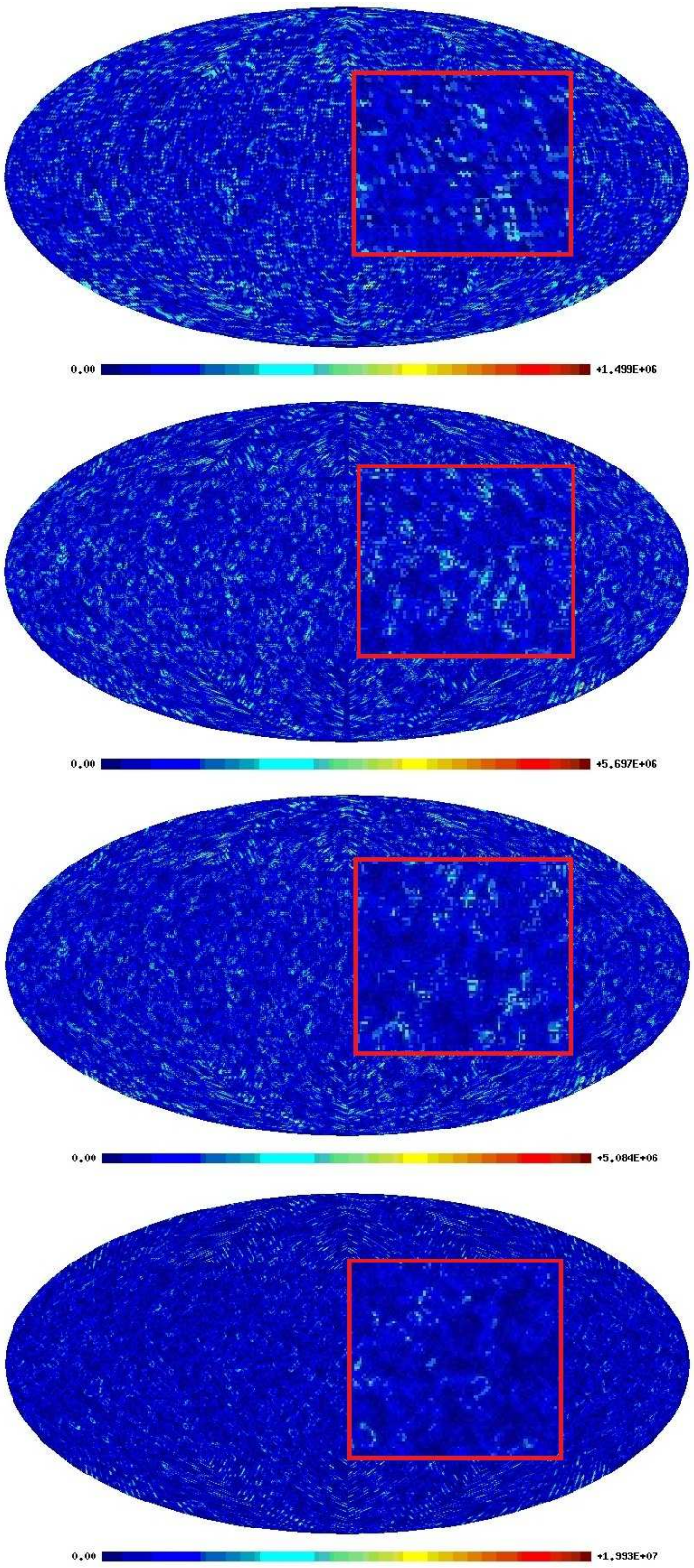

Figure 3.30: Top 2 diagrams: Laplacian-difference maps $\nabla^2\lambda^{T_{32\to 64}}$ at O_2 (top) and $\nabla^2\lambda^{T_{32\to 128}}$ at O_4 (next diagram down). Bottom 2 diagrams: $\nabla^4\lambda^{T_{32\to 128}}$ at O_4 (above bottom diagram) and $\nabla^2\lambda^{T_{32\to 256}}$ at O_2 (bottom), with a blown-up square region inside the red boxes. The maps contain jagged edge structures. The discrete underlying structure becomes more clear at higher orders and for a larger output map sampling resolution, characteristically different from the Gaussian maps seen in section 3.6.

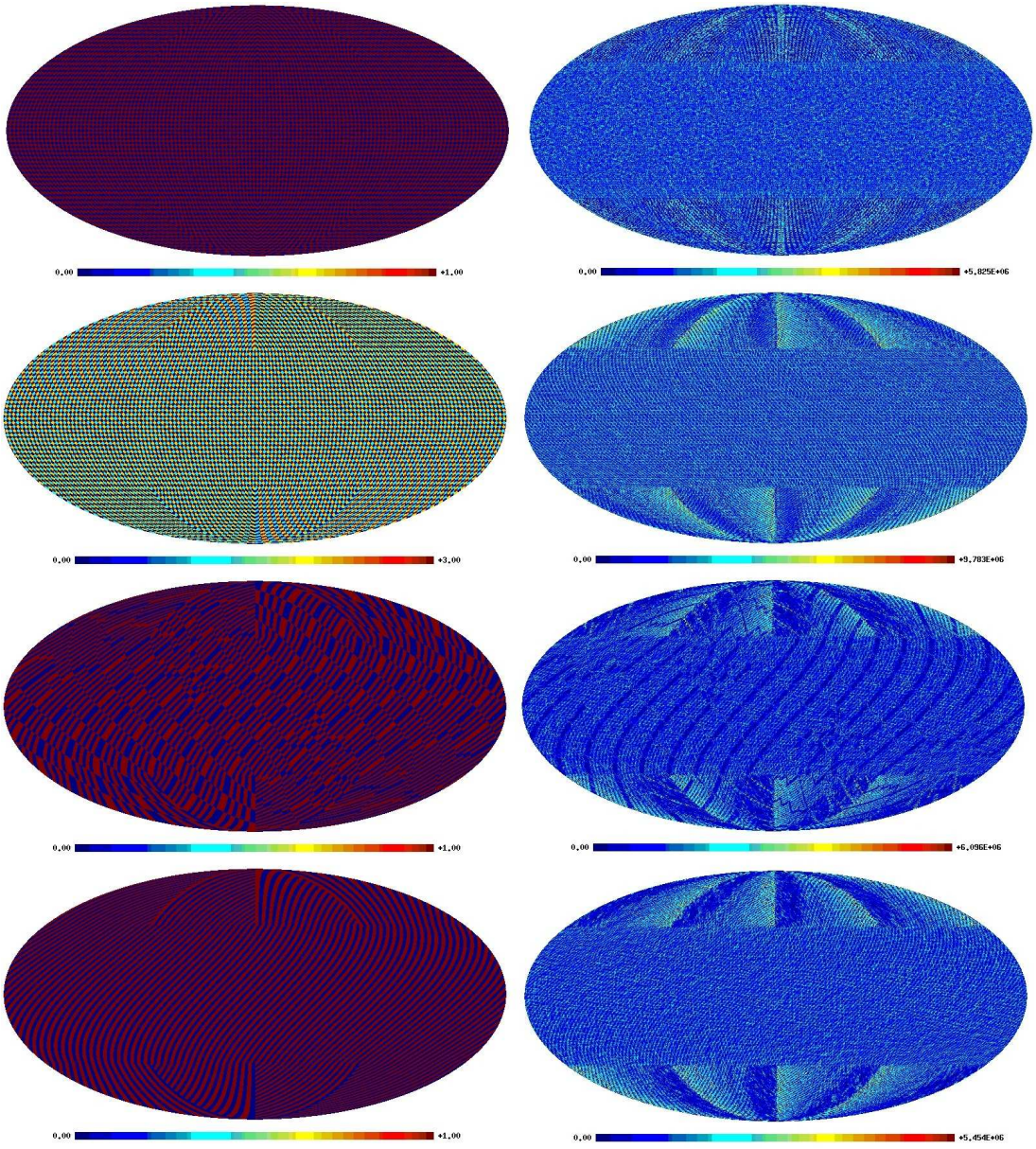

Figure 3.31: Mock string networks defined at $N_{\rm side} = 32$ and injected into $N_{\rm side} = 128$ CMB simulations. Left-to-right: Injection maps, Laplacian-difference maps $\nabla^2\lambda$ at O_2.Top-to-bottom: 'Binary', 'Quad', 'S-line' and 'L-line' injections.

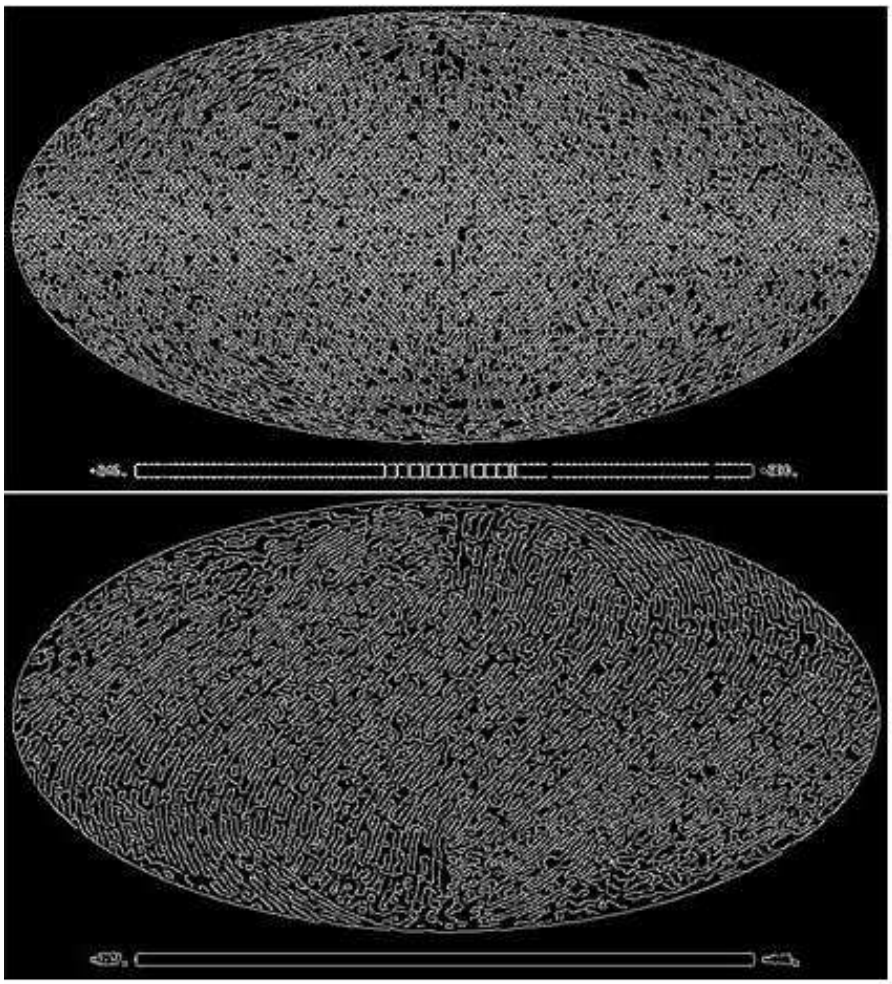

Figure 3.32: Results of a Canny-algorithm detection on the $T_{32\to128}$ map (top diagram) and CMB simulation + 'L-line' injection map (bottom diagram), as defined in Fig. 3.31. The Canny algorithm performs well for the finite resolution map, whilst the exact structure of the injection map is not entirely clear.

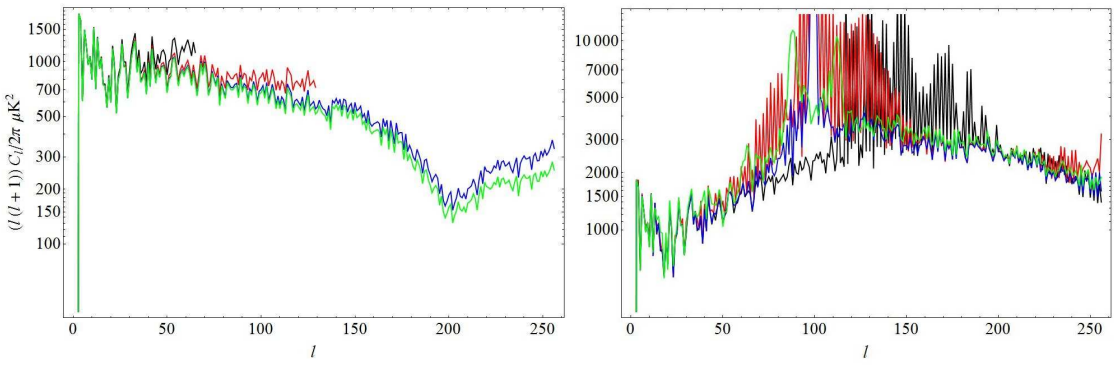

Figure 3.33: Power spectra for the finite CMB maps and the mock string networks. (Black, red, blue, green): Left diagram = ($T_{32\to32}$, $T_{32\to64}$, $T_{32\to128}$, $T_{32\to256}$). Right diagram = (Binary, Quad, L-line, S-line), as defined in Fig. 3.31.

3.8 Summary

The MasQU software package is a tool for calculating the derivatives of a field by finite-differencing, useful for constructing the scalar and pseudo-scalar fields $\nabla^4 e$ and $\nabla^4 b$. On the HEALPix sphere, the most popular pixelization for CMB analyses, technical details related to the pole — specifically, the coordinate singularity and decreased grid resolution in its immediate vicinity — motivates the study of rotated sampling methods. One result of this study was the construction of a method to accurately reconstruct the harmonic spectral coefficients of an input field. Since rotated sampling methods add considerable computation time to the software, then in the limit of high-resolution maps the pole problem may be better resolved by removing information in the troublesome regions.

On a masked sky, even at its lowest accuracy setting the MasQU software outperforms the raw harmonic calculation. A mock EBEX study was made which suggested that certainly a crude MasQU analysis may be advantageous compared to standard EBEX methods. In future, an improved implementation should be tested against alternative methods for solving the E/B mixing problem, in order to make a fair appraisal. The estimators used in the MasQU approach can be optimized by utilizing apodization techniques calculated from Fisher analysis and iterative matrix inversion techniques. The scalar field approach has the advantage of greatly reduced matrix sizes compared with methods that calculate the E- and B-modes directly.

Test applications of the Laplacian-difference method were also a success. By reverse-engineering, It is possible to obtain crude bounds on the cosmic string tension that are competitive with alternative methods, and may be further improved in combination with these methods. The Laplacian-difference method was also used to illustrate the uniqueness of signals from a finite-resolution CMB.

Chapter 4

Cosmology with MasQU

Having set up a number of problems which can be solved using the finite-difference method (chapter 2), manifested in the software package MasQU (chapter 3), an analysis is now made of current WMAP data and an inference of the detection bounds that can be probed with the upcoming Plank data. For the WMAP case, both the temperature anisotropy ILC map and the polarization HILC maps are analyzed.

4.1 WMAP and Planck

The famous temperature anisotropy map created from the WMAP data is constructed using the Internal Linear Combination (ILC) method, a weighted sum over the foreground-reduced maps of each frequency band. This map is not used directly as the dataset for the construction of the power spectrum, but rather as an approach to estimating the foreground-reduced anisotropy map. The idea is to sum the WMAP observations over its frequency bands (K, Ka, Q, V and W corresponding to a frequency range of 23 to 94 GHz), each band weighted in such a way as to keep the CMB signal response constant whilst approximately cancelling the galactic signal distribution. This allows one to gain a first estimate on the model-independent foreground noise; the next step is to use this as a guide for producing a more accurate foreground analysis using known astrophysics and, in the case of WMAP, a maximum entropy method spatial fit.

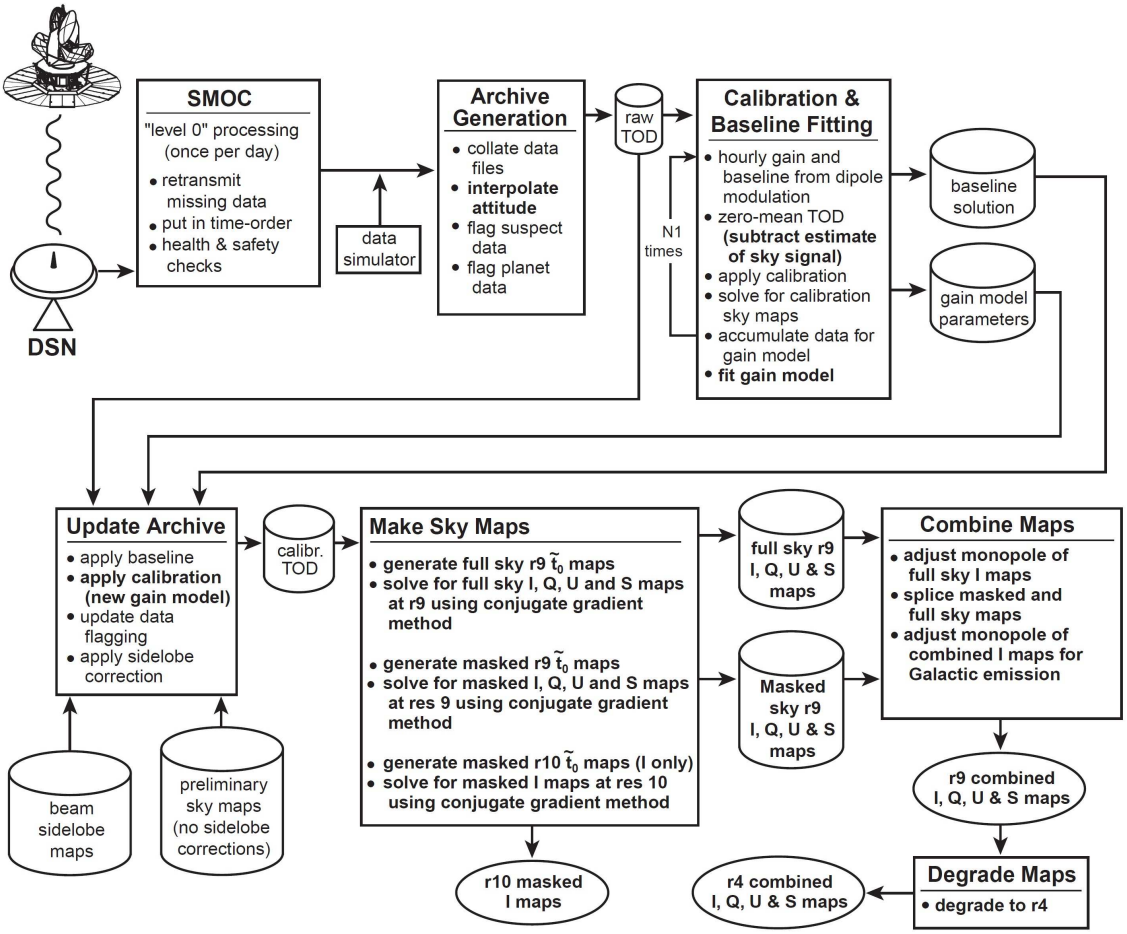

Figure 4.1: The WMAP map-making procedure for maps at each of the 5 frequency bands, from Jarosik et al [272].

Typically the major noise sources for the temperature case are free-free, synchrotron and (thermal) dust emission and point sources. Since not only is the ILC the first point of contact of observational cosmology with analysis after the time-ordered data analysis (see Fig. 4.1), but also a focal point for an array of searches and claims for CMB anomalies, one should perform an analysis on this map. It should be noted that the WMAP publications caution against the use of the ILC for cosmology. For the purposes here, instrumental issues such as beam profiles et cetera will not be considered. Following Hinshaw et al [273], for a simplistic negligible noise, uniform foreground model the ILC map is given by

$$T_{\rm ILC} = \sum_i \zeta_i T_i(p) = \sum_i \zeta_i (T_c(p) + S_i T_f(p)) = T_c(p) + \Gamma T_f(p) \tag{4.1}$$

where T_i is the frequency map, T_c the CMB contribution, $S_i T_f(p)$ the foreground

contribution and T_f the spatial distribution. In the WMAP analysis, this simplification is improved by splitting the sky map into 11 sections of the galactic plane (which dominates the noise contribution) and 1 part outside the galactic cut. There are also constraints for normalization

$$\sum_i \zeta_i = 1, \qquad \Gamma \equiv \sum_i \zeta_i S_i \tag{4.2}$$

isolating approximately only the CMB signal. One can determine the combination weights ζ_i by minimizing the variance of $T_{\rm ILC}$:

$$\sigma^2_{\rm ILC} = \left\langle T^2_{\rm ILC}(p) \right\rangle - \left\langle T_{\rm ILC}(p) \right\rangle^2 = \sigma_c^2 + 2\Gamma\sigma_{cf} + \Gamma^2\sigma_f^2 \tag{4.3}$$

with the brackets signifying an average over pixels; since each of the 12 regions has a discontinuous boundary, they must be treated independently with the boundary smoothed over at the combination phase for creating the full ILC map. Granted, the remaining noise correlations will take a non-simple form by definition of the simplicity of the removed noise model and due to the complications (boundary issues and non-linearity) of the map creation method. Following Hinshaw et al [273], the ILC variance is calculated by the linearized Lagrange method of Eriksen et al [274] by minimizing

$$\frac{\partial\sigma^2_{\rm ILC}}{\partial\zeta_i} = 2\frac{\partial\Gamma}{\partial\zeta_i}\sigma_{cf} + 2\Gamma\frac{\partial\Gamma}{\partial\zeta_i}\sigma_f^2, \tag{4.4}$$

so minimization gives

$$\Gamma = -\frac{\sigma_{cf}}{\sigma_f^2} \tag{4.5}$$

hence

$$T_{\rm ILC}(p) = T_c(p) - \frac{\sigma_{cf}}{\sigma_f^2}T_f(p), \qquad \sigma^2_{\rm ILC} = \sigma_c^2 - \frac{\sigma_{cf}^2}{\sigma_f^2} \tag{4.6}$$

This produces a bias $\sigma^2_{\rm ILC} \leq \sigma_c^2$ in the CMB map, of order $\sim 10\mu$K in the galactic plane. For the case of non-uniform foreground noise,

$$\sigma^2_{\rm ILC} = \left\langle T_c^2 \right\rangle - \left\langle T_c \right\rangle^2 + 2(\left\langle T_c\Gamma T_f \right\rangle - \left\langle T_c \right\rangle \left\langle \Gamma T_f \right\rangle) + (\left\langle \Gamma^2 T_f^2 \right\rangle - \left\langle \Gamma T_f \right\rangle^2) \tag{4.7}$$

with minimum variance solution

$$\left\langle \Gamma T_f \cdot S_i T_i \right\rangle = -\left\langle T_c \cdot S_i T_f \right\rangle \qquad \Rightarrow \qquad \sum_j \left\langle S_i T_f \cdot S_j T_f \right\rangle \zeta_j = -\left\langle T_c \cdot S_i T_f \right\rangle \tag{4.8}$$

where the 11 regions of the galactic plane are chosen such that the covariance between the CMB and the foreground is minimized (which provides the map bias). Hence the multi-frequency analogue of (4.5) is

$$\Gamma = -\sum_{ij} S_i \cdot (F^{-1})_{ij} \cdot C_j \tag{4.9}$$

with

$$F_{ij} \equiv \langle S_i T_f \cdot S_j T_f \rangle \qquad C_i \equiv \langle T_c \cdot S_i T_f \rangle \,. \tag{4.10}$$

Without an underlying model, bias correction is limited to the use of Monte Carlo simulations. For each region of the divided CMB map n, one finds the $\zeta_{i,n}$ by minimizing the variance of

$$T_n(p) = \sum_{i=1} \zeta_{n,i} T_i(p) \tag{4.11}$$

The full map is formed by combining the T_n; the boundaries are blended with a 1° Gaussian filter to minimize edge effects. The final combination is produced using weights for pixel p and the 12 regions R

$$w_n(p) = \begin{cases} 1 & p \in R_n \\ 0 & \text{else} \end{cases} \tag{4.12}$$

where the smoothing with a kernel correspondingly forms the smoothed weights $\bar{w}_n$. Finally, one calculates the conjugate gradient inverse:

$$T(p) = \frac{\sum_n \bar{w}_n(p) T(p)}{\sum_n \bar{w}_n} \tag{4.13}$$

to form the ILC map from the combinations of the 12 different regions. For the 7-year data, the full ILC map depends on the updated calibration and beam systematics [275]. According to Gold et al [275], the variance between the ILC map and CMB maps made with other techniques is less than $116\ \mu\mathrm{K}^2$.
Similarly, one can employ the Harmonic ILC (HILC [276]) approach for the noise-heavy WMAP maps via the following polarization map estimator:

$$\sum_k w^k(x)(Q(x,\nu_k) \pm iU(x,\nu_k)), \qquad \sum_k w^k(x) = 1 \tag{4.14}$$

with variance

$$\sigma^2 \approx C^2 + 2\left\langle \mathrm{Re}[(Q_{\mathrm{cmb}}(x) \pm iU_{\mathrm{cmb}}(x))\zeta(x)]\right\rangle + \left\langle |\zeta(x)|^2\right\rangle \tag{4.15}$$

where C^2 is the variance of the CMB polarization signal and $\zeta(x) = \sum_k w^k(Q_{fg}(x)\pm iU_{fg}(x))$. The linear weights can be determined by minimizing

$$\begin{aligned}\sum_{klm} \alpha^{k'k}_{l'm'lm}\tilde{w}^k_{lm} + \lambda_{l'm'} = \lambda_{00}\frac{\partial(-\sqrt{4\pi} + \partial\sum_i \bar{w}^k_{00})}{\partial \bar{w}^{k'}_{l'm'}} \\ + \frac{\partial\sum_{LM}|a_{\pm 2,LM}|^2}{\partial \bar{w}^{k'}_{l'm'}} + \sum_{l>0,m}\lambda_{lm}\frac{\partial\sum_i \bar{w}^k_{lm}}{\partial \bar{w}^{k'}_{l'm'}}\end{aligned} \tag{4.16}$$

where

$$\begin{aligned} w^k_{lm} &= \int w^k(\Omega)Y^*_{lm}(\Omega)d\Omega \\ \alpha^{k'k}_{l'm'lm} &= 2\mathrm{Re}\left[\sum_{LM}\hat{\gamma}^*_k(l',m',L,M)\gamma^*_k(l,m,L,M)\right] \\ a^k_{\pm 2,lm} &= \int {}_{\pm 2}Y^*_{lm}(\Omega)(Q(\Omega,\nu_k) \pm iU(\Omega,\nu_k))d\Omega \\ \gamma_k(l_1,m_1,l_3,m_3) &= \sum_{l_2m_2}(-1)^{m_2}\sqrt{\frac{(2l_1+1)(2l_2+1)(2l_3+1)}{4\pi}} \\ &\quad\times \begin{pmatrix} l_1 & l_2 & l_3 \\ m_1 & m_2 & -m_3\end{pmatrix}\begin{pmatrix} l_1 & l_2 & l_3 \\ 0 & \pm 2 & \mp 2\end{pmatrix} a^k_{\pm 2,l_2m_2}. \end{aligned} \tag{4.17}$$

By assuming independence of the linear weights, the variance on the E- and B-modes signals is

$$\begin{aligned} \sigma^2_{EE(BB)} &= \left\langle |Q_{E(B)}(\Omega) \pm iU_{E(B)}(\Omega)|^2\right\rangle \\ Q_E(\Omega) \pm iU_E(\Omega) &= -\sum_{lm} a^k_{E,lm\pm 2}Y_{lm}(\Omega) \\ Q_B(\Omega) \pm iU_B(\Omega) &= \mp i\sum_{lm} a^k_{B,lm\pm 2}Y_{lm}(\Omega). \end{aligned} \tag{4.18}$$

Since these weights are determined in harmonic space, one would expect that no boundary discontinuity issues exist as opposed to the standard WMAP ILC analysis (noting that the HILC method has simple application to the temperature anisotropy data).

Some tests shall be performed on the WMAP data, and it will be seen how the standard temperature ILC map necessarily has a previously unseen mask bound-

ary contribution; masked and unmasked B-mode analysis on the HILC map is also performed. Finally, note that the ILC-type maps are not the only possibility when it comes to the initial CMB analysis; alternative methods exist (and can be combined with the ILC method) such as maximum entropy methods [277], Wiener filtering, and so on. What separates the ILC approach is that there are very few assumptions used for the separated signals; it is in a sense, self-calibrating.
For completeness, the measurement of the angular power spectra then follows a complicated optimal combination of cross-power spectra after subtracting the best-fit galactic foreground templates, calculated with the help of the ILC, from each of the WMAP band-limited maps. This is approximately equal to forming the combined sky map

$$T = \frac{\sum_{i=3}^{10} T_i'/\sigma_{0,i}^2}{\sum_{i=3}^{10} 1/\sigma_{0,i}^2}, \tag{4.19}$$

where the T_i' are the best-fit foreground-subtracted sky maps over each of the frequencies i and $\sigma_{0,i}$ the noise per observation. Although a WMAP systematic is determined in this chapter it is unlikely to be particularly informative at this stage to perform the lengthy and complicated calculation of the power spectra with a systematic-corrected ILC map.
It is also useful to make predictions on how well the software can perform on future data; specifically the Planck mission, which the full-sky formalism is particularly suited to. Further full-sky missions such as the CMBPol EPIC mission are still at an early development phase, and so it is not necessary to consider their application. The main differences for the purposes of this thesis between the WMAP and Planck missions are the resolutions ($N_{\rm side} = 512$ versus $N_{\rm side} = 2048$), the scanning strategies for the full sky and the quality of polarization and temperature data. As stated previously (chapter 1), the WMAP method uses differential radiometers to infer the temperature anisotropy and polarization of the CMB; this takes advantage of the fact that the signal drifts ($1/f$ noise) of the WMAP horns are approximately identical [146], allowing for a nearly white-noise spectrum. The radiometers measure the brightness difference between two input beams $\sim 141^\circ$ apart. The polarization-sensitive differencing assemblies (DAs), are sensitive to the waveguide bands K1, Ka1, Q1, Q2, V1, V2, W1, W2, W3 and W4. Since each of the 20 radiometers is a two-channel device, then there are 40 data channels calibrated, combined to form the Stokes data. For a calibrated differential signal d_{ij} from a channel j of radiometer i, the differential intensity (temperature) data is calculated by

$$d = \frac{1}{2}(d_{13} + d_{14}) + \frac{1}{2}(d_{23} + d_{24}) \tag{4.20}$$

with the differential polarization data calculated by

$$p = \frac{1}{2}(d_{13} + d_{14}) - \frac{1}{2}(d_{23} + d_{24}). \tag{4.21}$$

For the calibrated instrument gain $\tilde{g}$ and baseline $\tilde{b}$ measured in flight, and actual gain and baseline values g and b with noise N, the calibrated differential signal is

$$\tilde{d} = \frac{g}{\tilde{g}}\Delta T + \frac{g}{\tilde{g}}N + \frac{b - \tilde{b}}{\tilde{g}}. \tag{4.22}$$

The WMAP scan pattern [278] is a compound spin and precession centered about the Sun-WMAP line, sweeping out a line-of-sight path that is reminiscent of a Spirograph pattern. This results in multi-angle scans of each pixel cross in order to symmetrize the beam response and a negligible time average of the differential data over an hourly calibration period in order to estimate the initial baseline. The differential data at time t and pixel i is used from orthogonal polarization channels at the polarization beam axis γ

$$\begin{aligned} d_1 &= T_i + Q_i \cos 2\gamma + U_i \sin 2\gamma \\ d_2 &= T_i - Q_i \cos 2\gamma - U_i \sin 2\gamma \end{aligned} \tag{4.23}$$

to construct the Stokes maps. For uniform azimuthal coverage and constant noise per pixel σ_0, the noise in Q and U is equal, uncorrelated and given by

$$\sigma_Q = \sigma_U = \sqrt{\frac{2}{n}}\sigma_0 \tag{4.24}$$

where n is the number of observations, implying that the polarization maps are $\sqrt{2}$ times noisier than the temperature.

By contrast, the Planck mission consists of two main instruments: the low-frequency instrument (LFI) and high-frequency instrument (HFI); the LFI has a frequency range of 27 to 77 GHz [279], consisting of an array of 22 pseudo-correlation radiometers, composed of 11 actively cooled (20 K) Front End Modules (FEMs), and 11 Back End Modules (BEMs) at 300K, each FEM and BEM set comprising two radiometers, connected by rectangular wave guides, which provide good insulation between the FEM and the BEM sections to avoid overloading the cryocooler. The scan strategy is a 1 rpm spin around an axis offset by 85 degrees from the telescope boresight (covering 1 degree of the sky per day), such that the observed sky patch traces a large circle on the sky [280], resulting in full

sky coverage in ~ 6 months.
It is expected that Planck will provide 10 times the sensitivity of WMAP and 3 times the angular resolution; Planck is then predicted [281] to be able to detect, for a standard ΛCDM model, a scalar-to-tensor r of $0.028 < r < 0.116$ at 95% CL, for an input value $r = 0.04$. Whether the Planck analysis follows an ILC-type procedure remains to be seen. Dick et al [282] have shown that component separation can be influenced significantly by calibration errors in Planck's sensitive instruments, leading to very different behaviour between ILC-type analysis and Independent Component Analysis (ICA)-type analysis. ICA methods are based on the assumption that each of the available observations is a different linear mixture of a number of statistically independent components and so do not typically assume a unit CMB response of each channel. Particularly, while ILC-type methods produce lower signal extraction error, the ICA-type approaches avoid biasing from miscalibration.

4.2 B-modes and r from WMAP and Planck

The WMAP data features a low signal-to-noise ratio S/N in the Q and U variables. In this sense one can only make a limited analysis of the polarization modes, by smoothing the WMAP maps with a Gaussian kernel. Figure 4.2 shows the smoothed Stokes maps and the resulting $\nabla^4 e$ and $\nabla^4 b$ calculations at the lowest order O_2; it can be seen that there is significant noise along the galactic plane. Since the consistency criterion of the $\nabla^4 b$ map is not satisfied, it can reasonably be stated that the map is consistent with zero primordial B-modes — the central feature in the map is a relic of the galaxy. This also suggests that for the cleaner Planck maps, it may be necessary to calculate at higher orders to obtain a reliable (i.e., not predominantly numerical noise) $\nabla^4 b$ map.
The utility of the software on the masked sky should also be tested. For this situation, the WMAP data is not smoothed, but the WMAP galaxy masks and point source catalogues are utilized to produce the sky masks used (Fig. 4.3). Figure 4.4 shows the calculated B-mode spectra, and the power the masked regions contribute to the B-mode sky.

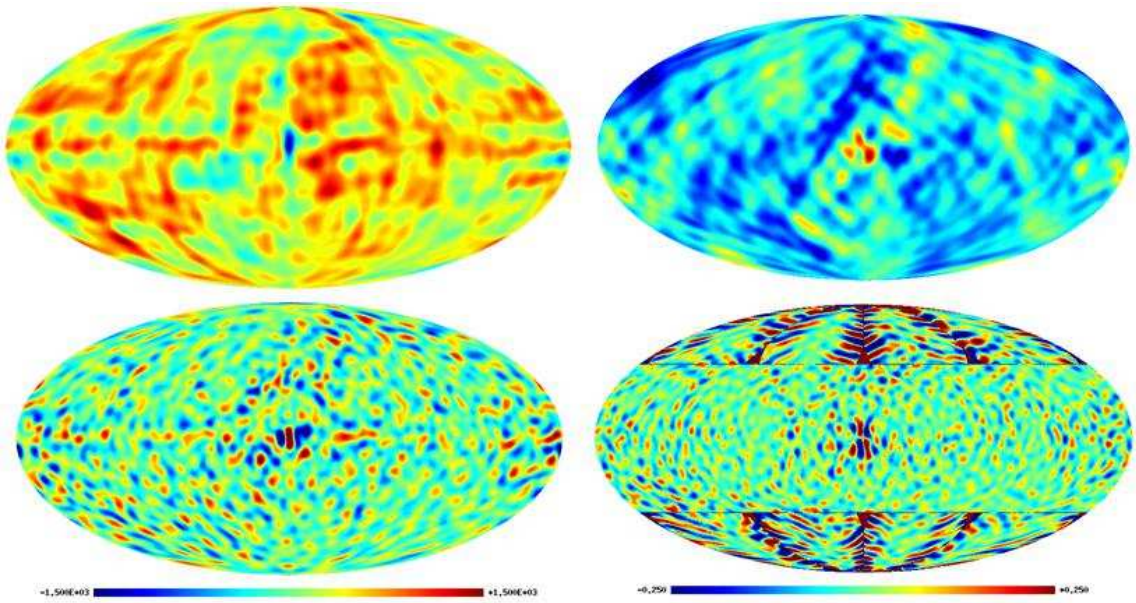

Figure 4.2: Left-to-right: Smoothed Q and U HILC source maps (top diagram) and O_2 $\nabla^4 e$, $\nabla^4 b$ maps (bottom diagram). The $\nabla^4 b$-map is consistent with a zero primordial B-mode signal due to the 'signal' jump at the polar/equator boundary; the e map on the other hand has a definite non-zero component.

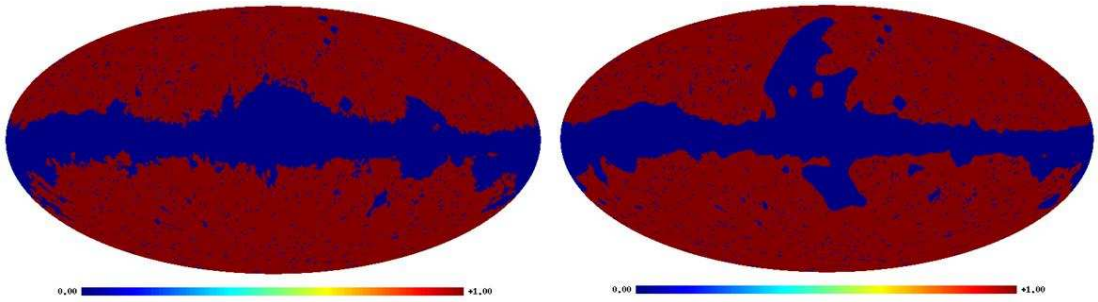

Figure 4.3: Combined galaxy-and-point-source WMAP-scale masks used for the temperature (left diagram) and polarization (right diagram) maps.

By operating on B-mode-free mock data at resolutions probed by the Planck satellite ($N_{\rm side} = 2048$), one can obtain the best-case-scenario limits on the B-mode sky that the software will probe, solutions to the pole problem notwithstanding. Since the scales of interest for inflation correspond to less than that probed by WMAP-size maps (Planck has a far greater signal-to-noise), the effect of masking can be approximated by the same differenced data obtained on the left-hand diagram of Fig. 4.4, applied to the full B-mode Planck sky in Fig. 4.5.

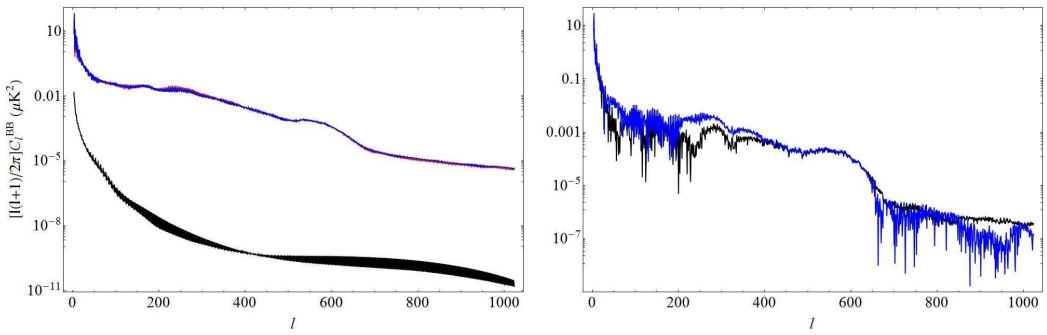

Figure 4.4: Left diagram: O_2 B-mode spectra from an unmasked smoothed HILC sky (black line), the unsmoothed galaxy masked sky (red line) and the combined-galaxy-and-point-source mask sky (blue line). Right diagram: Differences between the unsmoothed galaxy-masked and unmasked (black line), and combined-galaxy-and-point-source-masked and unmasked (blue line) B-mode spectra.

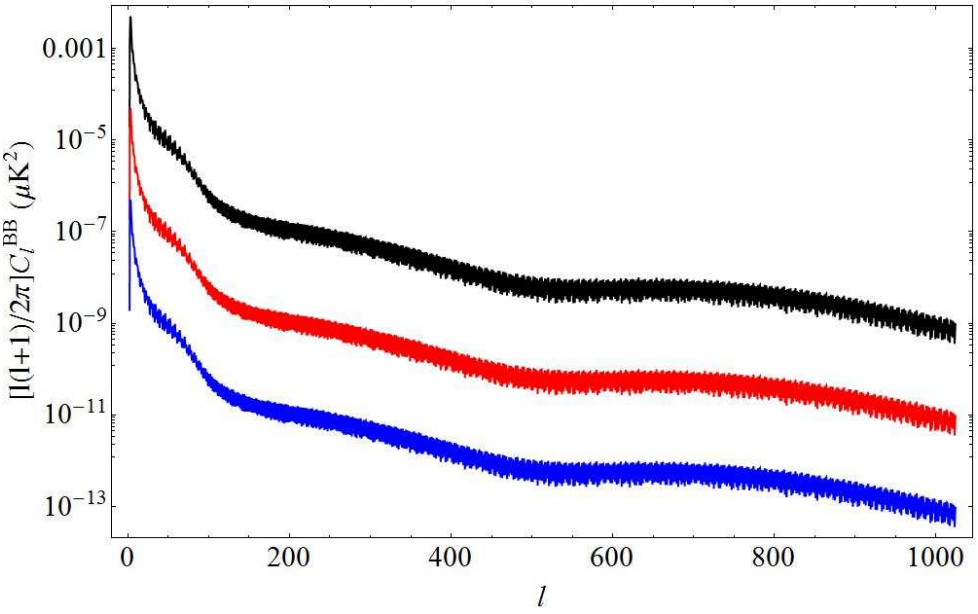

Figure 4.5: Extrapolated B-mode limits for the full-sky calculations on a Planck-resolution ($N_{\rm side} = 2048$) B-mode-free CMB simulation map, for stencil orders O_2 (black line), O_4 (red line) and O_6 (blue line). The $l = 4096$ limit is $\sim 10^{-17}$, $\sim 10^{-19}$ and $\sim 10^{-21}$ respectively.

To further test Planck sensitivity, one could compute models of the foreground using the Planck Sky Model[1], a set of programs for simulating the sky emission over

[1] `http://www.apc.univ-paris7.fr/APC_CS/Recherche/Adamis/PSM/psky-en.php`

the frequency ranges that Planck will measure. The PSM has advantages beyond computing the expected sky measurements, allowing the testing of the analysis pipeline. The simulation aspects of the PSM provide simulations of the CMB signal (Gaussian and non-Gaussian, with or without lensing), and foreground sources such as galactic emission (synchrotron, free-free, thermal dust, spinning dust), the Sunyaev-Zel'dovich effect (thermal and kinetic), point sources (radio point sources, infrared point sources and ultracompact H-II regions) and the infrared background. It would also be necessary to implement the apodization techniques discussed in chapter 3. This would be set for future work.

4.3 Anomalies and Defects

The defect-detecting aspect of the MasQU software is now employed to analyse the status of the 7-year WMAP ILC sky. First, the current status of anomalies from the WMAP literature is explored, conveniently summarised in Bennett et al [283].

4.3.1 WMAP Anomalies

Since the advent of CMB full-sky mapping there have been a number of claims of anomalies found in the microwave sky. By 'anomaly' one means a signal that is statistically unlikely, and so-called anomalies in the microwave sky could be signals of anything ranging from systematic errors to foreground or galactic sources to more exotic entities such as the defects that have already been discussed or signals from other universes [284].

The most famous of the alleged anomalies found so far are the cold spots [285], the alignment of the quadrupole and the octupole [286] and the low quadrupole moment [287], amongst other claims. Some of these can be seen in Fig. 4.6. The latest WMAP team analysis suggests that these anomalies are likely combinations of systematic errors and statistical insignificance; when the results of Planck are published, its different scanning strategy, coupled with the fact that Planck measures the absolute temperature rather than temperature differences, will make it possible to remove systematics from the contaminants.

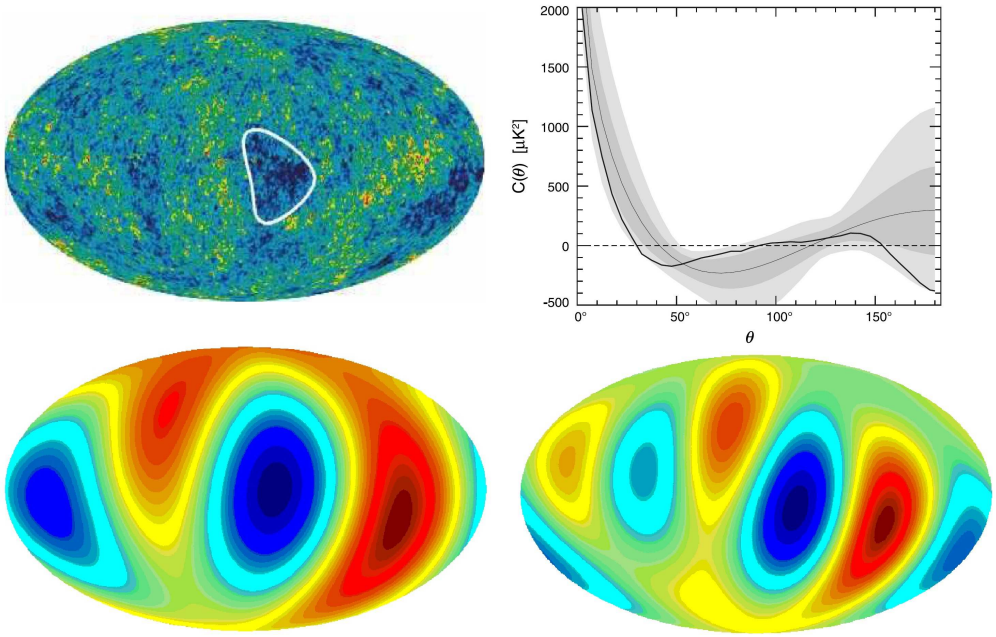

Figure 4.6: Top row: One of the WMAP cold spots (highlighted by the white line, left diagram) and the angular correlation function of the full WMAP sky (black line, right diagram; cited as evidence of a lack of large-scale power) versus 68% and 95% CL limits determined using Monte Carlo simulations, from Bennett et al [283]. Bottom row, left-to-right: the quadrupole ILC map and octupole ILC map: the alignment is striking. But is it statistically significant?

In particular, the two cold spots were found to be both consistent with standard ΛCDM CMB fluctuations, whilst the low quadrupole is acceptable within the 95% confidence range for the standard cosmological model and the lack of large-scale power has been attributed to the choice of statistic (exhibiting the care which must be taken with *a posteriori* statistics), whilst the quadrupole-octupole alignment is claimed to be an incidental alignment of primary and secondary anisotropies.
What this all appears to say is that, while the search for anomalies is a vital part of checking for systematics within the standard data analysis pipeline, one must be careful with thinking about probabilities versus the ease with which humans pick out patterns (which is precisely a selection-pressure-driven propensity); the example given by the WMAP team is the apparent image of Hawking's initials in the anisotropies. Given an infinite number of random sub-configurations of states there will always be some states which could be viewed as unusual due to their geometry and so forth, but which are only unusual in the sense that one *imposes* meaning on them; without an *a priori* theory to predict a particular statistical likelihood for a particular type of pattern, it is difficult to rigorously infer that a particular distribution is indeed anomalous.

Conversely, as Copi et al [288] put it: "..the agreement between theory and data is remarkable... this agreement should not be taken lightly; it shows our precise understanding of the causal physics on the last scattering surface. Even so, the cosmological model we arrive at is baroque, requiring the introduction at different scales and epochs of three sources of energy density that are only detected gravitationally — dark matter, dark energy and the inflaton. This alone should encourage us to continuously challenge the model and probe the observations particularly on scales larger than the horizon at the time of last scattering".

4.3.2 Anomaly Detection with MasQU

Having previously discussed the ILC map-making techniques, the Laplacian-difference analysis exposes the boundary of the galaxy cut very clearly; in order to emphasize this result, one can observe the Laplacian maps themselves, which show no such feature (Fig. 4.7). The needlet decompositions (Fig. 4.8) further enhance the galaxy boundary image over a number of scales. One should note the significant amount of power generated in the triangular regions of the HEALPix sphere featuring the most geometrically-deformed pixel stencils; this relic could be dealt with by a rotation of the data in the ϕ coordinate.
It can then be asked as to whether the discontinuity power contributes anything to the CMB anomalies. For some of the cases the method of running through the entire WMAP calibration is too cumbersome for this thesis. However, the boundary region (Fig. 4.9) can be isolated and the quadrupole and octopole power of this region removed from the ILC quadrupole and octopole. It is not very surprising that the region has a negligible effect on the orientation of these two multipoles, since the scale of the boundary is small in comparison. Figure 4.10 provides a crude calculation of the full contribution of the boundary region to the ILC temperature power spectrum using equation (2.121), with the dip in the power-spectral contribution corresponding to the boundary (smoothing) scale. It can be seen that the impact of the boundary region is small; however, as cosmological experiments probe the microwave sky with higher precision and theory discrimination becomes more sensitive to subtle differences in predicted power spectra, it may be necessary to ensure that excess power from the mask boundary does not bias results. Secondly, given recent claims of detections of non-Gaussianity [101, 102] it would certainly be necessary to account for the boundary region in any calculation of the nonlinear term f_{NL}.

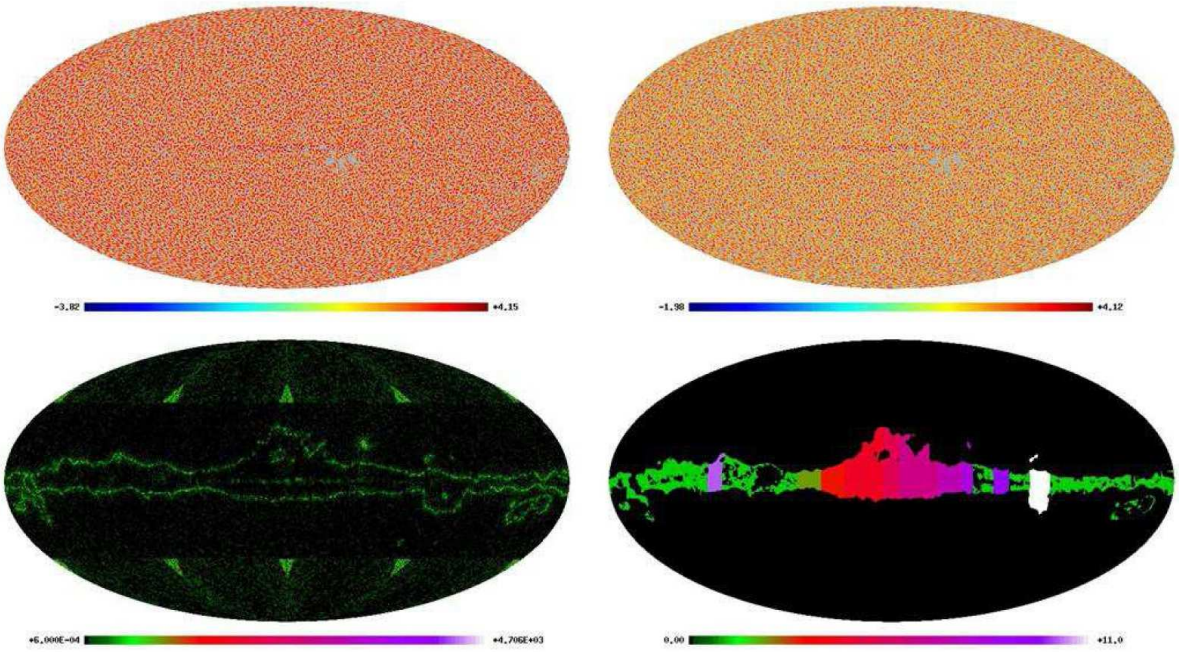

Figure 4.7: Top row: ILC log-scale Laplacian maps from the (left diagram) spectral (utilizing the $map2alm$ subroutine) method and (right diagram) the finite-differencing method calculated at order O_2. Bottom row: (left) the map of absolute differences between the Laplacian maps. The galaxy mask is quite apparent, as are a couple of signals which are likely galactic foreground sources. The triangular parts in the polar cap are relics of the calculation technique and HEALPix geometry. The bottom-right diagram is the mask map, with ILC technique cuttings shown.

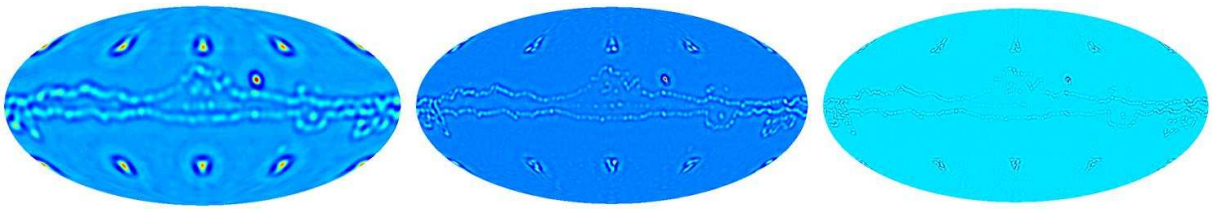

Figure 4.8: Left-to-right: Needlet maps for the boundary detection, at scales $j = 5$, 6 and 7, with $B = 2$.

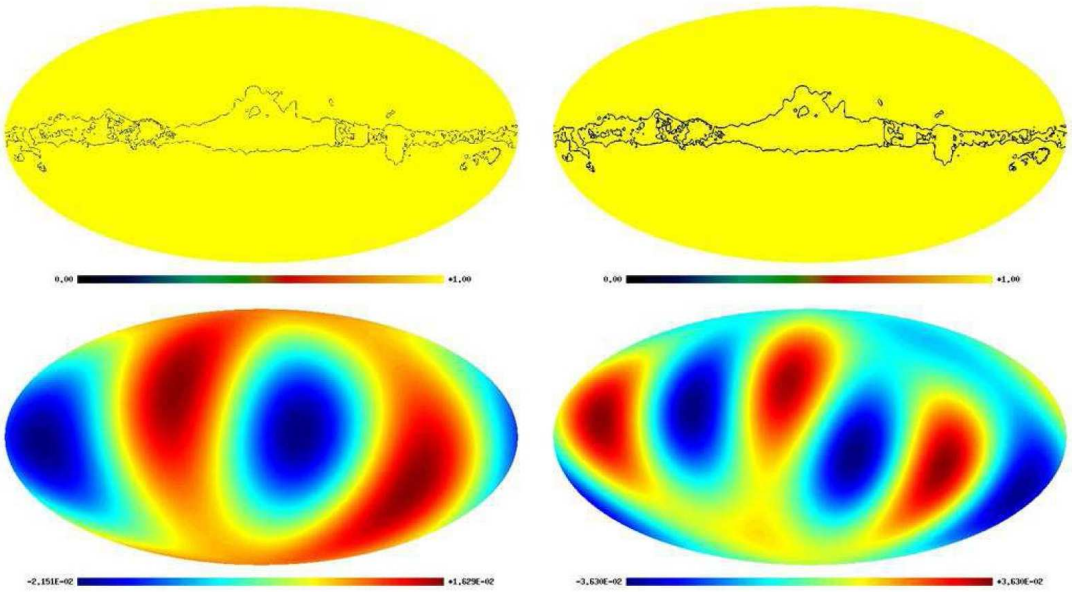

Figure 4.9: Top row: Boundary masks used, of varying thickness. Bottom row: quadrupole (left diagram) and octupole (right diagram) power calculated from the smaller boundary mask. The alignment of the quadrupole and octupole is essentially unchanged.

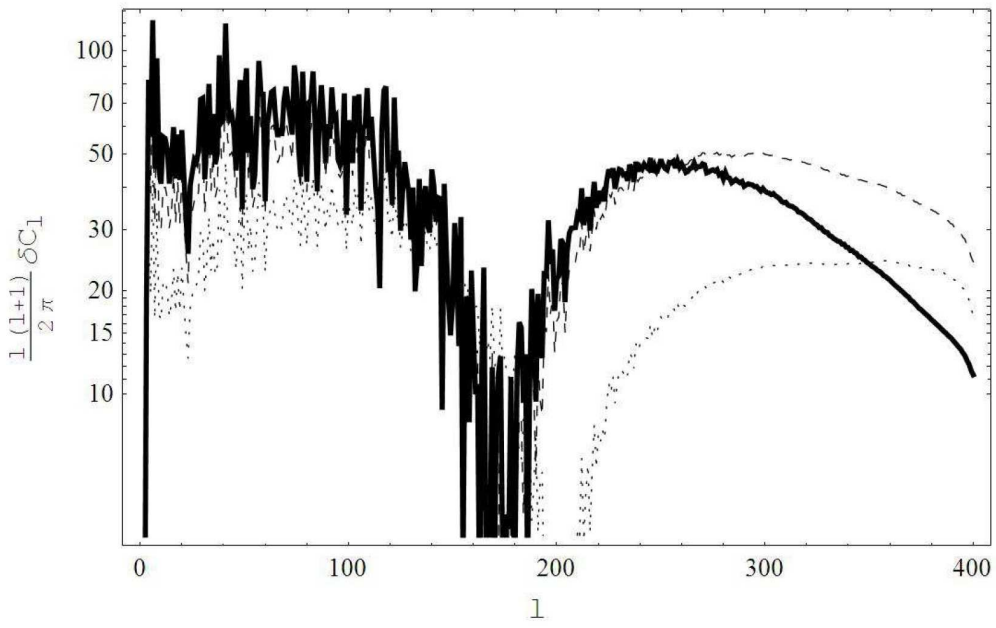

Figure 4.10: Differences between the boundary masked and unmasked ILC power spectra — the lines correspond to the thickest mask (thick line), thinnest mask (dotted line) and intermediate mask (dashed line). The dip in power at $l \sim 180$ corresponds roughly to the Gaussian smoothing scale across the galaxy boundary in the construction of the ILC map, so the difference between ILC and mode-uncoupled masked spectra at the mask scale is small.

This analysis can then be repeated on the HILC-generated maps. Whilst discontinuous power can still be found in the noisy galactic centre (Fig. 4.11), these maps are better-behaved. This suggests that the HILC method is preferable when producing power spectra; on the flip side, the harmonic nature of the map construction suggests that an ILC-type map, so long as smoothing of the cut mask boundaries is performed very carefully, would be better suited for the detection of localized anomalies such as cosmic strings. Further analysis, by removing the galaxy boundary (via a variety of boundary mask thicknesses) pre-Laplacian-difference calculation reveals by eye no signs of any anomalies. In the scalar maps, it seems that the Laplacian-difference method is more sensitive to systematic (gluing) discontinuities than physical (injection) discontinuities.

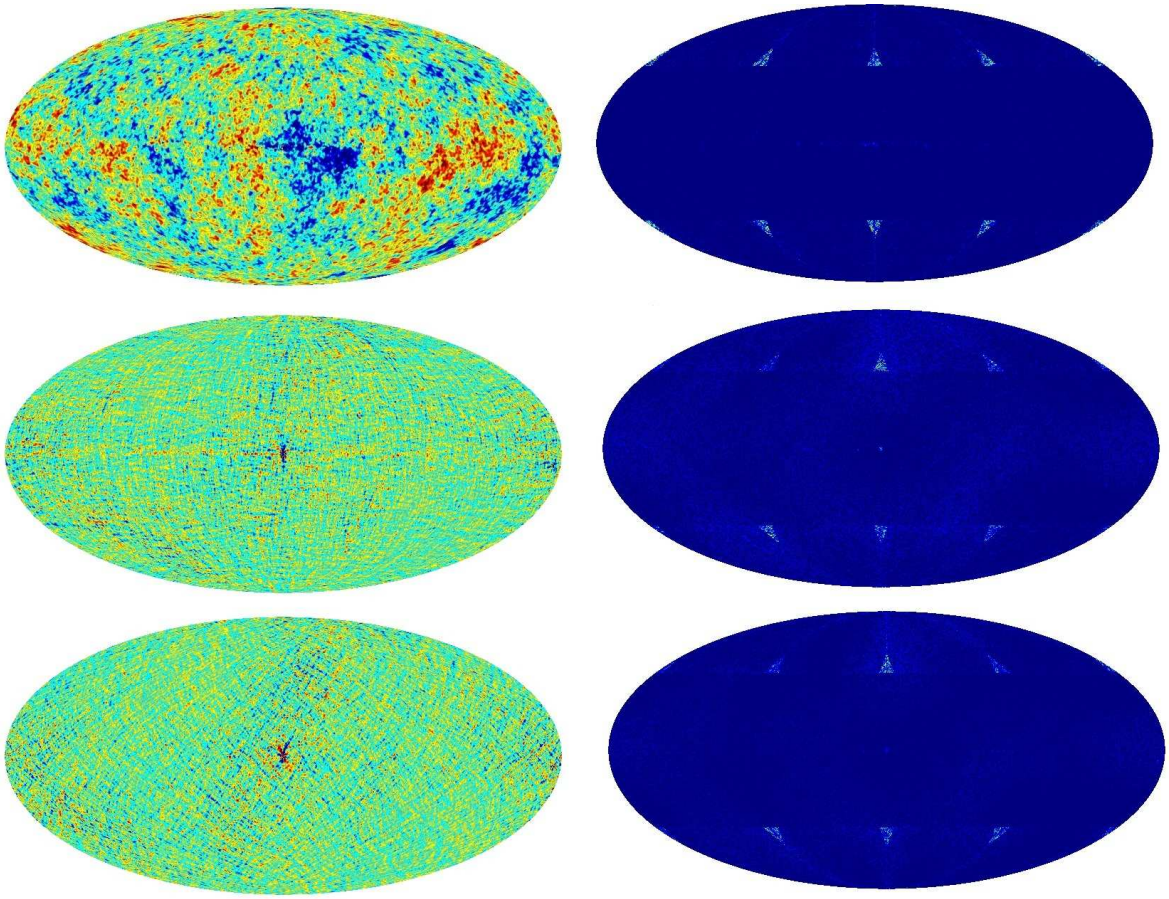

Figure 4.11: Top-to-bottom: Temperature, Q and U HILC source maps (left, not smoothed) and O_2 Laplacian-difference maps (right). Besides the galactic plane, the discontinuity signal is consistent with the null hypothesis.

In conclusion, the differenced-Laplacian finds no immediate evidence for anomalies such as strings, with the caveat that only lower-order calculations have been performed, coupled with by-eye detection on the needlet-decomposed maps.

This finding may change with higher-order calculations and a more rigorous examination. Also, since the signal in a pixel is an average over signals within the pixel area, it is possible that the results of the Planck Surveyor with an improved resolution, or more local balloon surveys such as the EBEX, and their successors, will test these results. The method did encounter a success: the detection of the smoothed galaxy boundary in the ILC map. It was found that the effect of excluding the boundary from the map was negligible, but that its mere detection might warrant added care in future surveys when performing map synthesis.

4.4 Summary

An initial utilization of MasQU suggests that it is well-suited to a clean, full-sky determination of the large-scale B-modes relevant to inflation, which should be provided by data from Planck and its successors. The operation of the software on the noisy WMAP polarization data is consistent with a non-zero E-mode signal and a zero B-mode signal, as should be expected.
The WMAP map-making method involves the initial construction of a foreground-reduced CMB map which is then used in later calibration. This map can be constructed using the real-space ILC method or the harmonic-space HILC method amongst others. The choice of map-making method predetermines the type of systematic error that may occur in analyses; systematic errors can in principle account for many of the anomalies found in current WMAP data. The Laplacian-difference method was able to detect the presence of a relic contaminant from the galaxy-removal technique in the ILC temperature map, a relic which does not exist in the HILC equivalent. No discernable evidence for defects in the CMB was found.

Chapter 5

Conclusions

In this thesis the motivation for, and the development of, local analysis methods for utilizing local real-space signals from the CMB in order to constrain cosmology have been presented. Chapter 1 involved an account of the current status of CMB studies for cosmology, and provided a whistlestop tour of the inflationary mechanism that may generate a number of observable features in the microwave sky: topological defects and primordial gravitational waves are the focal point of the chapter, since these have the most direct links with fundamental issues in physics. The use of non-Gaussianity in determining the nature of the inflationary mechanism, which would complement the determination of the tensor-to-scalar ratio r in probing the inflationary potential, was also discussed.
The second chapter indulged in a more explicit development of some current (and one invented) problems in the CMB literature, and the development of real-space methods with which to deal with them. Real-space scalar and pseudo-scalar analogues to the cosmological E- and B-modes were constructed, utilizing a general finite-differencing algorithm in order to avoid the mode-mixing issues that accompany harmonic transforms on a masked sky. This has a number of advantages over alternative methods, since it makes no assumptions about the Gaussianity of the signal, and does not discard phase-space information. The method also admits higher-order calculations to drive errors down. Next, the advantage of utilizing real-space scalar and pseudo-scalar fields for dealing with mode-transfer issues of uncoupled fields was shown. It transpired that, contrary to approaches which perform harmonic transforms directly on the Stokes polarization variables, the mode-transfer matrices for the e and b fields are the same as that for the temperature anisotropy field — allowing not only for simple calculations of the general forms of the matrices, but also (and more importantly) for numerical calculations which are less computationally expensive. It was found that

this method of developing real-space analogues to the polarization fields opened up an avenue for compactly calculating any number of higher n-point spectra, all corrected for mode-mixing. The finite-difference method was then combined with harmonic analyses to develop a method to expose discontinuous signals via the Laplacian-difference formalism, such as would be typical of the Kaiser-Stebbins effect from the presence of topological defects. This then motivated the discussion of alternative transform types, such as the needlet transform, which may be used to isolate the resultant discontinuity power. Finally, as a crude example of the potential that considering real-space fields has for developing new observational tests, a finite-resolution CMB scenario was invented, to be differentiated from the signal of a cosmic string network.

This then motivated the introduction of the MasQU software package, a tool for performing finite-differencing on the popular semi-regular HEALPix sphere. The construction of the package highlighted several technical problems likely to be repeated on other computational grids, related to the existence of poles on the sphere. A number of methods to solve this problem were explored, which significantly included a more exact method to calculate the harmonic coefficients on the HEALPix sphere. The MasQU software was found to reduce mode leakage significantly; mock EBEX tests showed this to be effective when compared with current methods. The issue of apodization was also explored, related to the mode-transfer matrices in chapter 2, and the scalar apodization method was found to have the advantage of a considerably faster computation time than the tensor apodization method constructed previously by Smith & Zaldarriaga. Next, the Laplacian-difference formalism was quantified through the use of toy models, finding that the method performs competitively with alternative methods at even the lowest orders of the calculation. This set up a brief analysis of the finite-resolution CMB scenario, which could be separated from string network scenarios by a judicious combination of real-space analysis and interpretation of the power spectrum features determined by the underlying physics.

Finally, the utility of MasQU on the observed sky was studied — quantifying the B-mode detection levels that Planck may yield utilizing the software, and finding that (to no surprise) the B-mode signal from the WMAP HILC maps is consistent with zero. Perhaps more importantly, the Laplacian-difference method found evidence of systematic noise in the ILC map from the galaxy boundary. Whilst this was found not to contribute to the so-called CMB anomalies, the Laplacian-difference method will clearly serve as a useful test for systematics in future CMB surveys.

The main technical development in this thesis, MasQU, and the provision of competitive bounds on the potential B-mode and defect signals from this method has demonstrated the power of the local approach. However, local techniques have much larger scope for producing quality scientific results. On the differencing side, the methods provided are general enough to satisfy the production of essentially any derivative field on any manifold in any number of dimensions. This alone suggests that there may be very wide uses for the software, especially since spherical symmetry is utilized so widely in the physics community. On the mathematical side, there is significant scope for extending the formalism by utilizing Laurent expansions or even the fractional calculus — with a physical motivation for such work yet to be discerned. This is coupled to the ease with which one can utilize the spin-weighted harmonics to produce calculable scalar fields configured to expose observables of interest. On the discontinuity-detecting side, there are many potential uses for the software. An exotic situation, the finite-resolution CMB, has been contructed as an example of how local techniques can be used to check for unusual physics signals. On a level more relevant to general astronomy, the utility of discontinuities could range from the detection of cosmic ray sources to characterizing transits.

The focus of methods for CMB analysis is currently placed firmly on the harmonic domain. This thesis has shown that focussing on a single analytical framework may not be the most efficient route to scientific discovery. The development of local, real-space methods — either in isolation, or more promisingly in combination with harmonic methods — such as presented in this thesis, should provide an important example of such an outlook.

Appendix

APPENDIX A

Spinors & Spherical Harmonics

The ordinary spherical harmonics are defined as functions which satisfy the scalar Laplace equation on the sphere. Starting from the Laplace-Beltrami equation and the metric on the 3-sphere

$$\nabla^2 F = \frac{1}{\sqrt{g}}\partial_i\left(\sqrt{g}\partial^j g_{ij}\right)F, \qquad g_{ij} = \text{Diag}(1, r^2, r^2\sin^2\theta) \tag{A.1}$$

yields the spherical Laplacian for a scalar function

$$\nabla^2 F = \frac{1}{r^2}\partial_r(r^2\partial_r F) + \frac{1}{r^2\sin\theta}\partial_\theta(\sin\theta\partial_\theta F) + \frac{1}{r^2\sin^2\theta}\partial_{\phi\phi}F. \tag{A.2}$$

By separation of variables, the function F can be described as $F(r,\theta,\phi) = R(r)\Theta(\theta)\Phi(\phi)$, and taking the angular part $f(\theta,\phi) = \Theta(\theta)\Phi(\phi)$ yields

$$\frac{\Phi}{\sin\theta}\frac{d}{d\theta}\left(\sin\theta\frac{d\Theta}{d\theta}\right) + \frac{\Theta}{\sin^2\theta}\frac{d^2\Phi}{d\phi^2} + l(l+1)\Theta\Phi = 0 \qquad l(l+1) = \frac{1}{R}\partial_r(r^2\partial_r R). \tag{A.3}$$

These are the equations the spherical harmonics must satisfy; one can set either of θ or ϕ-dependent part to a constant. Starting with the latter one then finds

$$\frac{1}{\Phi}\frac{d^2\Phi}{d\phi^2} = -m^2 \qquad \Rightarrow \qquad \Phi = Ae^{-im\phi} + Be^{im\phi}. \tag{A.4}$$

Substituting into the Laplacian gives

$$\Theta(\theta) = P_{lm}(\cos\theta). \tag{A.5}$$

The spherical harmonics [225] are then defined as

$$Y_{lm}(\theta,\phi) = (-1)^m \sqrt{\frac{2l+1}{4\pi}\frac{(l-m)!}{(l+m)!}} P_{lm}(\cos\theta) e^{im\phi}, \tag{A.6}$$

with orthogonality relation

$$\int_{\phi=0}^{2\pi}\int_{\theta=0}^{\pi} Y^*_{l_1m_1}(\theta,\phi) Y_{l_2m_2}(\theta,\phi)\sin\theta d\theta d\phi = \delta_{l_1l_2}\delta_{m_1m_2} \tag{A.7}$$

where P_{lm} are the associated Legendre functions

$$P_{lm}(x) = (1-x^2)^{m/2}\frac{d^m}{dx^m}P_l(x) \tag{A.8}$$

and P_l are the Legendre polynomials

$$P_l(x) = \sum_{r=0}^{l/2}(-1)^r \frac{(2l-2r)!}{2^l r!(l-2r)!} x^{l-2r}. \tag{A.9}$$

A deeper understanding of spherical harmonics and also generally rotations comes from the mathematical entities called spinors; spinors form an irreducible basis in the rotation and Lorentz groups, and are intrinsic to the standard formulation of quantum mechanics and quantum field theory along with uses in a wide range of mathematical fields. Spinors were developed by Cartan in 1913; they are elements of the complex vector space of the orthogonal groups $O(n)$ and are in some important sense more fundamental aspects of rotations than spatial vectors. This leads to their having unusual properties; under a rotation of angle $\theta \to \theta + 2\pi$, a spinor o transform as $o \to -o$.

Spinors are a representation of the double cover of a Lie group, called the Spin group (p, q). For physics, the spinors in $SO(3)$ and $SO(3,1)$ are of particular importance; the isomorphism $SL(2,C) \equiv \mathrm{Spin}(3,1)$ is responsible for the existence of two different complex spinors in 4 dimensions. In $SO(3)$, the isomorphism $SU(2) \cong \mathrm{Spin}(3)$ allows the construction of spinors by stereographically projecting the unit sphere onto the complex plane [289] (Fig. A.1).

By intersecting a sphere $\mathbb{S}^2$ with a complex plane $\mathbb{C}^2$, one can map a point P on $\mathbb{S}^2$ with coordinates (x, y, z), to a point P' on $\mathbb{C}^2$ with coordinates (X, Y, 0). Each point on $\mathbb{C}^2$ is then given by a complex number

$$\zeta = X + iY. \tag{A.10}$$

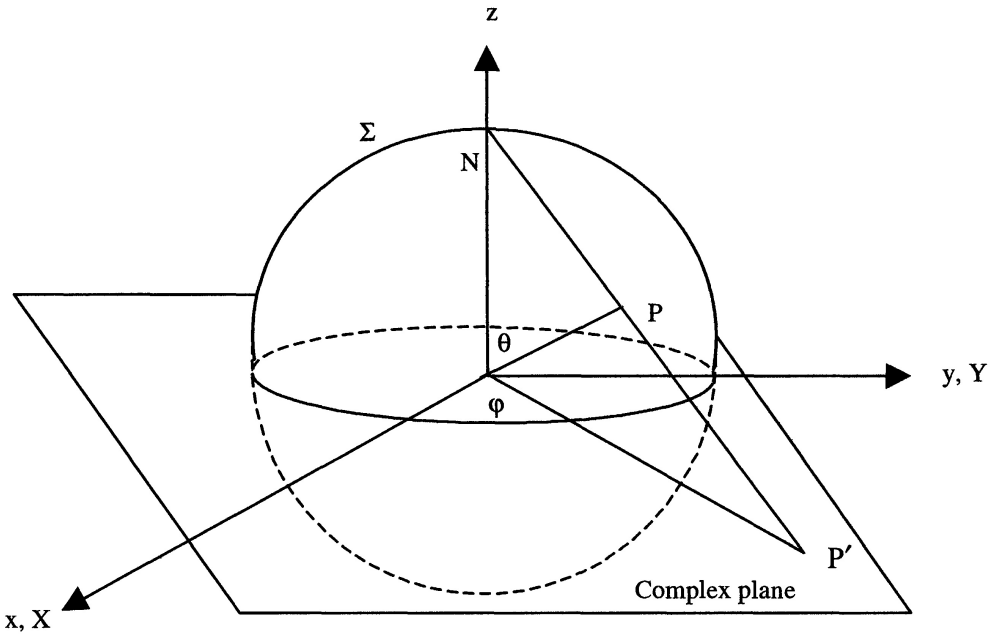

Figure A.1: Stereographic projection of $\mathbb{S}^2$ onto $\mathbb{C}^2$, from O'Donnell [290]

Using simple trigonometry it can be seen that

$$\frac{x}{X} = \frac{y}{Y} = 1 - z; \tag{A.11}$$

comparing the two previous equations then implies that

$$\zeta = \frac{x + iy}{1 - z}. \tag{A.12}$$

In spherical polar coordinates this can be written as

$$\zeta = e^{i\phi} \cos \frac{\theta}{2}, \tag{A.13}$$

by applying the standard transformations between Cartesian and spherical polar coordinates. The inverse relations are

$$x = \frac{\zeta + \bar{\zeta}}{\zeta\bar{\zeta} + 1}, \qquad y = \frac{i(\zeta - \bar{\zeta})}{\zeta\bar{\zeta} + 1}, \qquad z = \frac{\zeta\bar{\zeta} - 1}{\zeta\bar{\zeta} + 1} \tag{A.14}$$

where the overbar denotes conjugation. It will be preferable to represent the single complex parameter by a pair of complex components

$$\zeta = \frac{\epsilon}{\eta}; \tag{A.15}$$

the reason for doing this is so as to circumvent the problem of using an infinite coordinate to represent the north pole on the Riemann sphere. Hence one can rewrite the inverse relations as

$$x = \frac{\epsilon\bar{\eta} + \bar{\epsilon}\eta}{\epsilon\bar{\epsilon} + \eta\bar{\eta}}, \qquad y = \frac{i(\bar{\epsilon}\eta - \epsilon\bar{\eta})}{\epsilon\bar{\epsilon} + \eta\bar{\eta}}, \qquad z = \frac{\epsilon\bar{\epsilon} - \eta\bar{\eta}}{\epsilon\bar{\epsilon} + \eta\bar{\eta}}. \tag{A.16}$$

A spinor can then be represented using

$$o^A = \begin{pmatrix} \epsilon \\ \eta \end{pmatrix}. \tag{A.17}$$

Adapting from Varshalovich [225], spin functions in $\mathbb{S}^2$ with $2S+1$ elements are referred to as spin-S spin functions o_S^A,

$$o_S^A = \begin{pmatrix} o^{S-1}, \cdots, o^{S+1} \end{pmatrix}^T \tag{A.18}$$

where the operation of the spin operator yields

$$\hat{S}^2 o_s^A = S(S+1)o_s^A, \qquad \hat{S}_z o_s^A = A o_s^A. \tag{A.19}$$

The vector and tensor harmonics are defined such that they satisfy the vector and tensor Laplacians; the vector Laplacian is, for example, calculated from $\nabla \cdot (\nabla \times \mathbf{F}) = 0$ and $\nabla \times (\nabla \times \mathbf{F}) = \nabla(\nabla \cdot \mathbf{F}) - \nabla^2 \mathbf{F}$ to give

$$\begin{aligned} \nabla^2 \mathbf{F} = &\left(\nabla^2 F_r - \frac{2F_r}{r^2} - \frac{2}{r^2 \sin^2\theta} \partial_\theta (F_\theta \sin\theta) - \frac{2}{r^2 \sin^2\theta} \partial_\phi F_\phi \right) \hat{r} \\ &+ \left(\nabla^2 F_\theta - \frac{F_\theta}{r^2 \sin^2\theta} + \frac{2}{r^2} \partial_\theta F_r - \frac{2\cos\theta}{r^2 \sin^2\theta} \partial_\phi F_\phi \right) \hat{\theta} \\ &+ \left(\nabla^2 F_\phi - \frac{F_\phi}{r^2 \sin^2\theta} + \frac{2}{r^2 \sin^2\theta} \partial_\phi F_\phi + \frac{2\cos\theta}{r^2 \sin^2\theta} \partial_\phi F_\theta \right) \hat{\phi}. \end{aligned} \tag{A.20}$$

The tensor harmonics Y_{JM}^{LS} satisfy the operator rules

$$\begin{aligned} \hat{J}^2 Y_{JM}^{LS}(\theta,\phi) &= J(J+1) Y_{JM}^{LS}(\theta,\phi) \qquad & \hat{J}_z Y_{JM}^{LS}(\theta,\phi) &= M Y_{JM}^{LS}(\theta,\phi) \\ \hat{L}^2 Y_{JM}^{LS}(\theta,\phi) &= L(L+1) Y_{JM}^{LS}(\theta,\phi) \qquad & \hat{S}^2 Y_{JM}^{LS}(\theta,\phi) &= S(S+1) Y_{JM}^{LS}(\theta,\phi) \end{aligned} \tag{A.21}$$

and can be constructed from the product of the normal spherical harmonics and spinors as follows

$$Y_{JM}^{LS}(\theta,\phi) = \sum_{m\sigma} C_{LmS\sigma}^{JM} Y_{LM}(\theta,\phi) o_{S\sigma} \tag{A.22}$$

where the C are the Clebsch-Gordon coefficients. Particularly, the covariant spherical components of the tensor harmonics can be written

$$\left[Y^{LS}_{JM}(\theta,\phi)\right]_{\mu} = (-1)^{S-\mu} C^{JM}_{L,M+\mu,S-\mu} Y_{L,M+\mu}(\theta,\phi), \tag{A.23}$$

thus any tensor can be expanded via

$$F_S(\theta,\phi) = \sum_{JLM} A_{JLM} Y^{LS}_{JM}(\theta,\phi). \tag{A.24}$$

From this, one can define spinor and vector spherical harmonics

$$\Omega^{L}_{JM}(\theta,\phi) = Y^{LS}_{J\frac{1}{2}}(\theta,\phi) \qquad Y^{L}_{JM}(\theta,\phi) = Y^{LS}_{J1}(\theta,\phi). \tag{A.25}$$

Equivalently, one can use differential geometry to define the tensor harmonics by utilizing standard results that can be found in any textbook on differential geometry or general relativity, such as the definition of the metric connection

$$\Gamma^{a}_{bc} = \frac{1}{2} g^{ad} \left(g_{db,c} + g_{dc,b} - g_{bc,d}\right) \tag{A.26}$$

and the following covariant derivatives:

$$A_{;ab} = A_{,ab} - \Gamma^{c}_{ab} A_{,c} \tag{A.27}$$

where ${}_{,ab} \equiv \partial_{ab} \equiv \partial^2/\partial X^a \partial X^b$. Using a spherical basis for the metric

$$g_{ab}(\theta,\phi) = \begin{pmatrix} 1 & 0 \\ 0 & \sin^2\theta \end{pmatrix}, \tag{A.28}$$

and since the off-diagonal elements are zero the connection becomes

$$\Gamma^{a}_{bc} = \frac{1}{2} g^{aa} \left(g_{ab,c} + g_{ac,b} - g_{bc,a}\right) \tag{A.29}$$

where the connection elements are computed to be

$$\begin{aligned} \Gamma^{\theta}_{\phi\phi} &= -\frac{1}{2}(\sin\theta\cos\theta) \\ \Gamma^{\phi}_{\theta\phi} &= \Gamma^{\phi}_{\phi\theta} = \cot\theta \\ \Gamma^{\phi}_{\theta\theta} &= \Gamma^{\phi}_{\phi\phi} = \Gamma^{\theta}_{\phi\theta} = \Gamma^{\theta}_{\theta\phi} = \Gamma^{\theta}_{\theta\theta} = 0, \end{aligned} \tag{A.30}$$

one can quickly calculate the components of $Y_{(lm)ab}$:

$$\begin{aligned} Y_{(lm);\theta\theta} &= Y_{(lm),\theta\theta} \\ Y_{(lm);\theta\phi} &= Y_{(lm);\phi\theta} = Y_{(lm),\theta\phi} - \cot\theta Y_{(lm),\theta} \\ Y_{(lm);\phi\phi} &= Y_{(lm),\phi\phi} + \sin\theta\cos\theta Y_{(lm),\theta} \\ Y^{\theta}_{(lm);\theta} &= Y^{\theta}_{(lm),\theta} \\ Y^{\phi}_{(lm);\phi} &= Y^{\phi}_{(lm),\phi} + \cot\theta Y^{\theta}_{(lm)}. \end{aligned} \tag{A.31}$$

From the identities [291]

$$\begin{aligned} Y^{;ab}_{(lm);ab} &= (\nabla^2\nabla^2 + \nabla^2)Y_{(lm)} = l(l+1)(l(l+1)-1)Y_{(lm)} \\ \int Y_{(lm);ab}Y^{;ab*}_{(l'm')}d\Omega &= l(l+1)(l(l+1)-1)\delta_{ll'}\delta_{mm'}, \end{aligned} \tag{A.32}$$

the gradient and curl components of the tensor harmonics are defined in terms of covariant derivatives of the 2-sphere via

$$\begin{aligned} Y^{E}_{(lm)ab} &= N_l\left(Y_{(lm);ab} - \frac{1}{2}g_{ab}Y^{c}_{(lm);c}\right) = \frac{N_l}{2}\begin{pmatrix} W_{lm} & X_{lm}\sin\theta \\ X_{lm}\sin\theta & -W_{lm}\sin^2\theta \end{pmatrix} \\ Y^{B}_{(lm)ab} &= \frac{N_l}{2}\left(Y_{(lm);ac}\epsilon^{c}_{b} + Y_{(lm);bc}\epsilon^{c}_{a}\right) \end{aligned} \tag{A.33}$$

where $N_l = \sqrt{2(l-2)!/(l+2)!}$ is a normalization constant and

$$W_{lm} = 2\left(\frac{\partial^2}{\partial\theta^2} - l(l+1)\right)Y_{lm}, \qquad X_{lm} = 2im\csc\theta(\partial_\theta - \cot\theta)Y_{lm}. \tag{A.34}$$

Also, the standard permutation tensor has the following properties in two dimensions:

$$\begin{aligned} \epsilon_{ab} &= \sqrt{g}\begin{pmatrix} 0 & 1 \\ -1 & 0 \end{pmatrix} = \begin{pmatrix} 0 & \sin\theta \\ -\sin\theta & 0 \end{pmatrix} \\ \epsilon^{a}{}_{b} &= g^{ac}\epsilon_{cb} = \begin{pmatrix} 0 & \sin\theta \\ -\csc\theta & 0 \end{pmatrix} \end{aligned} \tag{A.35}$$

with $g = \mathrm{Det}[g_{ab}]$. The *spin-weighted* spherical harmonics are an alternative basis with which to calculate tensor properties on the sphere, initially formulated for application to gravitational waves. A quantity is said to have a spin weight s if it

transforms like [292, 289]

$$ {}_s\eta' \to e^{is\alpha}{}_s\eta. \tag{A.36} $$

The spin-weighted spherical harmonics are then a generalised form of the spherical harmonics for quantities with spin weight, where

$$ {}_sY_{lm} = \begin{cases} N_{slm}\eth_{s-1}\cdots\eth_0 Y_{lm} & 0 \leq s \leq l \\ N_{slm}(-1)^s\bar{\eth}_{-s+1}\cdots\bar{\eth}_0 Y_{lm} & -l \leq s \leq 0 \\ 0 & l < |s|, \end{cases} \tag{A.37} $$

the N_{slm} term is a normalization factor and the operators $\eth$ and its conjugate $\bar{\eth}$ are given by

$$ \begin{aligned} \eth_s{}_s\eta &= -(\sin)^s(\partial_\theta + i\csc\theta\partial_\phi)(\sin)^{-s}{}_s\eta \\ \bar{\eth}_s{}_s\eta &= -(\sin)^{-s}(\partial_\theta - i\csc\theta\partial_\phi)(\sin)^s{}_s\eta, \end{aligned} \tag{A.38} $$

which act to increment (or decrement for the complex conjugate) the spin-weight s of the spherical harmonic, i.e.,

$$ {}_2Y_{lm} \propto \eth_1\eth_0 Y_{lm}, \qquad {}_{-2}Y_{lm} \propto \bar{\eth}_{-1}\bar{\eth}_2 Y_{lm} \tag{A.39} $$

with the standard spherical harmonics identical to the spin $s = 0$ spin-weighted spherical harmonics. A useful explicit summation for constructing the spin-weighted harmonics is given by

$$ \begin{aligned} {}_sY_{lm}(\theta,\phi) = (-1)^m &\sqrt{\frac{(l+m)!(l+-m)!}{(l+s)!(l-s)!}}\left[\sin\left(\frac{\theta}{2}\right)\right]^{2l} \\ &\times\sum_{r=0}^{l-s}\begin{pmatrix} l-s \\ r \end{pmatrix}\begin{pmatrix} l+s \\ r+s-m \end{pmatrix}(-1)^{l-r-s}e^{im\phi}\left[\cot\left(\frac{\theta}{2}\right)\right]^{2r+s-m}. \end{aligned} \tag{A.40} $$

The spin-weighted basis then allows for a complete harmonic basis that includes the spinor-type rotations, due to the relations between the spin-weighted terms and the spinors given in section 2.2. The equivalence between the tensor and spin-weighted formalisms can be found in O'Donnell [290].

References

[1] Bowyer, J. & Jaffe, A. [2010], "Improved method for detecting local discontinuities in CMB data by finite-differencing", *Phys. Rev. D* **83** 023503 (arXiv:1011.1791)

[2] Bowyer, J., Jaffe, A. & Novikov, D. [2011], "MasQU: Finite Differences on Masked Irregular Stokes Q,U Grids", arXiv:1101.0520

[3] Einstein, A. [1905], "Zur Elektrodynamik bewegter Körper", *Annalen der Physik* **322** 891

[4] Einstein, A. [1916], "Die Grundlage der allgemeinen Relativitätstheorie", *Annalen der Physik* **354** 769

[5] Einstein, A. [1917], "Kosmologische Betrachtungen zur allgemeinen Relativittstheorie", *Sitzungsberichte der Königlich Preussische Akademie der Wissenschaften* 142

[6] Friedmann, A. [1922]. "Über die Krümmung des Raumes", *Zeitschrift für Physik 10* **1** 377

[7] Pais, A. [1982], "Subtle is the Lord: The science and life of Albert Einstein", Oxford University Press

[8] Lemaître, G. [1927], "Un Univers homogène de masse constante et de rayon croissant rendant compte de la vitesse radiale des nébuleuses extra-galactiques", *Annales de la Société Scientifique de Bruxelles*, **47** 49

[9] Hubble, E. [1929], "A Relation between Distance and Radial Velocity among Extra-Galactic Nebulae" *Proceedings of the National Academy of Sciences of the United States of America*, **15** 168

[10] Kragh, H. [1996], "Cosmology and Controversy", Princeton University Press.

[11] Bondi, H. & Gold, T. [1948], "The Steady-State Theory of the Expanding Universe", *Mon. Not. Roy. Astron. Soc.* **108** 252

[12] Mitton, S. [2005], "Fred Hoyle: A life in science", Aurum Press

[13] Alpher, R., Bethe, H. & Gamow, G. [1948], "The Origin of Chemical Elements", *Phys. Rev.* **73** 803

[14] Gamow, G. [1948]. "The evolution of the universe", *Nature* **162** 680

[15] Penzias, A. & Wilson, R. [1965], "A measurement of excess antenna temperature at 4080 Mc/s", *Astrophys. J.* **142**, 419

[16] Naselsky, P., Novikov, D. & Novikov, I. [2006], "The Physics of the Cosmic Microwave Background", Cambridge University Press

[17] Mather, J., Fixsen, D., Shafer, R., Mosier, C. & Wilkinson, D. [1999], "Calibrator Design for the COBE Far Infrared Absolute Spectrophotometer (FIRAS)", *Astrophys. J*, **512** 511 (arXiv:astro-ph/9810373)

[18] Peebles, J. & Yu, J. [1970]. "Primeval Adiabatic Perturbation in an Expanding Universe". *Astrophys. J.* **162** 815

[19] Smoot, G., Bennett, C., Kogut, A., Wright, E., Aymon, J., Boggess, N., Cheng, E., de Amici, G., Gulkis, S., Hauser, M., Hinshaw, G., Jackson, P., Janssen, M., Kaita, E., Kelsall, T., Keegstra, P., Lineweaver, C., Loewenstein, K., Lubin, P., Mather, J., Meyer, S., Moseley, S., Murdock, T., Rokke, L., Silverberg, R., Tenorio, L., Weiss, R. & Wilkinson, D. [1992], "Structure in the COBE differential microwave radiometer first-year maps". *Astrophys. J. Lett.* **396** 1

[20] Melchiorri, A., Ade, P., de Bernardis, P., Bock, J., Borrill, J., Boscaleri, A., Crill, B., De Troia, G., Farese, P., Ferreira, P., Ganga, K., de Gasperis, G., Giacometti, M., Hristov, V., Jaffe, A., Lange, A., Masi, S., Mauskopf, P., Miglio, L., Netterfield, C., Pascale, E., Piacentini, F., Romeo, G., Ruhl, J. & Vittorio, N. [2000], "A Measurement of Omega from the North American Test Flight of Boomerang". *Astrophys. J.* **536** 63, (arXiv:astro-ph/9911445)

[21] Jarosik, N., Bennett, C., Dunkley, J., Gold, B., Greason, M., Halpern, M., Hill, R., Hinshaw, G., Kogut, A., Komatsu, E., Larson, D., Limon, M., Meyer, S., Nolta, M., Odegard, N., Page, L., Smith, K., Spergel,

D., Tucker, G., Weiland, J., Wollack, E. & Wright, E. [2011] "Seven-Year Wilkinson Microwave Anisotropy Probe (WMAP) Observations: Sky Maps, Systematic Errors, and Basic Results" *Astrophys. J. Supp.* **192** 14(arXiv:1001.4744)

[22] Guth, A., "Inflationary universe: A possible solution to the horizon and flatness problems", *Phys. Rev. D* **23**, 347 (1981)

[23] The Planck Collaboration [2006], "The Scientific Programme of Planck", arXiv:astro-ph/0604069

[24] Wald, R. [1984], "General Relativity", University of Chicago Press

[25] Weinberg, S. [1972], "Gravitation and Cosmology", Wiley

[26] Eds. Bonometto, S., Gorini, V. & Moschella, U. [2002], "Modern Cosmology", IoP Publishing

[27] Dodelson, S. [2003], "Modern Cosmology", Academic Press

[28] Mukhanov, V.F. [2005], "Physical Foundations of Cosmology", Cambridge University Press

[29] Durrer, R. [2001], "The theory of CMB anisotropies", *J. Phys. Stud.* **5** 177 (arXiv:astro-ph/0109522)

[30] Liddle, A. & Lyth, D. [2000], "Cosmological Inflation and Large-Scale Structure", Cambridge University Press

[31] Riotto, A. [2002], "Inflation and the Theory of Cosmological Perturbations", arXiv:hep-ph/0210162

[32] Lyth, D. & Riotto, A. [1999], "Particle physics models of inflation and the cosmological density perturbation", *Phys. Rept.* **314** 1 (arXiv:hep-ph/9807278)

[33] Hughes, S. [2008] "Gravitational waves", Summer school in cosmology, The Abdus Salam International Centre for Theoretical Physics (ICTP).

[34] Loveday, J. [2002], "The Sloan Digital Sky Survey", *Contemporary Physics*, **43** 437 (arXiv:astro-ph/0207189)

[35] Abazajian, K. [2009], "The Seventh Data Release of the Sloan Digital Sky Survey", *Astrophys. J. Suppl.* **182** 543 (arXiv:0812.0649)

[36] Mather, J., Cheng, E., Cottingham, D., Eplee Jr, R., Fixsen, D.,Hewagama, T., Isaacman, R., Jensen, K., Meyer, S., Noerdlinger, P., Read, S., Rosen, L., Shafer, R., Wright, E., Bennett, C., Boggess, N.,Hauser, M., Kelsall, T., Moseley Jr., S., Silverberg, R., Smoot, G., Weiss, R. & Wilkinson, D. [1994], "Measurement of the cosmic microwave background spectrum by the COBE FIRAS instrument", *Astrophys. J.* **420** 439

[37] Amsler, C., Doser, M., Antonelli, M., Asner, D., Babu, K., Baer, H., Band, H., Barnett, R., Bergren, E., Beringer, J., Bernardi, G., Bertl, W., Bichsel, H., Biebel, O., Bloch, P., Blucher, E., Blusk, S., Cahn, R., Carena, M., Caso, C., Cecci, A., Chakraborty, D., Chen, M., Chivukula, R., Cowan, G., Dahl, O., D'Ambrosio, G., Damour, T., de Gouvea, A., DeGrand, T., Dobrescu, B., Drees, M., Edwards, D., Eidelman, S., Elvira, V., Erler, J., Ezhela, V., Feng, J., Fetscher, W., Fields, B., Foster, B., Gaisser, T., Garren, L., Gerber, H., Gerbier, G., Gherghetta, T., Giudice, G., Goodman, M., Grab, C., Gritsan, A., Grivaz, J., Groom, D., Gruenewald, M., Gurtu, A., Gutsche, T., Haber, H., Hagiwara, K., Hagmann, C., Hayes, K., Hernandez-Rey, J., Hikasa, K., Hinclilffe, I., Hoecker, A., Huston, J., Igo-Kemenes, P., Jackson, J., Johnson, K., Junk, T., Karlen, D., Kayser, B., Kirkby, D., Klein, S., Knowles, I., Kolda, C., Kowalewski, R., Kreitz, P., Krusche, B., Kuyanov, Y., Kwon, Y., Lahav, O., Langacker, P., Liddle, A., Ligeti, Z., Lin, C., Liss, T., Littenberg, L., Liu, J., Lugovsky, K., Lugovsky, S., Mahlke, H., Mangano, M., Mannel, T., Manohar, A., Marciano, W., Martin, A., Masoni, A., Milstead, D., Miquel, R., Moenig, K., Murayama, H., Nakamura, K., Narain, M., Nason, P., Navas, S., Nevski, P., Nir, Y., Olive, K., Pape, L., Patrignani, C., Peacock, J., Piepke, A., Punzi, G., Quadt, A., Raby, S., Raffelt, G., Rateliff, B., Renk, B., Richardson, P., Roesler, S., Rolli, S., Romaniouk, A., Rosenberg, L., Rosner, J., Sachrajda, C., Sakai, Y., Sarkar, S., Sauli, F., Schneider, O., Scott, D., Seligman, W., Shaevitz, M., Sjostrand, T., Smith, J., Smoot, G., Spanier, S., Spieler, H., Stahl, A., Stanev, T., Stone, S., Surniyoshi, T., Tanabashi, M., Terning, J., Titov, M., Tkachenko, N., Tornqvist, N., Tovey, D., Trilling, G., Trippe, T.,

Valencia, G., van Bibber, K., Vincter, M., Vogel, P., Ward, D., Watari, T., Vebber, B., Weiglein, G., Wells, J., Whalley, M., Wheeler, A., Wohl, C., Wolfenstein, L., Womersley, J., Woody, C., Workmnan, R., Yamamoto, A., Yao, W., Zenin, O., Zhang, J., Zhu, R. & Zyla, P. [2008], "Review of Particle Physics", *Phys. Lett. B* **667** 1

[38] Hannestad, S. [2004], "Neutrino mass bounds from cosmology", arXiv:hep-ph/0412181

[39] Seljak, U. & Zaldarriaga, M. [1996], "A Line of Sight Approach to Cosmic Microwave Background Anisotropies", *Astrophys. J.* **469** 437 (arXiv:astro-ph/9603033)

[40] Zwicky, F. [1933], "Die Rotverschiebung von extragalaktischen Nebeln", *Helvetica Physica Acta* **6** 110

[41] Rubin, V. & Ford, W. [1970], "Rotation of the Andromeda Nebula from a Spectroscopic Survey of Emission Regions", *Astrophys. J.* **159** 379

[42] Clowe, D., Bradac, M., Gonzalez, A., Markevitch, M., Randall, S., Jones, C. & Zaritsky, D. [2006], "A Direct Empirical Proof of the Existence of Dark Matter", *Astrophys. J.* **648** L109 (arXiv:astro-ph/0608407)

[43] Szelc, A. [2010], "Dark Matter Experimental Overview", *Acta Phys. Polon. B* **41** 1417 (arXiv:1010.3918)

[44] Sandick, P. [2010], "Particle Dark Matter: Status and Searches", in "Frank N. Bash Symposium 2009: New Horizons in Astronomy", eds. Stanford, L., Hao, L., Mao, Y. & Green , J., ASP Conference Proceedings (arXiv:1001.0942)

[45] Boylan-Kolchin, M., Springel, V., White, S., Jenkins, A. & Lemson, G. [2009], "Resolving Cosmic Structure Formation with the Millennium-II Simulation" *Mon. Not. Roy. Astron. Soc.* **398** 1150 (arXiv:0903.3041)

[46] Press, W. & Schechter, P. [1974], "Formation of Galaxies and Clusters of Galaxies by Self-Similar Gravitational Condensation", *Astrophys. J.* **187** 425

[47] Peacock, J. [1998], "Cosmological Physics", Cambridge University Press

[48] Evrard, A., MacFarland, T., Couchman, H., Colberg, J., Yoshida, N., White, S., Jenkins, A., Frenk, C., Pearce, F., Peacock, J. & Thomas, P. [2002], "Galaxy Clusters in Hubble Volume Simulations: Cosmological Constraints from Sky Survey Populations", *Astrophys. J.* **573** 7 (arXiv:astro-ph/0110246)

[49] Colless, M., Dalton, G., Maddox, S., Sutherland, W., Norberg, P., Cole, S., Bland-Hawthorn, J., Bridges, T., Cannon, R., Collins, C., Couch, W., Cross, N., Deeley, K., De Propris, R., Driver, S., Efstathiou, G., Ellis, R., Frenk, C., Glazebrook, K., Jackson, C., Lahav, O., Lewis, I., Lumsden, S., Madgwick, D., Peacock, J., Peterson, B., Price, I., Seaborne, M. & Taylor, K. [2001], "The 2dF Galaxy Redshift Survey: spectra and redshifts," *Mon. Not. Roy. Astron. Soc.* **328** 1039 (arXiv:astro-ph/0106498)

[50] Doroshkevich, A., Tucker, D., Allam, S. & Way, M. [2004], "Large Scale Structure in the SDSS Galaxy Survey", *Astron. & Astrophys.* **418** 7 (arXiv:astro-ph/0206301)

[51] Eisenstein, D., Zehavi, I., Hogg, D., Scoccimarro, R., Blanton, M., Nichol, R., Scranton, R., Seo, H-J., Tegmark, M., Zheng, Z., Anderson, S., Annis, J., Bahcall, N., Brinkmann, J., Burles, S., Castander, F., Connolly, A., Csabai, I., Doi, M., Fukugita, M., Frieman, J., Glazebrook, K., Gunn, J., Hendry, J., Hennessy, G., Ivezi, Z., Kent, S., Knapp, G., Lin, H., Loh, Y-S., Lupton, R., Margon, B., McKay, T., Meiksin, A., Munn, J., Pope, A., Richmond, M., Schlegel, D., Schneider, D., Shimasaku, K., Stoughton, C., Strauss, M., SubbaRao, M., Szalay, A., Szapudi, I., Tucker, D., Yanny, B. & York, D. [2005], "Detection of the Baryon Acoustic Peak in the Large-Scale Correlation Function of SDSS Luminous Red Galaxies", *Astrophys. J.* **633** 560 (arXiv:astro-ph/0501171)

[52] Bahcall, N., Dong, F., Bode, P., Kim, R., Annis, J., McKay, T., Hansen, S., Schroeder, J., Gunn, J., Ostriker, J., Postman, M., Nichol, R., Miller, C., Goto, T., Brinkmann, J., Knapp, G., Lamb, D., Schneider, D., Vogeley, M. & York, D. [2003], "The Cluster Mass Function from

Early Sloan Digital Sky Survey Data: Cosmological Implications", *Astrophys. J.* **585** 182 (arXiv:astro-ph/0205490)

[53] Crittenden, R.; Turok, N. [1996], "Looking for Λ with the Rees-Sciama Effect" *Phys. Rev. Lett.* **76** 575 (arXiv:astro-ph/9510072)

[54] Raccanelli, A., Bonaldi, A., Negrello, M., Matarrese, S., Tormen, G. & De Zotti, G. [2008], "A reassessment of the evidence of the Integrated Sachs-Wolfe effect through the WMAP-NVSS correlation", *Mon.Not. Roy. Astron. Soc.* **386** 2161 (arXiv:0802.0084)

[55] Skordis, C. & Silk, J. [2004], "A new method for measuring the CMB temperature quadrupole with an accuracy better than cosmic variance", arXiv:astro-ph/0402474

[56] Seljak, U. [2009], "Measuring primordial non-Gaussianity without cosmic variance" *Phys. Rev. Lett.* **102** 021302 (arXiv:0807.1770)

[57] Portsmouth, J. [2004], "Analysis of the Kamionkowski-Loeb method of reducing cosmic variance with CMB polarization", *Phys. Rev. D* **70** 063504 (arXiv:astro-ph/0402173)

[58] Kamionkowsi, M. & Loeb, A. [1997], "Getting Around Cosmic Variance", *Phys. Rev. D* **56** 4511 (arXiv:astro-ph/9703118)

[59] Tegmark, M. [1997], "How to measure CMB power spectra without losing information", *Phys. Rev. D* **55** 5895 (arXiv:astro-ph/9611174)

[60] Rees. M. [1968], "Polarization and Spectrum of the Primeval Radiation in an Anisotropic Universe", *Astrophys. J.*, **153** Ll

[61] Kamionkowski, M., Koswosky, A. & Stebbins, A. [1997], "Statistics of Cosmic Microwave Background Polarization", *Phys. Rev. D* **55** 7368 (arXiv:astro-ph/9611125)

[62] Hu, W. & White, M. [1997], "A CMB Polarization Primer", *New Astron.* **2** 323 (arXiv:astro-ph/9706147)

[63] Leitch , E., Kovac, J., Pryke, C., Carlstrom, J., Halverson, N., Holzapfel, W., Dragovan, M., Reddall, B. & Sandberg, E. [2002], "Measurement of polarization with the Degree Angular Scale Interferometer" *Nature* **420** 763 (arXiv:astro-ph/0209476)

[64] Linde, A. [2008], "Inflationary Cosmology", *Lect. Notes Phys.* **738** 1 (arXiv:0705.0164)

[65] Starobinsky, A. [1979], "Spectrum Of Relict Gravitational Radiation And The Early State Of The Universe", *JETP Lett.* **30** 682

[66] Starobinsky, A. [1980], "A New Type Of Isotropic Cosmological Models Without Singularity", *Phys. Lett. B* **91** 99

[67] Mukhanov, V. & Chibisov, G. [1981], "Quantum Fluctuation And Nonsingular Universe", *JETP Lett.* **33** 532

[68] Linde, A. [1982], "Scalar Field Fluctuations In Expanding Universe And The New Inflationary Universe Scenario", *Phys. Lett. B* **116** 335

[69] Linde, A. [1983], "Chaotic Inflation", *Phys. Lett. B* **129** 177

[70] Bunch, T. & Davies, P. [1978], "Quantum field theory in de Sitter space; renormalization by point splitting", *Proc. Roy. Soc. A* **354** 59

[71] Dvali, G. & Tye, H. [1999], "Brane Inflation", *Phys. Lett. B* **450** 72 (arXiv:hep-ph/9812483)

[72] Lebedev, O., Nilles, H. & Ratz, M. [2006], "De Sitter Vacua from Matter Superpotentials", *Phys. Lett. B* **636** 126 (arXiv:hep-th/0603047)

[73] Lyth, D. [2008], "Particle physics models of inflation", *Lect. Notes Phys.* **738** 81 (arXiv:hep-th/0702128)

[74] Albrecht, A. & Magueijo, J. [1999], "A time varying speed of light as a solution to cosmological puzzles", *Phys. Rev. D* **59** 043516 (arXiv:astro-ph/9811018)

[75] Magueijo, J. [2000], "Covariant and locally Lorentz-invariant varying speed of light theories", *Phys. Rev. D* **62** 103521 (arXiv:gr-qc/0007036)

[76] Lehners, J. [2008], "Ekpyrotic and cyclic cosmology", *Phys. Rep.* **465** 223 (arXiv:0806.1245)

[77] Buchbinder, E., Khoury, J., Ovrut, B. [2007], "On the Initial Conditions in New Ekpyrotic Cosmology", *JHEP* **0711** 076 (arXiv:0706.3903)

[78] Magueijo, J. [2008], "Speedy sound and cosmic structure", *Phys. Rev. Lett.* **100** 231302 (arXiv:0803.0859)

[79] Tegmark, M. [2008], "The Mathematical Universe", *Found. Phys.* **38** (arXiv:0704.0646)

[80] Maor, I., Krauss, L. & Starkman, G. [2008], "Anthropics and Myopics: Conditional Probabilities and the Cosmological Constant", *Phys. Rev. Lett.* **100** 041301 (arXiv:0709.0502)

[81] Trotta, R. & Starkman, G. [2006], "What's the trouble with anthropic reasoning?" *AIP Conference Proceedings* **878** 323 (arXiv:astro-ph/0610330)

[82] Smolin, L. [2004], "Scientific alternatives to the anthropic principle", in "Universe or Multiverse", ed. Carr, B., Cambridge University Press (arXiv:hep-th/0407213)

[83] Peskin, M. & Schroeder, D. [1995], "An Introduction to Quantum Field Theory", Addison-Wesley

[84] Weinberg, S. [1995] "The Quantum Theory of Fields, Vol 1: Foundations", Cambridge University Press

[85] Gangui, A. [2001], "Topological defects in cosmology", arXiv:astro-ph/0110285

[86] Kibble, T. [1976], "Topology of cosmic domains and strings", *J. Phys. A Math. Gen* **9** 1387

[87] Burgess, C. [2008], "String Cosmology: Cosmic Defects in the Lab", *Nature Physics* **4** 11

[88] Cruz, M., Turok, N., Vielva, P., Martinez-Gonzalez, E. & Hobson, M. [2007], "A cosmic microwave background feature consistent with a cosmic texture", *Science* **318** 1612 (arXiv:0710.5737)

[89] Brandenberger, R. [1993], "Topological Defects and Structure Formation", EPFL lectures, Lausanne, Switzerland (arXiv:astro-ph/9310041)

[90] Frolov, A. [2010], "Nonlinear dynamics and primordial curvature perturbations from preheating ", *Class. Quantum Grav.* **27** 124006 (arXiv:1004.3559)

[91] Vilenkin, A. & Shellard, E. [2000], "Cosmic strings and other topological defects", Cambridge University Press

[92] Kaiser, N. & Stebbins, A. [1984], "Microwave Anisotropy due to Cosmic Strings", *Nature* **310** 391

[93] Battye, R. & Moss, A. [2010], "Updated constraints on the cosmic string tension", *Phys. Rev. D* **82** 023521 (arXiv:1005.0479)

[94] Garcia-Bellido, J., Durrer, R., Fenu, E., Figueroa, D. & Kunz, M. [2011], "The local B-polarization of the CMB: a very sensitive probe of cosmic defects", *Phys. Lett. B* **695** 26 (arXiv:1003.0299)

[95] Komatsu, E. [2001], "The Pursuit of Non-Gaussian Fluctuations in the Cosmic Microwave Background", Ph.D. Thesis, Tohoku University, (arXiv:astro-ph/0206039)

[96] Yadav, A. & Wandelt, B. [2010], "Primordial Non-Gaussianity in the Cosmic Microwave Background", *Advances in Astron.* **2010** 1 (arXiv:1006.0275)

[97] Creminelli, P., Senatore, L., Zaldarriaga, M. & Tegmark, M. [2007], "Limits on f_{NL} parameters from WMAP 3yr data", *JCAP* **0703** 005 (arXiv:astro-ph/0610600)

[98] Baumann, D. [2009], "TASI Lectures on Inflation", arXiv:0907.5424

[99] Abramo, L. & Pereira, T. [2010], "Testing Gaussianity, homogeneity and isotropy with the cosmic microwave background", *Advances in Astron.* **2010** 1 (arXiv:1002.3173)

[100] Munshi, D., Coles, P., Cooray, A., Heavens, A. & Smidt, J. [2010], "Primordial Non-Gaussianity from a Joint Analysis of Cosmic Microwave Background Temperature and Polarization", arXiv:1002.4998

[101] McEwen, J., Hobson, M., Lasenby, A. & Mortlock, D. [2008], "A high-significance detection of non-Gaussianity in the WMAP 5-year

data using directional spherical wavelets", *Mon. Not. Roy. Astron. Soc.* **388** 659 (arXiv:0803.2157)

[102] Yadav, A. & Wandelt, B. [2008], "Detection of primordial non-Gaussianity (fNL) in the WMAP 3-year data at above 99.5% confidence", *Phys. Rev. Lett.* **100** 181 (arXiv:0712.1148)

[103] Senatore, L., Tassev, S. & Zaldarriaga, M. [2009], "Cosmological Perturbations at Second Order and Recombination Perturbed", *JCAP* **0908** 031 (arXiv:0812.3652)

[104] D'Amico, G., Bartolo, N., Matarrese, S. & Riotto, A. [2008], "CMB temperature anisotropies from third order gravitational perturbations", *JCAP* **0801** 005 (arXiv:0707.2894)

[105] Bowden, M., Taylor, A., Ganga, K., Ade, P., Bock, J., Cahill, G., Carlstrom, J., Church, S., Gear, W., Hinderks, J., Hu, W., Keating, B., Kovac, J., Lange, A., Leitch, E., Mallie, O., Melhuish, S., Murphy, J., Piccirillo, L., Pryke, C., Rusholme, B., O'Sullivan, C. & Thompson, K. [2004], "Scientific optimization of a ground-based CMB polarization experiment", *Mon. Not. Roy. Astron. Soc.* **349** 321 (arXiv:astro-ph/0309610)

[106] Gong, J. [2009], "The lessons from the running of the tensor-to-scalar ratio", *Phys. Rev. D* **79** 063520 (arXiv:0710.3835)

[107] Seery D., Lidsey J., & Sloth M. [2007], "The inflationary trispectrum", *JCAP* **0701** 027 (arXiv:astro-ph/0610210)

[108] Lewis, A. [2004], "Observable primordial vector modes", *Phys. Rev. D* **70** 043518 (arXiv:astro-ph/0403583)

[109] Christopherson, A. & Malik, K. [2010], "Can cosmological perturbations produce early universe vorticity?", arXiv:1010.4885

[110] Hertzberg, M., Tegmark, M. & Wilczek, F. [2008], "Axion Cosmology and the Energy Scale of Inflation" *Phys. Rev. D* **78** 083507 (arXiv:0807.1726)

[111] Kallosh, R., Sivanandam, N. & Soroush, M. [2008], "Axion Inflation and Gravity Waves in String Theory", *Phys. Rev. D* **77** 043501 (arXiv:0710.3429)

[112] Armendariz-Picon, C. [2007], "Why should primordial perturbations be in a vacuum state?", *JCAP* **0702** 031 (arXiv:astro-ph/0612288)

[113] Aguirre, A., Tegmark, M. & Layzer, D. [2010], "Born in an Infinite Universe: a Cosmological Interpretation of Quantum Mechanics", arXiv:1008.1066

[114] Perez, A., Sahlmann, H. & Sudarsky, D. [2006], "On the quantum origin of the seeds of cosmic structure", *Class. Quant. Grav.* **23** 2317 (arXiv:gr-qc/0508100)

[115] Valentini, A. [2009], "Beyond the Quantum", *Phys. World* **22N11** 32 (arXiv:1001.2758)

[116] Baskaran, D., Grischuk, L. & Polnarev, A. [2006], "Imprints of relic gravitational waves in cosmic microwave background radiation", *Phys.Rev. D* **74** 083008 (arXiv:gr-qc/0605100)

[117] Cabella, P., Natoli, P. & Silk, J. [2007], "Constraints on CPT violation from WMAP three year polarization data: a wavelet analysis", *Phys. Rev. D* **76** 123014 (arXiv:0705.0810)

[118] Carroll, S., Field, G. & Jackiw, R. [1990], "Limits on a Lorentz- and parity-violating modification of electrodynamics", *Phys. Rev. D* **41**, 1231

[119] Contaldi, C., Magueijo, J. & Smolin, L. [2008], "Anomalous CMB polarization and gravitational chirality", *Phys. Rev. Lett.* **101** 14110 (arXiv:0806.3082)

[120] Magueijo, J. & Benincasa, D. [2010], "Chiral vacuum fluctuations in quantum gravity", arXiv:1010.3552

[121] Satoh, M., Kanno, S. & Soda, J. [2008], "Circular Polarization of Primordial Gravitational Waves in String-inspired Inflationary Cosmology", *Phys. Rev. D* **77** 023526 (arXiv:0706.3585)

[122] Finelli, F. & Galaverni, M. [2009], "Rotation of Linear Polarization Plane and Circular Polarization from Cosmological Pseudoscalar Fields", *Phys. Rev. D* **79** 063002 (arXiv:0802.4210)

[123] Yamazaki, D., Ichiki, K., Kajino, T. & Mathews, G. [2008], "Effects of a primordial magnetic field on low and high multipoles of the CMB", *Phys. Rev. D* **77** 043005 (arXiv:0801.2572)

[124] Kristiansen, J. & Ferreira, P. [2008], "Constraining primordial magnetic fields with CMB polarization experiments", *Phys. Rev. D* **77** 123004 (arXiv:0803.3210)

[125] Miller, N., Shimon, M. & Keating, B. [2009], "CMB Polarization Systematics Due to Beam Asymmetry: Impact on Cosmological Birefringence", *Phys. Rev. D* **79** 103002 (arXiv:0903.1116)

[126] Lewis, A. & Challinor, A. [2006], "Weak Gravitational Lensing of the CMB", *Phys. Rept.* **429** 1 (arXiv:astro-ph/0601594)

[127] Aghanim, N., Majumdar, S. & Silk, J. [2008], "Secondary anisotropies of the CMB", *Rep. Prog. Phys.* **71** 066902 (arXiv:0711.0518)

[128] Li, C & Cooray, A. [2006], "Weak Lensing of the Cosmic Microwave Background by Foreground Gravitational Waves", *Phys. Rev. D* **74** 023521 (arXiv:astro-ph/0604179)

[129] Hanson, D., Challinor, A. & Lewis, A. [2009], "Weak lensing of the CMB", arXiv:0911.0612

[130] Choudhury, T. & Ferrara, A. [2006], "Physics of Cosmic Reionization", arXiv:astro-ph/0603149

[131] Ciardi, B. & Madau, P. [2003], "Probing Beyond the Epoch of Hydrogen Reionization with 21 Centimeter Radiation", *Astrophys. J.* **596** 1 (arXiv:astro-ph/0303249)

[132] Loeb, A. & Zaldarriaga, M. [2004], "Measuring the Small-Scale Power Spectrum of Cosmic Density Fluctuations Through 21 cm Tomography Prior to the Epoch of Structure Formation", *Phys. Rev. Lett.* **92** 211301 (arXiv:astro-ph/0312134)

[133] Santos, M., Cooray, A. & Knox, L. [2005], "Multifrequency analysis of 21 cm fluctuations from the Era of Reionization", *Astrophys. J.* **625** 575 (arXiv:astro-ph/0408515)

[134] Lazarian, A. [2001], "Polarized Microwave Radiation from Dust", arXiv:astro-ph/0101001

[135] Dickinson, C. [2010], "Polarized CMB Foregrounds: What do we know and how bad is it?", arXiv:1005.2572

[136] Carretti, E. [2010], "Galactic foregrounds and CMB polarization", arXiv:1008.4983

[137] Scoccola, C., Harari, D. & Mollerach, S. [2004], "B polarization of the CMB from Faraday rotation", *Phys. Rev. D* **70** 063003, (arXiv:astro-ph/0405396)

[138] Giovannini, M. & Kunze, K. [2009], "Birefringence, CMB polarization and magnetized B-mode", *Phys. Rev. D* **79** 087301 (arXiv:0812.2804)

[139] Gluscevic, V., Kamionkowski, M. & Cooray, A. [2009], "De-Rotation of the Cosmic Microwave Background Polarization: Full-Sky Formalism", *Phys. Rev. D* **80** 023510 (arXiv:0905.1687)

[140] Kim, J. [2007], "Optimizing interferometer experiments for CMB B mode measurement", *Mon. Not. Roy. Astron. Soc.* **375** 615-624 (arXiv:astro-ph/0611564)

[141] Pagano, L., de Bernardis, P., De Troia, G., Gubitosi, G., Masi, S., Melchiorri, A., Natoli, P., Piacentini, F. & Polenta, G. [2009], "CMB Polarization Systematics, Cosmological Birefringence and the Gravitational Waves Background", *Phys. Rev. D* **80** 043522 (arXiv:0905.1651)

[142] Hu, W., Hedman, M. & Zaldarriaga, M. [2003], "Benchmark Parameters for CMB Polarization Experiments", *Phys. Rev. D* **67** 043004, (arXiv:astro-ph/0210096)

[143] Yadav, A., Su, M. & Zaldarriaga, M., "Primordial B-mode Diagnostics and Self Calibrating the CMB Polarization", *Phys. Rev. D* **81** 063512 (arXiv:0912.3532)

[144] Philhour, B [2002], "Measurement of the Polarization of the Cosmic Microwave Background", Ph.D. thesis, California Institute of Technology

[145] Miller, N., Shimon, M. & Keating, B. [2009], "CMB Polarization Systematics Due to Beam Asymmetry: Impact on Cosmological Birefringence", *Phys. Rev. D* **79** 103002, (arXiv:0903.1116)

[146] Hinshaw, G., Barnes, C., Bennett, C., Greason, M., Halpern, M., Hill, R., Jarosik, N., Kogut, A., Limon, M., Meyer, S., Odegard, N., Page, L., Spergel, D., Tucker, G., Weiland, J., Wollack, E. & Wright, E. [2003], "First Year Wilkinson Microwave Anisotropy Probe (WMAP) Observations: Data Processing Methods and Systematic Errors Limits", *Astrophys. J. Supp.* **148** 63 (arXiv:astro-ph/0302222)

[147] Kogut, A., Spergel, D., Barnes, C., Bennett, C., Halpern, M., Hinshaw, G., Jarosik, N., Limon, M., Meyer, S., Page, L., Tucker, G., Wollack, E. & Wright, E. [2003], "Wilkinson Microwave Anisotropy Probe (WMAP) First Year Observations: TE Polarization", *Astrophys. J. Supp.* **148** 161 (arXiv:astro-ph/0302213)

[148] Komatsu, E., Dunkley, J., Nolta, M., Bennett, C., Gold, B., Hinshaw, G., Jarosik, N., Larson, D., Limon, M., Page, L., Spergel, D., Halpern, M., Hill, R., Kogut, A., Meyer, S., Tucker, G., Weiland, J., Wollack, E. & Wright, E. [2009], "Five-Year Wilkinson Microwave Anisotropy Probe (WMAP) Observations: Cosmological Interpretation", *Astrophys. J. Supp.* **180** 330 (arXiv:0803.0547)

[149] Komatsu, E., Smith, K., Dunkley, J., Bennett, C., Gold, B., Hinshaw, G., Jarosik, N., Larson, D., Nolta, M., Page, L., Spergel, D., Halpern, M., Hill, R., Kogut, A., Limon, M., Meyer, S., Odegard, N., Tucker, G., Weiland, J., Wollack, E. & Wright, E. [2011], "Seven-Year Wilkinson Microwave Anisotropy Probe (WMAP) Observations: Cosmological Interpretation", *Astrophys. J. Supp.* **192** 18 (arXiv:1001.4538)

[150] Samtleben, D. [2008], "QUIET — Measuring the CMB polarization with coherent detector arrays", arXiv:0806.4334

[151] Kovac, J., Leitch, E., Pryke, C., Carlstrom, J., Halverson, N. & Holzapfel, W. [2002], "Detection of polarization in the cosmic microwave background using DASI", *Nature* **420** 772 (arXiv:astro-ph/0209478)

[152] Montroy, T., Ade, P., Balbi, A., Bock, J., Bond, J., Borrill, J., Boscaleri, A., Cabella, P., Contaldi, C., Crill, B., de Bernardis, P., De Gasperis, G., de Oliveira-Costa, A., De Troia, G., di Stefano, G., Ganga, K., Hivon, E., Hristov, V., Iacoangeli, A., Jaffe, A., Kisner, T., Jones, W., Lange, A., Masi, S., Mauskopf, P., MacTavish, C., Melchiorri, A., Nati, F., Natoli, P., Netterfield, C., Pascale, E., Piacentini, F., Pogosyan, D., Polenta, G., Prunet, S., Ricciardi, S., Romeo, G., Ruhl, J., Torbet, E., Tegmark, M. & Vittorio, N. [2003], "Measuring CMB Polarization with BOOMERANG", *New Astron. Rev.* **47** 1057 (arXiv:astro-ph/0305593)

[153] Montroy, T., Ade, P., Bock, J., Bond, J., Borrill, J., Boscaleri, A., Cabella, P., Contaldi, C., Crill, B., de Bernardis, P., De Gasperis, G., de Oliveira-Costa, A., De Troia, G., di Stefano, G., Hivon, E., Jaffe, A., Kisner, T., Jones, W., Lange, A., Masi, S., Mauskopf, P., MacTavish, C., Melchiorri, A., Natoli, P., Netterfield, C., Pascale, E., Piacentini, F., Pogosyan, D., Polenta, G., Prunet, S., Ricciardi, S., Romeo, G., Ruhl, J., Santini, P., Tegmark, M., Veneziani, M. & Vittorio, N. [2006], "Cosmological Parameters from the 2003 flight of BOOMERANG", *Astrophys. J.* **647** 813 (arXiv:astro-ph/0507514)

[154] Readhead, A., Myers, S., Pearson, T., Sievers, J., Mason, B., Contaldi, C., Bond, J., Bustos, R., Altamirano, P., Achermann, C., Bronfman, L., Carlstrom, J., Cartwright, J., Casassus, S., Dickinson, C., Holzapfel, W., Kovac, J., Leitch, E., May, J., Padin, S., Pogosyan, D., Pospieszalski, M., Pryke, C., Reeves, R., Shepherd, M. & Torres, S. [2004], "Polarization Observations with the Cosmic Background Imager". *Science* **306** 836 (arXiv:astro-ph/0409569)

[155] The QUaD collaboration [2009], "Improved measurements of the temperature and polarization of the CMB from QUaD", *Astrophys. J.* **705** 978 (arXiv:0906.1003)

[156] The QUaD collaboration [2009], "QUaD: A High-Resolution Cosmic Microwave Background Polarimeter", *Astrophys. J.* **692** 1221 (arXiv:0805.1990)

[157] Tauber, J. *et al* [2010], "Planck pre-launch status: The Planck mission", *Astron. & Astrophys.* **520** A1

[158] Crill, B., Ade, P., Battistelli, E., Benton, S., Bihary, R., Bock, J., Bond, J., Brevik, J., Bryan, S., Contaldi, C., Dore, O., Farhang, M., Fissel, L., Golwala, S., Halpern, M., Hilton, G., Holmes, W., Hristov, V., Irwin, K., Jones, W., Kuo, C., Lange, A., Lawrie, C., MacTavish, C., Martin, T., Mason, P., Montroy, T., Netterfield, C., Pascale, E., Riley, D., Ruhl, J., Runyan, M., Trangsrud, A., Tucker, C., Turner, A., Viero, M. & Wiebe, D. [2008], "SPIDER: A Balloon-borne Large-scale CMB Polarimeter", arXiv:0807.1548

[159] Kaplan, J. [2009], "QUBIC, a bolometric interferometer to measure the B modes of the CMB" arXiv:0910.0391

[160] Errard, J. [2010], "The new generation CMB B-mode polarization experiment: POLARBEAR", arXiv:1011.0763

[161] Fraisse, A., Brown, J., Dobler, G., Dotson, J., Draine, B., Frisch, P., Haverkorn, M., Hirata, C., Jansson, R., Lazarian, A., Magalhes, A., Waelkens, A. & Wolleben, M. [2008], "CMBPol Mission Concept Study: Foreground Science Knowledge and Prospects", arXiv:0811.3920

[162] Cox, R. [1961], "The Algebra of Probable Inference", John Hopkins Press

[163] Verde, L. [2007], "A practical guide to Basic Statistical Techniques for Data Analysis in Cosmology", arXiv:0712.3028

[164] Mielczarek, J., Szydlowski, M. & Tambor, P. [2009], "Bayesian reasoning in cosmology", arXiv:0901.4075

[165] Babu, J. [2008], "2008 Summer School in Astrostatistics Lectures Notes", Summer school in astrostatistics, The Pennsylvania State University

[166] Skilling, J. [2010], "Foundations and Algorithms" in "Bayesian Methods in Cosmology', eds. Hobson, M., Jaffe, A.H., Liddle, A., Mukherjee, P. & Parkinson, D., Cambridge University Press

[167] Shannon, C. [1948], "A mathematical theory of communication", *Bell System Techn. J.* **27** 379

[168] Shannon, C. & Weaver, W. [1949], "The Mathematical Theory of Communication" University of Illinois Press

[169] Jaynes, E. [2003], "Probability Theory: The Logic of Science", Cambridge University Press

[170] MacKay, D. [2002], "Information Theory, Inference & Learning Algorithms", Cambridge University Press

[171] Zaldarriaga, M. & Seljak, U. [1997], "An All-Sky Analysis of Polarization in the Microwave Background", *Phys. Rev. D* **55** 1830 (arXiv:astro-ph/9609170)

[172] Klain, D. & Rota, G. [1997], "Introduction to geometric probability", Cambridge University Press

[173] Babich, D. [2005], "Optimal Estimation of Non-Gaussianity", *Phys. Rev. D* **72** 043003 (arXiv:astro-ph/0503375)

[174] Press, W., Flannery, B., Teukolsky, S. & Vetterling, W. [2007], "Numerical Recipes: The Art of Scientific Computing" 3rd Ed., Cambridge University Press

[175] Lewis, A. & Bridle, S. [2002], "Cosmological parameters from CMB and other data: a Monte-Carlo approach", *Phys. Rev. D* **66** 103511 (arXiv:astro-ph/0205436)

[176] Christensen, N., Meyer, R., Knox, L. & Luey, B. [2001], "Bayesian Methods for Cosmological Parameter Estimation from Cosmic Microwave Background Measurements", *Class. Quant. Grav.* **18** 2677 (arXiv:astro-ph/0103134)

[177] Metropolis, N., Rosenbluth, A., Rosenbluth, M., Teller, A. & Teller, E. [1953], "Equation of State Calculations by Fast Computing Machines", *J. Chem. Phys.* **21** 1087

[178] Hastings, W. [1970], "Monte Carlo sampling methods using Markov chains and their applications", *Biometrika* **57** 97

[179] Dunkley, J., Bucher, M., Ferreira, P., Moodley, K. & Skordis, C. [2005], "Fast and reliable MCMC for cosmological parameter estimation", *Mon. Not. Roy. Astron. Soc.* **356** 925 (arXiv:astro-ph/0405462)

[180] Raftery, A. & Lewis, S. [1992], "How many iterations in the Gibbs sampler?", in *Bayesian Statistics* Ed. Bernado, J., OUP

[181] Komatsu, E., Spergel, D. & Wandelt, B. [2005], "Measuring primordial non-Gaussianity in the cosmic microwave background", *Astrophys. J.* **634** 14 (arXiv:astro-ph/0305189)

[182] Creminell, P., Senatore, L. & Zaldarriaga, M. [2007], "Estimators for local non-Gaussianities", *JCAP* **0703** 019 (arXiv:astro-ph/0606001)

[183] Elsner, F., Wandelt, B., Schneider, M. [2010], "Probing local non-Gaussianities within a Bayesian framework", *Astron. & Astrophys.* **513** A59 (arXiv:1002.1713)

[184] Elsner, F. & Wandelt, B. [2010], "Local non-Gaussianity in the Cosmic Microwave Background the Bayesian way", *Astrophys. J.* **724** 1262 (arXiv:1010.1254)

[185] Stuart, A. & Ord, K. [2009], "Kendall's Advanced Theory of Statistics, Vol 1: Distribution Theory", 6th Ed., Wiley

[186] Bernardeau, F, Colombi, S., Gaztanaga, E. & Scoccimarro, R. [2002], "Large-Scale Structure of the Universe and Cosmological Perturbation Theory", *Phys. Rept.* **367** 1 (arXiv:astro-ph/0112551)

[187] Amndola, L. [1996], "Non-Gaussian Chi-squared method with the multivariate Edgeworth expansion", *Astro. Lett. and Communications* **33** 63 (arXiv:astro-ph/9810198)

[188] Rocha, G., Magueijo, J., Hobson, M. & Lasenby, A. [2001], "Bayesian joint estimation of non-Gaussianity and the power spectrum", *Phys. Rev. D* **64** 063512 (arXiv:astro-ph/0008070)

[189] Gaztanaga, E., Fosalba, P. & Elizalde, E. [2000], "Gravitational Evolution of the Large-Scale Probability Density Distribution: The Edgeworth & Gamma Expansions", *Astrophys. J.* **539** 522 (arXiv:astro-ph/9906296)

[190] Newman, E. & Penrose, R. [1966], "Note on the Bondi-Metzner-Sachs Group", *J. Math. Phys.* **7** 863

[191] Lewis, A., Challinor, A. & Turok, N. [2002], "Analysis of CMB polarization on an incomplete sky", *Phys. Rev. D* **65** 023505 (arXiv:astro-ph/0106536)

[192] Bunn, E. [2008], "E/B Mode Mixing", arXiv:0811.0111

[193] Efstathiou, G. [2006], "Hybrid Estimation of CMB Polarization Power Spectra", *Mon. Not. Roy. Astron. Soc.* **370** 343 (arXiv:astro-ph/0601107)

[194] Smith, K. [2006], "Pseudo-C_ℓ estimators which do not mix E and B modes", *Phys. Rev. D* **74** 083002 (arXiv:astro-ph/0511629)

[195] Zhao, W. & Baskaran, D. [2010], "Separating E and B types of polarization on an incomplete sky", *Phys. Rev. D* **82** 023001 (arXiv:1005.1201)

[196] Kim, J. & Naselsky, P. [2010], "CMB E/B decomposition of incomplete sky: a pixel space approach", *Astron. & Astrophys.* **519** A104 (arXiv:1003.2911)

[197] Kim, J. [2010], "How to make clean separation of CMB E and B mode from incomplete sky data", arXiv:1010.2636

[198] Bunn, E. [2010], "Efficient decomposition of cosmic microwave background polarization maps into pure E, pure B, and ambiguous components", arXiv:1008.0827

[199] Cao, L. & Fang, L. [2009], "A wavelet-Galerkin algorithm of the E/B decomposition of CMB polarization maps", *Astrophysical Journal* **706** 1545 (arXiv:0910.4697)

[200] Geller, D., Hansen, F., Marinucci, D., Kerkyacharian, G. & Picard, D. [2008], "Spin Needlets for Cosmic Microwave Background Polarization Data Analysis", *Phys. Rev. D* **78** 123533 (arXiv:0811.2881)

[201] Kostov, I., Ponsot, B. & Serban, D. [2004], "Boundary Liouville Theory and 2D Quantum Gravity", *Nucl. Phys. B* **683** 309 (arXiv:hep-th/0307189)

[202] Rovelli, C. [2004], "Quantum Gravity", Cambridge University Press

[203] Tanaka, T., Amemiya, F., Shimano, M., Harada, T. & Tamaki, T. [2010], "Discretisation parameter and operator ordering in loop quantum cosmology with the cosmological constant", arXiv:1005.2518

[204] Zumbusch, G. [2009], "Finite Element, Discontinuous Galerkin, and Finite Difference Evolution Schemes in Spacetime", *Class. Quant. Grav.* **26** 175011 (arXiv:0901.0851)

[205] Chirvasa, M. & Husa, S. [2010], "Finite Difference Methods for Second Order in Space, First Order in Time Hyperbolic Systems and the Linear Shifted Wave Equation as a Model Problem in Numerical Relativity", *J. Comput. Phys* (arXiv:0812.3752)

[206] Motamed, M., Babiuc, M., Szilagyi, B., Kreiss, H. & Winicour, J. [2006], "Finite difference schemes for second order systems describing black holes", *Phys. Rev. D* **73** 124008 (arXiv:gr-qc/0604010)

[207] Calabrese, G., Hinder, I. & Husa, S. [2006], "Numerical stability for finite difference approximations of Einstein's equations", *J. Comput. Phys.* **218** 607 (arXiv:gr-qc/0503056)

[208] Mignone, A., Tzeferacos, P. & Bodo, G. [2010], "High-order conservative finite difference GLM-MHD schemes for cell-centered MHD", arXiv:1001.2832

[209] Ng, C., Rosenberg, D., Germaschewski, K., Pouquet, A. & Bhattacharjee, A. [2007], "A comparison of spectral element and finite difference methods using statically refined nonconforming grids for the MHD island coalescence instability problem", (arXiv:0711.3868)

[210] Marcus, M. & Minc, H. [1992], 'A Survey of Matrix Theory and Matrix Inequalities', Dover

[211] Ames,W. [1977], "Numerical Methods for Partial Differential Equations", Academic Press

[212] Li, J. [2005], "General explicit difference formulas for numerical differentiation", *J. Comp. & Ap. Math.* **183** 29

[213] Milne-Thompson, L. M., [1933] "The Calculus of Finite Differences", MacMillan and Company

[214] Horn, R. & Johnson, C. [1985], "Matrix Analysis", Cambridge University Press

[215] Arfken, G. [1985], "Mathematical Methods for Physicists", Academic Press

[216] Hivon, E., Gorski, K., Netterfield, C., Crill, B., Prunet, S. & Hansen, F. [2002], "MASTER of the CMB Anisotropy Power Spectrum: A Fast Method for Statistical Analysis of Large and Complex CMB Data Sets", *Astrophys. J.* **567** 2 (arXiv:astro-ph/0105302)

[217] Smith, K. & Zaldarriaga, M. [2007], "A general solution to the E-B mixing problem", *Phys. Rev. D* **76** 043001 (arXiv:astro-ph/0610059)

[218] Spergel, D. & Goldberg, D. [1999], "The Microwave Background Bispectrum, Paper I: Basic Formalism", *Phys. Rev. D* **59** 103001 (arXiv:astro-ph/9811252)

[219] Babich, D. & Zaldarriaga, M. [2004], "Primordial Bispectrum Information from CMB Polarization", *Phys. Rev. D* **70** 083005 (astro-ph/0408455)

[220] Yadav, A., Komatsu, E. & Wandelt, B. [2007], "Fast Estimator of Primordial Non-Gaussianity from Temperature and Polarization Anisotropies in the Cosmic Microwave Background ", *Astrophys. J.* **664** 680 (arXiv:astro-ph/0701921)

[221] Shiraishi, M., Yokoyama, S., Nitta, D., Ichiki, K. & Takahashi, K. [2010], "Analytic formulae of the CMB bispectra generated from non-Gaussianity in the tensor and vector perturbations" *Phys. Rev. D* **82** 103505 (arXiv:1003.2096)

[222] Cooray, A. [2001], "Squared temperature-temperature power spectrum as a probe of the CMB bispectrum", *Phys. Rev. D* **64** 043516 (arXiv:astro-ph/0105415)

[223] Regan, D., Shellard, E. & Fergusson, J. [2010], "General CMB and Primordial Trispectrum Estimation", arXiv:1004.2915

[224] Kamionkowski, M., Smith, T. & Heavens, A. [2010], "The CMB Bispectrum, Trispectrum, non-Gaussianity, and the Cramer-Rao Bound" arXiv:1010.0251

[225] Varshalovich, D., Moskalev, A. & Khersonskii, V. [1988], "Quantum Theory of Angular Momentum", World Scientific

[226] Souradeep, T. & Hajian, A. [2005], "Statistical isotropy of CMB anisotropy from WMAP", arXiv:astro-ph/0502248

[227] Souradeep, T., Hajian, A. & Basak, S. [2006], "Measuring Statistical Isotropy of CMB Anisotropy", *New Astron. Rev.* **50** 889 (arXiv:astro-ph/0607577)

[228] Runge, C. [1901], "Über empirische Funktionen und die Interpolation zwischen äquidistanten Ordinaten", *Zeitschrift für Mathematik und Physik* **46** 224

[229] Carslaw, H. [1930] "Introduction to the theory of Fourier's series and integrals", 3rd Ed., Dover Publications

[230] Gelb, A. [1997], "The resolution of the Gibbs phenomenon for spherical harmonics", *Math. Comput.* **66** 699

[231] Marinucci, D., Pietrobon, D., Balbi, A., Baldi, P., Cabella, P., Kerkyacharian, G., Natoli, P., Picard, D. & Vittorio, N. [2008], "Spherical Needlets for CMB Data Analysis", *Mon. Not. Roy. Astron. Soc.* **383** 539 (arXiv:0707.0844)

[232] Canny, J. [1986], "A computational approach to edge detection", *IEEE Trans. Pattern Analysis and Machine Intelligence* **8** 679

[233] Danos, R & Brandenberger, R. [2010], "Canny Algorithm, Cosmic Strings and the Cosmic Microwave Background", *Int. J. Mod. Phys. D* **19** 183 (arXiv:0811.2004)

[234] Benabed, K. & Bernardeau, F. [1999], "Cosmic string lens effects on CMB polarization patterns", arXiv:astro-ph/9906161

[235] Martinez-Gonzalez, E., Gallegos, J., Argueso, F., Cayon, L. & Sanz, J. [2002], "The performance of spherical wavelets to detect non-Gaussianity in the CMB sky", *Mon. Not. Roy. Astron. Soc.* **336** 22 (arXiv:astro-ph/0111284)

[236] Baldi, P., Kerkyacharian, G., Marinucci, D. & Picard, D. [2009], "Asymptotics for spherical needlets", *Annals of Statistics* **37** 1150 (arXiv:math/0606599)

[237] Starck, J., Moudden, Y. & Bobin, J. [2009], "Polarized wavelets and curvelets on the sphere", arXiv:0902.0574

[238] Baldi, P., Kerkyacharian, G., Marinucci, D. & Picard, D. [2007], "Subsampling needlet coefficients on the sphere", arXiv:0706.4169

[239] Brown, L. [1994], "Renormalization from Lorentz to Landau (and Beyond)", Springer-Verlag

[240] Misner, C., Thorne, K. & Wheeler, J. [1973], "Gravitation", Freeman

[241] Veneziano, G. [1986], "A Stringy Nature Needs Just Two Constants", *Europhys. Lett.* **2** 199

[242] Amati, D., Ciafaloni, M. & Veneziano, G. [1989], "Can spacetime be probed below the string size? " *Phys. Lett. B* **216** 41

[243] Lizzi, F. [2008], "The Structure of Spacetime and Noncommutative Geometry", arXiv:0811.0268

[244] Lizzi, F., Mangano, G., Miele, G. & Peloso, M. [2002], "Cosmological perturbations and short distance physics from Noncommutative Geometry", *JHEP* **0206** 049 (arXiv:hep-th/0203099)

[245] Bombelli, L., Lee, J., Meyer, D. & Sorkin, R. [1987], "Space-time as a causal set", *Phys. Rev. Lett.* **59** 521

[246] Kowalski-Glikman, J. [2005], "Introduction to Doubly Special Relativity", *Lect. Notes Phys.* **669** 131 (arXiv:hep-th/0405273)

[247] Snyder, H. (1947), "Quantized space-time", *Phys. Rev. D* **67** 3841

[248] Ashoorioon, A., Kempf, A. & Mann, R. [2005], "Minimum Length Cutoff in Inflation and Uniqueness of the Action", *Phys. Rev. D* **71** 023503 (arXiv:astro-ph/0410139)

[249] Kowalski-Glikman, J. [2001], "Testing Dispersion Relations of Quantum κ-Poincar Algebra on Cosmological Ground", *Phys. Lett. B* **499** 1 (arXiv:astro-ph/0006250)

[250] Niemeyer, J. & Parentani, R. [2001], "Trans-Planckian dispersion and scale-invariance of inflationary perturbations", *Phys. Rev. D* **64** 101301 (arXiv:astro-ph/0101451)

[251] Kempf, A. & Niemeyer, J. [2001], "Perturbation spectrum in inflation with cutoff", *Phys. Rev. D* **64** 103501 (arXiv:astro-ph/0103225)

[252] Easther, R., Greene, B., Kinney, W. & Shiu, G. [2003], "Imprints of Short Distance Physics On Inflationary Cosmology", *Phys. Rev. D* **67** 063508 (arXiv:hep-th/0110226)

[253] 't Hooft, G. [1993], "Dimensional Reduction in Quantum Gravity", arXiv:gr-qc/9310026

[254] Bousso, R. [2002], "The holographic principle", *Rev. Mod. Phys.* **74** 825, (arXiv:hep-th/0203101)

[255] Bardeen, J., Carter, B. & Hawking, S. [1973]. "The four laws of black hole mechanics", *Comm. Math. Phys.* **31** 161

[256] Bekenstein, J. [1973], "Black holes and entropy", *Phys. Rev. D* **7** 2333

[257] Bousso, R. [2000], "Positive vacuum energy and the N-bound", *JHEP* **0011** 038, (arXiv:hep-th/0010252)

[258] Hogan, C. [2005] "Discrete Quantum Spectrum of Observable Correlations from Inflation", arXiv:astro-ph/0504364

[259] Hogan, C. [2002], "Holographic Discreteness of Inflationary Perturbations", *Phys. Rev. D* **66** 023521 (arXiv:astro-ph/0201020)

[260] Golub, G. & van Loen, C. [1996], "Matrix Computations", 3rd ed., John Hopkins Press

[261] Gorski, K., Hivon, E., Banday, A., Wandelt, B., Hansen, F., Reinecke, M. & Bartelman, M. [2005], "HEALPix – a Framework for High Resolution Discretization, and Fast Analysis of Data Distributed on the Sphere", *Astrophys. J.* **622** 759 (arXiv:astro-ph/0409513)

[262] Gorski, K., Wandelt, B., Hansen, F., Hivon, E. & Banday, A. [1999], "The HEALPix Primer", arXiv:astro-ph/9905275

[263] White, R. & Stemwedel, S. [1992], "The Quadrilateralized Spherical Cube and Quad-Tree For All Sky Data" in *ASP Conf. Ser.* **25** 379, *Astronomical Data Analysis, Software and Systems I*, eds. Worrall, D., Biemesderfer, C. & Barnes, J.

[264] Doroshkevich, A.G., Naselsky, P., Verkhodanov, O., Novikov, D., Turchaninov, V., Novikov, I., Christensen, P. & Chiang, L. [2005], "Gauss-Legendre Sky Pixelization (GLESP) for CMB maps", *Int. J. Mod. Phys. D* **14** 275 (arXiv:astro-ph/0305537)

[265] Anderson, E., Bai, Z., Bischof, C., Blackford, S., Demmel, J., Dongarra, J., Du Croz, J., Greenbaum, A., Hammarling, S., McKenney, A. & Sorensen, D. [1999], "LAPACK User's Guide", 3rd Ed., SIAM

[266] Wedin, P. & Wikstrom. G. [2002], "First Order Error Analysis of a Linear System of Equations by use of Error Propagation Matrices connected to the Pseudoinverse Solution", Technical Report UMINF-02.16, Department of Computing Science, Umea University

[267] Yakimiw, E. [1996], "Accurate computation of weights in classical Gauss-Christoffel quadrature rules", *J. Comp. Phys.* **129** 406

[268] Gradshteyn, I. & Ryzhik, I. [2007], "Table of Integrals, Series and Products, 7th Ed.", Academic Press

[269] Oxley, P., Ade, P., Baccigalupi, C., deBernardis, P., Cho, H–M., Devlin, M., Hanany, S., Johnson, B., Jones, T., Lee, A., Matsumura, T., Miller, A., Milligan, M., Renbarger, T., Spieler, H., Stompor, R., Tucker, G. & Zaldarriaga, M. [2004], "The EBEX Experiment", *Proc. SPIEInt. Soc. Opt. Eng.* **5543** 320 (arXiv:astro-ph/0501111)

[270] Stivoli, F., Grain, J., Leach, S., Tristram, M., Baccigalupi, C. & Stompor, R. [2010], "Maximum likelihood, parametric component separation and CMB B-mode detection in suborbital experiments", *Mon. Not. Roy. Astron. Soc.* **408** 2319 (arXiv:1004.4756)

[271] Shewchuk, J. [1994], "An Introduction to the Conjugate Gradient Method without the agonzing pain", ACM Technical Report

[272] Jarosik, N., Barnes, C., Greason, M., Hill, R., Nolta, M., Odegard, N., Weiland, J., Bean, R., Bennett, C., Dor, O., Halpern, M., Hinshaw, G., Kogut, A., Komatsu, E., Limon, M., Meyer, S., Page, L., Spergel, D., Tucker, G., Wollack, E. & Wright, E. [2007], "Three-Year Wilkinson Microwave Anisotropy Probe (WMAP) Observations: Beam Profiles, Data Processing, Radiometer Characterization and Systematic Error Limits", *Astrophys. J. Suppl.* **170** 263 (arXiv:astro-ph/0603452)

[273] Hinshaw, G., Nolta, M., Bennett, C., Bean, R., Dor, O., Greason, M., Halpern, M., Hill, R., Jarosik, N., Kogut, A., Komatsu, E., Limon, M., Odegard, N., Meyer, S., Page, L., Peiris, H., Spergel, D., Tucker, G., Verde, L., Weiland, J., Wollack, E. & Wright, E. [2007], "Three-Year Wilkinson Microwave Anisotropy Probe (WMAP) Observations: Temperature Analysis", *Astrophys. J. Suppl.* **170** 288 (arXiv:astro-ph/0603451)

[274] Eriksen, H., Banday, A., Gorski, K. & Lilje, P. [2004], "On Foreground Removal from the Wilkinson Microwave Anisotropy Probe Data by an Internal Linear Combination Method: Limitations and Implications", *Astrophys. J.* **612** 633 (arXiv:astro-ph/0403098)

[275] Gold, B., Odegard, N., Weiland, J., Hill, R., Kogut, A., Bennett, C., Hinshaw, G., Chen, X., Dunkley, J., Halpern, M., Jarosik, N., Komatsu, E., Larson, D., Limon, M., Meyer, S., Nolta, M., Page, L., Smith, K., Spergel, D., Tucker, G., Wollack, E. & Wright, E. [2010], "Seven-Year Wilkinson Microwave Anisotropy Probe (WMAP) Observations: Galactic Foreground Emission", *Astrophys. J. Supp.* **192** 15 (arXiv:1001.4555)

[276] Kim, J., Naselsky, P. & Christensen, P. [2009], "CMB polarization map derived from the WMAP 5 year data through Harmonic Internal Linear Combination", *Phys. Rev. D* **79** 023003 (arXiv:0810.4008)

[277] Doroshkevich, A. & Verkhodanov, O. [2010], "CMB component separation in the pixel domain", arXiv:1008.4094

[278] Bennett, C., Bay, M., Halpern, M., Hinshaw, G., Jackson, C., Jarosik, N., Kogut, A., Limon, M., Meyer, S., Page, L., Spergel, D., Tucker, G., Wilkinson, D., Wollack, E. & Wright, E. [2003], "The Microwave Anisotropy Probe (MAP) Mission", *Astrophys. J.* **583** 1 (arXiv:astro-ph/0301158)

[279] D'Arcangelo, O., Figini, L., Simonetto, A., Villa, F., Pecora, M., Battaglia, P., Bersanelli, M., Butler, R., Cuttaia, F., Garavaglia, S., Guzzi, P., Mandolesi, N., Mennella, A., Morgante, G., Pagan, L. & Valenziano, L. [2009], "The Planck-LFI flight model composite waveguides", *JINST* **4** T12007 (arXiv:1001.4711)

[280] Dupac, X. & Tauber, J. [2005], "Scanning strategy for mapping the Cosmic Microwave Background anisotropies with Planck", *Astron. & Astrophys.* **430** 363 (arXiv:astro-ph/0409405)

[281] Burigana, C., Destri, C., de Vega, H., Gruppuso, A., Mandolesi, N., Natoli, P. & Sanchez, N. [2010], "Forecast for the Planck precision on the tensor to scalar ratio and other cosmological parameters", *Astrophys. J.* **724** 528 (arXiv:1003.6108)

[282] Dick, J., Remazeilles, M. & Delabrouille, J. [2009], "Impact of calibration errors on CMB component separation using FastICA and ILC", arXiv:0907.3105

[283] Bennett, C., Hill, R., Hinshaw, G., Larson, D., Smith, K., Dunkley, J., Gold, B., Halpern, M., Jarosik, N., Kogut, A., Komatsu, E., Limon, M., Meyer, S., Nolta, M., Odegard, N., Page, L., Spergel, D., Tucker, G., Weiland, J., Wollack, E. & Wright, E. [2011], "Seven-Year Wilkinson Microwave Anisotropy Probe (WMAP) Observations: Are There Cosmic Microwave Background Anomalies?", *Astrophys. J. Supp.* **192** 17 (arXiv:1001.4758)

[284] Feeney, S., Johnson, M., Mortlock, D. & Peiris, H. [2010], "First Observational Tests of Eternal Inflation", arXiv:1012.1995

[285] Zhang, R. & Huterer, D. [2010], "Disks in the sky: A reassessment of the WMAP "cold spot""*Astroparticle Phys.* **33** 69 (arXiv:0908.3988)

[286] Tegmark, M., de Oliveira-Costa, A. & Hamilton, A. [2003], "A high resolution foreground cleaned CMB map from WMAP", *Phys. Rev. D* **68** 123523 (arXiv:astro-ph/0302496)

[287] Bennett, C., Smoot, G., Hinshaw, G., Wright, E., Kogut, A., De Amici, G., Meyer, S., Weiss, R., Wilkinson, D., Gulkis, S., Janssen, M., Boggess, N., Cheng, E., Hauser, M., Kelsall, T., Mather, J., Moseley, S., Murdock, T. & Silverberg, R. [1992], "Preliminary Separations of Galactic and Cosmic Microwave Emission for the COBE Differential Microwave Radiometer", *Astrophys. J.* **396** L7

[288] Copi, C., Huterer, D., Schwarz, D. & Starkman, G. [2010], "Large-angle anomalies in the CMB", *Advances in Astron.* vol. 2010 1 (arXiv:1004.5602)

[289] Torres del Castillo, G. [2003], "3-D Spinors, Spin-Weighted Functions and Their Applications", Birkhauser

[290] O'Donnell, P. [2003],"Introduction to 2-Spinors in General Relativity", World Scientific

[291] Stebbins, A. [1996], "Weak lensing on the celestial sphere", (arXiv:astro-ph/9609149)

[292] Goldberg, J., Macfarlane, A., Newman, E., Rohrlich, F. & Sudarshan, E. [1967], "Spin-s Spherical Harmonics and $\eth$", *J. Math. Phys.* **8** 2155